Evolution of irradiation defects in fusion structural steels at high temperatures

Zur Erlangung des akademischen Grades eines

Doktors der Ingenieurwissenschaften (Dr.-Ing.)

von der KIT-Fakultät für Maschinenbau des

Karlsruher Instituts für Technologie (KIT)

angenommene

Dissertation

von

M. Sc. Qian Yuan

aus

Shanghai, China

Tag der mündlichen Prüfung:	14. Dezember 2022
Referent:	Prof. Dr.-Ing. Jarir Aktaa
Korreferent:	Prof. Dr. rer. nat. Anton Möslang

Abstract

Reduced-activation ferritic martensitic (RAFM) steel EUROFER97 is a candidate structural material for the first wall of future nuclear fusion reactor DEMO. Despite many advantages over traditional austenitic steels used in nuclear fission reactors such as excellent resistance against high dose irradiation swelling, lower radio activation levels, etc., the deterioration of its mechanical properties by irradiation hardening and embrittlement induced by the neutron irradiation under the harsh working environment is still inevitable. Over the last decades, several studies have shown that post-irradiation annealing (PIA) is an effective way to substantially recover degraded mechanical properties. For material scientists, it is crucial to understand the underlying mechanisms in terms of the microstructure evolution at elevated temperature and link the corresponding microstructural changes to the recovery of the mechanical properties.

In this work, transmission electron microscopy (TEM) was used to characterize the radiation-induced defects like dislocation loops and cavities. Due to the samples magnetism and radioactivity issues, focused-ion beam (FIB) equipped with a scanning electron microscope (SEM) was utilized to prepare TEM lamella for microstructural characterization. Extensive TEM investigations were performed on as-irradiated EUROFER97 (15 dpa, 330 °C). The nature of the dislocation loop was determined by inside-outside technique. In addition, quantitative analysis of dislocation loops was carried out via weak-beam microscopy and scanning transmission electron microscopy (STEM) with high-angle annular dark field (HAADF) detector. Furthermore, nanometer-sized cavities were identified with TEM bright-field through-focal series. Also, in-situ TEM investigations were performed, in which both thermal ramping and isothermal annealing experiments were conceptualized and conducted at different time-temperature schemes. Thereby, dislocation loop evolution was predominantly observed with the help of dislocation loop-map based on the crystallographic information under kinematical bright-field condition.

TEM investigations show that PIA at 550 °C for 3 hours results in a reduction of dislocation loop density with a simultaneous increase in their mean size and formation of dislocation lines/networks. In addition, concurrent shrinkage phenomenon was observed for both ½<111> and <100> type loops. Moreover, ½<111> type loops shrank faster than their <100>

counterparts. The annealing behavior of dislocation loops appears to be vacancy/interstitial diffusion driven and it falls between the two extremes of isolated loop shrinkage/annihilation and their coarsening. The dominance of one phenomenon over the other defines the overall loop size evolution. The in-situ TEM annealing experiments indicate that the loop shrinkage is apparently caused by their curvature force. Nevertheless, the spontaneous evolution of the loops neighboring microstructure substantially determines their annealing kinetics. Hence, loop annealing kinetics are discussed based on the various scenarios originating in terms of the presence or absence of neighboring sources and sinks. Besides, influence of loop type, alloying elements segregation and free surfaces of the thin-foils are also discussed. Moreover, a clear coarsening of the quasi-circular <100> loops into their rectilinear versions is revealed via isothermal annealing experiments at 550 °C. The coarsening phenomenon is a non-conservative climb process, which is discussed in terms of the movement of jogs while considering the change in the iron's elastic anisotropy with temperature and loops lowest energy directions. Furthermore, observed interaction of the coarsened <100> loops and thereafter their merging to form large loops of various geometries are presented and discussed. Lastly, a pronounced microstructural transition from dislocation loops dominated to dislocation line/network dominated microstructure with continued annealing is presented.

Similar to the dislocation loop evolution, a reduction of cavity density with increment in their mean size was observed as well. Additionally, in-situ TEM annealing experiments present their pronounced shrinkage at temperatures above 500 °C. Despite their inhomogeneous distribution and comparably lower density than dislocation loops, their shrinkage via vacancy emission upon annealing modifies the local vacancy concentration; and hence, promotes loop evolution in their vicinity. Furthermore, simulations based on rate theory demonstrates the low level of helium content inside the cavities which hinder the continuous vacancy emission and stopped their further shrinkage at elevated temperature. Finally, the obtained microstructural statistics from TEM isothermal annealing experiments and bulk material annealing experiments were correlated to the radiation-induced hardening via dispersed barrier hardening (DBH) model. The observed microstructural recovery upon PIA partially clarify the recovery of mechanical properties by healing irradiation-induced defects.

Kurzfassung

Der niedrig aktivierbare ferritisch/martensitische (*engl.:* RAFM) EUROFER97-Stahl ist ein Strukturmaterialkandidat für die erste Wand des zukünftigen Kernfusionsreaktors DEMO. Zu den Vorteilen von RAFM-Stählen gegenüber konventionellen austenitischen Stählen, die in Kernspaltungsreaktoren verwendet werden, gehören die ausgezeichnete Widerstandsfähigkeit gegenüber der Schwellung unter hochdosierter Bestrahlung, geringerer Radioaktivität usw. Trotzdem ist die Verschlechterung ihrer mechanischen Eigenschaften (z.B. Verfestigung), die durch die Neutronenbestrahlung in der rauen Arbeitsumgebung verursacht wird, immer noch unvermeidbar. In den letzten Jahrzehnten haben Studien gezeigt, dass das Ausheilwärmebehandlungen nach der Bestrahlung (*engl.:* PIA) ein effektiver Weg ist, um die degradierte mechanischen Eigenschaften im Wesentlichen wieder ausheilen zu können. Für Materialwissenschaftler ist es entscheidend, den zugrundeliegenden Mechanismus im Hinblick auf die Gefügeentwicklung bei erhöhter Temperatur zu verstehen und die entsprechende Gefügeänderung mit der Ausheilung der mechanischeren Eigenschaften zu verknüpfen.

In dieser Arbeit wurde Transmissionselektronenmikroskopie (TEM) verwendet, um die strahlungsinduzierten Defekte wie z.B. Versetzungsringe und Hohlräume zu charakterisieren. Aufgrund der Magnetismus- und Radioaktivitätsprobleme der Proben wurde ein mit einem Rasterelektronenmikroskop (REM) ausgestatteter fokussierter Ionenstrahl (FIB) verwendet, um TEM-Lamellen für die mikrostruktuelle Charakterisierung vorzubereiten. Umfangreiche TEM-Untersuchungen wurden an bestrahltem EUROFER97-Stahl (15 dpa, 330 °C) durchgeführt. Es wurde festgestellt, dass die Versetzungsringe in EUROFER97 vom interstitiellen Typ sind. Darüber hinaus wurde eine quantitative Analyse von Versetzungsringen mittels die weak-beam-Technik und Rastertransmissionselektronenmikroskop (RTEM) mit einem sogenannten *high-angle annular dark field* (*engl.:* HAADF) -Detektor durchgeführt. Darüber hinaus wurden Hohlräume (im Nanometermaßstab) mit Hellfeld-Abbildung mit der sogenannten *through-focal series technique* identifiziert. Für in-situ-TEM-Untersuchungen wurden sowohl Aufheizungs- als auch isotherme Ausheilwärmebehandlungen konzipiert und bei unterschiedlichen Zeit-Temperatur-Verläufen durchgeführt. Außerdem wurde die Entwicklung der Versetzungsringe hauptsächlich mit Hilfe der sogenannten *dislocation loop-map* basierend auf den kristallographischen Informationen unter kinematischen Hellfeldbedingungen beobachtet.

Die TEM-Untersuchung zeigen, dass PIA bei 550 °C für 3 Stunden zu einer Abnahme der Versetzungsringedichte, bei gleichzeitiger Erhöhung ihrer mittleren Größe und Bildung von Versetzungslinien/-netzwerken, führt. Zusätzlich wurde die Reduzierung der mittleren Größe sowohl für ½<111>- als auch für <100>-Ringe beobachtet, wobei letztere deutlich langsamer schrumpften. Das Temperverhalten der Ringe scheint durch Diffusion von Leerstellen/Zwischengitteratomen getrieben zu sein und liegt zwischen den beiden Extremen der Schrumpfung/Auslöschung der isolierten Ringe und deren Vergröberung. Die Dominanz des einen Phänomens über das andere bestimmt die Entwicklung der Gesamtgröße der Ringe. In-situ-TEM-Ausheilwärmebehandlungen zeigen, dass die treibende Kraft für das Schrumpfen der Ringe ihre Krümmungskraft ist. Jedoch hängt die Kinetik des Schrumpfens eines Ringes auch von der spontanen Entwicklung des umgebenden Gefüges ab. Die Kinetik der Ringe wird daher im Hinblick auf die verschiedenen Szenarien diskutiert, die sich aus dem Vorhandensein oder Fehlen von lokalen externen Quellen und Senken, vorwiegend für Punktdefekten ergeben. Außerdem werden der Einfluss des Ringtyps, der Seigerung der Legierungselemente und der freien Oberfläche von TEM-Lamellen diskutiert. Darüber hinaus zeigt sich durch isotherme Ausheilwärmebehandlung bei 550 °C eine deutliche Vergröberung der quasi-kreisförmigen <100>-Ringe in ihre geradlinigen Versionen. Das Vergröberungsphänomen ist ein nicht-konservativer Kletterprozess, der in Bezug auf die Bewegung von Jogs diskutiert wird, wobei die Änderung der elastischen Anisotropie des Eisens mit der Temperatur berücksichtigt wird. Darüber hinaus werden beobachtete Interaktionen der vergröberten <100>-Ringe und ihre anschließende Verschmelzung zu großen Ringen verschiedener Geometrien vorgestellt und diskutiert. Schließlich wird einen ausgeprägten mikrostrukturellen Übergang von einem durch Versetzungsringe dominierten zu einem durch Versetzungslinien/-netzwerken dominierten Gefüge mit fortgesetztem Tempern präsentiert.

Ähnlich wie bei der Entwicklung von Versetzungsringen wurde auch eine Verringerung der Hohlraumdichte mit der Zunahme ihrer mittleren Größe beobachtet. Darüber hinaus zeigen in-situ-TEM Ausheilwärmebehandlungen ihre ausgeprägte Schrumpfung beim Ausheilwärmebehandlungen über 500 °C. Trotz ihrer inhomogenen Verteilung und der im Vergleich zu Versetzungsringen geringeren Dichte beeinflusst die Schrumpfung von Hohlräumen beim Tempern durch Leerstellenemission die lokale Leerstellenkonzentration und fördert somit die Entwicklung der Ringe in ihrer Umgebung. Darüber hinaus zeigen auf der Ratentheorie basierende Simulationen, dass der geringe Heliumgehalt in den Hohlräumen sowohl die kontinuierliche Leerstellenemission als auch das weitere Schrumpfen der Hohlräume bei erhöhter Temperatur verhindert. Schließlich wurden die erhaltenen Statistiken

zum Gefüge aus isothermen Ausheilwärmebehandlungen und makroskopischen Ausheilwärmebehandlungen über das sogenannte Dispersed Barrier Hardening (DBH) Modell mit dem strahlungsinduzierten Härten korreliert. Die beobachtete Erholung des Gefüges nach PIA erklärt teilweise die Erholung der durch Neutronenstrahlung induzierten Verfestigung in EUROFER97-Stahl.

Acknowledgements

Firstly, I would like to express my sincere thanks to Prof. Dr.-Ing. Jarir Aktaa, my primary supervisor and referent, for offering me this great opportunity to carry out research in his department. His advice and support always nudge me in the right direction. In addition, I would like to extend my sincere thanks to Prof. Dr. rer. nat. Anton Möslang for reviewing this thesis and for being my co-referent during Ph.D. defense. Moreover, I take this opportunity to thank Prof. Dr-Ing. Hans-Jörg Bauer for chairing my defense.

Also, I would like to express my special gratitude to my supervisor Dr.-Ing. Ermile Gaganidze, who guided me throughout this work. New ideas always initiated after valuable discussions with him and thus his guidance substantially improves my work. I am also grateful to Dr.-Ing. Ankur Chauhan (currently assistant Professor at Indian Institute of Science) for his co-supervision. I have enormously benefited from his vast knowledge of material characterization as well as his editorial skills. In addition, I would like to thank Dr.-Ing. Christian Dethloff for his co-supervision and particularly the introduction of TEM.

I wish to express my thanks to Dr. Benjamin Kaiser for the training of FIB-SEM and Dr. Jie Gao for the beneficial scientific discussions. Additionally, I would like to thank Dr. rer. nat. Dimitri Litvinov and Dr. Michael Klimenkov for the training of TEM. Furthermore, massive thanks to my colleagues and friends Dr.-Ing. Thomas Emmerich, Dr.-Ing. Thilo Grammes and Mr. Mark B. Mcenroe in reviewing my thesis and helping me to improve the language.

I wish to express my special thanks to Dr.-Ing. Hans-Christian Schneider, Dipl.-Ing. Rolf Rolli and all the technicians from Fusion Materials Laboratory (FML) in our institute. Without their support, this work would not have been possible. Here, special thanks to Ms. Beate Hallmeier and Mr. Sven Lautensack for their frequent help in handing radioactive materials.

Last but not least, many thanks to Prof. Dr. mont. Christoph Kirchlechner, Prof. Dr.-Ing. Marc Kamlah and Ms. Jana Herzog for managing and organizing the institute seminar and summer school. These wonderful events provide a nice scientific atmosphere for Ph.D. students. Moreover, special thanks to Dr. Dirk Radloff for organizing KIT fusion PhD seminar, which is very necessary for Ph.D. students to broaden our visions and extend our networks.

My Ph.D. life would certainly haven been boring without my colleagues and friends, Silva Basu, Yijing Zhen, Melina Blem, Elvina Gaisina, Christina Manoli, Mathias Jetter, Roshan Rajakrishnan, Kaiju Lu, Dr. Mario Walter, Thimo Metzler and etc.. Most importantly, I would like to thank my family for their endless supports during the past years.

Finally, I would like to thank EUROFusion program as this work has been carried out within the framework of the EUROfusion Consortium and has received funding from the Euratom research and training programme 2014–2018 and 2019-2020 under grant agreement No 633053.

Karlsruhe, August 2022 Qian Yuan

List of abbreviations

ADF	Annular Dark Field
APT	Atom Probe Tomography
BB	Breeding Blanket
BM	Blanket Modules
BCC	Body-Centered Cubic
BF	Bright-Field
CD	Cluster Dynamics
CRT	Cathode-Ray Tube
CVD	Chemical Vapor Deposition
DBF	Dynamical Bright-Field
DBH	Dispersed Barrier Hardening
DBTT	Ductile-to-Brittle Transition Temperature
DEMO	Demonstration Fusion Power Plant
DF	Dark-Field
DI	Deionized
DP	Diffraction Pattern
EBSD	Electron Back-Scatter Diffraction
EDX	Energy Dispersive X-Ray Spectroscopy
EELS	Electron Energy Loss Spectroscopy
FEG	Field Emission Gun
FIB	Focused-Ion Beam
FKH	Friedel Kroupa Hirsch
F/M	Ferritic/Martensitic
FML	Fusion Materials Laboratory
FS/RH	Finish-Start/Right-Hand
FW	First Wall
GIF	Graphics Interchange Format
HAADF	High-Angle Annular Dark Field
HFR	High Flux Reactor

HR-TEM	High-Resolution Transmission Electron Microscopy
ITER	International Thermonuclear Experimental Reactor
IVC	In-Vessel Components
KBF	Kinematic Bright-Field
KIT	Karlsruhe Institute of Technology
LAS	Low-Activation Steels
LM	Light Microscopy
LMIS	Liquid Metal Ion Source
MCP	Multichannel Plate
MD	Molecular Dynamics
NHE	Non-Hardening Embrittlement
OR	Ostwald Ripening
PAG	Austenitic Grain Boundaries
PAS	Positron Annihilation Spectroscopy
PFIB	Plasma-FIB
PIA	Post-Irradiation Annealing
PIPS	Precision Ion Polishing System
PKA	Primary Knock-on Atom
RAFM	Reduced-Activation Ferritic Martensitic
RSS	Root-Sum-Square
SAD	Selected-Area Diffraction
SANS	Small Angle Neutron Scattering
SEM	Scanning Electron Microscopy
SIA	Self-Interstitial Atom
SRIM	Stopping and Range of Ions in Matter
STEM	Scanning Transmission Electron Microscopy
TEM	Transmission Electron Microscopy
UTS	Ultimate Tensile Strength
WB	Weak-Beam
WBDF	Weak-Beam Dark-Field
WTZ	Wissenschaftlich-Technische Zusammenarbeit

List of notations

C_v	vacancy concentration
E_f^V	formation energy of vacancy
S_f^V	entropy of vacancy
T	temperature
a_0	lattice constant
b	Burgers vector
τ_s	shear stress
μ	shear modulus
l	loops spacing
σ_{FR}	Stress required to initiate a Frank-Read source
$\Delta\sigma_y$	yield stress
N	defects density
$N_{\frac{1}{2}<111>}$	½<111> type loop density
$N_{<100>}$	<100> type loop density
d	defects size
$d_{\frac{1}{2}<111>}$	½<111> type loop size
$d_{<100>}$	<100> type loop size
α	strength factor
M	Taylor factor
τ_{LR}	long-range stress
ρ_d	dislocation density
$\Delta\sigma_s$	saturation stress of hardening
Φ	irradiation dose
Φ_0	scaling dose
r	radius of the loop
D_v	vacancy diffusion coefficient
D	self-diffusion coefficient
G	shear modules

Γ	stacking fault energy
Ω	atomic volume
R_{max}	maximum radius to which a loop can grow
$N_{g=110}$	loop density under g=110 condition
$N_{g=002}$	loop density under g=002 condition
R_x	dislocation loop shrinkage rate
d_x	loop size at x seconds
d_{x-t}	loop size at $x-t$ seconds
C_d	vacancy concentration at dislocation loop
C_{EQ}	thermal equilibrium vacancy concentration
E	line tension of the loop
$\Delta\sigma_{tot(loop)}$	dislocation loops induced hardening
$\sigma_{\frac{1}{2}<111>loop}$	½<111> type loop induced hardening
$\Delta\sigma_{<100>loop}$	<100> type loop induced hardening
$\alpha_{\frac{1}{2}<111>}$	strength factor ½<111> type loop
$\alpha_{<100>}$	strength factor <100> type loop
c	light speed
D	deuterium
T	tritium
^{4}He	helium nucleus
V_n	vacancy clusters

Content

Chapter 1 Introduction

1.1 Nuclear fusion – opportunities and challenges

An energy crisis is a global challenge for the humans. Currently, fossil fuels including petroleum, coal and natural gas are the main energy sources. The burning of these fossil fuels produces extremely large amounts of greenhouse gases (e.g. carbon dioxide (CO_2)), and thus causes global warming and ocean acidification. Apart from the serious environmental damage, fossil fuels reserves are depleting rapidly with the increasing energy demand. Therefore, energy from carbon neutral sources like sunlight, wind, tide etc. are receiving immense attention. However, such renewable energy sources are variable in nature (i.e. they are availability dependent) and are typically not as cost-effective as traditional fossil fuels. For instance, the energy efficiency, the percentage of solar energy that is being converted into useable electricity, for the most commercially used solar cells is still less than 25%. Therefore, alternative-efficient sources are required which shall be clean and can fulfil our constant growing energy demand. In this quest nuclear energy should be considered as an option. For instance, about 445 nuclear fission reactors in 32 countries provide about 10% of the world's supply of electricity [1]. Nevertheless, the perfect nuclear safety can not be guaranteed despite of the improved safety of reactors in the past decades and sever design-basis accident such as Chernobyl disaster due to design deficiencies as well as failure to follow operating procedures might still happen. Moreover, the highly radioactive waste produced by fission reaction require long-term storage, which arises additional safety issues.

In the 20^{th} century, scientists recognized that massive energy released from nuclear fusion in stars elucidates the longevity of stellar heat and light. So as for sun, fusion reaction occurs in the extreme density and temperature in the sun, where the hydrogen nuclei collide and fuse into heavier helium atoms and release great amounts of energy. According to Einstein's Mass-energy equation $E=mc^2$, the tiny loss of mass multiplied by the square of the speed of light causes a tremendous amount of energy release. For instance, fusion of hydrogen isotopes, i.e. deuterium (D) and tritium (T) creates a helium (^4He), frees a neutron and releases totally 17.6 MeV energy (including 3.5 MeV carried by emitted helium and 14.1 MeV by emitted neutron). If such huge amounts of energy is achievable on earth, nuclear fusion would belong to the best solutions for energy crisis in the long-term perspective of energy resource availability and

sustainability. However, the D-T fusion requires utmost high temperature (more than 100 million °C [1]) and plasma density (around 1 million of the atmosphere [1]) so that the repulsive electrostatic force between two heavy isotopes of hydrogen (i.e. D and T) can be overcome; and thus enabling them fusing together. Such condition can be achieved by realizing and sustaining the plasma where constituent atoms are in ionized states. Nevertheless, no structural material can survive under such a high temperature. Hence, a feasible approach is using magnetic fields to confine the fusion fuels in form of plasma.

Early in 1950, Soviet physicists initially conceptualized a device, which applied a powerful magnetic field to confine plasma in the shape of a torus. Till 2021, this so-called tokamak concept is still regarded as the leading candidate for a practical fusion reactor to produce controlled thermonuclear fusion power. Figure 1-1 presents the largest tokamak type machine International Thermonuclear Experimental Reactor (ITER) currently under construction [2]. Under high temperature and pressure the charged particles of plasma can be well controlled by the massive magnetic coils placed around the vessel so that the plasma will be shaped and confined away from the vessel walls.

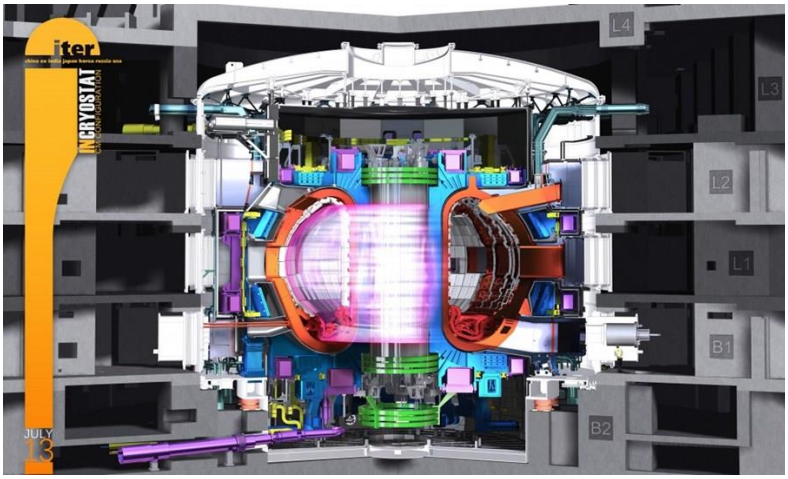

Figure 1-1: Cutaway diagram of largest tokamak in the world designed by ITER [2].

The heart of tokamak is a doughnut-shaped vacuum chamber, which is mainly protected by the blanket modules (BM) and divertor. As one of the most important in-vessel components (IVC), blanket modules in ITER are composed of a detachable first wall (FW) and a main shield block. First wall is the outmost part of the blanket module, which will be additionally covered by a thin ~1-2 mm layer of tungsten to shield the structural steel from high particle flux. Since directly facing the hot plasma, the first wall is designed to remove the heat load, while the shield blocks are used to provide nuclear shielding for the vacuum vessel and coil system [2]. As the operating conditions in future DEMOnstration (DEMO) power plants is conceived more severe

than in ITER, reduced-activation ferritic/martensitic (RAFM) steels form the primary structural materials in future fusion reactors mainly due to its cavity swelling resistance against austenitic steels (see section 2.1). In addition, as ITER's successor, DEMOs have adopted the breeding blanket (BB) concepts [3]. Unlike deuterium, which can be easily extracted from the seawater, the supply of tritium is very limited. However, tritium can also be supplied within the tokamak via the interaction of neutrons escaped from the plasma and lithium contained in the blanket during D-T fusion process. Such tritium self-sustainment would be applied in future fusion power plants.

Apart from the temperature and plasma density, confinement time is another driving factor that decide fusion energy efficiency. The record of the longest plasma sustainable retention time is 6 minutes and 30 seconds achieved by the Tore Supra tokamak in France [2]. The fusion triple product of three parameters, plasma density (n), confinement time (τ) and temperature (T) dictates if the reaction is self-sustainable or not. The Japanese JT-60 has so far accomplished the highest value of fusion triple product among all devices [2]. The power released by fusion reactions must exceed the required heating power so that the nuclear fusion makes sense, i.e. Q>1. Here, Q is the fusion energy gain factor, which is the ratio of the fusion power produced in a nuclear fusion reactor to the power required to maintain the plasma in the steady state. As the most prominent and documented DEMO-class reactor design by European Union (EU), EU-DEMO is designed for much higher fusion energy power gain [4].

1.2 Motivation and objective

Selecting high-performance structural materials which can endure harsh working environment is critical and challenging for nuclear fusion material research and development (R&D). As candidate structural materials for the FW and BB of future fusion energy generation reactors, RAFM steels have been extensively studied in the past few decades [5]. Their operating temperature window for FW and BB is between 350 to 550 °C [6]. At temperature lower than 350 °C, neutron irradiation typically results in a strong hardening and embrittlement [7]. However, the degraded mechanical properties can be significantly recovered by post-irradiation annealing (PIA) [8]

. For material scientists, it is interesting to understand the temperature effect on the recovery of the mechanical properties and link it to the corresponding microstructure evolution.

Understanding radiation effects on materials requires insights into their microstructure. The microstructure evolution in nuclear structural materials are typically studied by modern

computer simulations and advanced experimental techniques [9]. A variety of modelling methods are used to predict the evolution of microstructural defects upon neutron irradiation, as presented in Figure 1-2. Starting from the smallest length and shortest time scale, *ab initio* calculation and molecular dynamics (MD) provides picosecond to nanosecond timescales simulation, which covers the production of point defects at the initial stage as a result of particle matter interaction [10, 11]. However, the timescale for the generation of point defects is so short that no experimental technique is available to capture their dynamic evolution. In addition, as using MD methods to simulate multi-million atom calculation is extremely time-consuming, kinetic Monte Carlo (kMC) simulation [12, 13] and cluster dynamics (CD)/rate theory [14, 15] have been extensively applied to model the microstructure evolution upon irradiation at larger length and time scales.

Among various experimental techniques such as atom probe tomography (APT), positron annihilation spectroscopy (PAS) and small angle neutron scattering (SANS), TEM provides most detailed information of irradiation-induced defects, such as their density, size distribution, nature (e.g. interstitial type or vacancy type dislocation loops) etc. [16]. Point defects clusters grown to about 2 nm, can be observed and identified as irradiation-induced dislocation loops or cavities via transmission electron microscopy (TEM). In addition, larger defects can also be determined by scanning electron microscopy (SEM) [17] and light microscopy (LM) [18]. On the other hand, the obtained information from abovementioned experimental methods can also be compared and cross-checked with the results from computer simulation.

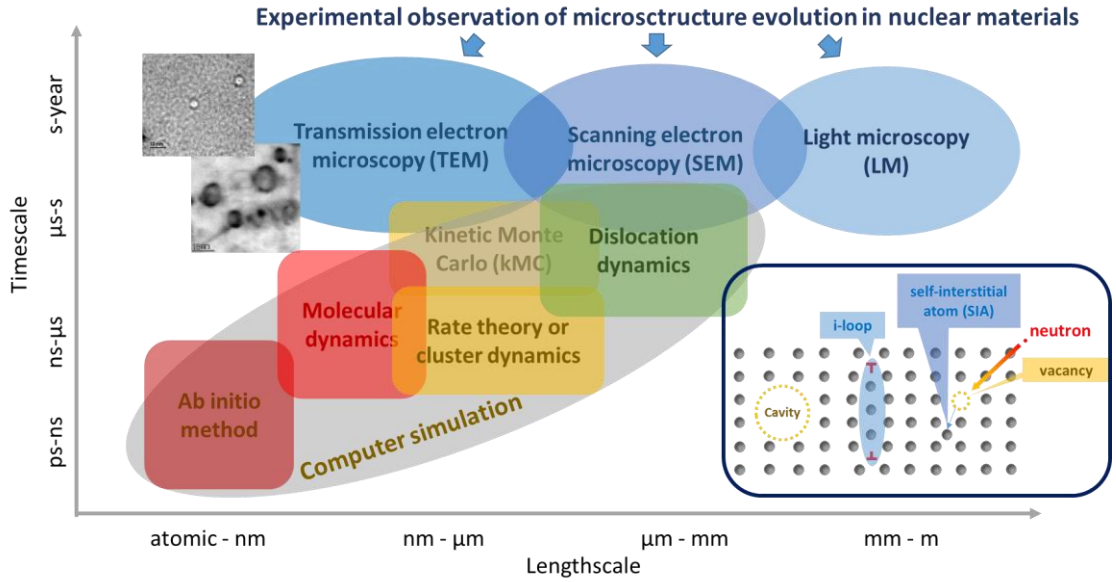

Figure 1-2: Illustration of experimental (microscopy) and computer simulation approach to the investigation of microstructure evolution in nuclear materials. Individual microscopy techniques are

presented in the elliptical schematics whereas simulation methods are shown in square schematics. In addition, fundamental irradiation-induced defects such as self-interstitial atom, vacancy, interstitial type dislocation loop (i-loop) and cavity are illustrated in the inset on the right lower side of the figure.

Although the process of the production of defect upon irradiation cannot be accessed via TEM, their evolution (such as migration, coalescence etc.) at elevated temperature has been widely studied by in-situ TEM over the past decades [19-23]. Generally, defects annihilation and coarsening are the two main phenomena directly obtained by in-situ TEM, which eventually alter the overall defects density and size distribution. The long-range thermally activated diffusion of point defects at elevated temperature is the primary driving force for microstructure evolution [24]. In addition, the elastic interaction of defects driven by the accumulation of fluctuating stress field upon irradiation also influences the microstructure evolution even at absolute zero [25]. It should be mentioned that microstructure evolution in nuclear structural materials revealed by in-situ TEM mainly refers to the evolution of irradiation-induced dislocation loops and cavities. Particularly, for dislocation loops in bcc metals, special attention was paid on investigating the dynamical behaviour of ½<111> and <100> type dislocation loops and their interaction [26]. In most nuclear structural materials, more defects appear to be "annealed out" at higher irradiation temperature [27]. Here, "annealed out" does not necessarily means defects are totally disappeared, instead, the "annealed out" defects can also be absorbed by other defects which ultimately leads to their total density reduction.

PIA has been proven to be an effective method to substantially improve the degraded mechanical properties [8, 28, 29]. In addition, considering defects' evolution at elevated temperature revealed by in-situ TEM, it can be hypothesized that the recovery of the mechanical properties after PIA is strongly linked to the recovery of the microstructure. This gives rise to the motivation of this work and its objective, namely to understand the underlying mechanism of the recovery of mechanical properties from microstructural aspect.

1.3 Structure of thesis

The content of the thesis is structured and divided into five chapters. Chapter 1 firstly introduces a general background of this topic and specifies the motivation and object of this thesis. In Chapter 2, several candidature structural materials for nuclear fusion applications are firstly compared and among them, RAFM steels are selected due to their advantageous properties against other candidates. The following section outlines the fundamental irradiation-induced defects including their formation and migration upon irradiation. In addition, as the most significant irradiation-induced defects in bcc metals, dislocation loops with two types of

Burgers vector ½<111> and <100> are reviewed in pure α-iron, Fe-Cr steels and RAFM steels, respectively. Furthermore, discussion of correlation of irradiation-induced defects and mechanical properties with given examples (RAFM steels) is also accessed in this chapter. The last section in this chapter describes the temperature effect (i.e. PIA) on the recovery of mechanical properties in EUROFER97 steels. Besides, this section highlights the importance of a systematical investigation on the microstructure evolution upon elevated temperatures in EUROFER97, which supposedly provides convincible interpretation of the recovery of the mechanical properties.

Apart from a short introduction of the material investigated in this work, Chapter 3 brings the readers to the experimental sections and addresses the speciality of characterizing nuclear materials in terms of sample preparations and subsequent microstructure investigations. Although there are various techniques of characterizing irradiation-induced defects, TEM is currently still the main method to directly observe and identify such small defects. Particularly, in order to "see" irradiation-induced dislocation loops and distinguish those from other defects, a series of combined techniques are documented for TEM specimen preparation in this chapter. In addition, due to specific diffraction contrast of irradiation-induced dislocation loops, dedicated imaging techniques are introduced for their identification and quantification. Since another challenge in this work is to understand dislocation loop annealing kinetics, direct observation of their behaviour at elevated temperatures is required. Hence, a unique imaging technique with the help of "dislocation loop map" which is dedicated for in-situ observation is presented herein. Moreover, the in-situ TEM annealing setup used is illustrated in the last section of this chapter.

Chapter 4 presents TEM annealing study on the microstructure evolution in neutron-irradiated EUROFER97. As PIA modifies the dislocation loops microstructure, special attention was paid on to their annealing kinetics. Dedicated in-situ TEM experiments such as isothermal annealing and dynamical ramping tests were therefore carried out and the results are presented in this chapter. As EUROFER97 steel exhibits complex microstructure, loop evolution does not simply follow traditional Ostwald ripening mechanism where large loops "eat" small ones. Instead, the presence of external sinks and sources strongly dictates the annealing behaviour of dislocation loops and thus the discussion is conducted not only by examining the intrinsic factors, but also considering many extrinsic factors, for instance, the surface effects. As evident, free surfaces of the thin-foils (TEM lamellae) act as strong sinks for point defects; and hence, in-situ experiments do not depict the bulk microstructure evolution upon PIA completely. Therefore,

quantitative analysis was carried out on bulk materials to delineate and verify the phenomena observed from in-situ experiments. In addition, the obtained data from TEM investigation on bulk materials was used to correlate with irradiation-induced hardening. The corresponding results and discussion are presented in the last section of this chapter.

The last chapter concludes the entire work and proposes possible future investigations. This work provides both theoretical and experimental references for other candidature structural materials/components' R&D in future fusion application.

Chapter 2 Current state of research

2.1 Reduced-activation structural materials for fusion applications

From the physical and mechanical properties viewpoint, withstanding high-energy neutron flux and thermomechanical stresses are critical prerequisites for selecting reliable structural materials used in future fusion reactor. Such a harsh environment is known to deteriorate material microstructure, and hence, their mechanical properties. The interaction of 14.1 MeV neutrons with target materials and resultant radiation-induced microstructure will be discussed in the next section.

Another constraint for material selection is safety and environmental issues. The aim of waste management is to avoid geological repository. The disposal scenarios depend strongly on the induced residual radioactivity in the structural material. Therefore, low-activation steels (LAS) with low-activation elements such as C, Si, Ti, Fe, Cr and V are qualified and have been extensively studied over the past decades. At the beginning of the material selection, several candidate low activation structural materials such as austenitic stainless steels [30], vanadium alloys [31] and SiC_f/SiC composites [32] are all discarded due to degradation of their mechanical properties under neutron irradiation. For instance, though austenitic stainless steel 316(N) is widely used in fission reactor, it is not suitable for high dose applications (e.g. in future demonstration reactors doses will be 20-50 dpa) due to irradiation-induced swelling [30]. In addition, the shortcomings for vanadium alloys and SiC_f/SiC composites cannot be overlooked. The former suffers from low temperature irradiation embrittlement and lack of reliable protective coating [31], while the latter from low thermal conductivity and low fracture toughness [32].

Reduced-activation ferritic/martensitic (RAFM) steels are presently considered to be the most promising structural materials and have also been extensively studied in the past decades [33]. The reasons are mainly twofold. Compared with the austenitic stainless steels, RAFM steels possess excellent resistance against high dose irradiation swelling [34] as well as high temperature helium embrittlement [35]. Moreover, alloying elements in RAFM steels are strictly selected so that the highly radioactive and volatile nuclides are minimized and long-lived radioactive isotopes are decayed below the recycling limit. In addition, as impurities, the

undesirable alloying elements such as Mo and Nb are replaced by W, V and Ta [36, 37]. For instance, F82H and EUROFER97 are the two representative RAFM steels containing following main major elements: Fe, Cr, W, V, Ta. Though both of them have achieved the greatest technical maturity, they still exhibit only satisfactory mechanical properties at elevated temperature [34, 37]. The restriction of their usage together with the effects of neutron-irradiation will be introduced in section 2.2 and 2.3.

2.2 Irradiation-induced defects

As major neutron induced defects, irradiation-induced dislocation loops make a dominant contribution to the hardening of EUROFER97. To understand how these loops originate, formation and migration of the irradiation-induced point defects in terms of their basic configurations will be firstly introduced in this section. Thereafter, clustering/agglomeration of these point defects under irradiation and subsequent thermal diffusion will be reviewed for pure α-iron, Fe-Cr steels and RAFM steels.

2.2.1 Production of irradiation-induced point defects

Typically, neutrons in nuclear reactors consist both thermal neutrons and fast neutrons. The former are captured or absorbed by atomic nucleus and alter the chemical composition of the materials followed by nuclear transmutation reactions whereas the latter is primarily responsible for the displacement damage accumulation, which mainly depends on the high energy spectra of the reactors. In addition, it is worth to mention that the high energetic 14.1 MeV neutrons also produce helium and hydrogen as the transmutation products of Fe atoms in steels in the near-plasma regions [38]. The impacting neutrons collide with the lattice atoms and might cause the creation of displacement cascade. The ballistic collision among lattice atoms occurs if the energy transferred to the primary knock-on atom (PKA) exceeds the threshold displacement energy (i.e., the energy required to displace a lattice atom from its lattice position). The timescale for such collision cascade is extremely short (~100 ps) which can merely be accessed via computer simulation. Figure 2-1(a-c) illustrates the timescale and corresponding three stages of primary damage processes of collision cascade during irradiation [11]. After extremely short linear collision cascade (~0.1 ps), the temperature reaches maximum value and the system can be considered to be in a thermodynamic liquid-like state. This so-called heat spike or thermal spike develops in several pico-seconds and results in a maximum volume of the cascade (Figure 2-1b). The molten material subsequently cools down to the ambient temperature,

leaving behind few point defects, namely self-interstitial atoms (SIAs) and vacancies (Figure 2-1c).

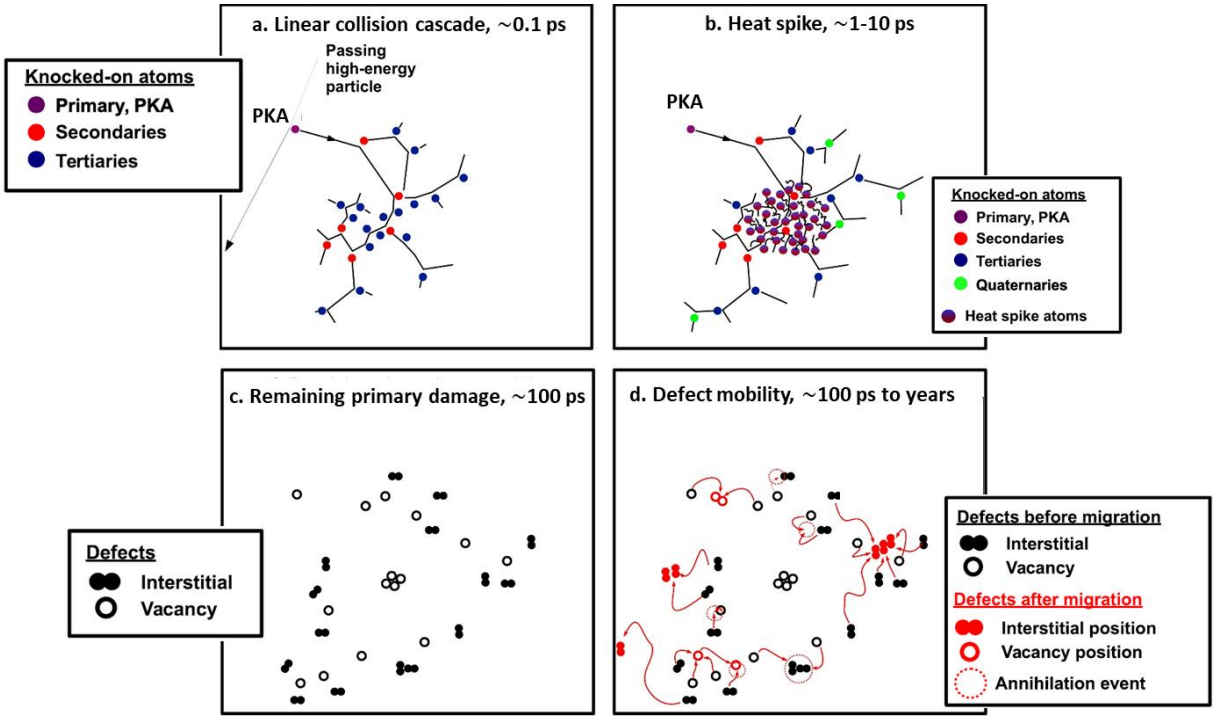

Figure 2-1: Schematic description of the time scales and physical processes occurring during irradiation of bulk materials. Frames a-c indicate a single primary damage process, d the ensuing defect mobility (adapted from [11]).

After the primary damage event, the irradiation-induced point defects are mobile under certain time-temperature regime. As illustrated in Figure 2-1d, these SIAs and vacancies can either cluster or annihilate via thermally activated diffusion. In general, the SIAs have lower migration energies than vacancies. Hence, they are more mobile than vacancies at specific irradiation temperature [39]. For example, at lower temperature, small SIAs either agglomerate into larger clusters or recombine with vacancies and/or annihilate at sinks such as dislocations and grain boundaries. At higher temperature, once vacancies are activated, they coalesce to form vacancy-type dislocation loops and/or three-dimensional cavities. Meanwhile, SIAs cluster further grow to form interstitial-type loops. It is necessary to note that in addition to temperature effects, the pure elastic interaction among the defects as well drives the overall microstructure evolution. To exclude the temperature effect, very recently, Derlet and Dudarev have simulated the defects evolution at T=0 and indicate that merely stress-driven process upon irradiation results in the swelling phenomenon [25]. Detailed interstitial and vacancy configurations and their diffusion mechanisms will be described in the next sub-section.

2.2.2 Stability and mobility of irradiation-induced point defects in bcc metals

- **Irradiation-induced self-interstitial atoms (SIAs)**

Single interstitial atom in the bcc lattice locates either on octahedral site (Figure 2-2a) or tetrahedral site (Figure 2-2b). There are 6 octahedral sites and 12 tetrahedral sites per unit cell. However, due to their higher formation energy (see Table 2-1), they are not as stable as split interstitial configurations. This so-called dumbbell, as illustrated in Figure 2-2c and d, consists two atoms "sharing" one single lattice site and arranges themselves in the lowest energy orientation owing to the repellency of the atom cores. Studies based on computer simulation indicate that the most stable interstitial configuration in α-Fe is <110> dumbbell [40]. In addition, *ab initio* calculations also confirm the existence of <110> nuclei [41]. Furthermore, the most stable multiple interstitials are configured by two <110> dumbbells locate on the nearest neighbor sites, i.e., di-interstitials (see Figure 2-2e). Fu et al. [42] proposed that SIAs and <110> di-interstitials migrate three dimensionally via nearest-neighbor translation-rotation jumps. Nevertheless, they become unstable in the growth process and prefer to align themselves in <111> directions and form clusters [43]. If the interstitial clusters are large enough they will transform into dislocation loops with Burgers vector ½<111> and will be identified as loop-like feature under TEM. Indeed, ½<111> loops are generally observed under TEM in bcc metals [16]. However, the experimental observation of their counterparts <100> loops is unexpected due to their higher formation energy. In sub-section 2.2.3, a detailed description and comparison of both type of irradiation-induced dislocation loops will be introduced.

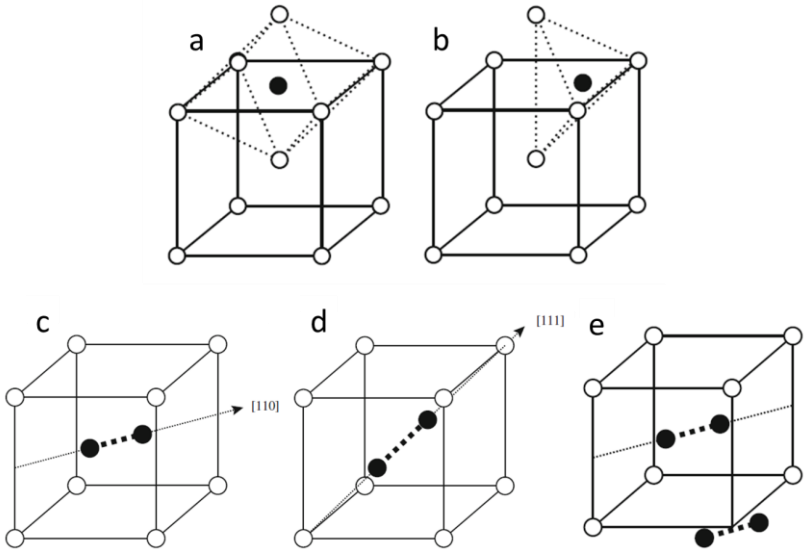

Figure 2-2: Schematics of bcc interstitial sites configurations: (a) octahedral, (b) tetrahedral, (c) [110] dumbbell, (d) [111] dumbbell. And (e) two <110> dumbbells on the nearest neighbour sites. Black balls present SIAs whilst white balls present lattice atoms (adapted from [39]).

Table 2-1: Formation energy of different type of self-interstitials and dumbbells in several bcc metals (unit in eV) [40]. The lowest energy for a given metal is underlined in the table.

Crystal	<110> dumbbell	<111> dumbbell	<100> dumbbell	Crowdion	Octahedral	Tetrahedral
V	4.23	4.72	4.98	4.70	4.84	4.82
Nb	4.54	4.88	4.85	4.95	4.91	4.95
Ta	6.97	7.31	8.16	7.31	8.08	7.75
Cr	4.14	3.58	3.99	3.58	4.04	4.09
Mo	7.08	7.28	7.23	7.24	7.61	7.58
W	9.71	9.02	9.88	8.99	10.06	10.05
Fe	3.93	3.98	4.75	3.99	4.77	4.43

- **Irradiation-induced vacancies**

Another type of basic irradiation-induced point defect in the metal lattice is vacancy [44]. If the lattice atoms are removed from their original sites due to the kinetic energy transferred from incoming neutrons, vacancies are thus created. Figure 2-3a presents a single vacancy located at the body-center site. The presence of vacancies in the unit cell produces lattice strain/deformation with a negative low relaxation volume which is opposite to the appearance of SIAs. If more than one atom is missing, multiple vacancies are thus formed in a unit cell (see Figure 2-3b-d). Such configurations are often observed in irradiated metals [39]. These small vacancy clusters (V_n) can migrate by successive nearest-neighbor mono-vacancy jumps [45]. In addition, computer simulation indicates that tetra-vacancy is the smallest immobile nucleus for vacancy clusters formation and they can only migrate by dissociation [46]. For larger vacancy clusters, their mobility decreases with increasing cluster size [45].

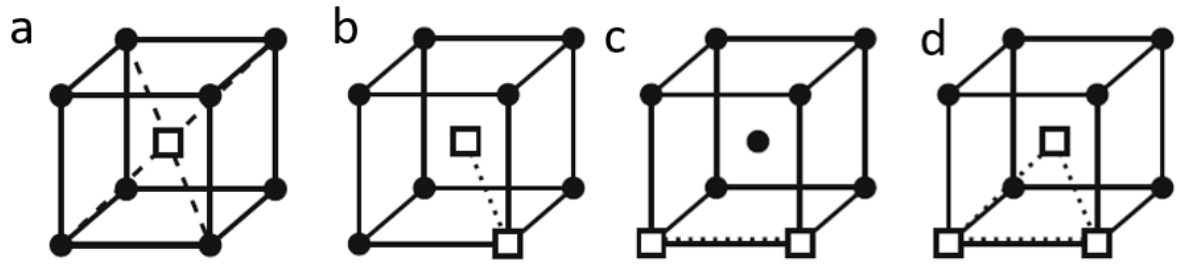

Figure 2-3: Multiple vacancy configurations in the bcc lattice. (a) single vacancy, (b) di-vacancies in <111> orientation, (c) di-vacancies in <100> orientation and (d) tetra-vacancies. Black balls represent lattice atoms and blank squares represent vacancies (adapted from [39]).

It should be emphasized that apart from irradiation-induced vacancies, thermal vacancies also exist in the metal due to thermal motion of atoms. Their concentration C_v can be expressed as [39]:

$$C_v = \exp\left(\frac{S_f^V}{k}\right)\exp\left(\frac{-E_f^V}{kT}\right), \qquad \text{Equation 2-1}$$

where E_f^V is the formation energy of vacancy, S_f^V is the entropy of vacancy, k is Boltzmann's constant and T is absolute temperature [39]. In metals, typical values for E_f^V are ~1 eV, which is only ~¼ of the formation energy of SIAs; and thus, vacancies are considerably easy to form than SIAs. Therefore, vacancies are the dominated point defects under thermal equilibrium condition. Additionally, in order to minimize the overall free energy of a system, vacancies are usually bound to oversized solute/impurity atoms, which act as efficient traps for vacancies in the lattice.

2.2.3 Radiation-induced dislocation loops in bcc metal

The agglomeration/clustering of SIAs or vacancies under irradiation and their subsequent thermal diffusion give rise to the possibility of forming dislocation loops. In bcc metals, these clusters can grow to an analyzable size with disc-shaped platelets of interstitials or vacancies and are believed to be prismatic type [47]. The magnitude and direction of Burgers vector delineate the lattice distortion induced by the loops. Prismatic loops in bcc metals have perfect Burgers vector which is perpendicular to the line direction of the loop periphery. In addition, loops with Burgers vector ½<111> and <100> have been identified in bcc metals by extensive TEM investigations [48]. Most of the fundamental research on irradiation-induced dislocation loops in bcc metals are based on studying pure α-iron due to its relatively simple microstructure than that of alloyed versions. Therefore, dislocation loops will be firstly reviewed in pure α-iron, followed by in Fe-Cr steels and RAFM steels.

- **Dislocation loops in irradiated pure α-iron**

As mentioned in section 2.2.2, the pair of split configuration (two <110> dumbbells) is stable in bcc lattice and acts as nucleus for further clustering. Early in 1965, Eyre and Bullough postulate that interstitial loops nucleate on a {110} plane by combining added interstitials since the d-spacing between {110} planes is the largest in the bcc lattice [49]. However, as the platelet of spilt interstitials on the {110} plane continues to grow, the configuration will develop into a single extra layer with a stack fault in the lattice. Since the faulted ½<110> loop is energy unfavourable, due to its high stacking fault energy, the following dislocation reactions are

required to eliminate such stacking fault (see Equation 2-2) and the corresponding <110> shear mechanism might be responsible for the formation of ½<111> and <100> loops [49].

$$\frac{a}{2}[110] + \frac{a}{2}[00\bar{1}] \rightarrow \frac{a}{2}[11\bar{1}]$$
$$\frac{a}{2}[110] + \frac{a}{2}[\bar{1}10] \rightarrow a[010] \qquad \text{Equation 2-2}$$

Dislocation loop energy estimation based on continuum elasticity (elastic energy is proportion to b^2) simply indicates ½<111> loops are energetically favoured than <100> loops. In addition, *ab initio* calculation indicates the <110>-<111> cross-over occurs at clusters containing five and more interstitials [43]. In other words, <111> orientations become more favourable with increasing cluster size. Furthermore, MD simulations [50, 51] have shown the rapid one-dimensional diffusion of small interstitial clusters in pure α-iron. Soon afterwards, Arakawa et al. [52] using in-situ TEM upon heating pure α-iron, observed the nanometer-sized ½<111> dislocation loop moved in a direction parallel to its Burgers vector in the absence of external stresses, see Figure 2-4. Such experimental observation directly confirms the results obtained from computer simulations.

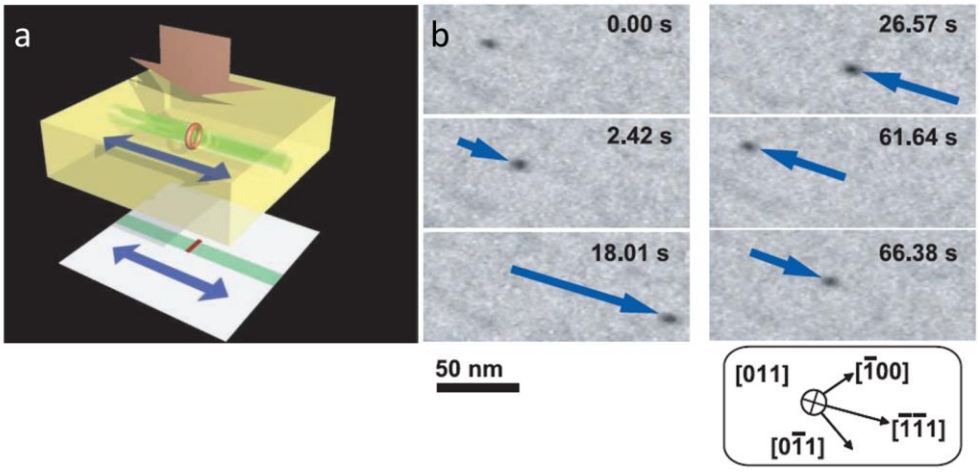

Figure 2-4: (a) Schematic view of the observation of the one-dimensional glide motion of a nanometres sized interstitial-type prismatic perfect dislocation loop by TEM. The red ring is the loop. The direction of the motion of the loop is parallel to its Burgers vector. (b) One-dimensional motion of an almost isolated $\frac{1}{2}[11\bar{1}]$ loop at 575 K. The observation axis is approximately along [011] direction. The reflection adopted is g = 200. The diameter of the loop is 5.9 ± 0.2 nm. A loop almost continuously moves in a direction parallel to its Burgers vector [52] /Reprinted with permission from AAAS.

Compared with ½<111> loops, the presence of <100> loops revealed by TEM is indeed unexpected from energy viewpoint. Over the past decades, the formation mechanisms of <100> loops have been widely studied and still remain a puzzle [41, 49, 53-56]. Table 2-2 summarizes

the main possible formation mechanisms for <100> loop predicted by computer simulation under irradiation (except the first one). Generally, all responsible formation mechanisms are only valid under specific conditions. For instance, Marian et al. [41] proposed that the <100> loop can be formed by the reactions of two ½<111> loops:

$$\frac{a}{2}[111] + \frac{a}{2}[1\bar{1}\bar{1}] \rightarrow a[100] \qquad \text{Equation 2-3}$$

However, the <111> reaction mechanism requires the colliding <111> loops with similar size and overlapping glide cylinders. Additionally, Chen et al. [57] proposed that ½<111> loop can directly transform into <100> loop at elevated temperature. However, such mechanism is only valid for loops with very small size (4-SIA clusters). Furthermore, <100> loops are also suggested to be transformed from C15 Laves phase interstitial clusters [54]. Though the existence of C15 structure has been supported by molecular dynamics (MD) simulation and *ab initio* calculation, solid experimental evidence is not yet available. Moreover, Granberg et al. [58] demonstrated that <100> loops can form when cascades overlap with random pre-existing primary radiation damage. Nevertheless, the required dose rate in MD simulation is so high that the precondition of <100> loop formation is extremely stringent. Using large-scale MD simulations with up to 220 million atoms, Peng et al. [35] proposed that SIAs can be punched out to form <100> loops only in picoseconds by the supersonic shockwave generated in the cascade. It is worth to notice that the <100> loops formed under such mechanism is in general smaller than ½<111> loops.

Table 2-2: Summary of possible <100> dislocation loop formation mechanisms revealed by computer simulations.

Mechanisms	**Methods**	**References**
<110> dislocation shear reaction (Equation 2-2)	continuum elasticity dislocation theory prediction	Eyre and Bullough [49]
<111> dislocation reaction	atomistic modelling/ Kinetic Monte Carlo simulations	Marian et al. [41], Xu et al. [59]
<111> transformation without dislocation reaction	MD simulations	Chen et al. [57]
C15 transformation	MD/*Ab initio* calculation	Zhang et al. [54], Alexander et al. [55]
Cascade debris overlap mechanism	MD simulations	Granberg et al. [58]
Punch mechanism by supersonic shockwave	MD simulations	Peng et al. [56]

Typically, as the activation energy for <100> loops is very high, they are practically immobile and act as biased sinks for mobile cascade-produced ½<111> loops [41]. However, Gao et al. [60] recently proposed a new mechanism via MD simulations that <100> loops can also diffuse by changing the habit plane between {100} and the {110} planes. Figure 2-5 illustrates two representative paths for a <100> loop to diffuse one Burgers vector distance from the habit plane {100} to {110}. In addition, this was also confirmed by performing in-situ TEM experiments. However, such habit plane rotation mechanism needs stringent conditions: high temperature and small loop size.

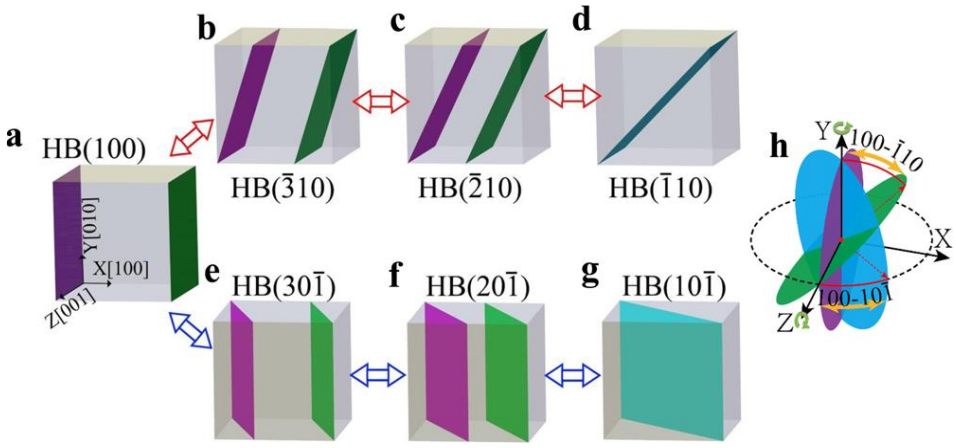

Figure 2-5: Schematic of diffusion mechanism of a <100> loop on the (100) habit plane with b = [100]. Its habit plane can change from **a** (100) to **b** ($\bar{3}$10), the **c** ($\bar{2}$10), to the **d** ($\bar{1}$10) (path 1) or to the **e** (30$\bar{1}$), the **f** (20$\bar{1}$), and the **g** (10$\bar{1}$) (path 2). The schematic of the two paths and the cross point are shown on the right-side **h**. The different habit planes are marked by purple, green, and blue colour, respectively [60].

Furthermore, the formation and stability of both type loops could also be altered by many extrinsic factors, such as the alloying elements in RAFM steels, and radiation/annealing temperature. In next sub-section, the role of Cr will be elucidated via comparing dislocation loops in pure α-iron and a series of Fe-Cr binary alloy.

- **Dislocation loops in irradiated Fe-Cr steel**

Before introducing radiation-induced loops in RAFM steels, a short review on dislocation loops in Fe-Cr binary alloys is essential to understand the role of Cr on microstructure evolution under irradiation. As a powerful alloying element, Cr is usually added to steels for improving oxidation resistance and high temperature strength. In addition, alloying of Cr is found to suppress void swelling [61]. Furthermore, the modification of precentral content of Cr in Fe-Cr steels gives rise to different dislocation loop density and mean size after irradiation [62, 63]. For instance, Porollo et al. [64] found that more Cr content in the neutron-irradiated binary alloy

at 400 °C leads to the reduction of loop size and increase of loop density. Besides, a mixed population of <100> and ½<111> loops is observed in Fe-12Cr and Fe-18Cr alloys which indicates that Cr content also alters <100> and ½<111> loop fraction.

As mentioned above, nanometer-sized ½<111> loops in pure α-iron can undergo one-dimensional diffusion at elevated temperature. To further study the effects of Cr on the mobility of these ½<111> loops, Arakawa et al. [65] carried out in-situ TEM electron irradiation and subsequent annealing experiments on both pure α-iron and Fe-9Cr alloy, respectively. In comparison to loops' coarsening and their higher mobility in pure α-iron, loops' motion in Fe-9Cr alloy was hardly observed at all examined temperatures. This clearly indicates that Cr suppresses the motion of ½<111> loops at elevated temperature.

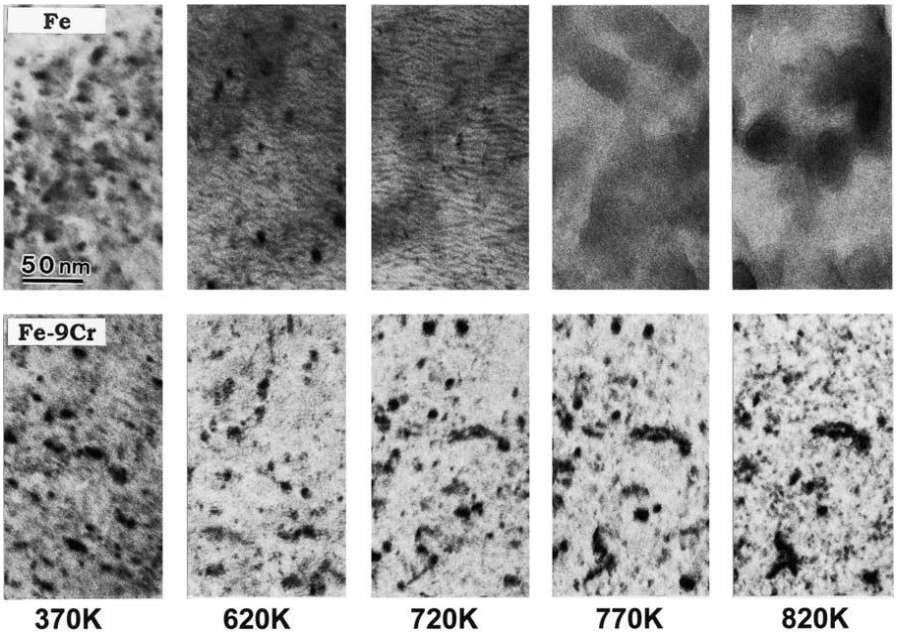

Figure 2-6: Microstructural variation in pure Fe and Fe-9Cr alloy under thermal annealing subsequent to high-energy electron irradiation with a beam flux of $9 \times 10^{22} \frac{e^-}{m^2}$ to a flux of $3 \times 10^{25} \frac{e^-}{m^2}$ at 110 K [65].

- **Dislocation loops in neutron-irradiated RAFM steels**

Though RAFM steels such as F82H and EUROFER97 possess excellent high dose irradiation swelling resistance, their degraded mechanical properties under irradiation at low temperatures limit their application in future fusion reactors. Dislocation loops, for instance, are regarded as the main contributors to the hardening of the RAFM steels at low-irradiation temperatures. In general, dislocation loop density and their size are important input parameters for hardening models, such as dispersed barrier hardening (DBH) or Friedel Kroupa Hirsch (FKH) models, to

predict irradiation hardening. Detailed correlation of microstructural and mechanical properties of RAFM steels will be introduced in the next section.

In EUROFER97, loops with both types of Burgers vector ½<111> and <100> have been confirmed to coexist after neutron irradiation [48, 66]. In addition, their density and size are shown to strongly depend on the irradiation temperature. Table 2-3 summarizes results from TEM analysis on dislocation loops in three kinds of ferritic/martensitic steels after neutron irradiation. A comprehensive TEM study of neutron-irradiated EUROFER97 from the researchers from Karlsruhe Institute of Technology (KIT) [27, 66, 67] indicates that small dislocation loops exist at high density under low temperature irradiation (< 350 °C) whereas high temperature irradiation leads to an increase of loop size and reduction of loop density. In addition, a domination of <100> loops is formed at higher irradiation temperature (> 350 °C). This phenomenon is supported by the TEM results from another ferritic/martensitic steel, T91 under comparable irradiation conditions [68].

It is worthy to note that <100> loop type fraction shows significant difference at low irradiation temperature based on different studies. In the TEM analysis of F82H carried out by Schäublin et al [69], the resolvable loops were identified to be <100> type whilst most small black dots cannot be distinguished as loops or precipitates. The loop type fraction in their study is therefore missing. By TEM investigation of dislocation loops in neutron-irradiated EUROFER97 steel, Klimenkov et al. [27] clearly demonstrate that ½<111> loops including black dots are dominated after irradiation at 250 °C and 300 °C. However, as loops smaller than 5 nm are considered as black dots in their study, the statistical method ($g \cdot b$ analysis) is accordingly applied which give rise to a statistical error of about 18%. In fact, the defect definition criteria substantially influence dislocation loop analysis. Dethloff et al. [48] made a clear separation in calculating dislocation loops and black dots density of neutron-irradiated EUROFER97. Apparently, the cumulative densities for loops and black dots presented in Table 2-3 (with irradiation condition of 15 dpa at 330 °C) are much higher than those excluding black dots. Therefore, the resultant ½<111> and <100> loop type fraction is also different. In this work, more detailed TEM investigations of dislocation loops/black dots in neutron-irradiated EUROFER97 were carried out via different imaging techniques and the results is presented in Chapter 4.

Table 2-3: Summary of results from TEM analysis on dislocation loops (black dots) in ferritic/martensitic steel F82H, EUROFER97 and T91 after neutron irradiation.

Material	Campaign	Dose (dpa)	T_{irr} (°C)	Defect Types	Density ($\times 10^{21}/m^3$)	Mean size (nm)	<100> number fraction (%)	References
F82H	HFR	9.2	310	-	28	6,9	uncertain	[69]
F82H	HFR	2.9	331	-	54	16,3	uncertain	[69]
EUROFER97	HFR	15	300	Loops	6.1	3.3 ± 0.2	77	[66]
EUROFER97	BOR-60	15	330	Loops	6.9	6.1 ± 0.3	72	[48]
EUROFER97	BOR-60	15	330	Loops+black dots	20	3.4 ± 0.2	45	[48]
EUROFER97	BOR-60	32	330	Loops	8.3	5.1 ± 0.3	27	[48]
EUROFER97	BOR-60	32	330	Loops+black dots	24	4.8 ± 0.3	31	[48]
EUROFER97	HFR	13.4 ± 0.7	250	Loops+black dots	~16.5	5	9	[27]
EUROFER97	HFR	14.6± 0.7	300	Loops+black dots	~46	6.52	26	[27]
EUROFER97	HFR	17.4 ± 0.5	350	Loops+black dots	~4.67	42.3	80	[27]
EUROFER97	HFR	17.2 ± 0.7	400	Loops+black dots	~2.25	101.5	90	[27]
EUROFER97	HFR	18.1 ± 0.3	450	Loops+black dots	~0.08	170	88	[27]
T91	BOR-60	17.1	376	Loops	2.9	21.8 ± 0.5	dominant	[68]
T91	BOR-60	35.1	378	Loops	1.9	22.9 ± 1.2	dominant	[68]
T91	BOR-60	18.6	415	Loops	2	25.8 ± 0.9	dominant	[68]

2.3 Radiation effects on mechanical properties

This section introduces the irradiation-induced hardening and embrittlement in RAFM steels. The correlation of the irradiation-induced defects (such as dislocation loops) and mechanical properties is discussed along with dispersed barrier hardening (DBH) model. In addition, the influence of irradiation temperature and dose on the degradation of materials mechanical properties is also discussed.

2.3.1 Irradiation hardening

As-mentioned previously, neutron irradiation yields defects such as dislocation loops/black dots and voids. These defects act as impeding obstacles for line dislocations during plastic deformation; and hence, cause strong strengthening by source hardening and friction hardening [70]. Source hardening is generally believed to be generated by the pinning or locking of line dislocations by impurity atoms. Equation 2-4 [70] presents the shear stress (τ_s) required to overcome source hardening in terms of loop spacing,

$$\tau_s = \frac{0.18\mu b}{l} \qquad \text{Equation 2-4}$$

where μ is the shear modulus, b is the Burgers vector of a gliding dislocation, l is the loops spacing. According to Singh et al. [71], the required stress for source hardening is considerably less than that to initiate a Frank-Read source ($\sigma_{FR} = \frac{\mu b}{l}$).

Friction hardening, on the other hand, refers to the stress required to resist dislocation motion hindered by irradiation-induced defects during plastic deformation. In addition, the increment in the yield strength is dictated by the defects dispersed in the material, which produces short-range stress when the moving dislocation encounter them. Equation 2-5 [70] correlates the increment in the yield strength ($\Delta\sigma_y$) to the density (N) and size (d) of the defects.

$$\Delta\sigma_y = \alpha M \mu b \sqrt{Nd} \qquad \text{Equation 2-5}$$

where α is the strength of the specific barrier in terms of the Orowan hardening model. M is the Taylor factor (3.06 for bcc metal) [72]. Equation 2-5 is therefore termed as dispersion barrier hardening (DBH) model after the original formulation of Seeger [73]. Table 2-4 lists stress increment caused by irradiation hardening based on different obstacle types. It is worth mentioning that DBH model is often applied in cases where the moving dislocation contacts the obstacles, which leads to short-range forces. For long-range stress fields which arises from the

moving dislocation and components of dislocation network, the increment of stress (τ_{LR}) is expressed as:

$$\tau_{LR} = \alpha\mu b\sqrt{\rho_d} \quad \text{Equation 2-6}$$

where ρ_d is the dislocation density. The total applied shear stress required to move the dislocation consists of both long-range and short-range forces. Nevertheless, as a true irradiated microstructure might consist of various types of defects, the superposition of hardening mechanisms becomes considerably complicated. For instance, root-sum-square (RSS) model [74] best fits for obstacles with similar strength whereas linear-sum model is better in cases where the strengths become more dissimilar [70]. Additionally, a combination of the abovementioned models is applied if the microstructure exhibits extensive obstacle strength [75].

Table 2-4: Strength of various obstacle types causing source and friction hardening in irradiated metals [70].

Type of strengthening	**Obstacle classification**	**Obstacle type**	**Stress increment**	**Value of α**
Source		Loops	$\tau_s = \frac{0.18\mu b}{l}$ (isolated dislocation loop)	
Friction	Long-range	Dislocation network	$\tau_{LR} = \alpha\mu b\sqrt{\rho_d}$	<0.2 [70]
	Short-range	Precipitates and voids	$\Delta\sigma_y = \alpha M\mu b\sqrt{Nd}$	1.0 bowing 0.3-0.5 cutting [70]
		Dislocation loops		0.25-0.5 [70]
		Black dots		<0.2 [70]

In fact, DBH model is extensively used to predict irradiation hardening caused by defects such as dislocation loops and voids in RAFM steels. For instance, Klimenkov et al. [27] predicted the yield strength in EUROFER97 at five different irradiation temperatures by applying RSS model and compared the corresponding results with the experimental measured data. As presented in Figure 2-7, the results at higher irradiation temperature (≥350 °C) are in good agreement. However, as evident, the difference at lower irradiation temperatures (250 °C and 300 °C) is obvious and related to the underestimation of the small defects that cannot be

resolved under TEM. Therefore, one should be cautious in employing DBH model, if the material contains high density of small undistinguishable defects.

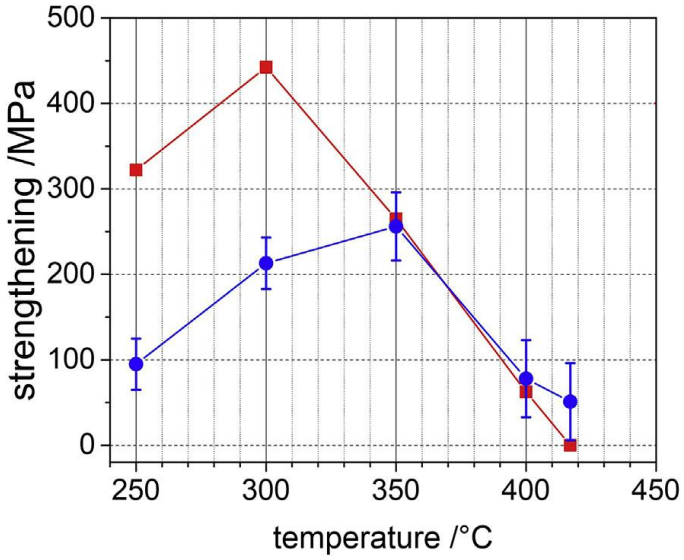

Figure 2-7: Radiation-induced hardening measured by tensile test (red squares) and calculated based on DBH model (blue circles) [27].

Besides the influence of irradiation temperature on hardening, Gaganidze et al. [6] summarized the effect of irradiation doses on the increment of yield strength of EUROFER97 and other RAFM steels at low irradiation and testing temperature ranges (see Figure 2-8). As evident in Figure 2-8, considerable increment in the yield stress of selected RAFM steels with the damage doses can be identified under neutron irradiation. In addition, the hardening shows a tendency to saturate at dose above 10 dpa. By incorporating DBH model, Gaganidze et al. [76] qualitatively described the evolution of hardening with dose up to 70 dpa based on Whapham and Makin model [77] as following:

$$\Delta\sigma = \Delta\sigma_s \sqrt{1 - \exp(-\frac{\Phi}{\Phi_0})} \qquad \text{Equation 2-7}$$

where $\Delta\sigma_s$ is the saturation value of hardening, Φ denotes the irradiation dose and Φ_0 is the scaling dose characterizing how fast the saturation of N (defect density) sets in. $\Delta\sigma_s$ and Φ_0 can be easily accessed via least square fit of the experimental data, which therefore indicates a significant decrease of hardening rate at achievable damage dose. Above all, irradiation temperature and dose are the two important factors, which determine the defects density and size distribution in the material; and thus, influence its strength. High density of defects such as dislocation loops not only harden the material, but also leads to embrittlement at operating

temperature. In the next sub-section, the embrittlement behavior of EUROFER97 after neutron-irradiation will be introduced.

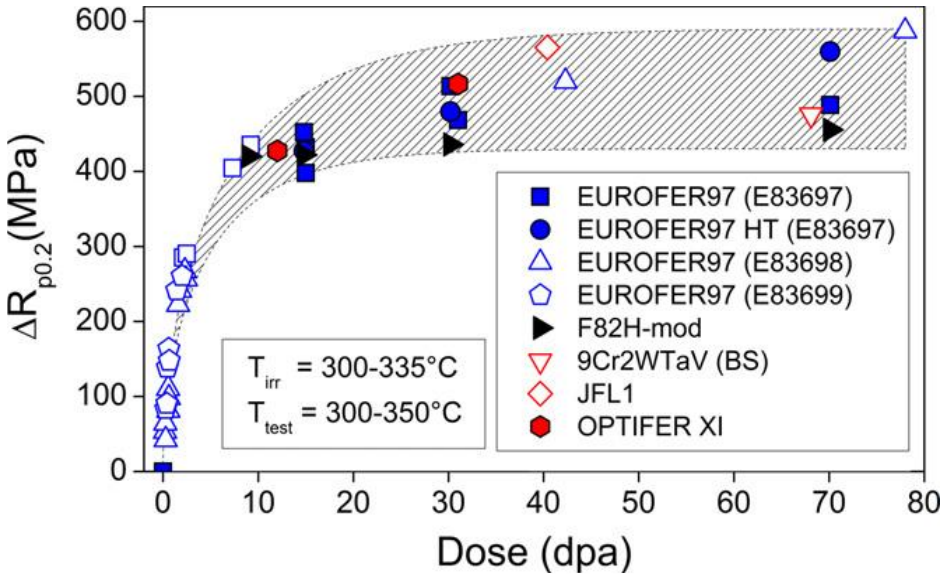

Figure 2-8: Irradiation hardening vs. irradiation dose for EUROFER97 and other RAFM steels for T_{irr}=300-335 °C and T_{test}=300-350 °C. The full symbols represent KIT results. The open symbols are from different European irradiation experiments carried out by SCK-CEN, NRG, CEA. The hatched area marks the scattering band for high dose results and is guide for the eye [6].

2.3.2 Irradiation embrittlement

As mentioned above, irradiation-induced defects act as obstacles and thus trigger materials' hardening. Typically, irradiation hardening contributed by defects such as dislocation loops/black dots, cavities and etc. directly leads to materials' embrittlement [78]. On the other hand, irradiation embrittlement also includes various non-hardening embrittlement (NHE) processes, for instance, precipitation of brittle laves phases on prior austenitic grain boundaries (PAGs) and/or decoration of helium bubbles on PAGs [79]. Therefore, irradiation embrittlement is in general a combination of hardening and non-hardening embrittlement processes.

In EUROFER97, dislocation loops contribute to material embrittlement under comparatively lower irradiation temperatures due to their high density. Figure 2-9 presents the impact energy to test temperature curves for EUROFER97 in the unirradiated state and after neutron irradiation in different European irradiation campaigns at temperatures between 300 and 350 °C [8]. Evidently, the ductile-to-brittle transition temperature (DBTT) shifts remarkably towards higher values at irradiation temperatures well below 340 °C. Similar studies in other RAFM steels also indicate that low temperature irradiation leads to a strong degradation of tensile properties as well as impact properties [76]. On the other hand, it is also ought to mention the

upper application temperature which is typically determined by creep strength of the material [80]. Therefore, the operation temperature window for RAFM steels is suggested to be between 350 and 550 °C [2].

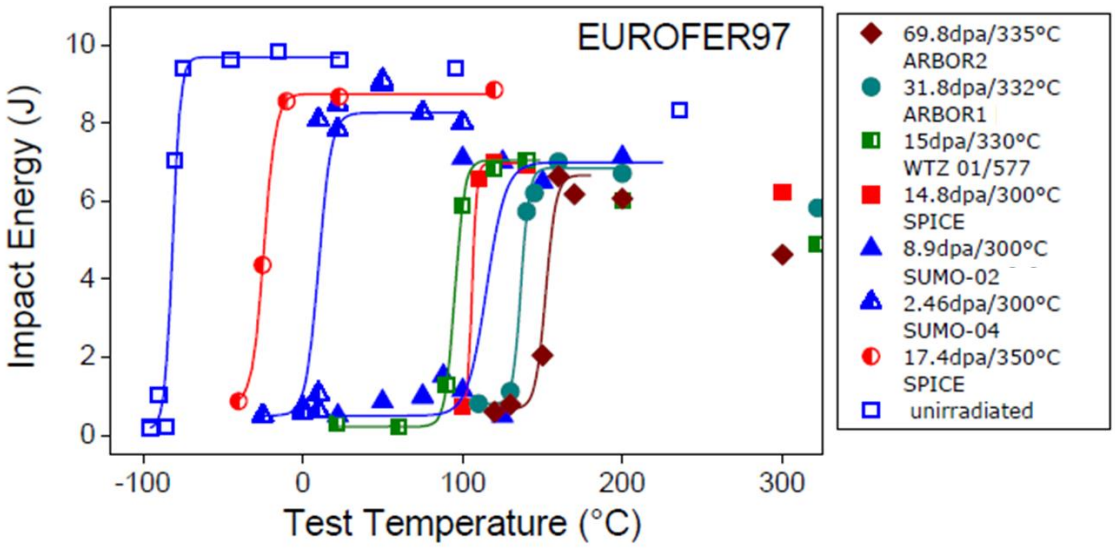

Figure 2-9: Impact energy vs. test temperature of EUROFER97 in unirradiated condition and after neutron irradiations in different European irradiation programmes (irradiation conditions and programmes are given in the figure legend) [8].

Similar to the influence of dose on irradiation hardening, the relationship of the increment in DBTT ($\Delta DBTT$) to dose can also be qualitatively assessed based on the experimental results. For a phenomenological description of the dose dependence of irradiation embrittlement, Gaganidze et al. [76] further developed Equation 2-8 in reference of Equation 2-7 as:

$$\Delta DBTT = \Delta DBTT_s \sqrt{1 - \exp(-\frac{\Phi}{\Phi_0})} \qquad \text{Equation 2-8}$$

where $\Delta DBTT_s$ is the saturation embrittlement. It is interesting to note that the data fitted for EUROFER97 (from Figure 2-10) are best described with Φ_0 =16.7 dpa, which is substantially higher than that (Φ_0 =7.3 dpa) for hardening. In other words, the hardening saturation is reached at lower levels of damage dose. This suggests a non-hardening embrittlement (NHE) mechanism in addition to the hardening embrittlement with the NHE mechanism dominates at high irradiation doses [76]. In contrast, irradiation embrittlement occurring at low damage doses is mainly hardening embrittlement where the increment of DBTT is nearly proportional to the increment of yield strength.

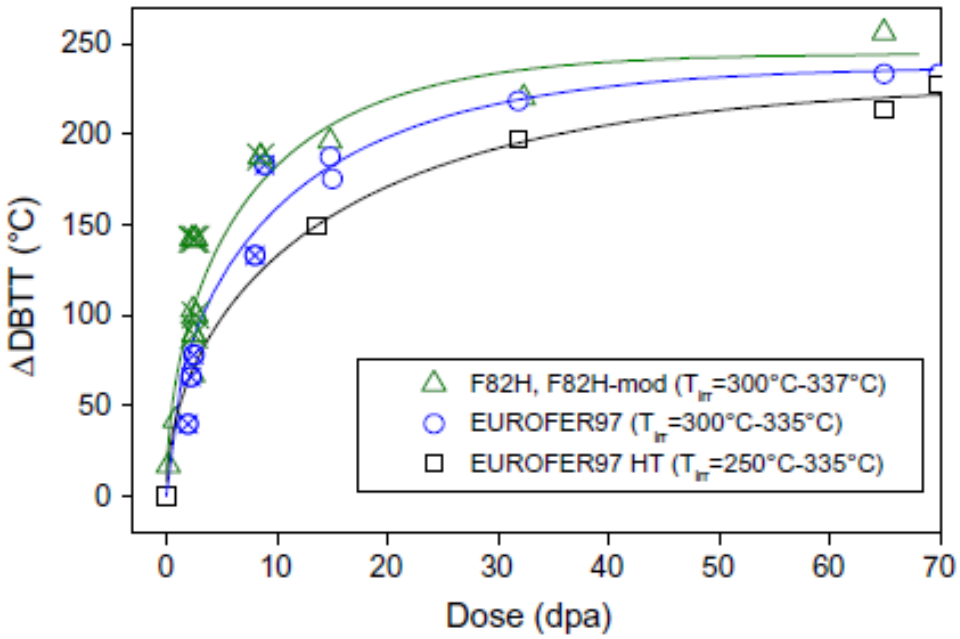

Figure 2-10: Irradiation shifts of the DBTT vs. irradiation dose for EUROFER97, EUROFER97 HT and F82H steels. The open symbols represent KIT results and the crossed symbols are from [81]. The irradiation temperatures are indicated in the figure legend. The solid lines are a model description for the data using Equation 2-8 [76].

One of the effective solutions to reverse irradiation hardening and embrittlement is annealing the material under specific conditions after irradiation. Exposing to elevated temperature, the irradiation-induced defects might be annealed out so that the mechanical properties can be recovered to certain extend. In the next section, post-irradiation annealing (PIA) will be introduced in terms of the alteration of mechanical properties and corresponding microstructural evolution.

2.4 Post-irradiation annealing (PIA)

In this section, post-irradiation annealing (PIA) will be introduced as an effective way to recover the mechanical properties, which are degraded after neutron irradiation. In addition, the recovery of the mechanical properties is supposedly correlated to the evolution of microstructures such as dislocation loops under thermal annealing. Therefore, the introduction of dislocation loop evolution at elevated temperature is also accessed herein. Furthermore, the formation of dislocation networks accompanied with reduction of loop density is presented by means of a case study.

2.4.1 Effects on mechanical properties

In the past decades, major post-irradiation annealing (PIA) investigations focused on austenitic stainless steels have shown improvement/recovery in the degraded mechanical properties [82-84]. Therefore, such a method is extensively applied in nuclear fission technologies. Similarly, a proper post-irradiation temperature exposure is also a viable approach to favorably modify neutron irradiation-induced defects; and thus, recovering mechanical properties of the structural materials used in future fusion reactor. A decade ago, Gaganidze et al. [85] systematically examined the mechanical properties of RAFM steels after neutron irradiation. Particularly, they showed a completely recovery of the uniform strain and substantial recovery of total strain of neutron-irradiated EUROFER97 after 1 hour annealing at 550 °C.

Figure 2-11a presents the remarkable recovery of yield strength and ultimate tensile strength (UTS) for EUROFER97 in two PIA conditions, compared with that of as-irradiated condition [8]. In contrast to PIA at 550 °C for 1 hour, 3 hours' annealing results in a further recovery of yield and ultimate tensile strength. In addition to the recovery of tensile properties, the impact property is also substantially improved after such annealing processes.

As presented in Figure 2-11b, a decrease in DBTT by 178 °C is obtained after annealing at 70 dpa irradiated EUROFER97 sample at 550 °C for 3 hours, which leads to a residual DBTT shift of 48 °C in comparison with the unirradiated condition. Additionally, the impact properties are almost completely recovered after PIA at 550 °C for 3 h in the sample with initial damage dose of 15 dpa. Furthermore, Schneider et al. [86] also demonstrated that PIA can be applied repeatedly to remove the neutron damage and substantially extend lifetime of EUROFER based steels. Since PIA at 550 °C would neither affect the structural integrity nor the microstructure of the components, it would be a proper reference annealing temperature for future studies and applications.

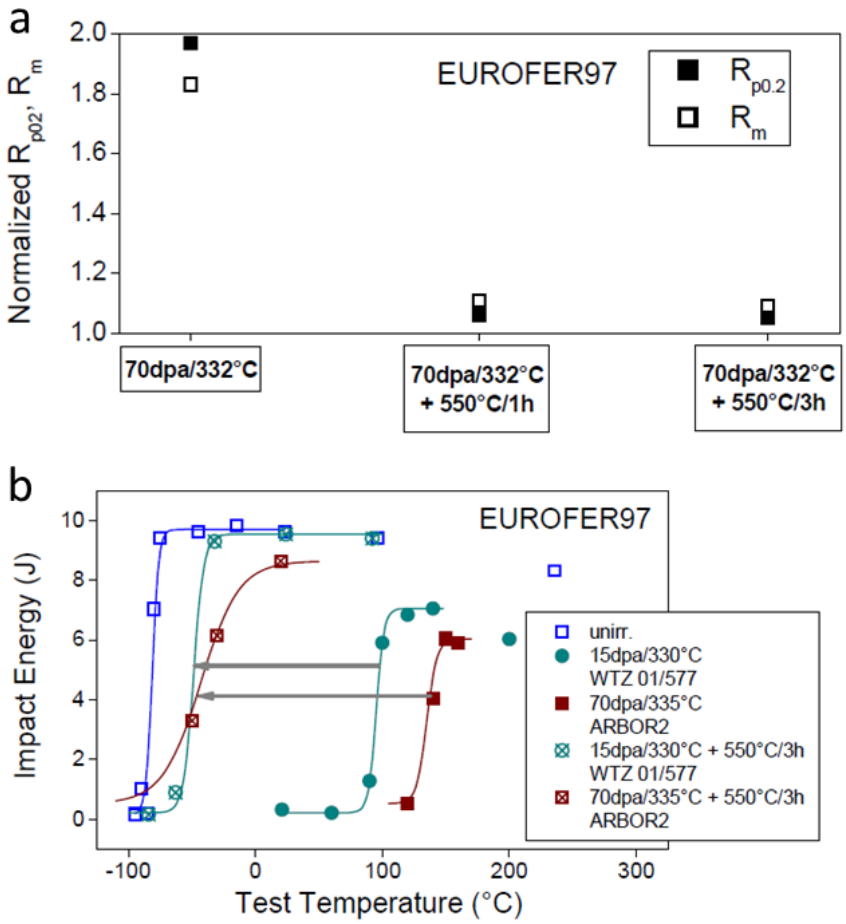

Figure 2-11: (a) Yield and ultimate tensile strengths for irradiated EUROFER97 (ARBOR 2) normalized with respect to the corresponding unirradiated values in the as-irradiated condition and after post-irradiation annealing. (b) Impact energy vs. test temperature for EUROFER from the WTZ 01/577 and ARBOR 2 irradiations in the as irradiated condition and after post-irradiation annealing at 550 °C for 3h. The results in the reference unirradiated condition are also included. The lines are fits to the ductile-to-brittle transition regions as described in [87]. The arrows indicate recovery of the DBTT [8].

2.4.2 Dislocation loop evolution at elevated temperature

In the last century, majority of annealing studies of dislocation loops have been carried out on austenitic steels used in fission technologies [82, 83, 88-90]. Early in 1968, J. J. Holmes et al. [82] revealed microstructure response of a neutron-irradiated austenitic steel over the temperature range from 23 to 871 °C via TEM. A transformation of Frank sessile loops into perfect dislocation loops was observed at 593 °C for 1 hour. Subsequently, these perfect loops migrated and interacted to form complex dislocation networks. Lastly, the networks and cavities were annealed out upon annealing at about 760 °C. Although the yield strength did not reach the unirradiated value, loops were annihilated, and a corresponding decrease of yield strength occurred at above 532 °C. This representative example clearly demonstrated that PIA could initially lead to a microstructural transition from dislocation loops to dislocation networks and

ultimately “removing” all the remaining neutron irradiation-induced defects. This study can be taken as an experimental reference for PIA application to bcc metals, particularly to F/M steels. Jiao et al. [68] also showed that dislocation networks in T91 were only formed at higher irradiation temperature (460 °C and 524 °C) whereas dislocation loops were merely observed at lower irradiation temperature (376 to 415 °C).

In section 2.2.3, dislocation loops in bcc metals have already been introduced in terms of their density, size and types. An in-depth understanding of the recovery mechanism mentioned above necessarily requires a direct experimental observation of their microstructure evolution, especially “seeing” nanometer-sized dislocation loops behavior at elevated temperatures. Such cutting-edge experiments can only be realized via in-situ TEM annealing experiments. In fact, Yao et al. [26] through their dedicated in-situ ion-irradiation TEM experiments on pure α-iron showed that the small mobile ½<111> loops were subsumed by sessile <100> loops at temperatures above 450 °C. Moreover, at 500 °C, <100> loops developed into large dislocation networks, and no visible ½<111> loops were formed. Therefore, it is obvious that loops behavior is strongly temperature-dependent and hence, a proper temperature exposure can be used as an effective approach to modify the corresponding microstructure.

It is noteworthy that the short-range elastic force between adjacent loops plays significant role to their coarsening/growth. For instance, a single large loop can be formed by two adjacent loops with the same Burgers vector growing and colliding side by side [91]. In some cases, loop coarsening/growth can also be realized by two small loops with different Burgers vectors. Arakawa et al. [92] experimentally demonstrated how a large loop absorbed a smaller one. It was shown that upon collision of two loops, a junction was initially formed and moved towards the far end of the smaller loop. Finally, a large single loop was thereby formed. These two examples evidently show that in addition to the temperature effect, the elastic interaction of the loops is another important factor, which enhance the overall microstructure evolution during PIA.

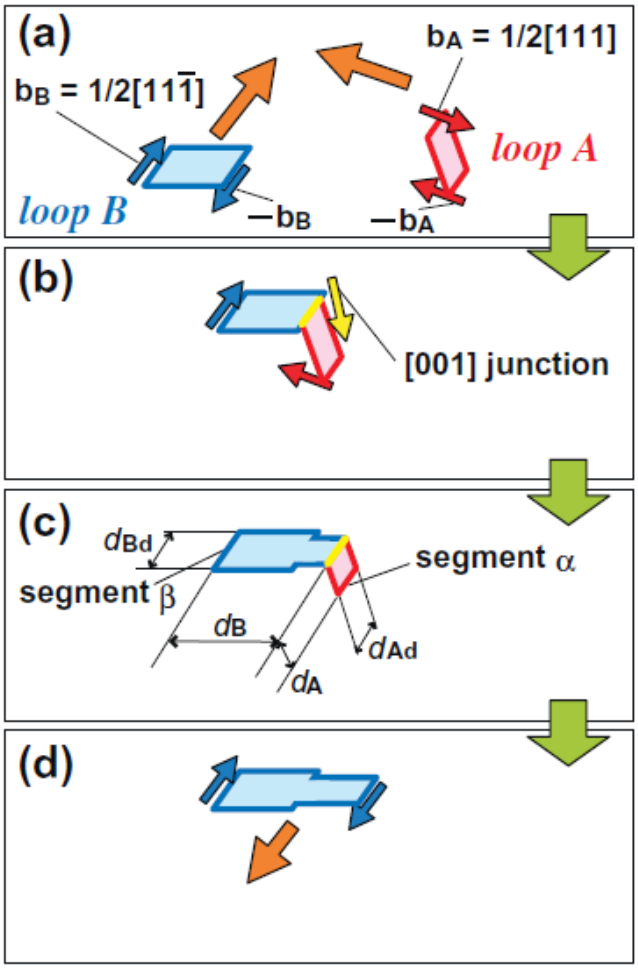

Figure 2-12: Scheme showing the process of collision and subsequent reaction between loop A and loop B. For simplicity, loops are shown as squares, rectangles or their combinations. The orange arrows represent the direction of the onward movement of the corresponding loops. Arrows attached to segments show the directions of the Burgers vectors of the corresponding segments. Here, the directions of the segments approximately parallel to the direction of the view were set to be from the near to the far side. Burgers vector directions were determined by finish-start/right-hand (FS/RH) convention [92, 93].

Nevertheless, in some cases, loop coarsening is usually accompanied by the shrinkage/annihilation of small loops if external sources and sinks are not available in the proximity. These sinks and sources can be pre-existed dislocations, cavities and grain boundaries. Assuming an extreme case where only dislocation loops exist in the material, then large loops grow at the cost of small loops since the point defects during the long-range diffusion process must be conserved. On the contrary, if loops are surrounded by enough external sinks and sources, their annealing behavior will be strongly dictated by the spontaneous evolution of these neighboring microstructural features. In such conditions, these loops evolve isolated and their annealing kinetics does not necessarily flow the conservation law as mentioned in the first scenario. Burton and Speight [94] systematically studied the isolated loop

annealing kinetics. They applied the spherical diffusion model to elucidate the isolated loop shrinkage behavior. This equation is given as:

$$\left(\frac{d}{dr}\right)\left[r^2 D_v \left(\frac{dC}{dr}\right)\right] = 0 \qquad \text{Equation 2-9}$$

where r is the radius of the loop, C_v the vacancy concentration and D_v the vacancy diffusion coefficient. This equation can be solved by the setting boundary condition where vacancy concentration at positions some distance away from the isolated loop can be maintained as equilibrium. Loop's shrinkage rate can be thereby expressed as Equation 2-10 and Equation 2-11 for interstitial type loop and for vacancy type loop, respectively [94],

For interstitial loop $$\frac{dr}{dt} = \frac{2D}{b}\left\{\exp\left[-\left(\frac{Gb}{r} + \frac{\Gamma}{b}\right)\frac{\Omega}{kT}\right] - 1\right\} \qquad \text{Equation 2-10}$$

For vacancy loop $$\frac{dr}{dt} = \frac{2D}{b}\{1 - \exp\left[-(\frac{Gb}{r} + \frac{\Gamma}{b})\frac{\Omega}{kT}\right]\} \qquad \text{Equation 2-11}$$

where D is self-diffusion coefficient, G is the shear modules, b is the Burgers vector, Γ is the stacking fault energy, Ω is the atomic volume (~b^3), k is the Boltzmann constant and T is the absolute temperature. For small unfaulted interstitial loops (i.e. r is small and Γ=0), their shrinkage rate is predominantly driven by the annealing temperature (the exponential term in Equation 2-10 is close to 1). Equation 2-10 can be simplified as

$$\frac{dr}{dt} = -2D/b \qquad \text{Equation 2-12}$$

where shrinkage rate is directly driven by the diffusivity; and hence, the corresponding annealing temperature. Nevertheless, dislocation loop annealing kinetics is more complicated as what Equation 2-10, Equation 2-11 or Equation 2-12 predicts because any alteration of defects evolution in the vicinity could either accelerate or hinder their shrinkage. Therefore, the overall dislocation loop annealing behavior falls between loops annihilation/shrinkage and their growth/coarsening, which largely depends on the spatial distribution of pre-existing defects and their synergic high temperature evolution. A detailed description of the dislocation loop evolution in neutron-irradiated EUROFER97 is missing. This motivates the present investigations carried out within the framework of this PhD work.

2.4.3 Presence of dislocation networks

The coarsened dislocation loops will encounter each other and eventually evolve into dislocation lines/networks. The frequency of loops interaction and their subsequent coalescence

is governed by loops and line dislocations density. If dislocation loops are contributing to the formation of dislocation networks, their size are therefore limited by the network density as described by Equation 2-13 [95].

$$(\pi R_{max}^2)\rho_d = 1 \qquad \text{Equation 2-13}$$

R_{max} represents the maximum radius to which a loop can grow. ρ_d represents dislocation density. However, R_{max} is usually difficult to be obtained directly from experiments. As mentioned in section 2.2.3, Klimenkov et al. [27] studied the irradiation temperature effect on dislocation microstructure in ERUOFER97 and they showed a clear transition of dislocation microstructure from loops to networks which occurred at irradiation temperatures in the range from 400 to 415 °C in EUROFER97 (see . Figure 2-13a).

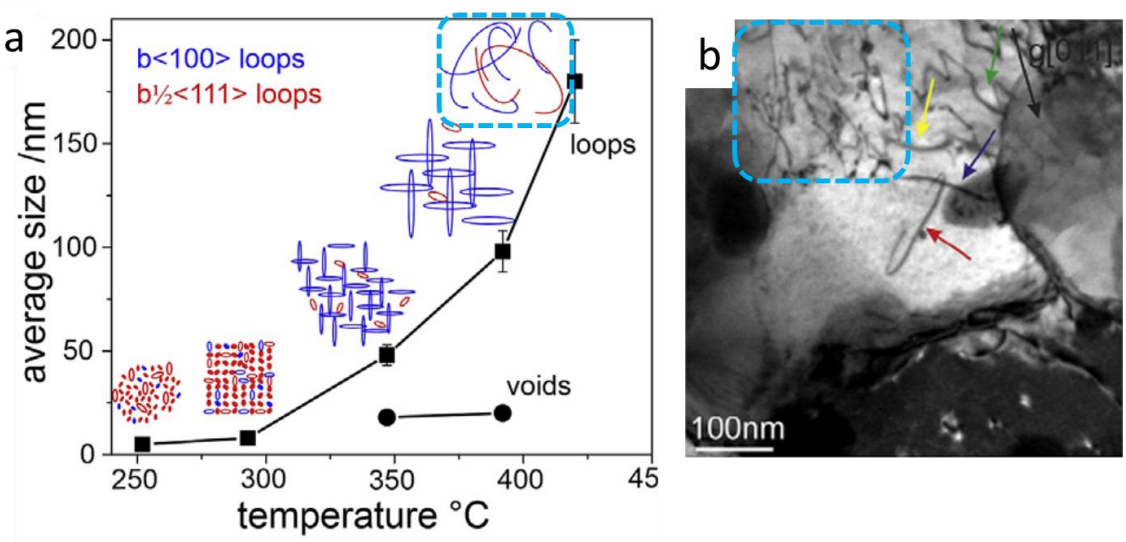

Figure 2-13: (a) Dependence of average size of dislocation loops (black squares) and voids (black circles) on irradiation temperature in neutron-irradiated EUROFER97. <100> loops and ½<111> loops are illustrated with blue and red above the data point respectively. Networks of line dislocations is highlighted with light blue frame. (b) DF TEM images with reverse contrast of EUROFER97 irradiated at 415 °C obtained using reflection g=[01-1]. The <100> loops are marked with red and blue arrows while ½<111> loops are marked with yellow and green arrows. In addition, network of dislocation lines is marked with a light blue frame (adapted from [27]).

However, the statistic of dislocation loops and networks at 415 °C is relatively poor. The reason is twofold. Firstly, as the size of measured dislocation "bows" (section of dislocation loop) is larger than the TEM specimen thickness (~100 nm), only a part of the loop is visible. Therefore, the actual loop size can be underestimated. Secondly, these "bows" cannot be explicitly distinguished with pre-existed curved dislocations. Nevertheless, their study still depicted

dislocation loop coarsening phenomenon, which is accompanied with the formation of dislocation networks.

The question is now will the dislocation loops also undergo such evolution upon simple annealing at high temperature? If it happens, how they coarsen/annihilate and incorporate into dislocation networks? To further clarify the dynamic process of microstructure evolution and deepen the understanding, isothermal in-situ TEM thin-foil annealing experiments as well as bulk annealing experiments were carried out and results are reported quantitatively in Chapter 4. The effects of local vacancy supersaturation are considered to elucidate the annealing kinetics of dislocation loops. Several possible scenarios based on loops neighbouring microstructure evolution are presented and discussed. In addition, the influence of loop type, alloying elements segregation and free surfaces of TEM-lamellae on annealing kinetics of dislocation loops are also discussed.

Chapter 3 Experimental

This chapter described the microstructural characterization of neutron-irradiated EUFOER97 via transmission electron microscopy (TEM). Various TEM specimen preparation methods dedicated for neutron-irradiated materials are primarily documented in detail. In addition, the working principles of TEM and its application in studying radiation-induced defects such as dislocation loops and voids are presented with given examples. Furthermore, in-situ TEM annealing experimental setup used in this work is presented in the last section.

3.1 Investigated material

The European Union reference batch of EUROFER97 steel was produced by Böhler Austria GmbH with a composition of 8.91 Cr, 1.08 W, 0.48 Mn, 0.20 V, 0.14 Ta, 0.006 Ti, 0.12 C (wt%, Fe balance). For the early development and investigation of EUROFER please refer to [96-98]. In addition, detailed description of the specifications for the chemical composition of EUROFER 97 can be found in appendix 1 and in [7] as well. The material was delivered in a normalized (980 °C for 0.5 h) and tempered (760 °C for 1.5 h) condition.

For unirradiated EUROFER97 steel, the complex microstructure presents a hierarchical structure which is mainly characterized by prior austenite grain (PAG) boundaries, packet boundaries, block boundaries and the martensitic lath boundaries [99, 100], as illustrated in Figure 3-1a. P. Fernandez et al. show the size of PAGs in the range of 6.7 -11 μm for the 14 mm plate and 8-9.4 μm for the 25 mm thickness plate [101]. The PAGs are separated by the packet boundaries. Inside each packets, there are blocks (∼3.1 μm measured by EBSD [102]) with the same set of parallel planes but different crystal orientations. The blocks contain lath martensitic microstructure, which share the same crystallographic orientations. Figure 3-1b shows a high density of precipitates (bright contrast) located in grain boundaries [103].

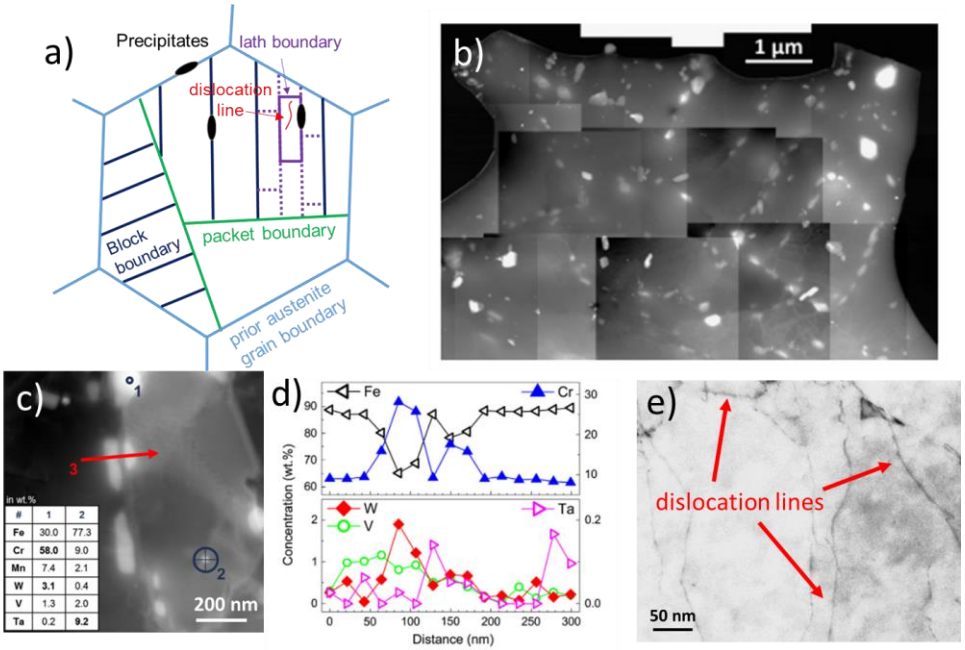

Figure 3-1: (a) Scheme of unirradiated EUROFER97 microstructure. (b) The precipitates show a bright contrast against the ferritic matrix in HAADF-STEM micrograph. (c) Typical precipitates structure with EDX measurements at position 1 and 2. Results of EDX point measurements at position 1 and 2 are given in the table within (c). In addition, the result of line scan (marked red arrow in (c)) is plotted in (d). (e) High magnification BF-TEM micrograph presents clear dislocations microstructure ((b-d is from [103] while (e) is adapted from [67]).

According to energy-dispersive X-ray spectroscopy EDX analysis (Figure 3-1c and d) [103], there are two types of precipitates in unirradiated EUROFER 97 steel namely, MX and $M_{23}C_6$. Here, M refers to the substitutional alloying elements as Cr, Mn, V etc.; X refers to interstitial alloying elements such as C and N. The large elongated precipitates $M_{23}C_6$ decorating PAG and lath boundaries were found to be enriched in Cr and W, and complementarily depleted in Fe. In addition, the MX type precipitates distribute homogenously in the matrix with a spherical shape and is determined to be Ta enriched (for instance, TaC). Furthermore, the estimated dislocation density in unirradiated EUROFER97 is about $10^{14} m^2$ [48].

The neutron irradiation experiments were performed on EUROFER97 (heat 83697) in the BOR-60 fast reactor, Russia under following condition: 15 dpa, 330 °C and neutron flux is 1.8×10^{19} $m^2 s^{-1}$[104]. Dislocation loops and voids are the main radiation-induced defects. Detailed defects analysis are documented separately in section 4.1.

3.2 TEM specimen preparations

In this section, different methods of preparing neutron-irradiated TEM specimen are introduced. Unlike traditional TEM specimen preparations, handling neutron-irradiated specimen requires

specific attention due to radioactivity issue. In general, traditional electro-polishing, which is introduced in section 3.2.1, provides the best TEM specimen quality (i.e. artifacts-free). However, considering radioactivity and other issues, focused-ion beam (FIB) polishing is extensively adopted in preparing radioactive TEM specimen. Section 3.2.2 introduces the working principles of FIB and describes the procedures of fabricating lamellae via FIB polishing. Besides, to remove the ion beam induced damage from FIB polishing, post-FIB processing such as using Ar^+ beam polishing and electro-flash polishing are further introduced in section 3.2.3. Conclusively, these techniques are compared and one of the abovementioned methods is primarily used in preparing neutron-irradiated EUROFER97.

3.2.1 Electro-polishing (Jet polishing)

Neutron-irradiated TEM specimens were initially manufactured in the Hot Cells at the Fusion Materials Laboratory (FML) of KIT via traditional electro-polishing (jet polishing) [48, 66, 67, 103]. For this purpose, slices of about 150-250 µm thickness with a cross-sectional area of 3×4 mm^2 were cut from the undeformed parts of impact tested neutron-irradiated EUROFER97 specimens. Figure 3-2 shows the experimental setup of electro-polishing neutron-irradiated specimens with a Tenupol-5 jet polisher [105].

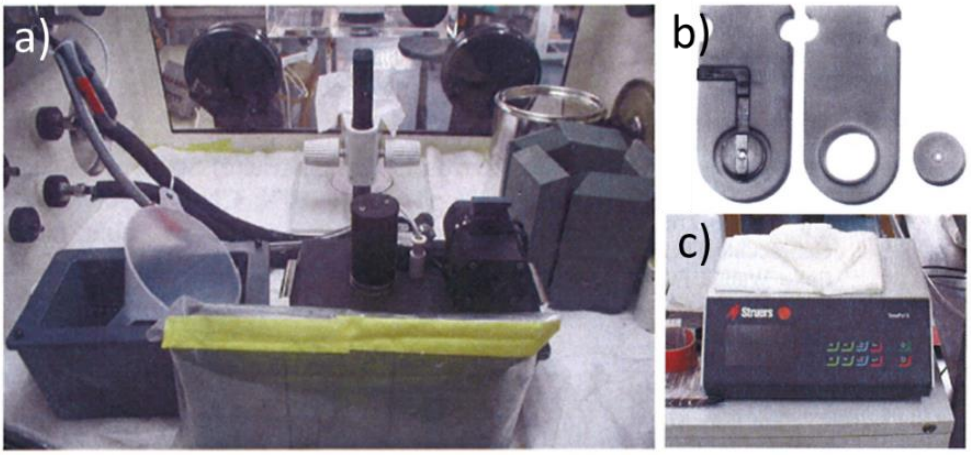

Figure 3-2: (a) Main part of Tenupol-5 jet polisher is placed in the glovebox in the electro-chemistry station in the Hot Cells of FML. (b) Specimen holder for electro-polishing. (c) Parameters such as voltage, current and time can be controlled via the control panel of the Tenupol-5 jet polisher [105].

The specimen within the holder is immersed in the electrolyte solution made of 80% methanol and 20% sulfuric acid at room temperature. Setting typical voltage of 11.5 V and typical current of 50 mA, jet solution comes from both sides of the specimen gently removing the eroded material until a small hole is formed in the specimen. Subsequently, the specimen is immersed in the bath with ethanol for cleaning. In order to reduce the effects of ferromagnetism which

disturbs TEM observation, disc of 1 mm in diameter with the electron-transparent region is punched out. Afterwards, the 1 mm discs is placed in foldable copper net for the final TEM investigation. In addition, the rest of the specimen with electro-polished areas are used for the later FIB lift-outs as shown in Figure 3-3.

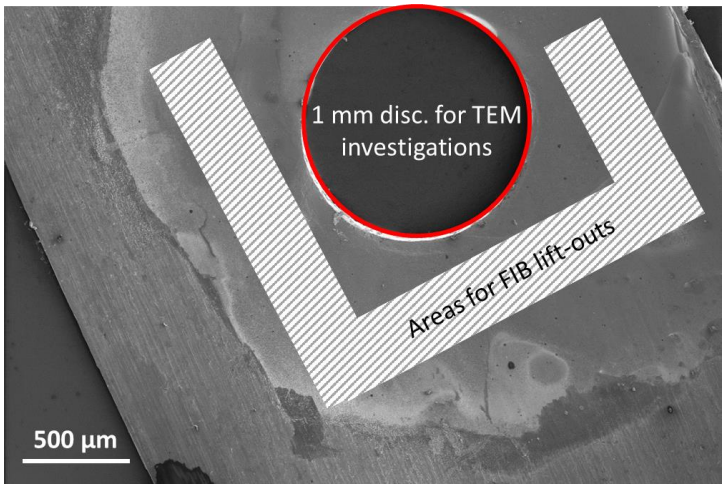

Figure 3-3: SEM micrograph of neutron-irradiated EUROFER97 after electro-polishing. The punched out 1 mm disc marked with red circle is directly used for TEM investigation while the rest marked areas are used for the later FIB lift-out procedure.

3.2.2 Focused-ion beam (FIB) polishing

For systematic investigation of the temperature influence on defects evolution in neutron-irradiated EUROFER97, more than 20 electro-polished samples are mandatory. However, such preparation as mentioned in the above section requires close-in, hands-on manipulation of samples for a long period of time. In addition, due to the small grain size and strong magnetic problems, a frequent alignment of electron beam is inevitable. Such inconvenience largely influences the accuracy and continuity when performing in-situ TEM investigations. Therefore, to avoid the influence of sample's magnetism on the TEM electron beam and to further minimize the radioactivity exposure during microstructural investigations, a finely focused-ion beam (FIB) equipped with a scanning electron microscope (SEM) (FEI Scios) was utilized to fabricate electron transparent lamellae for TEM investigations. Such a dual-beam system (see Figure 3-4) enable a high-resolution imaging and flexible micromachining in single platform. Due to its low melting temperature (30 °C), low volatility and low vapour pressure, Ga^+ liquid metal ion source (LMIS) is used as ion source for imaging and micromachining.

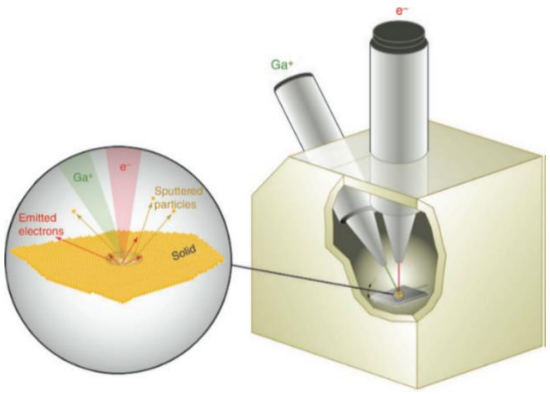

Figure 3-4: Schematic illustration of a dual-beam FIB-SEM instrument. Expanded view shows the electrons and ion beam sample interaction [106].

Figure 3-5 shows three general working principles of using FIB to prepare TEM lamellae. 1) Imaging: Similar to the imaging principle in SEM , as the FIB is raster scanned over the sample, the detector collects secondary particles (secondary Ga^+ and electrons) for imaging (see in Figure 3-5a) [107]. The biased detector called multichannel plate (MCP) as shown in (a) is used to collect secondary particles for imaging. Since the Ga^+ are more or less implanted in the sample during FIB operation, ion beam exposure time should be as short as possible to avoid potential beam induced damages. 2) Milling: In general, ion beams are used to mill/etch the sample material. In other words, ion-beam physically sputtered material from the sample as shown in Figure 3-5b. In addition, the sputtering yield largely depends on the angle between surface normal and beam direction [107]. 3) Deposition: The whole process is in essence chemical vapour deposition (CVD). In FEI Scios, the deposited protection metal is platinum (Pt). As illustrated in Figure 3-5c, the precursor gases are sprayed on the sample by a fine Pt needle and then adsorb on the sample surface. These adsorbed precursor gases are subsequently decomposed by the FIB. Finally, the Pt remains as protection layer (thin film) on the sample whilst the volatile reaction products desorb from the sample surface and evacuated by the vacuum system.

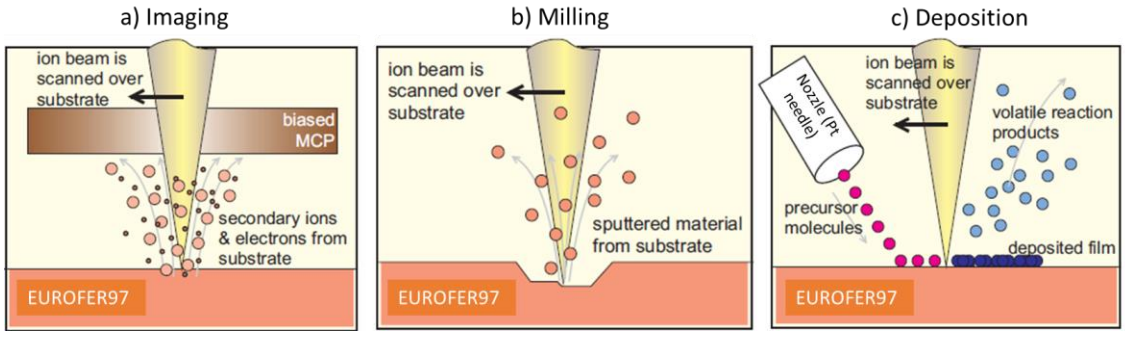

Figure 3-5: Illustration of three representative working principle of FIB. (a) imaging, (b) milling and (c) deposition. (adapted from [107]).

A routine procedure of TEM lamella fabrication includes two steps. 1) The TEM lamella is in-situ lifted-out from the undeformed regions of the above-mentioned marked shadow areas in Figure 3-3 and attached/welded onto the molybdenum TEM half-grid via Pt deposition (see, Figure 3-6a-d). 2) Afterwards, the lamella were carefully thinned down to electron transparency (to a thickness of ~ 100 nm) with multiple passes of a low-energy ion beam (see, Figure 3-6e). For details on the procedure for determining the optimized parameters, please refer to appendix 2.

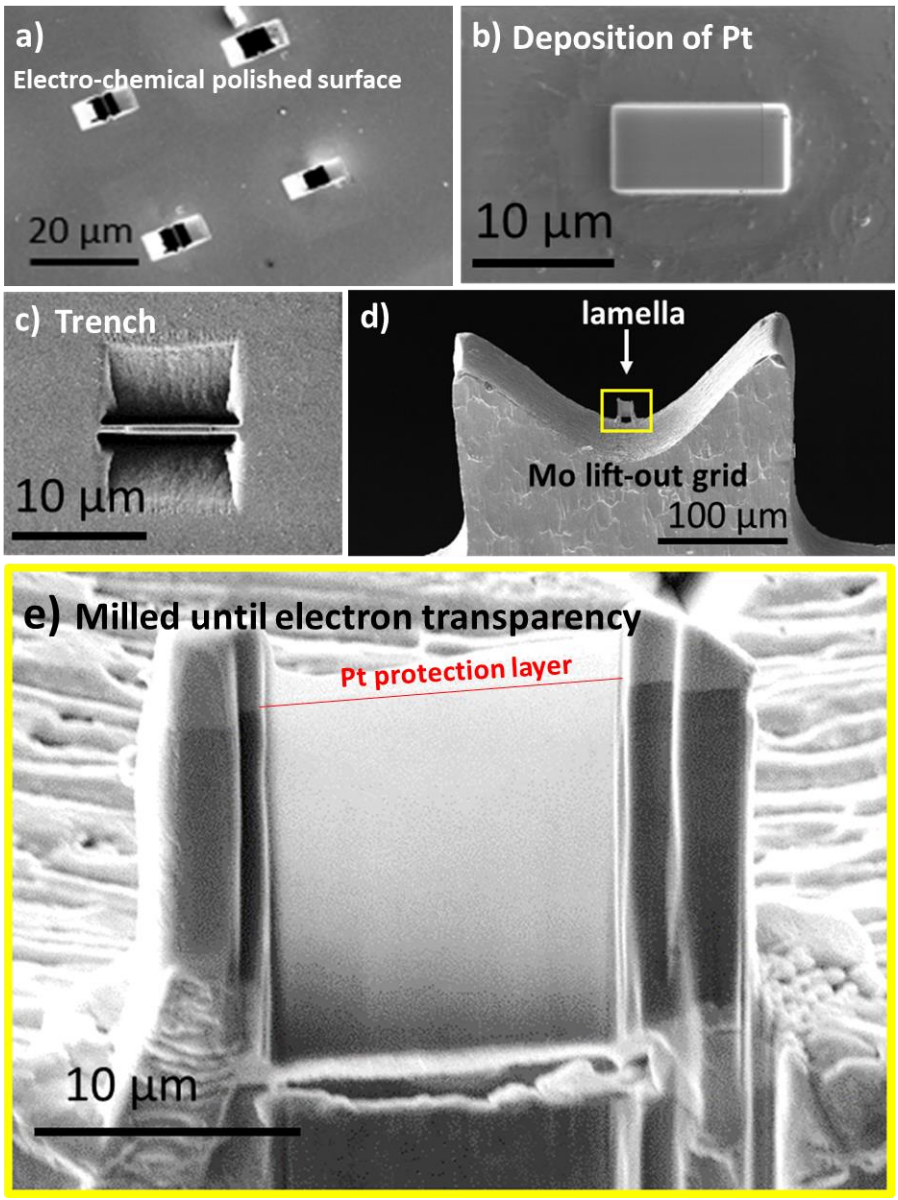

Figure 3-6: (a-d) A series of SEM images show the procedure of lamella fabrication for in-situ PIA TEM investigations. (a) Presents electro-chemically polished surface with remnant trenched sites of lamella lift-outs. Lamella fabrication procedure is as following: (b) Firstly, platinum deposition was carried out on the pristine electro-polished surface to minimize Ga^+ ion-beam damage and curtaining effect induced by the imperfection of the surface. (c) Thereafter, thin lamella was trenched out by removing material from the both sides until its thickness remains about 1 µm. (d) The lamella was then lifted-out using

easy lift W tip and welded onto the Mo TEM-half grid by Pt deposition. (e) Electron transparent thin lamella fixed on the Mo TEM half-grid after final milling [108].

Based on the SRIM (Stopping and Range of Ions in Matter) calculation, Huang et al. [109] suggest that a ~7 nm deep damaged surface layer (one side) can be induced from 5 kV Ga^+ beam energy at 1.5° angle of incidence in a Fe-based alloy. Therefore, lower beam energy, current and proper angle of incidence are three key factors to optimize the milling recipe. In addition, the recipe was tested on more than 10 unirradiated lamellae prior applying it to the neutron-irradiated lamellae so that ion-beam-induced defects (larger than 2 nm) can be excluded. Consequently, thickness of lamella was gradually reduced via adopting the parameters of the optimized cleaning pattern procedure (see Table 3-1). Apparently, FIB induced-damage is indeed minimized to a large extent as presented in TEM micrograph (see Figure 3-7).

Table 3-1: Parameters used for the final milling. Initially, the sample stage is tilted to 52° so that the incident ion beam is parallel to lamella surface.

Milling pattern	**Voltage (kV)**	**Current (pA)**	**Angle of incidence**	**Thickness (μm)**
Clean cross-section	30	300	± 1.3	~ 1
Clean cross-section	30	100	± 1.3	~ 0.8
Clean cross-section	16	48	± 1.3	~ 0.6
Clean cross-section	8	75	± 1.7	~ 0.4
Clean cross-section	5	15	± 3	~ 0.1
Clean cross-section	2	8	± 5	< ~ 0.1

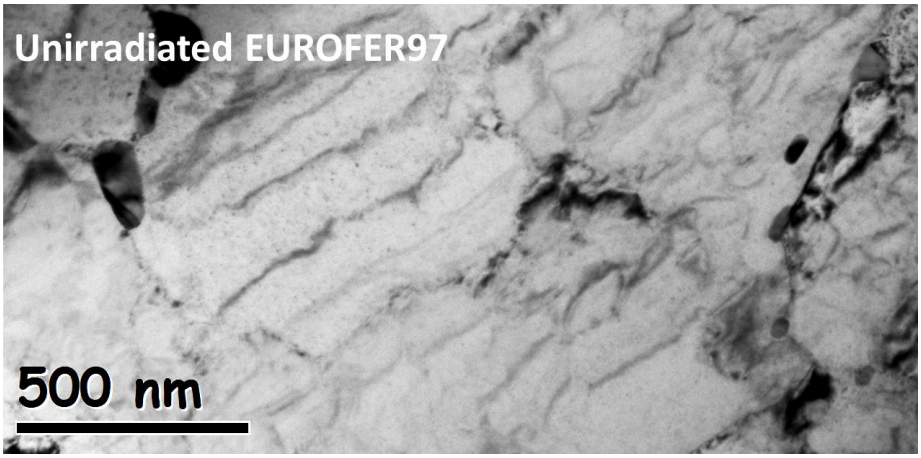

Figure 3-7: TEM micrograph of an unirradiated EUROFER97 lamella which was prepared using above optimized procedure and indicates a nearly artifacts-free microstructure [108].

3.2.3 Post-FIB processing

As a supplementary method to further reduce or mitigate the Ga^+ beam damage during FIB processing, Gatan precision ion polishing system (PIPS-2) is occasionally used to prepare high-quality lift-out specimens after FIB processing. Instead of using Ga^+, PIPS-2 use Ar^+ to sputter target material with even lower energy (<2 keV). Similar to the final milling procedure in FIB, the beam energy, current and angle of incidence are attentively chosen to finish the last step. Figure 3-8a shows a representative TEM micrograph of an unirradiated EUROFER97 prepared via such procedures (FIB+PIPS-2). The lamella was firstly thinned via FIB till ~150 nm and subsequently transferred to PIPS-2 for post-processing. With gradually reduced beam energy (from 1 keV to 300 eV), the lamella was finally thinned to ~50 nm. To be remarked, the incident angle in PIPS-2 should not be too low due to the re-deposition from Mo lift-out grid [110].

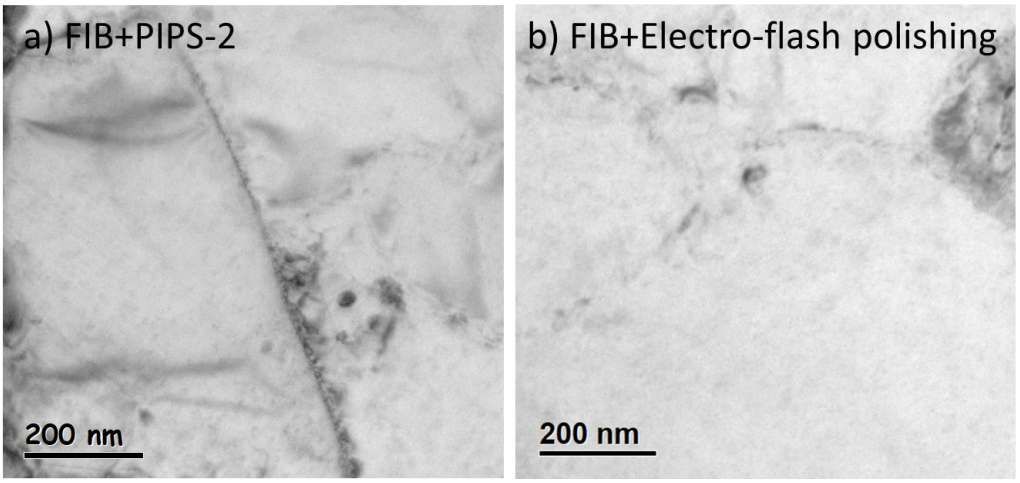

Figure 3-8: BF-TEM micrographs of unirradiated EUROFER97 lamellae prepared by (a) FIB + PIPS-2 and (b) FIB + electro-flash polishing. Both micrographs show a nearly ion-beam damage-free microstructure.

Since the working principles of both FIB and PIPS-2 systems are based on using ion beam, artifacts such as ion beam induced damage and re-deposition produced during such processing cannot be fully eliminated. Therefore, another post-FIB processing method, called electro-flash polishing, is adopted as an alternative to PIPS-2. As its name suggests, electro-flash polishing is an ultra-fast electro-polishing approach to remove the ion-beam damage at the thin-foil surfaces. Circuit diagram shown in Figure 3-9 illustrates the working principle of electro-flash polishing. A Mo lift-out grid with welded lamella is clamped by an Au-coated tweezer and worked as anode whilst the steel plate is used as cathode. Both the anode and cathode are then immersed into the abovementioned electrolyte (80% methanol and 20% sulfuric acid) at room temperature.

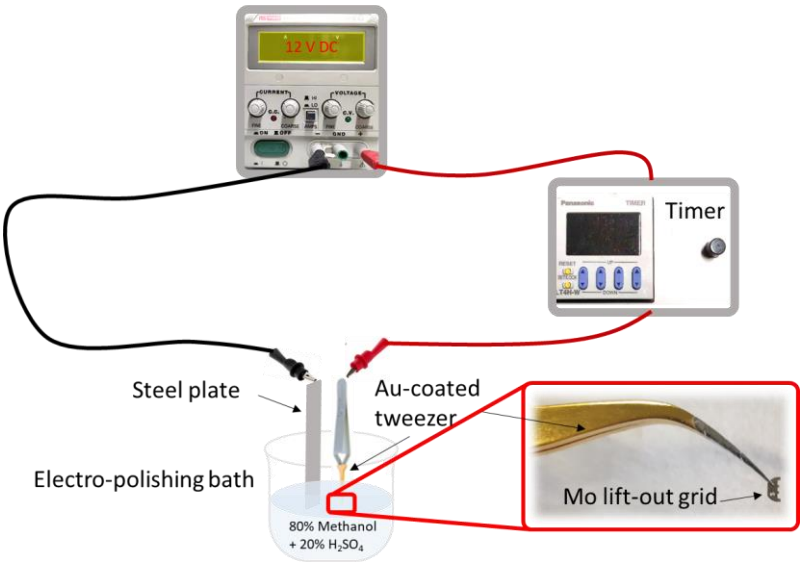

Figure 3-9: Circuit diagram of electro-flash polishing. The experimental setup consists of an electrolytic cell where the sample hold in Au coated tweezer acts as anode and the steel plate is used as cathode. In addition, a millisecond time resolution timer connected with the power supply allows the current to pass through for a very short time (~20 ms). Magnified image shows the Mo lift-out grid clamped by a gold tweezer.

The polishing time is set by a time relay, which is directly connected to the power supply. Unlike jet polishing, the targeted U-I values cannot be easily achieved by electro-flash polishing. Therefore, after several trails on unirradiated EUROFER97, approximately 40 nm thick material could be removed in 20 milliseconds (thickness measured via electron energy loss spectroscopy). Lastly, the lamella is immediately immerged into three cleaning baths with deionized (DI) water and ethanol (twice cleaning) respectively. Figure 3-8b shows a representative microstructure of unirradiated EUROFER97 after electro-flash polishing. Apparently, almost no black dots and other FIB induced artifacts can be observed.

- **Comparisons on neutron-irradiated TEM specimen preparations**

A firm understanding towards the pros and cons of each fabrication technique is crucial to prepare TEM specimens for dedicated TEM investigations. Although electro-polishing produces artifacts-free TEM specimen, radioactivity and electromagnetic problems limit its application, particularly in in-situ TEM annealing investigations. Therefore, FIB polishing technique is nowadays widely adopted in the fabrication of neutron-irradiated TEM specimen. However, the ion beam induced damage is an inevitable issue, which more or less influences the accuracy of defects analysis. Post-FIB processing might be helpful, but any carelessness during the preparations might let the hard work go to waste. For example, re-deposition from lift-out grid (Mo/Cu) looks similar to black dots, which influences dislocation loop density calculation. In addition, any mishandling during electro-flash polishing might result in the loss of the whole lamella. Besides, the etching rate of electro-flash polishing is strongly influenced by the lift-out grid material (Mo/Cu), the welding material (Pt) and even the tweezer while being dipped into the electrolyte [111]. Furthermore, the crystallographic orientation plays a role on the etching rate. Some of the grains is fully etched (in the presence of holes) while the others remain un-etched. For in-situ TEM annealing experiments, the existence of holes in the lamella cause internal stresses, and thus, might lead to misinterpretations of the results.

In conclusion, in spite of the enormous experiments effort, FIB polishing with optimized recipe is therefore predominantly used in the fabrication of TEM specimens in this work. In general, most FIB induced damage is similar to the irradiation-induced black dot (size less than 2 nm). Therefore, to avoid any inappropriate estimation, the black dot features are excluded in this work.

3.3 Microstructure characterization techniques

Transmission electron microscopy (TEM) is arguably the most powerful method to characterize radiation-induced defects such as dislocation loops and voids. Since TEM can be used in various modes, this section mainly emphasizes how it is applied in characterizing radiation-induced defects. Section 3.3.1 first summarizes the main working principles of TEM and scanning transmission electron microscopy (STEM). By comparing different diffraction contrast mechanisms, section 3.3.2 introduces several imaging techniques/conditions that are routinely used in characterization of dislocations. Section 3.3.3 describes qualitative and quantitative methods in analyzing dislocation loops and voids via TEM/STEM techniques. Lastly, the in-situ TEM annealing setup is introduced in section 3.3.4.

3.3.1 Transmission electron microscopy

- **Transmission electron microscopy (TEM)**

It is well known that optical microscope use light for illumination and magnifying the small objects with the help of a combination of glass lenses. Analogously, TEM operates on the same basic principle as the optical microscope but uses a beam of electrons instead of light. Since the wavelength of electrons is far shorter than that of visible light, the images taken by transmission electron microscopy is of higher resolution than that from optical microscope. Furthermore, like the design of optical lenses, electrons beam can be controlled by the electron lenses by using electromagnetic coils.

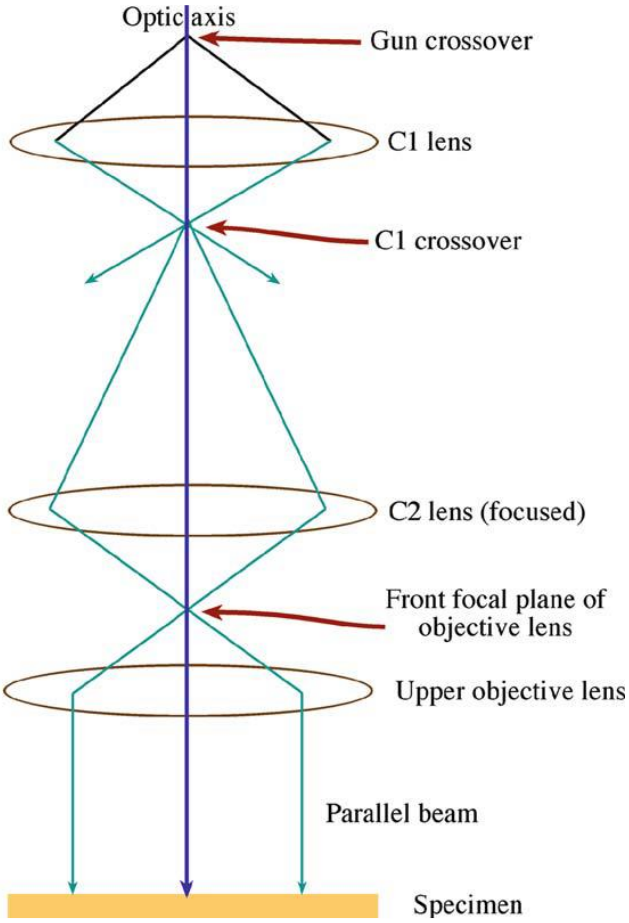

Figure 3-10: Simplified illustration of the illumination system in TEM mode with parallel beam. Using the C1 and C2 lenses to image the source at the front-focal plane of the condenser-objective lens, thus creating a parallel beam at the specimen plane [112].

In general, the transmission electron microscope can be divided into illumination system, objective lens/stage, and imaging system. The illumination system consists of the electron gun and several condenser lenses that focus the electrons onto the specimen. As shown in Figure 3-10, in the TEM mode, the first two condenser lenses (C1, C2) are adjusted to illuminate the

specimen with parallel beams of electrons emitted from the electron gun. In addition, for FEI TECNAI G^2 F20 X-TWIN microscope, a field emission gun (FEG) is applied which exhibits better brightness and longer lifetime than other electron sources. Furthermore, in order to avoid the collisions between the high-energy electrons and air molecules, a high vacuum is maintained inside the column of TEM to prevent the loss of energy of these electrons. Furthermore, an airlock is employed in the design of specimen stage, so that no air is introduced when the specimen is inserted into the TEM column.

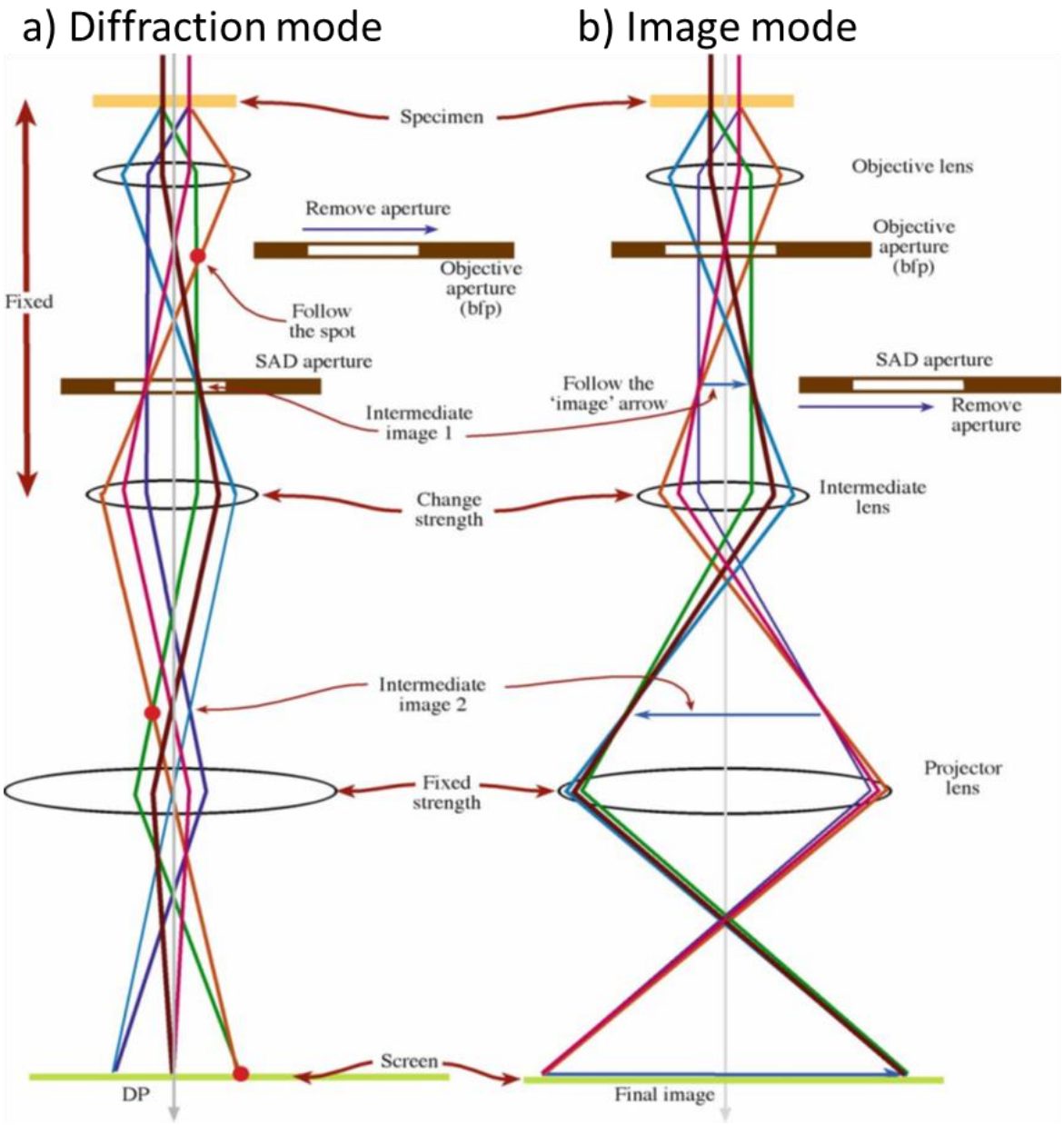

Figure 3-11: A highly simplified diagram shows the two basic operations of TEM imaging system involve (a) diffraction mode: projecting the DP onto the viewing screen and (b) image mode: projecting the image onto the screen. In each case the intermediate lens selects either the back focal plane (a) or the image plane (b) of the objective lens as its object [112].

The TEM imaging system typically contains objective lens, intermediate lens, and projector lens. The combination of these lenses produce a magnified image (or a diffraction pattern (DP)) of the specimen on the viewing screen. For diffraction mode (Figure 3-11a), the imaging-system lenses is so adjusted that the back focal plane of the objective lens acts as the object plane for the intermediate lens. Diffraction pattern is thereby projected onto the viewing screen. By readjusting the intermediate lens, the image is projected onto the viewing screen in the image mode (Figure 3-11b). In addition, since the direct-beam is often so intense that it will damage the detection camera in DP mode, selected-area diffraction (SAD) is often used to reduce such effect. Moreover, SAD is also operated to select a specific area of the specimen to contribute to the DP. It is noteworthy that modern TEM columns, such as FEI TECNAI G^2 F20 X-TWIN microscope, have many more lenses in their imaging systems, which give greater flexibility in terms of magnification and focusing range for both images and DPs.

As beams of electrons interact with the specimen, electrons scattered in the forward directions are focused in the back focal plane; and thus, forms diffraction pattern. Either bright-field (BF) or dark-field (DF) mode can be operated by placing an aperture in the back focal plane of the objective lens. If the aperture allows only direct beam to pass, then BF image is formed. On the contrary, DF image is formed when the diffracted beam is selected. Practically, more complicated imaging techniques such as kinematic bright-field (KBF) and weak-beam dark-field (WBDF) techniques are widely used in characterizing radiation-induced defects. More descriptions about these imaging techniques and corresponding contrast mechanisms are presented in the next section.

- **Scanning transmission electron microscopy (STEM)**

Unlike parallel beam mode in TEM, the illumination system of STEM is operated in the convergent beam mode. The convergent beam (called probe) scans parallel to the optic axis and is thereby used to localize the signals coming from the specimen. Figure 3-12 presents the working principle of forming a scanning image in STEM mode. The same scan coils are used to scan the beam on the specimen and compute display synchronously.

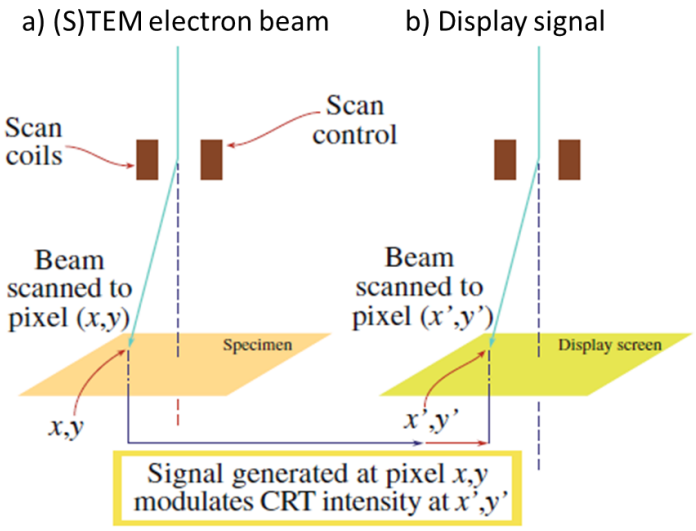

Figure 3-12: The principle of forming a scanning image, showing how the same scan coils in the microscope control (a) the beam-scan on the specimen and (b) the beam-scan on the computer display screen of the STEM. Signal generated at pixel x, y modulates cathode-ray tube (CRT) intensity at x', y' [112] .

As shown in Figure 3-13, the generated signals can be detected by BF detector or annular DF (ADF) detector. Similar to TEM BF imaging where objective aperture is inserted onto the plane of DP, the BF detector in STEM BF mode is placed onto the axis of the microscope and intercepts only direct-beam electrons. Hence, the images taken from BF detector are equivalent to TEM BF images. On the contrary, imaging mechanisms of STEM DF and TEM DF is fundamentally different. Surrounding the BF detector, ADF detector is used to collect the most of scattered electrons for STEM ADF imaging. However, in TEM DF mode, only a fraction of the scattered electrons is permitted to enter the objective aperture. Therefore, as ADF detector collects more signals, STEM DF image is less noisy than TEM DF image. In addition, the image contrast of STEM ADF can be easily improved by adjusting the camera length (L). If the ADF detector gathers electrons scattered through an angle of > 50 mards, Bragg effects are mostly avoided. Such a detector is called high-angle ADF or HAADF detector. Because the HAADF detector gathers electrons scattered by high atomic number (Z) elements due to the strong electrostatic interaction between their nucleus and electrons, STEM-HAADF image is usually called Z-contrast image.

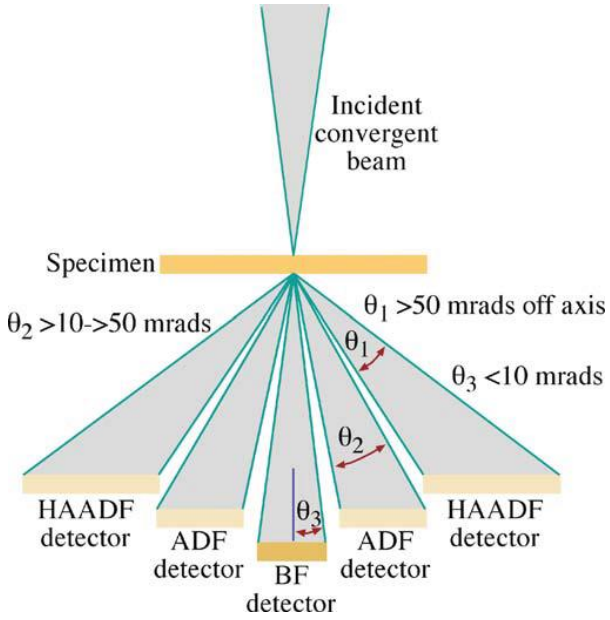

Figure 3-13: Schematic for detector setup in a STEM mode. The BF and ADF detectors are shown along with the range of electron scattering angles (θ_1 and θ_2) gathered by each detector. In addition, HAADF detector only gathers electrons scattered through an angle (θ_3) of > 50 mrads (~3°) [113].

In FEI TECNAI G^2 F20 X-TWIN microscope, TEM mode and STEM mode can be easily switched by additional equipment, such as scanning coils, detectors, and necessary circuitry. In addition, the FEI TECNAI G^2 F20 X-TWIN used in this work is equipped with energy dispersive X-ray spectroscopy (EDX) and electron energy loss spectroscopy (EELS), which allows analytical measurements.

3.3.2 TEM Imaging contrast

A proper interpretation of TEM micrographs depends largely on the understanding of image contrast. In general, the contrast of TEM micrographs arises because of the scattering of the incident beam by the specimen. In radiation-induced defects' studies, diffraction contrast tends to dominate. Typically, the presence of a defect in the specimen causes a local bending of the lattice plane; and hence, the defect strain field give rise to local changes in diffracting conditions. Furthermore, the image characteristics depend sensitively on the diffraction conditions chosen. Therefore, to get good strong diffraction contrast in both BF and DF images, two-beam conditions are well-suited for the investigation of the small radiation-induced defects such as dislocation loops. Furthermore, the excitation error s_g, which is the deviation parameter from the exact Bragg condition, specifies the diffraction condition [114, 115]. Additionally, the determination of s_g can be realized via Kikuchi patterns [116, 117]. More detailed descriptions of two-beam conditions are introduced in the following section.

- **Two-beam dynamical condition**

Two-beam condition means, besides the strong direct-beam, only one diffracted-beam g is excited. For dynamic two-beam condition, the intensity of diffracted-beam g is similar to that of the direct-beam. As shown in Figure 3-14a, the Ewald-sphere [118] cuts both the direct-beam and diffracted-beam (reflection) g. The foil is tilted so that one set of diffracting planes (hkl) is at, or very close to the Bragg's condition. Due to the very small distance of the reciprocal lattice point G from the Ewald-sphere, s_g is therefore zero or very small under such diffraction condition. For the diffraction pattern, since g is exactly at the Bragg condition, the g Kikuchi line just passes through the g reflection. However, owing to the strong dynamic interaction between the two beams, such condition is not suitable to imaging small dislocation loops [16].

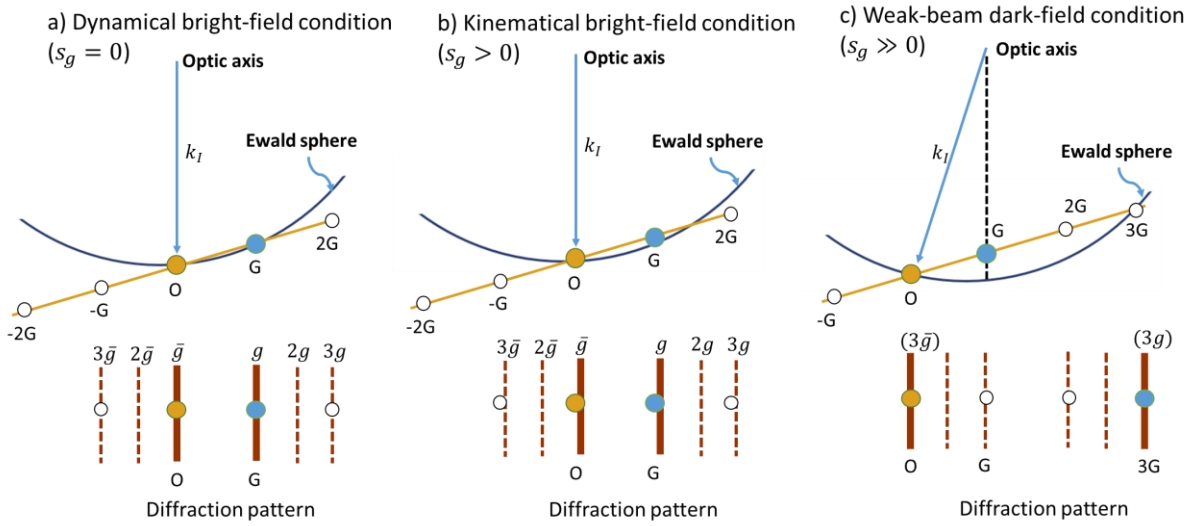

Figure 3-14: Schematic representations of three diffraction conditions used in diffraction contrast imaging: (a) dynamical bright-field (DBF) condition, (b) kinematical bright-field (KBF) condition and (c) weak-beam dark-field (WBDF) condition. In each case, the Ewald sphere is sketched with corresponding schematic diffraction patterns (DP) showing the position of the relevant Kikuchi lines. The curvature of the Ewald sphere is exaggerated for clarity. For KBF condition, the foil is tilted slightly away from exact Bragg condition so that G is inside the Ewald sphere ($s_g > 0$). For WBDF condition, the foil is tilted well away from the exact Bragg condition so that both the direct-beam and 3g refection are strongly excited whilst the g is weakly excited ($s_g \gg 0$) (adapted from [119]).

- **Kinematical bright-field condition (KBF)**

An effective approach to avoid the strong (dynamic) two-beam effect is by setting kinematical condition with a small positive deviation parameter ($s_g > 0$), as shown in Figure 3-14b. Often, the magnitude of s_g is not specified explicitly. For KBF condition, the foil is tilted just sufficiently away from the Bragg condition so that most of the dynamical contrast will be lost. In other words, the g Kikuchi line is a little bit on the right side of the g reflection in diffraction

pattern. The effective extinction distance [115] is consequently reduced and the dislocations become narrower [16]. KBF condition is therefore, suitable to image small dislocation loops (compare 3 marked dislocation loops in Figure 3-15a. However, one should be very cautious when using kinematical condition to determine the loop size, because the loop size varies considerably at different depth [16, 120].

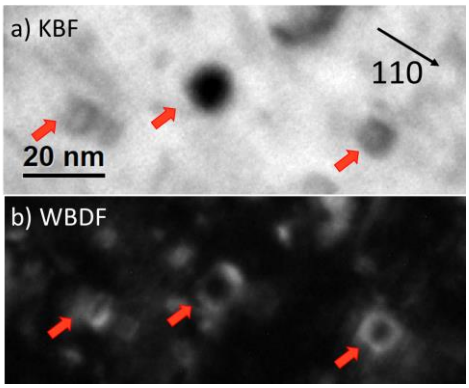

Figure 3-15: A comparison of dislocation loop images in a neutron-irradiated EUROFER97 (15 dpa, 330 °C) formed using (a) KBF and (b) WBDF conditions. The micrographs were taken under $g = \{110\}$ diffraction condition. The 3 dislocation loops (marked with red arrows) in WBDF condition appear narrower than in KBF condition.

- **Weak-beam dark-field condition (WBDF)**

Since there is a high density of dislocation loops, which are less than 5 nm, in neutron-irradiated EUROFER97 (15 dpa, 330 °C) [48, 67], WBDF condition is considered to be the most suitable approach to identify such small loops. Under such condition, the thin-foil is tilted so that in regions away from the dislocations, the diffracting planes are well away from the Bragg condition. As shown in Figure 3-14c, the Ewald sphere cuts the line of systematic reflections at the point $3g$, and only g reflection under the optical axis is weakly exited ($s_g \gg 0$). For this reason, the average image intensity is very low. Therefore, it is called $g(3g)$ WBDF condition. Nevertheless, in regions close to the dislocations, the local strain-field may bend the reflecting plane back towards the Bragg condition, as shown in Figure 3-16. This leads to a significant improvement of the dislocation peak intensity relative to the low intensity of the surrounding background. Figure 3-15b presents 3 dislocation loops under WBDF condition. These 3 loops show distinct contrast than the image taken under KBF condition (Figure 3-15a). In general, for quantitative measurements from interpretable image, s_g should be no less than $2 \times 10^{-1}\ nm^{-1}$. For imaging dislocations, such condition gives rise to a narrow (<2 nm) high-contrast image peak located close to the dislocation core [121]. For a detailed determination of the value of s_g, see appendix 3.

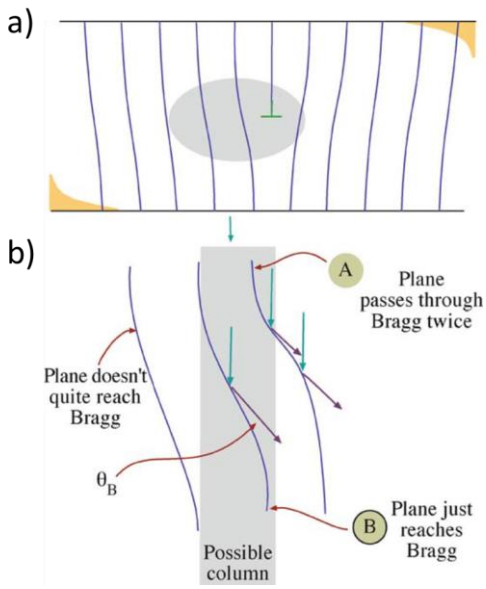

Figure 3-16: Illustration of WB images from strained regions of the specimen show high intensity only from those regions where the diffracting planes are bent back into the Bragg condition. This illustration is for an edge dislocation. (b) Presents the core region selected in (a)[119].

- **Down-zone condition**

Down-zone condition (down-axis condition) can be obtained by tilting the thin-foil to a zone-axis orientation. Except for the direct-beam, the diffracted-beam are almost equally excited. Therefore, the majority of the loops present contrast in a single micrograph, which provides advantage in determination of the dislocation loop density. An example of dislocation loops under such condition is shown in Figure 3-17. This HAADF-STEM micrograph showcases a high density of dislocation loops (including black dots) co-existing with pre-existed dislocations in neutron-irradiated EUROFER97.

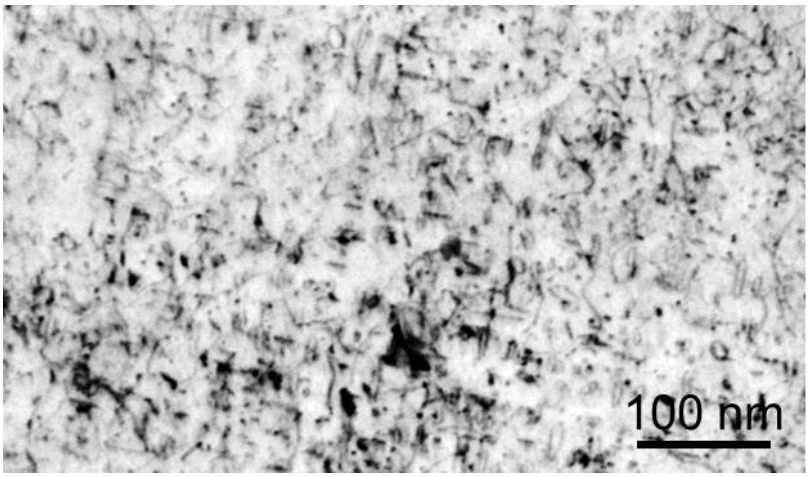

Figure 3-17: A representative microstructure of neutron-irradiated EUROFER97 (15 dpa, 330 °C) taken via HAADF-STEM (with inverted-contrast) close to the [110] zone-axis orientation.

3.3.3 Characterization of radiation-induced defects

- **Nature of dislocation loop**

The nature of the dislocation loop can be determined by a well-known inside-outside technique, which is illustrated in Figure 3-18. An interstitial loop lying on planes inclined to the incident beam, is imaged under KBF/WBDF condition with $s_g > 0$ using diffraction vector shown. The regions surrounding dislocation cores diffract strongly due to the local strain fields, and the image peak therefore lies inside or outside the projected position of the dislocation core. Inside-contrast arise when $(g \cdot b)s_g < 0$, outside-contrast when $(g \cdot b)s_g > 0$. However, such inside or outside-contrast behavior of the loop only tells the sign of $g \cdot b$ (notice under KBF/WBDF condition, $s_g > 0$). To further identify whether the loop is interstitial or vacancy type, the inclination of the loop must be determined. For an edge interstitial loop, b is upward-drawn loop normal n (i.e., $b \cdot n > 0$ and $b \cdot z < 0$, where z is the incident beam direction). In a similar way, if $b \cdot z > 0$, then the loop is of vacancy type. For detailed example, see Ref. [122].

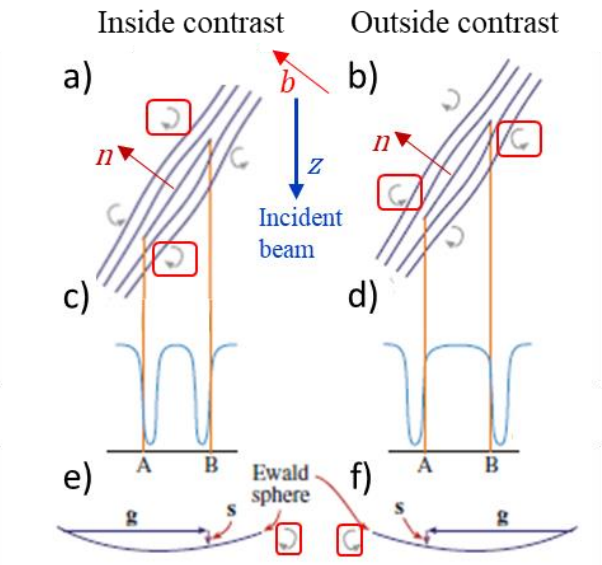

Figure 3-18: (a, b) Structure of an interstitial loop relative to the diffracting plane (orange lines). Arrows show the rotation of the diffracting planes around the dislocation. (c, d) Position of the image contrast relative to the projected dislocation position, Inside-contrast occurs when clockwise rotation of the diffracting planes brings them into the Bragg condition. Outside-contrast occurs for the counterclockwise case. (e, f) The relationship between g, s, and the sense of rotation (adapted from [123]).

- **Analysis of dislocation loop**

In literature, dislocation loops with two types of Burgers vector ½<111> and <100> have been confirmed to coexist in neutron-irradiated EUROFER97 [48, 66, 67, 124]. If Burgers vectors

of these loops are perpendicular to the selected reflection ($g \cdot b = 0$), these loops will be out-of-contrast (i.e., invisible). In general, four g conditions near the same zone axis should be applied to access loops' Burgers vector and density. However, due to EUROFER97's small grain size and magnetism issue [27], such $g \cdot b$ analysis with 4 g reflections require huge experimental efforts. Furthermore, as there is a high density of small loops (with size less than 5 nm) in the WTZ irradiated EUROFER97, it is almost impossible to trace individual loops in different micrographs. Therefore, two low-indexed g-vectors near [100] or [110] zone axis are adopted for quantitative analysis. This method provides an easy and fast way to access ½<111> and <100> loop density and fraction without identifying individual loop's Burgers vector; and hence, is appropriate for statistical analysis. According to the truth table (see appendix 4), $2/3$ of <100> loops and half of the ½<111> loop are visible simultaneously under $g = 110$. Similarly, 1/3 of <100> loops and all ½<111> loops are visible under $g = 002$. Hence, loop density under $g = 110$ and $g = 002$ can be estimated by:

$$N_{g=110} = \frac{2}{3} N_{<100>} + \frac{1}{2} N_{\frac{1}{2}<111>}$$
$$N_{g=002} = \frac{1}{3} N_{<100>} + N_{\frac{1}{2}<111>} \qquad \text{Equation 3-1}$$

where $N_{<100>}$ and $N_{\frac{1}{2}<111>}$ are <100> and ½<111> loop density respectively. By solving these equations, <100> and ½<111> loop density can be expressed as:

$$N_{<100>} = 2N_{g=110} - N_{g=002}$$
$$N_{\frac{1}{2}<111>} = -\frac{2}{3} N_{g=110} + \frac{4}{3} N_{g=002} \qquad \text{Equation 3-2}$$

Hence, the total loop density can be calculated as the sum of $N_{<100>}$ and $N_{\frac{1}{2}<111>}$. Additionally, the fraction of <100> and ½<111> loops can be easily calculated.

Besides $g \cdot b$ invisibility criterion, the Burgers vector of individual loop can also be determined with the help of dislocation-loop map [125]. Loop's projection on the viewing screen substantially depends on its habit plane and nearby zone axis. For instance, as shown in Figure 3-19, <100> loops present edge-on contrast whereas ½<111> loops show elliptical contrast near [100] zone axis. Similarly, dislocation-loop map near [110] zone axis can also be easily obtained (see Ref.[125]). It is noteworthy that both [100] and [110] zone axis are ideal orientations for studying <100> and ½<111> type loops, since they present pronounced difference in their shape/contrast under specific diffraction conditions.

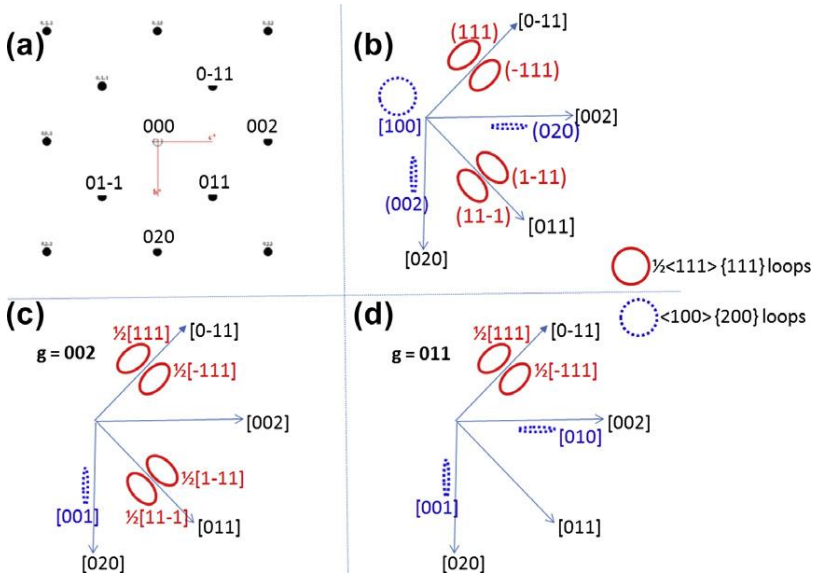

Figure 3-19: (a) Simulated diffraction pattern of bcc-Fe under [100] zone axis, (b) corresponding dislocation-loop map without considering $g \cdot b$ invisibility criterion, (c) and (d) show the projected dislocation-loop excited by g=002 and g=011, respectively. Dislocation loops considered are limited to <100> {200} and ½<111> {111}. Loops in (b) are represented by the habit plane, while those in (c) and (d) are indicated by their Burgers vector [125].

A representative micrograph taken via WBDF technique with g = 020 diffraction condition near [100] zone axis is shown in Figure 3-20. As evident, the irradiated microstructure manifests homogenous distribution of the dark-contrast dislocation loops. According to the simulated dislocation-loop map in right [125], the edge-on loops marked with blue circles are found to be of <100> type, while the elliptical-shaped loops marked with red circles are identified to be of ½<111> type. For such elliptical loops, the major axis is taken as a measure of their size.

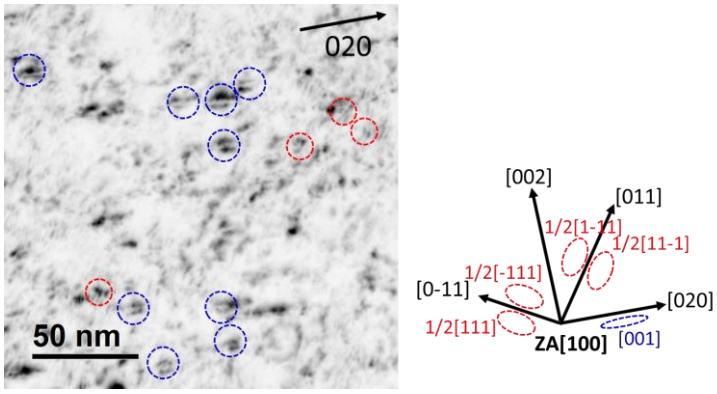

Figure 3-20: Inverted-contrast TEM-WBDF micrographs taken under g(4.1g) diffraction condition with g = (020) with near [100] zone axis presents representative as-irradiated (15 dpa, 330 °C) EUROFER97 microstructure (a magnified micrograph adapted from [126]) . A high density of nano-scale dark-contrast features visible in the micrograph are irradiation-induced dislocation loops. According to the corresponding simulated loop map in right image [125], the edge-on loops are identified to be <100> type (marked with blue circles) while the elliptical loops are identified to be ½<111> type (marked with red circles).

- **Characterization of voids**

Previous works show that the mean size of voids in neutron-irradiated EUROFER97 (15 dpa, 330 °C) is less than 5 nm [66, 67]. Therefore, these nanometer-sized voids are often best imaged in an out-of-focus imaging condition. The contrast arises from a weak absorption component and a phase-contrast component due to defocus, the latter giving Fresnel fringes near the edge of the void [16]. The contrast of voids tends to be better under kinematical rather than the dynamical diffraction condition, because nearby dislocations are less dominant under kinematical condition. Voids can be imaged by using BF through-focal series with thin foil tilted well away from the Bragg condition for all reflections [16]. Under such condition, voids appear as white dots surrounded by a bright fringe in underfocus micrographs, and as dark dots surrounded by a bright fringe in overfocus micrographs. Besides, voids are invisible in the in-focus micrographs. Figure 3-21 presents voids' contrast evolution in neutron-irradiated EUROFER97 at infocus, overfocus and underfocus conditions. The best contrast is usually obtained in the underfocus condition (Figure 3-21c), where the first dark fringe is commonly used to delineate the edge of the voids [127, 128]. The size of spherical void, for instance, in the magnified Figure 3-21c can be measured by the diameter of the first dark Fresnel fringe. However, for voids smaller than about 2 nm, the size cannot be measured accurately [127, 128].

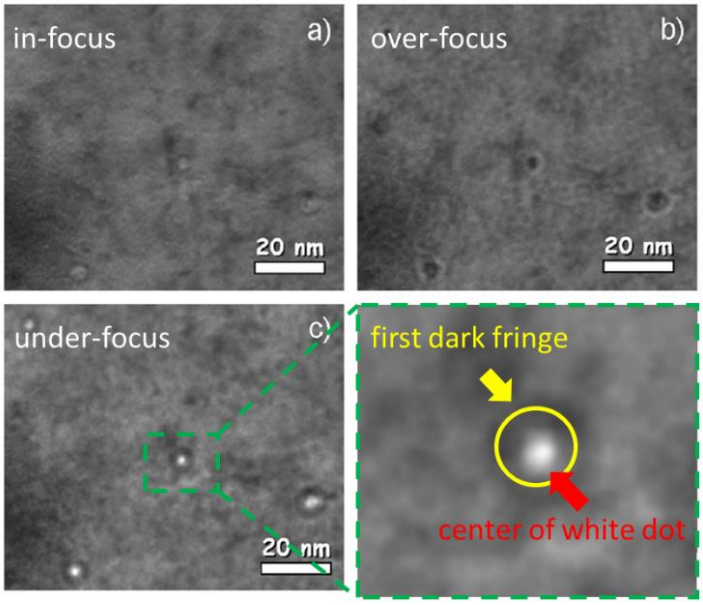

Figure 3-21: Voids in a neutron-irradiated (15 dpa, 330 °C) EUROFER97 sample. The KBF images were taken with g={211} near <111> zone axis: (a) focused image, voids are hardly visible, (b) overfocus, 2 µm, (c) underfocus, -2 µm. Clear dark fringe and white dot can be detected in magnified micrograph (c). (adapted from [67])

- **Thickness measurement**

Electron energy loss spectroscopy (EELS) allows a fast and reliable measurement of sample thickness in TEM. It is well established that EELS can provide an approximate value of thickness of crystalline specimens by straightforward integration of EEL spectrum [129]. The ratio of specimen thickness (t) to the characteristic mean free path (λ) for inelastic scattering for the material is given by [129, 130]:

$$\frac{t}{\lambda} = ln\left(\frac{I_t}{I_0}\right)$$

where I_t is the total number of electrons per square meter per second in the EEL spectrum and I_0 is the number of electrons per square meter per second that did not lose energy (the zero-loss peak). Figure 3-22 shows a representative low-loss EEL spectrum acquired from a EUROFER97 TEM sample. The low-loss spectrum includes two peaks namely a sharp zero loss peak (I_0) and broad plasmon peak (I_p). The intensity of total number of electrons in the EEL spectrum (I_t) is equal to the sum of the intensity of zero loss peak (I_0) and plasmon peak (I_p). Hence, the right part of the equation can be easily obtained from a built in option in Gatan Digital Micrograph software.

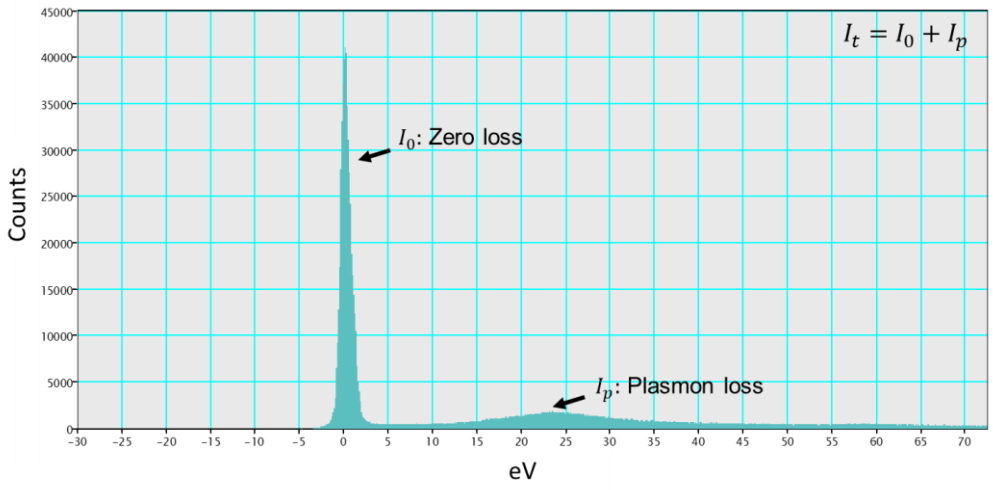

Figure 3-22: A representative low-loss EELS spectrum acquired from a EUROFER97 TEM sample. I_0 is the intensity of sharp zero loss peak while I_p is the intensity of broad plasmon signal induced by inelastic scattering from outer-shell electrons.

Egerton et al. [129] measured λ in 11 materials and found it is dependent on the measured material's atomic number, incident energy (200 kV is the present case) and collection semi-angle (determined by the camera length selected and the physical size of the entrance aperture). The mean inelastic scattering path for Iron is round 100 nm with an accuracy of about 90%

[129]. In the present study, the relative log-ratio method in Gatan Digital Micrograph software was applied to measure the thickness of TEM thin-foils. The EEL spectrum was acquired via EELS spectrometer installed on a FEI Tecnai G^2 F20 X-TWIN microscope equipped with a post-column GIF Tridiem energy filter.

3.3.4 In-situ TEM annealing

In-situ TEM annealing allows dynamic observation of microstructural evolution at elevated temperatures. The time- and temperature-dependent dynamic process of radiation-induced defects such as dislocation loops and cavities can be technically well traced and their annealing kinetics can be therefore studied. Figure 3-23 illustrates the setup for in-situ TEM annealing experiments, where a FEI Tecnai G^2 F20 X-TWIN microscope operating at 200 kV equipped with a Gatan double-tilt heating holder (Model 652) was employed. In addition, the temperature is controlled via the multiple-functional panel of the Gatan temperature controller (Model 1905). Annealing temperature is monitored by using in holder built-in thermocouples (Type T, K and R), which are not in direct contact with the TEM specimen.

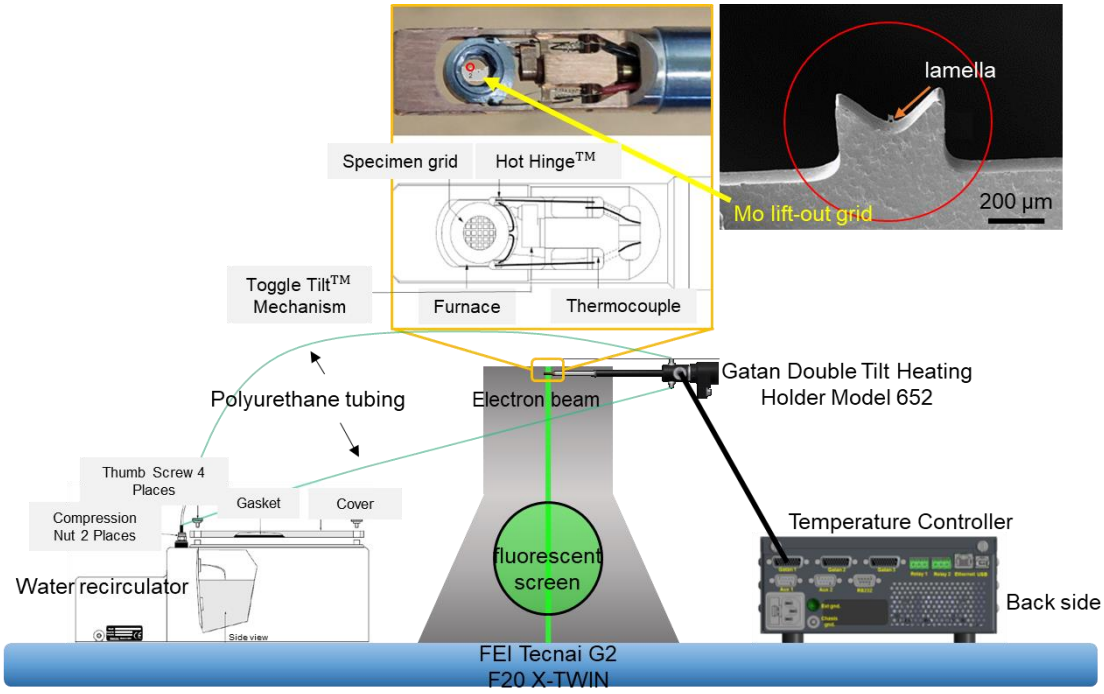

Figure 3-23: Schematic of in-situ TEM annealing setup: A simplified schematic of a high-resolution FEI Tecnai G^2 F20 X-TWIN microscope is equipped with a Gatan double-tilt heating holder (Model 652), which is connected with a Gatan temperature controller (Model 1905) and a water recirculator. The magnified yellow frame presents a real image and a corresponding drawing of the front part of the holder. The Mo lift-out grid with one of the tongs is further magnified as presented in the SEM micrograph. A marked lamella is welded on the Mo lift-out grid for in-situ TEM annealing experiment. (Schematics of temperature controller, water recirculator and front part of the holder are taken from the Gatan double-tilt heating holder handbook).

The lamella with Mo lift-out grid is sandwiched between two tantalum washers (not shown in the image) to avoid diffusion bonding to the furnace assembly during heating. As the PIA temperatures in this study is above 500 °C, a water recirculator with a stainless steel tank filled with 2.5 liters of distilled water at ambient room temperature is connected to the temperature controller. Once the operating temperature reaches 500 °C, the water recirculator automatically start to work. Furthermore, the available Gatan digital micrograph software assisted in observing real-time microstructure evolution, capturing images and recording videos at a time resolution from 20 to 30 frames per second (fps).

In this work, different annealing schemes including ramping and isothermal thin-foil annealing experiments are introduced in detail in the following chapter (section 4.2 and 4.3) respectively. In addition, considering the surface effect and thus avoiding biased results in the quantitative analysis, dedicated isothermal thick-foil annealing experiments were designed and conducted as supplementary experiments (see section 4.4).

Chapter 4 Results and Discussion

Temperature effects on irradiation-induced defects in neutron-irradiated EUROFER97 steel were studied via TEM investigations in this work. Section 4.1 provides an overall microstructural picture of the initial (as-irradiated condition) and final states (PIA at 550 °C for 3 hours) of the samples from the bulk materials. Hence, most of the quantitative results obtained from as-irradiated and bulk-annealed samples were used as reference in this chapter. Section 4.2 presents a dedicated in-situ TEM annealing study mainly focused on the isolated irradiation-induced defects evolution. The dynamic behaviour of the isolated dislocation loop and cavity were initially accessed from different in-situ temperature ramping experiments. A more general and systematic investigations on dislocation loop evolution and their annealing kinetics were carried out via isothermal in-situ TEM annealing experiments on thin-foils, which are presented in section 4.3. In contrast to the bulk annealing results (section 4.1), loop coarsening and the formation of dislocation lines/networks were not in general observed in thin-foil annealing experiments conducted at 550 °C. The discrepancy is attributed to surface effects, which are known to play critical role in thin-foil annealing experiments. Therefore, to clarify the inconsistency between thin-foil (section 4.1) and bulk annealing experiments (section 4.2 and 4.3) and to delineate various associated mechanisms on EUROFER97, dedicated isothermal thick-foil PIA investigations were carried out, which are presented in section 4.4. The results of quantitative analysis of radiation-induced defects from section 4.1 to section 4.4 are summarized and compared in section 4.5. In addition, the dispersed barrier hardening (DBH) model is used to predict and elucidate the contribution from dislocation loops and other irradiation-induced defects to the recovery of hardening.

4.1 Post-irradiation annealing bulk EUROFER97 steel

As presented in section 2.4.1, recent post-irradiation annealing (PIA) investigations on the neutron-irradiated EUROFER97 steel has led to a nearly complete recovery of the mechanical properties. To investigate the possible responsible microstructural processes, quantitative transmission electron microscopy (TEM) investigations on the neutron-irradiated (330 °C, 15 dpa) and subsequently annealed (550 °C, 3 h) EUROFER97 steel have been carried out. The investigated TEM lamellae were lifted out from the bulk samples. Different imaging techniques

are applied to characterize irradiation-induced dislocation loops and cavities in as-irradiated and PIA samples. Quantitative results acquired from as-irradiated samples in this work are also compared with those from previous works in which samples were prepared via electro-polishing.

The results of dislocation loop density and size distribution of as-irradiated samples in this study matches the previous studies in which the samples were prepared via electro-polishing [67]. In addition, it was observed that 3 hours PIA at 550 °C leads to a reduction of dislocation loop density with a simultaneous increase in their mean size. Interestingly, a microstructure transition from dislocation loops to dislocation lines/networks was also noticed. Also, a reduction of cavity density with increment in their mean size was observed. Furthermore, the annealing behavior of these aforementioned microstructures and possible annealing mechanisms were discussed based on the current TEM results. Parts of the work presented in this section has already been published in Ref. [126].

4.1.1 Materials and experimental

The "Wissenschaftlich-Technische Zusammenarbeit 01/577" (WTZ) irradiation experiments were performed on miniaturized Charpy impact samples of EUROFER97 in BOR-60 fast reactor of SSC RIAR in Dimitrovgrad under following condition: 15 dpa, 330 °C. The both irradiated and post-irradiation annealed (at 550 °C with a temperature ramp of ~ 2.9 K/min and held for 3h) impact samples were mechanically tested, for detailed descriptions of PIA experiments please refer to section 2.4.1. For microstructure investigations, firstly, 1 mm disc TEM samples were prepared out of undeformed parts of irradiated and post-irradiation annealed impact samples by cutting thin slices and subsequent electrolytic polishing. For the detailed samples preparation procedures please refer to section 3.2.1. Subsequently, FEI Scios focused-ion beam (FIB) scanning electron microscope (SEM) was utilized to prepare TEM lamellae [27]. For detailed FIB processing of neutron-irradiated EUROFER97, please refer to section 3.2.2 and Figure 3-6 [126] .

A high-resolution FEI Tecnai Tecnai microscope operating at 200 kV equipped with a FEI double-tilt holder and a high-angle annular dark-field (HAADF) scanning TEM (STEM) detector was employed for quantitative investigations of microstructure. The thicknesses of surveyed areas were determined by electron energy loss spectroscopy (EELS) log-ratio method with about 10% uncertainty [129] as described in section 3.3.3. Generally, g·b analysis (g is the diffraction vector) in combination with weak beam dark-field (WBDF) technique was used to identify the Burgers vector and calculate the dislocation loop density in irradiated material [30]. Underestimation of the loop density due to partial invisibility was resolved by using the

statistical method for Burgers vector analysis [31]. The resolution limit for dislocation loops in terms of diameter was about 2 nm, and thus, it led to an underestimation of defect density with statistical error of about 20%. Additionally, bright-field (BF) and HAADF-STEM techniques were used to quantify and characterize microstructure [126].

4.1.2 Dislocation loops and lines/networks evolution

- **Dislocation loops nature**

In this work, the nature of the dislocation loop was further determined and confirmed by inside-outside technique on the TEM lamellae (For more technical details, please refer to 3.3.3). As shown in Figure 4-1, dislocation loops presents inside-contrast under $g = 0\bar{1}\bar{1}$ condition and outside-contrast under $g = 011$ condition. According to the corresponding simulated dislocation-loop map near [100] zone axis [16], the Burgers vector of the marked edge-on loops can be identified as $\pm a_0[010]$ or $\pm a_0[001]$. Since inside-contrast (Figure 4-1a) is valid under condition $(g \cdot b)s_g < 0$ ($g = 0\bar{1}\bar{1}$; $s_g > 0$), the Burgers vector can be determined as $a_0[010]$ and $a_0[001]$ rather than $a_0[0\bar{1}0]$ and $a_0[00\bar{1}]$. Additionally, as incident electron beam is downwards ($z = [00\bar{1}]$) , thus $b \cdot z < 0$ ($a_0[001]$). Therefore, the marked [001] loops are of interstitial nature whereas the nature of the marked [010] loop can not be determined as $b \cdot z = 0$.

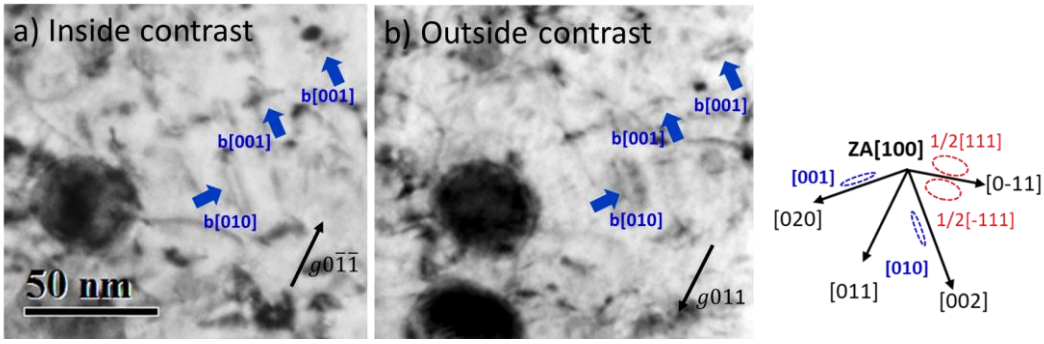

Figure 4-1: KBF-TEM micrographs present the inside-outside-contrast of three large <100> loops in a neutron-irradiated EUROFER97. The micrographs were taken under $g = 0\bar{1}\bar{1}$ (a) and $g = 011$ (b) diffraction conditions near zone axis [100]. According to the corresponding simulated dislocation-loop map [125], three large edge-on loops marked with blue arrows are identified to be <100> type. Apparently, dislocation loops presents inside-contrast under $g = 0\bar{1}\bar{1}$ condition and outside-contrast under $g = 011$ condition.

- **As-irradiated condition**

Detailed microstructural characterization of EUROFER97 steel prepared via electro-polishing after WTZ irradiation (15 dpa, 330 °C) has been carried out several times [48, 66, 67, 103].

Similar to microstructure of the electro-polished samples, an example of the representative microstructure from FIB prepared sample under inverted WBDF and HAADF-STEM conditions are presented in Figure 4-2a and Figure 4-3a, respectively. As evident, under both conditions, the irradiated microstructure manifests homogenous distribution of the dark-contrast dislocation loops. Furthermore, the loops exhibit strong double-arc contrast and elliptical shape in WBDF condition. These are a result of their projection, as loops habit plane are inclined to the camera viewing screen [16, 126].

For loops quantitative analysis, several images were acquired and analyzed under both WBDF and HAADF-STEM conditions. For example, the WBDF conditions $g(4.1g)$ with g = {002} diffraction vector and $g(6.1g)$ with g = {110} diffraction vector were analyzed, resulting in the loop densities of 3.3 x 10^{21} m^{-3} and 4.0 x 10^{21} m^{-3}, and mean sizes of 4.4 nm and 6.2 nm, respectively. Here, the major axis of an elliptical loop was taken as a measure of its size. By applying the loop invisibility criteria and the statistical method for Burgers vector determination [16], the visible loops were found to be of both ½ <111> and <100> types, with 27% and 73% fraction, respectively. Furthermore, upon employing statistical method [16] in two different size regimes (i.e. above and below the loop mean size), the smaller loops are mostly found to be of ½ <111> type and the larger ones are dominantly <100> type. On the basis of this WBDF analysis, the total loop density and loop mean size were determined to be 6.4 x 10^{21} m^{-3} and 6.2 nm, respectively. Moreover, from HAADF-STEM investigations, the total visible loop density in irradiated state was estimated to be about 12.1 x 10^{21} m^{-3}, with the mean size of 7 nm. Apparently, using HAADF-STEM technique the estimated loop density is approximately two times higher than that measured via WBDF technique. This can be associated to fact that all HAADF-STEM micrographs are taken close to the zone-axis orientations. And therefore, several excited Bragg's diffracted beams are captured by HAADF-STEM detector in comparison to the few conditions used during WBDF analyses [131]. Consequently, the estimated total loop density using HAADF-STEM mode technique is higher [126]. Furthermore, though HAADF-STEM technique provides atomic (Z) contrast, solute clusters or small precipitates that are generally visible under atom probe tomography (APT) are beyond STEM resolution [103, 132].

- **Post-irradiation annealed at 550 °C for 3 hours**

In order to investigate the effect of PIA, similar investigations were performed on lamellae prepared from post-irradiation annealed samples. Figure 4-2b and Figure 4-3b present the representative microstructure after PIA under WBDF and HAADF-STEM conditions,

respectively. Clearly, in contrast to the irradiated state, the annealed microstructure manifests a significantly lower dislocation loop density along with the frequent observations of dislocation lines/networks. Using line-intercept method, the observed dislocations density is found to be of the order of 10^{22} m^{-2}, which is higher than that of the irradiated state [48]. It is noteworthy that the quantitative estimation of the dislocation density in irradiated state was not possible due to the presence of the high density of dislocation loops. For loops quantitative analysis in annealed state, identical WBDF conditions, $g(4.1g)$ with g = {002} diffraction vector and $g(6.1g)$ with g = {110} diffraction vector were analyzed, resulting in loop densities of 1.3 x 10^{21} m^{-3} and 1.1 x 10^{21} m^{-3}, and mean sizes of 5.2 nm and 9.3 nm, respectively. By applying the loop invisibility criteria and the statistical method for Burgers vector determination [16], the visible loops were still found to be of both ½ <111> and <100> types, but with 52% and 48% fraction, respectively.

Table 4-1: Summary of quantitative data of the dislocation loops in the WTZ irradiated and post-irradiation annealed (550 °C/3h) EUROFER97 samples [126].

Condition	Technique	Total loop density (x 10^{21} m^{-3})	Loop diameter (nm)
WTZ irradiated	WBDF	6.4 ± 1.9	6.2 ± 0.6
	HAADF-STEM	12.1 ± 0.7	7 ± 0.8
WTZ irradiated + 550 °C/3h	WBDF	2 ± 0.6	8 ± 0.6
	HAADF-STEM	4.1 ± 0.4	13 ± 0.9

On the basis of this WBDF analysis the total loop density and loop mean size after PIA were estimated to be 2.0 x 10^{21} m^{-3} and 8.0 nm, respectively. Furthermore, from HAADF-STEM investigations, the total loop density after PIA was estimated to be about 4.1 x 10^{21} m^{-3}, with the mean size of about 13 nm. A summary of the quantitative data of the dislocation loops is listed in Table 4-1 [126]. Finally, upon comparison with the irradiated state, PIA results in a reduction of the total loop density by 69% and 66% from WBDF and HAADF-STEM analysis, respectively [126]. It is essential to note that in contrast to the WBDF analysis, the coarsening phenomenon observed via HAADF-STEM is more pronounced. The discrepancy is originated from the loops contrast under selected reflections where some part of the coarsened loops,

especially in irregular shape are invisible under WBDF mode, and as a result, leads to an underestimation of loop mean size.

Additionally, the comparison of the dislocation loop size distribution obtained via WBDF and HAADF-STEM investigations after WTZ irradiation and PIA conditions are shown in Figure 4-4. As evident, a clear reduction of the dislocation loop density as well as an obvious shift of their size distribution towards higher size is apparent upon PIA. This suggests that the loop mean size increase is not exclusively a result of smaller loop shrinkage/annihilation but is also associated to the actual loop coarsening upon PIA. However, though additional investigations are required for confirmation, the mechanisms such as loop shrinkage, annihilation, coarsening and their coalescence could be active and linked to the present observations [126].

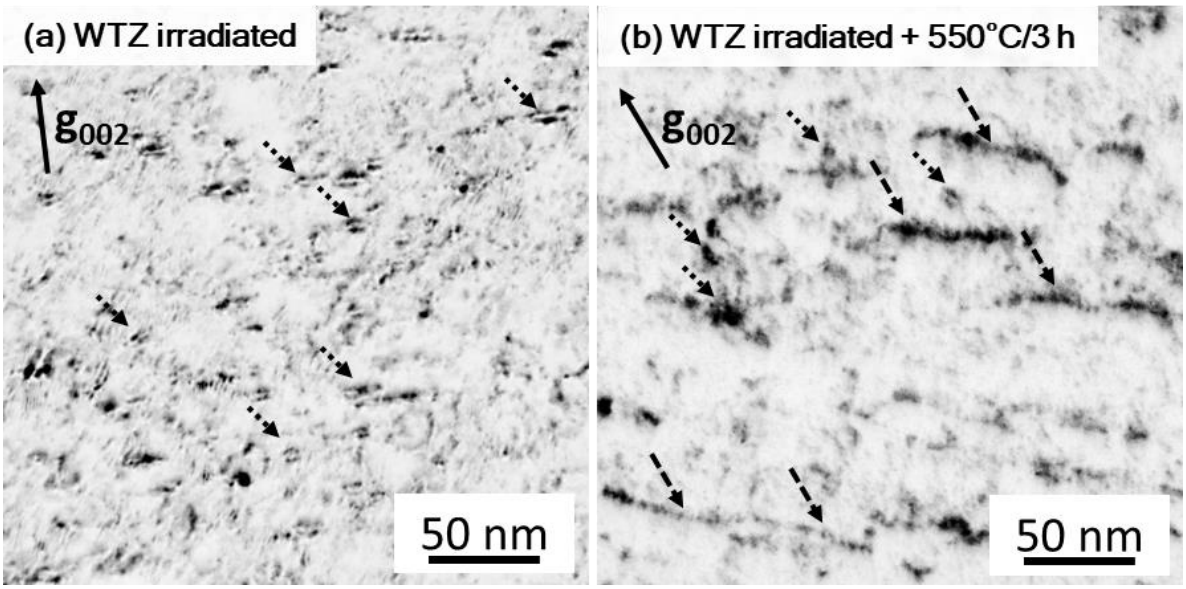

Figure 4-2: Inverted contrast WBDF micrographs taken under g(4.1g) diffraction condition with g = {002} diffraction vector present representative microstructures of (a) WTZ irradiated (15 dpa, 330 °C) and (b) subsequently annealed (550 °C/3h) EUROFER97 samples. The uniformly-distributed double-arc elliptical shaped dislocation loops in irradiated state (marked by dotted arrow) appear to have annealed out upon PIA. In addition, dislocation segments (marked by dashed arrow in (b)) are more commonly observed after PIA [126].

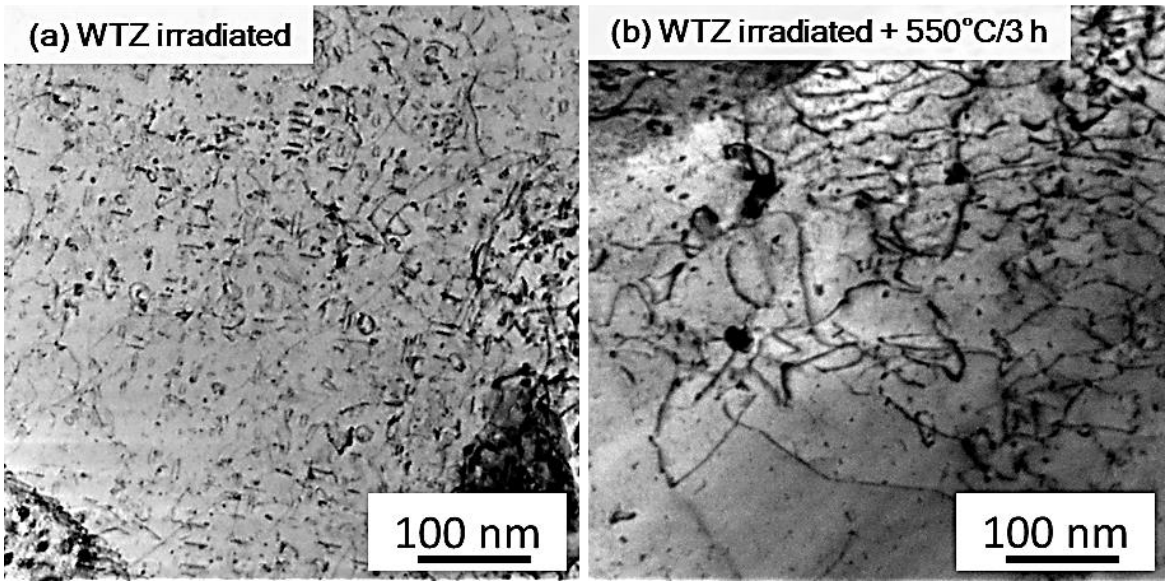

Figure 4-3: Inverted-contrast HAADF-STEM micrographs taken close to the <110> zone-axis orientations present a representative microstructure of a (a) WTZ irradiated (15 dpa, 330 °C) and (b) subsequently annealed (550 °C/3h) EUROFER97 samples. As evident, in contrast to the irradiated state, a significant reduction in dislocation loop density and increment in dislocation lines/networks density is apparent upon PIA [126].

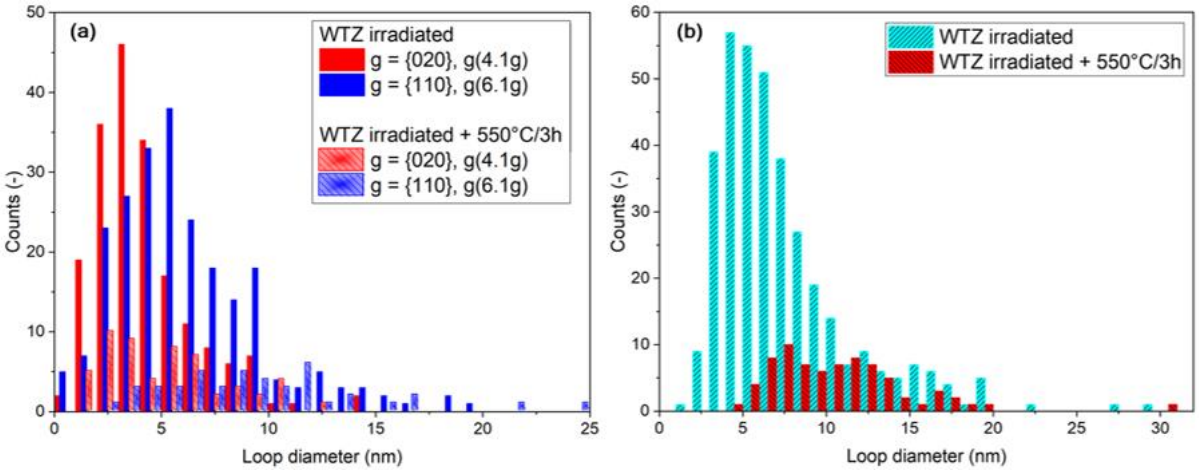

Figure 4-4: Dislocation loop size distributions for the WTZ irradiated and post-irradiation annealed (550 °C/3h) EUROFER97 samples estimated via (a) WBDF and (b) HAADF-STEM techniques. A clear reduction in dislocation loop density and distribution shift towards higher size is apparent upon PIA [126].

4.1.3 Voids and cavities

- **As-irradiated condition**

Upon neutron irradiation, vacancies are created in the displacement cascades which can aggregate to form voids (agglomeration of vacancies) or cavities (clusters of vacancies that contain helium). In the investigated EUROFER97, only very small amount of boron content

(about 10 wt. ppm) is present in the unirradiated microstructure. Thus, only little amount of He would have transmuted from boron during WTZ irradiation (15 dpa, 330 °C) [66]; consequently, some cavities and voids are expected to exit in the investigated EUROFER97. Note that for better description hereafter the word "cavities" are used to represent both voids and cavities. Investigation of cavities formation after WTZ irradiation has also been reported before [67]. However, the statistics of the previous measurement were poor; and hence, additional investigations and analyses were carried out to reconfirm previous results. By using standard technique of TEM bright-field through-focal series, several micrographs under +1.5 µm over-focus and -1.5 µm under-focus conditions were acquired. In general, the irradiated microstructure exhibits an inhomogeneous distribution of cavities. Figure 4-5a and b show cavities distribution in a region with relatively uniform density. The contrast of the cavities changed from a white dot with a black fringe in an under-focused image (Figure 4-5a) to a dark dot with a white Fresnel fringe in the over-focused image (Figure 4-5b). Contrary to the regions with relatively uniform density, several cavity free regions that are hundreds of nanometers across (about 66300 mm^2) were also observed. This inhomogeneity appears to be an effect of the material's inherent local chemical composition variation; for example, the boron distribution [6, 133]. Using several micrographs, cavity size distribution was determined and is shown in Figure 4-6a. The mean cavity diameter is estimated to be 2.1 nm and the density is determined to be 3.0 x 10^{21} m^{-3}. This measured cavity density is one order of magnitude higher than that reported before (3.6 x 10^{20} m^{-3}) [67] but comparable to those observed after ARBOR-1 (2.3 x 10^{21} m^{-3}, mean diameter 1.6 nm) and SPICE (6.3 x 10^{21} m^{-3}, mean diameter 2.3 nm) irradiations [66, 126].

- **Post-irradiation annealed at 550 °C for 3 hours**

In order to investigate the effect of PIA, similar investigations were performed on the post-irradiation annealed samples (WTZ irradiated + 550 °C/3h). Figure 4-5c and d show cavities distribution in a region comparable to that shown for the irradiated case with relatively uniform density. Again, using several micrographs, cavities distribution was determined for the post-irradiation annealed samples, which is shown in Figure 4-6b. Here, their mean diameter is estimated to be 2.9 nm and their density is determined to be 1.5 x 10^{21} m^{-3} after PIA. Therefore, upon comparison with the irradiated state, an appreciable reduction in the cavity density (~50%) and increment in their size (~36 %) is apparent upon PIA [126].

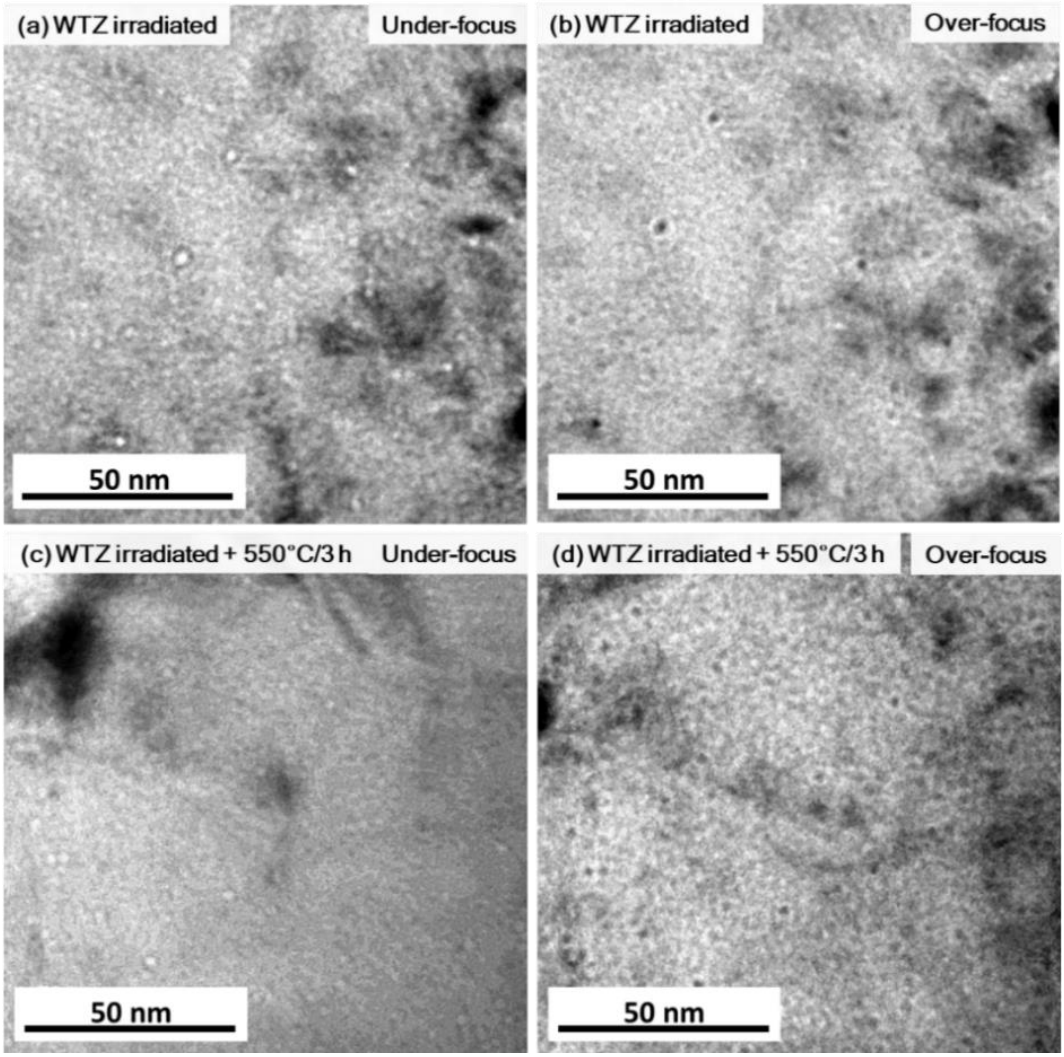

Figure 4-5: Typical BF-micrographs present cavity distribution in a (a, b) WTZ irradiated (15 dpa, 330 °C) and (c, d) subsequently annealed (550 °C/3h) EUROFER97 samples. (a/c taken at under-focus -1.5 μm condition and b/d at over-focus +1.5 μm condition) [126].

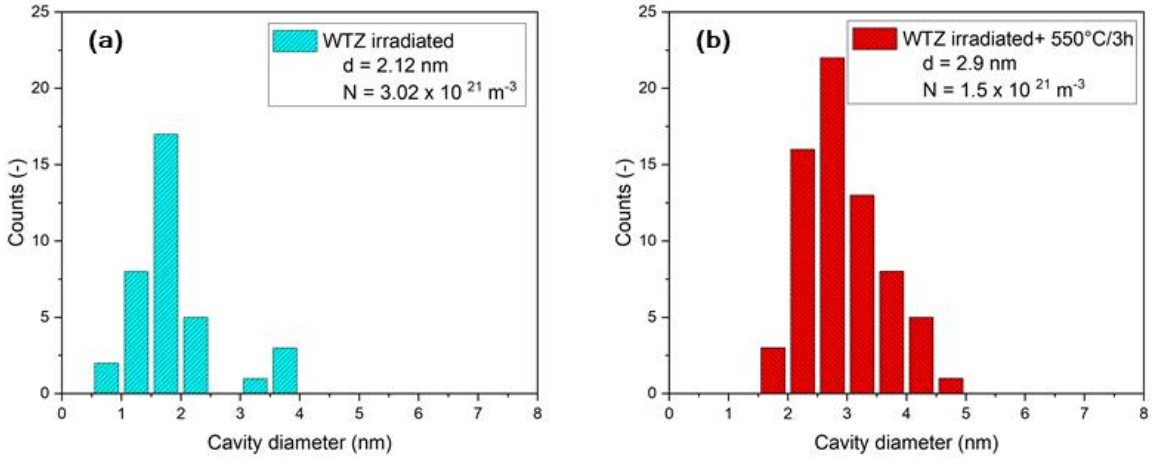

Figure 4-6: Cavities size distribution along with their average size d and volume density N for the WTZ irradiated and post-irradiation annealed EUROFER97 samples. An appreciable reduction in the cavity density and increment in their size is apparent upon PIA [126].

4.1.4 Discussion

In this work, TEM investigations on the neutron-irradiated and subsequently annealed EUROFER97 samples were carried out to understand the effect of annealing on irradiation-induced defects. Both WBDF and HAADF-STEM investigations reveal a reduction of dislocation loop density with a simultaneous increase in their mean size (see

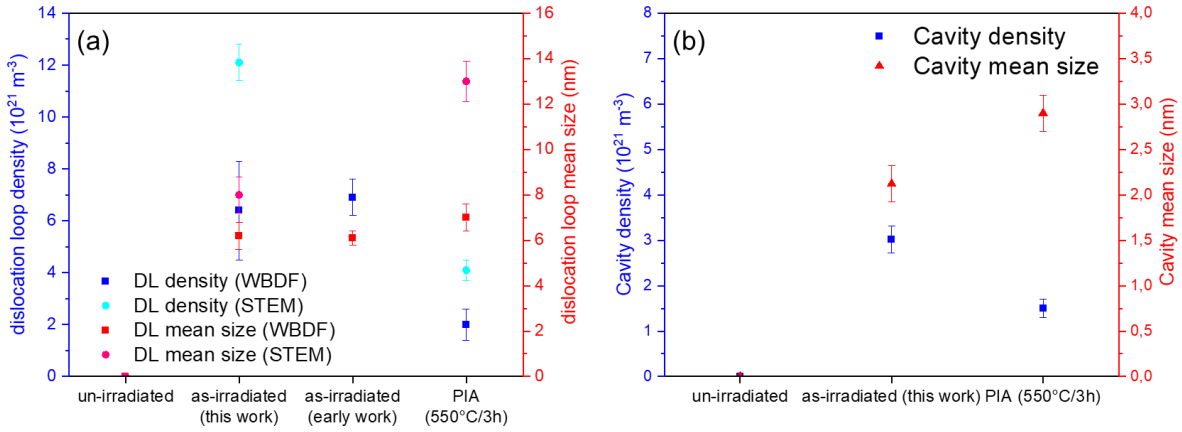

Figure 4-7a) and formation or extension of dislocation lines/networks upon PIA. In addition, the results of quantitative analysis of dislocation loops under as-irradiated condition from this work is comparable to that of the early work [66]. This indicates that FIB procedures applied in this work also provides high quality TEM samples as it is the case by preparation via electro-polishing. In addition, a reduction of cavity density with increment in their mean size was observed (see

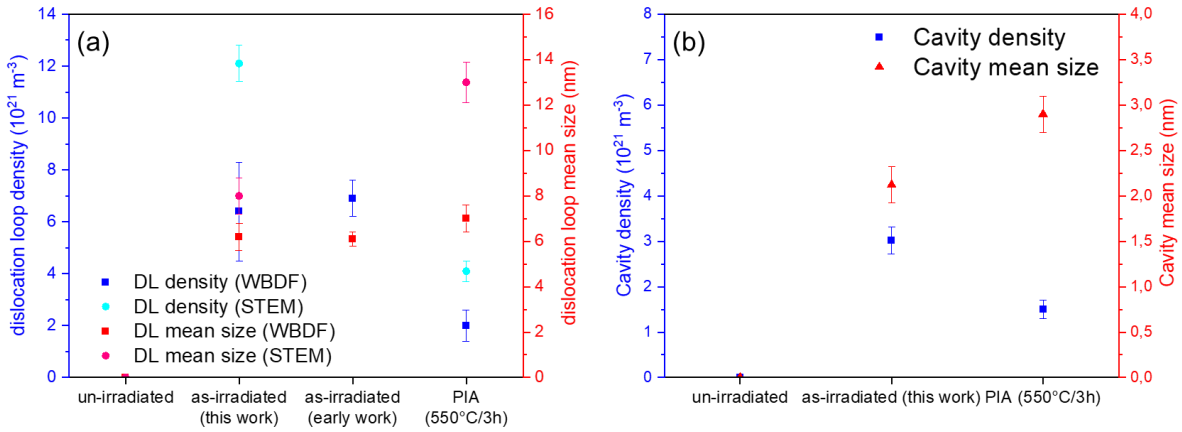

Figure 4-7b). The cavity density and mean size from the early work [67] are excluded in the comparison due to the poor statistics, as very few cavities were counted.

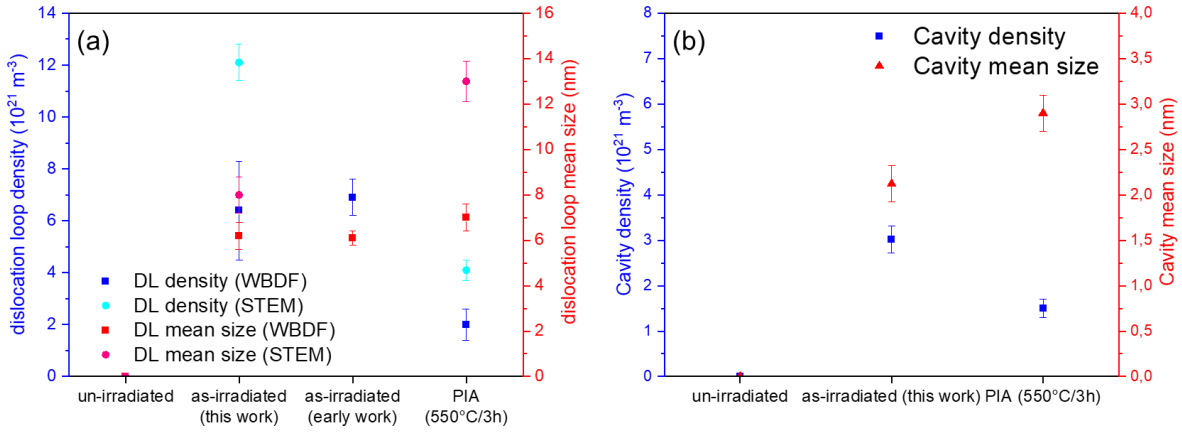

Figure 4-7: Summary of microstructural investigation on irradiation defects and comparison for as-irradiated condition (15 dpa/330 °C) from this work and early work [66] and post-irradiation annealed condition (550 °C/3h), respectively. Results for dislocation loop density and mean size are presented in a) whilst results for cavity density and mean size are presented in b).

Though not as much for RAFM steels, similar PIA observations have also been reported before for other irradiated austenitic steels [82-84, 94, 134-136], which is associated with the recovering of the material's hardening and embrittlement behaviour. These observations have usually been linked to the mechanisms that are either long-range vacancy/interstitial diffusion controlled or depend on the short-range elastic interaction forces between adjacent loops due to their glide and climb [94, 126].

The reduction of the dislocation loop density upon PIA can be a result of their 1) annihilation and/or 2) coarsening. The dominance of one phenomenon over the other defines the overall loop size evolution. Loop shrinkage and their disappearance have been reported in the past upon annealing of irradiated pure α-iron, Fe-9%Cr alloy and austenitic steels [44, 65, 89, 90, 136]. It is known that excess vacancies exist in matrix at elevated temperatures due to the increase in the thermal equilibrium vacancies. And therefore, at the chosen annealing temperature, vacancies can move in the matrix and flow into sinks, such as surfaces, grain boundaries, dislocation tangles and dislocation loops [89]. Concerning interstitial type loops, vacancies are attracted to its peripheral high compressive strain field region [137], since the vacancy concentration at the loop is lower than the thermal equilibrium concentration [24]. Here, the incoming vacancies will annihilate with the loop's peripheral self-interstitial atoms, which firstly leads to their shrinkage (progressive reduction of the loop size) and finally, their complete annihilation [126]. Detailed discussion based on in-situ annealing investigations on neutron-irradiated EUROFER97 steel will be presented in section 4.2 and 4.3.

In general, two diffusion-controlled mechanisms of loop coarsening can occur upon annealing: 1) growth of individual loops via absorption of highly mobile interstitials and/or emission of vacancies and 2) merging of two or more dislocation loops. Moll et al. [138] upon annealing irradiated pure α-iron with low initial dislocation density at 577 °C reported significant coarsening of loops via the emission of vacancies. This coarsening is accompanied by the reduction of dislocation loop density, due to their coalescence [138]. In general, the coalescence or merging of loops befalls once they are sufficiently large to interact and no other external sources and sinks exist nearby but loops themselves [24, 94, 138]. The loops interaction is also known to be both loop size and type dependent. For example, the emission and absorption rate of vacancies and interstitials, respectively, is greater for the large loops than for the relatively small loops [138]. So, in order to conserve the total number of vacancies/interstitials, the larger loops grow at an expense of smaller ones [88, 94]. This coarsening is similar to the particle coarsening (Oswald ripening) in the material where the total amount of solute remains constant. Additionally, since <100> type dislocation loops is generally larger it has been shown to coarsen faster than their ½ <111> counterparts [139]. Furthermore, for BCC iron, Masters [140] proposed and Xu et al. [59] via kinetic Monte Carlo simulation showed that two small ½ <111> type dislocation loops can coalesce to form one larger <100> type dislocation loop or one larger ½ <111> type dislocation loop. Arakawa et al. [92] via in-situ annealing investigations showed similar results for irradiated pure α-iron. Besides, interstitial loops in pure α-iron are known to be mobile [12, 26, 50, 52]. Therefore, for the glissile loops, a further mechanism of coarsening can arise as a result of the direct elastic interaction force between adjacent loops [26]. The forces exerted by one loop on the other can make them move together by glide and/or climb, which can lead to their coalescence [26, 126].

In contrast to pure α-iron, different alloying elements (Cr, Ni, Si, Mn and P) are known to decorate loops periphery in irradiated EUROFER97 in order to relax associated dilatational-strain field [65, 132]. This segregation is known to suppress dislocation loop evolution upon annealing. For example, Aarakawa et al. [65] showed suppressed loops mobility as well as their shrinkage by Cr addition in irradiated pure α-iron during in-situ annealing. Yoshida et al. [141] additionally suggested that Cr at dislocation loops could reduce the absorbing reaction between dislocation loops and interstitials, which could suppress their coarsening behaviour. Moreover, elastic forces governed glide plus climb mechanism is more likely to be active in high purity metals (e.g. pure α-iron) than in their alloyed counterparts such as EUROFER97, where loops are generally sessile. In spite of all this, substantial recovery of the irradiated EUROFER97

microstructure is observed upon PIA. Therefore, from present investigations it can be concluded that the annealing behaviour of dislocation loops in the irradiated EUROFER97 is primarily vacancy/interstitial diffusion driven and it falls somewhere between the two extremes of isolated loop shrinkage/annihilation and their coarsening, depending upon the absence or presence of the external sources and sinks [126].

Concerning dislocation lines/networks, both ferritic-martensitic (T91) [134] and cold-worked austenitic stainless steels [142] show reduction in their density upon irradiation, prominently at higher doses. This has been attributed to the irradiation-induced dislocations-climb (by absorbing point defects) which leads to mutual annihilation of the line dislocations [142]. However, prominent increment in dislocation lines/networks density is apparent upon PIA. This can be effect of the loops interaction during coarsening/coalescence process which could lead to the formation of dislocation lines/networks [134, 138]. Figure 4-8 shows an example of the possible loop-loop and dislocation line-loop interactions, along with the newly formed dislocation lines/networks. Here, some of the dislocations are seen to be highly curved which gives impression that they might be a part of large coarsened dislocation loops. Indeed, Klimenkov et al. [27] found "curved dislocation lines" in the neutron-irradiated EUROFER97 (16.3 dpa, 400-450 °C) that were a part of the large dislocation loops. Besides, interstitial loops/clusters that are absorbed by the background dislocations could further lead to their extension. Masters [143] for ion-irradiated iron proposed that <100> loops upon interaction with glide dislocations can convert into glissile dislocations. Similar to the present case, dislocation lines/network formation were also observed upon annealing irradiated pure α-iron in [138] and in austenitic steels [83, 126, 134, 144]. Dedicated experiments demonstrating such processes in neutron-irradiated EUROFER97 steel were carried out and presented in section 4.4.

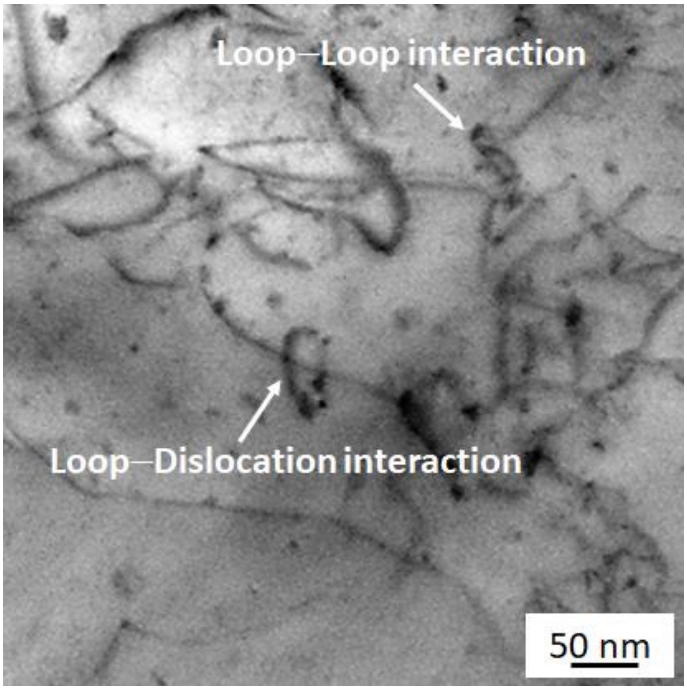

Figure 4-8: HAADF-STEM micrograph reveals possible loop-loop and dislocation-loop interactions, along with the newly formed dislocation lines/networks, in a post-irradiation annealed EUROFER97 sample [126].

In the present study, analogous to the loops behaviour, upon PIA cavity density reduction and their mean size increment were also observed. Similar observations have also been reported before upon annealing He-ion irradiated RAFM steel at 550 °C [145]. However, though in the investigated EUROFER97 the cavities are mostly vacancy clusters, along with few that can be He stabilized, similar mechanisms as those generally proposed for the He bubbles coarsening might be operating in the present case. The two qualitative coarsening mechanisms that explain such observations upon annealing are: 1. Vacancy or their cluster migration and coalescence and 2. Ostwald ripening. The former mechanism is achieved via diffusion of matrix atoms (i.e. cavities themselves) whereas the latter mechanism manifest a vacancy fluxes driven process where the vacancies firstly dissociate from smaller cavities and consequently being re-absorbed by the larger cavities due to differences in the thermal equilibrium vacancy concentration in the neighbourhood [146]. The activation energy of Ostwald ripening mechanism is hence expected to be much higher than that of the migration and coalescence one [146]. Therefore, vacancy migration and coalescence and Ostwald ripening mechanisms are expected to be dominant at relatively low and high temperatures, respectively [146]. And since, local vacancies around cavities are easier frequent source, migration and coalescence mechanism appears to be the main possible mechanism of the cavities growth. Additionally, cavities coarsening is also substantially complicated in the presence of and close to precipitates, dislocations and grain boundaries [146]. And as significant dislocation activities were observed which will be

presented in section 4.2, the cavities sweeping by dislocation motion can also contribute to their coarsening [126].

Since irradiation-induced defects (for e.g. dislocation loops, cavities, segregation, solute clusters and precipitates) are known to act as a barrier for dislocations motion [132], healing of these defects during PIA could lead to the recovery of the mechanical properties [76, 147]. Indeed, previous PIA investigations on EUROFER97 has led to a nearly complete recovery of the low temperature hardening [8, 76, 104]. Present TEM investigations also supports above results as substantial recovery of the irradiated microstructure, in terms of the reduction of the loop (~ 66%) and cavity (~ 50%) density, is observed upon PIA.

4.1.5 Summary

TEM investigations on the neutron-irradiated and subsequently annealed EUROFER97 samples were carried out to understand the effect of annealing on irradiation-induced defects. Both WBDF and HAADF-STEM investigations reveal a reduction of dislocation loop density with a simultaneous increase in their mean size and formation of dislocation lines/networks upon PIA. Additionally, a reduction of cavity density with increment in their mean size was observed. The annealing behaviour of dislocation loops is primarily vacancy/interstitial diffusion driven and it falls somewhere between the two extremes of isolated loop shrinkage/annihilation and their coarsening. Out of these two phenomena, the one that transpires depend on the presence or absence of the external sources and sinks in the loops' neighbourhood. These competing mechanisms define the overall loop size distribution evolution upon PIA. Additionally, vacancy or their cluster migration and coalescence could be the main mechanism for cavities coarsening. However, to understand different operating mechanism, detailed systematic isothermal in-situ annealing experiments are required. Nevertheless, the observed microstructural recovery upon PIA explains the partial recovery of mechanical properties by healing irradiation-induced defects [126].

4.2 Annihilation kinetics of irradiation-induced defects in EUROFER97 steel

This section documents in-situ TEM annealing investigations on neutron irradiated EUROFER97 at elevated temperatures. It compiles and provides first direct observations of the dislocation loop evolution and reveals underlying recovery mechanisms during PIA of neutron irradiated EUROFER97 steel. In addition, the annealing kinetics of ½<111> and <100> type

loops are further discussed and compared. Parts of the work presented in this section has been published in Ref. [148].

The second part of this section will present direct observation of cavity shrinkage upon annealing above 500 °C. Interestingly, cavity stopped shrinking at high temperatures around 550 °C rather than being annealed out. Parts of this work will soon be published in Ref. [149].

4.2.1 Materials and experimental

For description about as-irradiated material (15 dpa, 330 °C) and TEM lamellae preparation, the reader is referred to section 4.1.1. The in-situ TEM annealing experiments were carried out via different annealing schemes as follows.

- **In-situ TEM annealing of dislocation loops**

A high-resolution FEI Tecnai G^2 F20 X-TWIN microscope operating at 200 kV equipped with a Gatan double-tilt heating holder (Model 652) was employed for in-situ annealing experiments. The lamella was first heated up to 550 °C with a temperature ramp of 9 K/min and held for two hours. As in such experiments, specimen's drift is an inevitable issue, for analysing microstructure evolution, the same area of interest was tracked carefully during the whole span of the experiment. The available Gatan digital micrograph software assisted in observing real-time microstructure evolution, capturing images and recording videos for detailed analysis. Same diffraction condition (g(4.1g) using g = 002 diffraction vector near [100] zone axis) was maintained during the whole duration of experiment to negate specimen's bending effects. The same lamella was further heated up to 600 °C with a temperature ramp of 1 K/min and held for two hours before finally cooling down to room temperature gradually. Since, both ½<111> and <100> type loops manifest characteristic shapes under specific zone axis orientation [125], they were identified during PIA using simulated dislocation-loop map with crystallographic information (for more details see Ref. [125]). The isolated ½<111> loops were recorded under kinematic bright-field (KBF) condition; whereas <100> loops were captured under weak beam dark-field (WBDF) condition [148].

- **In-situ TEM annealing of cavity**

Before in-situ TEM annealing, a cavity was spotted using conventional TEM bright-field through-focal series. The thickness of the surveyed region was measured to be about 100 nm using electron energy loss spectroscopy (EELS). This cavity was chosen as monitoring object as there was a precipitate nearby which can be used for location correction during image drifting

caused by heating. TEM lamella was firstly heated up to 330 °C within 10 minutes, and then held for 4 minutes to check possible evolution of the cavity. Afterward, the specimen was further heated to 550 °C with a temperature ramp of 22 °C/min. After reaching 550 °C, the temperature was kept constant for another 5 minutes [149].

4.2.2 Dislocation loop shrinkage via dynamic annealing from 550 to 600 °C

Figure 4-9 presents PIA time-temperature profile along with loop size distribution and inverted WBDF micrographs at three different annealing conditions. The nano-scale dark-contrast features visible in the inverted WBDF micrographs are the high density of dislocation loops (e.g., see three marked loops with arrows). After annealing for 2h at 550 °C, no noticeable change in the visible loop density was observed in comparison to that of the as-irradiated state ($3.94 \times 10^{21} m^{-3}$). However, upon increasing temperature to 600 °C, loops dark-contrast frequency decreased gradually with time, more prominently after 2h of annealing, due to the noticeable reduction (~ 48%) in the visible loop density ($2.05 \times 10^{21} m^{-3}$). Additionally, as shown in the inset, the visible loop size distribution also shows similar trend with a progressive shift towards higher size upon increasing temperature and with increasing annealing time. This also led to an increase in visible loop mean size from 8.8 nm at 550 °C to 13.7 nm after annealing at 600 °C for 2h, an increase of ~ 55%. The loop mean size and density evolution upon PIA can be associated to their coarsening and/or shrinkage/annihilation [148]. Though coarsening in general was observed in this annealing experiment, a more dedicated and systematic isothermal annealing investigation of dislocation loop coarsening was carried out and will be presented in section 4.4. In this work, focus was put on to the linked concurrent loop shrinkage phenomenon, which was discerned for several loops and is as follows.

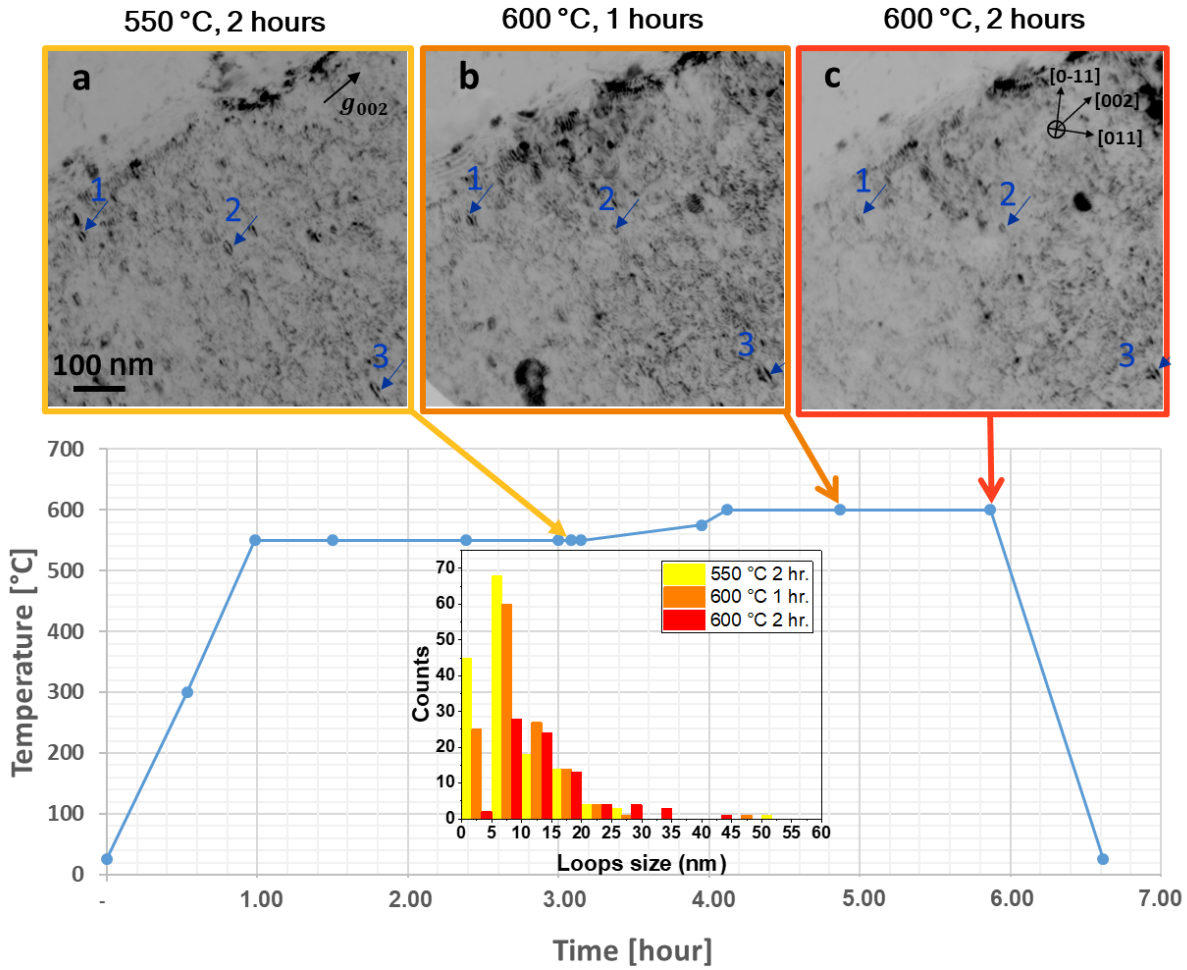

Figure 4-9: In-situ PIA time-temperature profile along with loop size distributions (in inset) and inverted WBDF micrographs at three different annealing time points under g(4.1g) diffraction condition using g = 002 diffraction vector near [100] zone axis. The nano-scale dark-contrast features visible in the micrographs are the high density of dislocation loops (e.g. three sessile <100> loops are marked with blue arrows). The loop density deceased (witnessed as the frequency reduction of the dark-contrast features) and their mean size increased (seen as a right shift of the loop size distribution) more prominently after annealing at 600°C for 2h (adapted from [148]).

A sequential KBF-TEM micrographs series taken under g(4.1g) diffraction condition with g = 002 diffraction vector near [100] zone axis in Figure 4-10(a-e) show fast shrinkage of a relatively large (~ 40 nm) isolated loop (1) during PIA. This shrinkage phenomenon was observed after 15 minutes during 600 °C annealing. According to the simulated dislocation loops map for [100] zone axis [125], this marked loop is identified to be ½<111> type. Figure 4-10(f-j) illustrate the corresponding schematic view of the loop's shrinkage process. As it is evident, initially the marked ½<111> loop shows elliptic shape (Figure 4-10a, f), as the loop habit plane {111} is inclined to the camera viewing screen [125]. With the progress of the PIA time, and under no external forces, the loop began to shrink and move along [011] direction until it undertakes black dot morphology. Another similar example of the fast shrinkage phenomenon for a small (~ 10 nm) isolated ½<111> type loop (2) is shown in Figure 4-11. In

the both above cases, shrinkage appears to be independent of the other loops. The loop size evolution during shrinkage phenomenon is reported in Table 4-2. The shrinkage rate (R_x) is estimated for both above-mentioned loops as:

$$R_x = \frac{d_{x-t} - d_x}{t} \qquad \text{Equation 4-1}$$

where d_x and d_{x-t} are the loop sizes at x and $x - t$ seconds, respectively and the time period t is 10 seconds for loops 1 and 4 seconds for loops 2. The results of the estimated loop shrinkage rate are listed in Table 4-2 and also plotted against loop diameter in Figure 4-13. Therefore, based on the loop size evolution, it is evident that shrinkage rate increases with decreasing loop size and becomes extremely fast at smaller sizes (< 10 nm) [148].

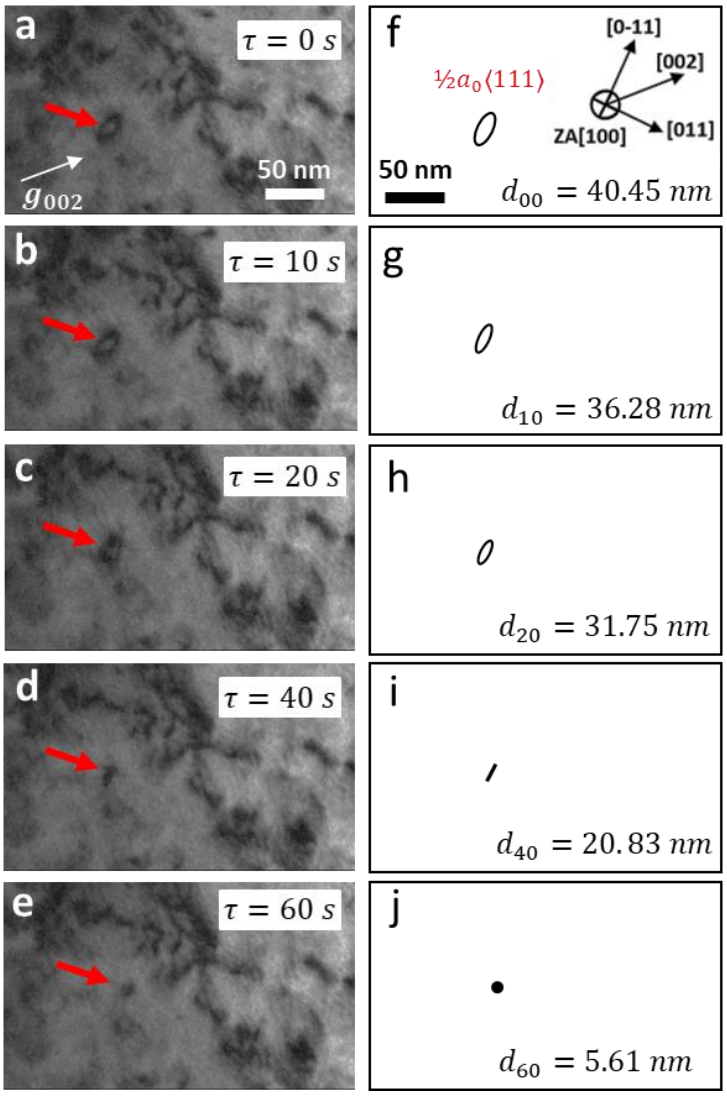

Figure 4-10: In-situ KBF-TEM micrographs (a-e) show the shrinkage process of a relatively large (~ 40 nm) isolated interstitial ½<111> type dislocation loop (1) in EUROFER97 at 600 °C. The images were taken under g(4.1g) diffraction condition with g = 002 diffraction vector near [100] zone axis. Images (f-j) illustrate corresponding schematics of the marked isolated loop shrinkage process [148].

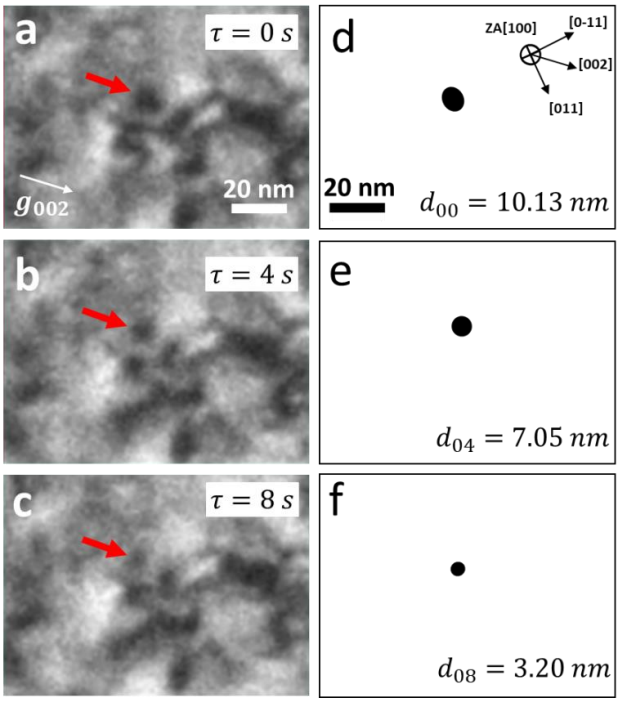

Figure 4-11: In-situ KBF-TEM micrographs (a-c) show example of the shrinkage process of a small (~ 10 nm) isolated interstitial ½<111> type dislocation loop (2) in EUROFER97 at 600 °C. The images were taken under g(4.1g) diffraction condition with g = 002 diffraction vector near [100] zone axis. Images (d-f) illustrate corresponding schematics of the marked isolated loop shrinkage process. It is also noteworthy that the neighbouring dislocations tangles changed their configuration as the marked loop shrank [148].

Table 4-2: Two ½<111> type interstitial loop size and shrinkage rate evolution during 600 °C annealing [148].

Loop number	**Time [s]**	**Loop diameter (d) [nm]**	**Shrinkage rate (R) [nm/s]**
Loop 1	0	40.45	-
	10	36.28	0.42
	20	31.75	0.45
	30	26.56	0.52
	40	20.83	0.57
	50	14.17	0.67
	60	5.61	0.86
Loop 2	0	10.13	-
	4	7.05	0.77
	8	3.20	0.96

It is important to note that such fast shrinkage phenomenon was mostly observed close to the dislocation tangles (see Figure 4-10 and Figure 4-11), indicating that these tangles must be acting as a source and sink for the point defects (i.e. vacancies and interstitials). Thus, it appears that loops in the population can behave as an isolated loop and shrink independently, if sufficient external point defects sources and sinks (such as dislocations, voids and grain boundaries) are available in the neighbourhood [94]. Furthermore, by emitting and absorbing point defects, dislocation segments can also move off their glide plane, as was indeed observed in the present case. Consequently, interstitial loops/clusters can also be absorbed by the present dislocations [148].

4.2.3 Cavity shrinkage via dynamic annealing up to 550 °C

The annealing roadmap is shown in Figure 4-12 (left panel). For the annealing duration, cavity evolution was recorded. Figure 4-12 (right panel from a-i) shows cavity evolution at several representative temperatures. Initially, no profound morphological change of the cavity was observed below 500 °C. Significant cavity shrinkage was then observed upon annealing from 500 to 550 °C. Additionally, cavity size remained unchanged at 550 °C [149].

It is well-known that helium atoms play a stabilizer role in the formation and evolution of helium-containing cavities (i.e. helium bubbles) [150]. If the cavity contains several helium atoms, escaping of vacancies and/or helium atoms during cavity shrinkage will be prohibited. Thus, the shrinking cavity observed here is likely to be a helium-containing bubble. The helium content in the cavity, however, should be small, considering the slow helium production and accumulation (< 10 appm [124]) in the presently investigated neutron-irradiated EUROFER97 steel [149]. Furthermore, a model based on rate theory was built to simulate the heating course and verify the conjecture of the presence of helium in the cavity (for description of the model and associated results see in Ref. [149]).

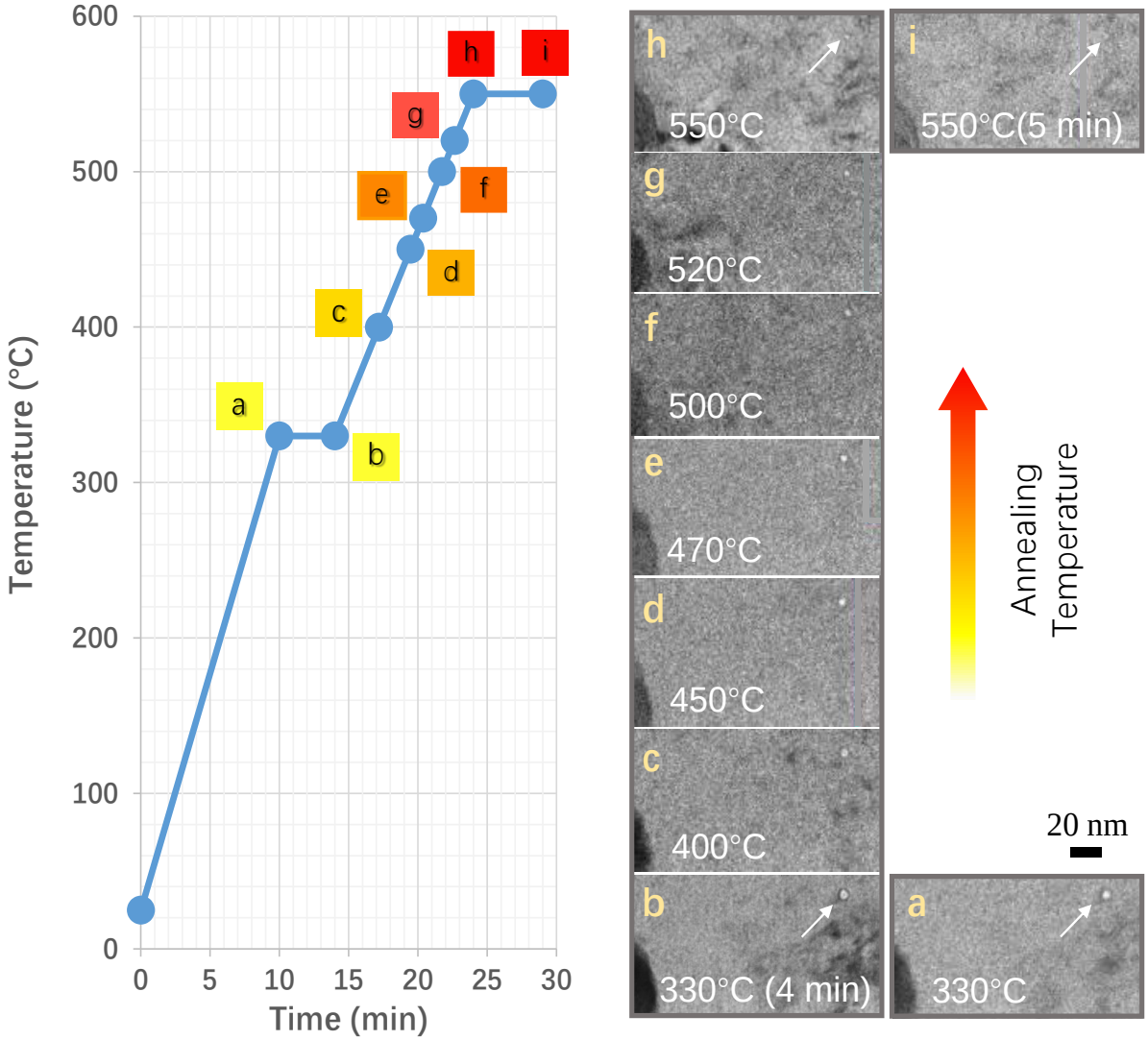

Figure 4-12: In-situ TEM observation upon annealing. Left panel: temperature profile as a function of time. Right panel: cavity morphologies at various heating temperatures [149].

4.2.4 Discussion

4.2.4.1 Dislocation loop annealing kinetics

Dislocation loops are also known to be the sources and sinks for points defects [94]. Besides, excess vacancies exist in matrix at elevated temperatures, due to increase in the thermal equilibrium vacancies. During PIA, these temperature-mobilized vacancies will be attracted to the loop's periphery, an area of high compressive strain and lower vacancy concentration [90, 137]. Burton and Speight [94] proposed that it is the "line tension" that gives rise to a vacancy supersaturation at loops because of their curvature. Consequently, the self-interstitial atoms (SIAs) on the loop's periphery will be annihilated by the flux of incoming vacancies; and thereby, reducing loop's size. As the loop shrinks, this modifies associated vacancy

concentration gradient due to momentarily depletion of vacancies around the loop. In general, the vacancy concentration (C_d) at the loop is given by [94]:

$$C_d = C_{EQ} exp(\frac{-2E\Omega}{br_1 kT}) \qquad \text{Equation 4-2}$$

where C_{EQ} is the thermal equilibrium vacancy concentration, b is the Burgers vector, Ω is the atomic volume (~b^3), E is the line tension of the loop (~$Gb^2/2$), r_1 is the radius of the loop, k is the Boltzmann constant and T is the absolute temperature. From above equation, it can be inferred that the smaller the loop, the lower is the vacancy concentration (C_d) at the loop. And hence, a comparatively larger vacancy concentration gradient ($C_{EQ} - C_d$) towards smaller loop, will results in its faster shrinkage. Consequently, it can be concluded that the shrinkage of the isolated interstitial loop is presumably due to the absorption of thermal equilibrium vacancies; and its shrinkage rate increases with decreasing the loop size [148].

Burton and Speight [94] described the vacancy mediated shrinkage rate based on the spherical diffusion approximation for an isolated interstitial loop, which can maintain the thermal equilibrium vacancy concentration at some distance away from the loop. In addition, as all dislocation loops observed in this work are prismatic dislocation loops, the stacking fault energy term can be neglected. Hence, the shrinkage rate can be simplified as following equation:

$$\frac{dr}{dt} = \frac{2D}{b}\left\{\exp(-\frac{Gb\Omega}{rkT}) - 1\right\} \qquad \text{Equation 4-3}$$

where r is the radius of the loop, D is self-diffusion coefficient in pure α-iron, G is the shear modules. The self-diffusion coefficient is extrapolated to 600 °C on the basis of available data for pure α-iron [151], resulting $D = 1.24 \times 10^{-15}$ cm^2/s. Burgers vector of ½<111> type loops is calculated with lattice parameter of BCC iron, $a_0 = 0.28\,nm$ [67]. For comparison with the experimentally determined shrinkage rate, the theoretically calculated one is also plotted against loop diameter in Figure 4-13 [148].

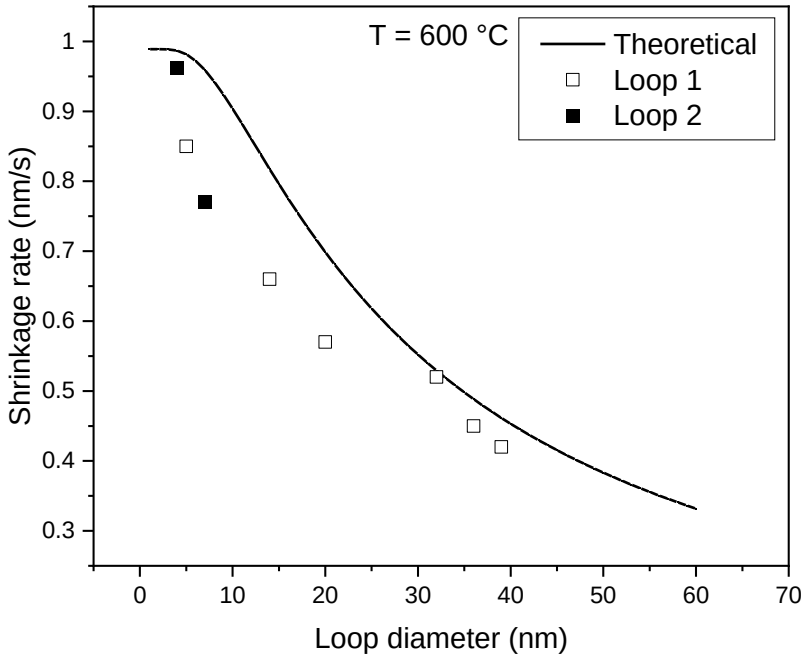

Figure 4-13: ½<111> interstitial loop shrinkage rate vs diameter plot at 600 °C. Black line illustrates theoretically calculated shrinkage rate based on Equation 4-3. Square data points are experimentally determined shrinkage rate for marked loops in Figure 2 and 3 (for details of experimental measurements see Table 4-2) [148].

It is evident from Figure 4-13 that both theoretical and experimental shrinkage rate exhibits similar trends, as it increases with decreasing loop size. Additionally, the difference observed in the magnitude of experimental and theoretical shrinkage rates in Figure 4-13 could be due to several factors. Firstly, the vacancy diffusivity in Fe-Cr alloy is lower than in the pure iron (in Equation 4-2 self-diffusion coefficient for pure iron was used) [152], which implies a slower loop shrinkage rate in EUROFER97 than in pure iron. Secondly, the segregation of alloying elements such as Cr, Ni, Si, Mn and P at the loops peripheral tensile strain field region could also suppress their shrinkage [132, 153]. Arakawa et al. [65] found that at elevated temperatures the ½<111> loop shrinkage and motion are significantly suppressed by Cr segregation at the loops periphery owing to the migration of couples of Cr and a vacancy towards loops and trapping of Cr at the periphery of loops. Lastly, if loops are unable to maintain thermal equilibrium vacancy concentration to the required extent, due to the presence of the other unresolvable smaller loops or insufficient vacancy sources, this could also lower the shrinkage rate. These factors are discussed in more detail later in this section and section 4.3.6 [148].

In contrast to the above-mentioned fast shrinking loops, several extremely slow shrinking loops were also observed. According to the simulated loop map for [100] zone axis [125], three marked large loops in Figure 4-9(a-c) are identified to be <100> type. These observed loops are

found to be sessile and shrank slowly over long-time range. Their sizes evolution at three different annealing time points is listed in Table 4-3. As evident, via annealing from 500 °C, 2h to 600 °C, 2h, the marked 1, 2 and 3 loops shrank with the mean size reduction of 15%, 42% and 23%, respectively. Their cumulative average shrinkage rate was estimated to be several nanometers per hour, which is significantly lower than that of the presented ½<111> type loops (see in Table 4-2) [148].

Table 4-3: Three <100> type loop size evolution at three different annealing time points [148].

Annealing condition	**Loop 1 size [nm]**	**Loop 2 size [nm]**	**Loop 3 size [nm]**
550 °C, 2 hours	21.8	27.7	54.2
600 °C, 1 hour	20.4	20.4	47.5
600 °C, 2 hours	18.6	16.2	42.0

In general, Equation 4-3 provides a guideline and predicts relatively slower shrinkage rate for the <100> type loops than their similar size ½<111> counterparts. This is accounted in terms of Burgers vector b in Equation 4-3, provided that the required thermal equilibrium vacancy concentration is maintained some distance away from the loops. However, such drastic slow shrinkage behavior of the presented <100> type loops suggests that for these loops either the elemental segregation effects are more severe or their required thermal equilibrium vacancy concentration is not maintained [148].

As mentioned previously, elemental segregation at dislocation loops could influence their shrinkage behavior immensely. This could also be related to the intrinsic nature of the loop type. For example, alloying elements can preferentially segregate around <100> type loops than their ½<111> counterparts, owning to their less densely packed {100} habit plane (more free atomic space for segregation). Borodin et al. [154] proposed that it is the reduction of the associated elastic strain that leads to the preferential elemental segregation on the {100} planes on which <100> type loops lie. Therefore, a comparatively higher elemental segregation around <100> type loops than their ½<111> counterparts could retard their shrinkage greatly. Additionally, segregation is also reported to be loop size dependent, as Cr enrichment was estimated to increase with loop size [153]. This is due to the fact that the negative pressure in the loops peripheral tensile strain field region decreases dramatically with increasing loop size [155]. And as a result, smaller loops due to lower elemental enrichment will shrink faster than their larger counterparts [148].

Another additional factor, nearby loops' population, could impact loop shrinkage behaviour considerably. In contrast to the above-shown examples of fast shrinking isolated ½<111> type loops, several relatively small loops are present in the close proximity of the marked <100> type loops in Figure 4-9a. This can be clearly seen from the enlarged view of one of the marked loops (2) in Figure 4-14. These smaller loops/clusters (which could be of both ½<111> or <100> types) will preferentially attract thermal vacancies more than their nearby larger counterparts (discussed before). And as smaller loops shrink first and fast (compare Figure 4-14a and Figure 4-14b), the depletion of the vacancies would reduce the required thermal equilibrium vacancy concentration for the shrinkage of the neighboring larger loops, leading to their delayed shrinkage. However, such a scenario could also exist for large ½<111> type loops, also leading to their similar slower shrinkage. Therefore, loops neighbouring microstructure also has a significant effect on the loops' shrinkage behaviour in EUROFER97.

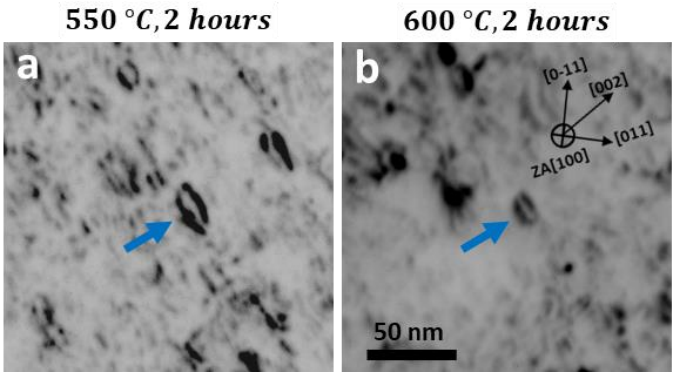

Figure 4-14: Inverted WBDF micrographs showing enlarged view of one of the marked loop (2) in Figure 4-9 at (a) 550 °C, 2h and (b) 600 °C, 2h annealing time points. It is noteworthy that the smaller loops next to the marked large <100> type loop in (a) appear to have annealed out in (b). This is due to fact that the smaller loops are able to preferentially attract thermal vacancies (from the neighboring dislocation tangles) more than their nearby larger counterparts, leading to the latter's delayed shrinkage, as it is unable to maintain required thermal equilibrium vacancy concentration [148].

4.2.4.2 Cavity annealing kinetics

Typical annealing behaviour of radiation-induced cavities (if isolated) is that the cavity shrinks by vacancy emission and consequently, its size reduces to zero (i.e. it anneals out). If the cavity contains helium, it changes its size either by emission or absorption of vacancies, until the surface tension is balanced by the internal gas pressure [24]. Recent cluster dynamics simulations [149] suggested that the observed cavity (as presented in Figure 4-12) was a helium bubble containing about 8680 vacancies and 600 helium atoms. Such low He/Vac ratio, agrees well with a previous statement that the helium transmutation from inhomogeneously distributed boron-rich clusters leads to heterogeneous distribution in neutron-irradiated EUROFER97 steel

[124]. In addition, the He/Vac ratio is extremely sensitive to temperatures over 500 °C, which increased from 0.07 (after neutron irradiation) to 0.65 (PIA at 550 °C) [149]. As higher He/Vac ratio configuration is more energetically favourable during annealing [149], cavities' shrinkage via continuous vacancy emission is strongly retarded and thus it appears stable at 550 °C. Therefore, the annealing kinetics of the cavity is governed by vacancy emission which is significantly controlled by the He/Vac ratio.

It should be mentioned that due to the difficulty in identifying small cavities (less than 2 nm) at elevated temperatures, the majority of observed cavities are typically large and few of them appeared stable until annealing up to 600 °C (see section 4.3.6, Figure 4-23). This can be attributed to i) non-identical He/Vac ratio of bubbles after neutron irradiation; ii) the energy barrier of vacancy emission from larger bubbles is higher than that from smaller ones configured with the same He/Vac ratio [149]. Nevertheless, an overall cavity coarsening phenomenon as presented in 4.1.3 was not observed in this current in-situ investigations. Since surfaces are known as free vacancy sinks [156], the emitted vacancies from the shrunk cavities might be absorbed by the free surfaces before they reach their neighbouring cavities. Furthermore, as density of radiation-induced loops (including black dots) in the current investigated material [48] is an order of magnitude higher than that of cavities, the probability for emitted vacancies to encounter dislocation loops is much higher than encountering other cavities. On the other hand, the vacancy emission of cavities might also cause local vacancy supersaturation which contributes to the interstitial loop shrinkage. The influence of dislocation loops on cavities evolution is discussed in section 4.3.6.

4.2.5 Summary

In summary, neutron-irradiated EUROFER97 steel was annealed under specific time-temperature schemes to reveal underlying recovery mechanisms during PIA. The irradiation-induced dislocation loop density decreased and their mean size increased prominently upon increasing temperature from 550 °C to 600 °C and with increasing annealing time. Concurrent shrinkage phenomenon was directly observed for both ½<111> and <100> type loops and is found to be vacancy diffusion driven. In general, loops' neighboring microstructure dictates their shrinkage behavior. Fast shrinkage of the isolated loops was mostly observed close to the dislocation tangles, which are able to provide required thermal equilibrium vacancy concentration for their shrinkage. Additionally, in absence of sufficient vacancy sources, loops in the population compete for vacancies, based on their size and type; thereby, influencing each other's shrinkage behavior [148].

Loop's shrinkage rate is a function of its radius, as it increases with decreasing loop size, due to comparatively larger vacancy concentration gradient towards smaller loop. Furthermore, the observed <100> type loops are found sessile and shrank significantly slower than their observed ½<111> type counterparts. Apart from the neighboring microstructure effect, this primarily appears to be the consequence of the preferential elemental segregation around <100> type loops, based on the corresponding less densely packed {100} habit plane as well as the reduction of the plane's associated elastic strain [148].

Furthermore, in-situ observation as well shows the shrinkage of cavities upon annealing from 500 °C to 550 °C. A nanometre-sized cavity initially stood stable until the annealing temperatures reached 500 °C. Pronounced shrinkage of this cavity was then observed from 500 °C to 550 °C. The shrinkage behaviour is predominantly governed by the vacancy emission while the He/Vac ratio might influence its further shrinkage. Interestingly, the shrinkage stopped at around 550 °C and the cavity remained stable. The simulation based on rate theory revealed that a low level of helium content inside the cavity prohibit the continuous vacancy emission and thus the cavity was not annealed out. Nevertheless, neither dislocation loop nor cavity was found to be coarsened at 550 °C which does not match the results from section 4.1. Therefore, in the next section, isothermal in-situ annealing experiments will be introduced to elucidate the temperature influence on annealing kinetics of irradiation-induced defects.

4.3 Post-irradiation isothermal thin-foil annealing (in-situ TEM annealing)

As presented in section 4.1, upon characterizing bulk post-irradiation annealed samples of EUROFER97 steel by transmission electron microscopy (TEM), a reduction of the loop density with a simultaneous increase in their mean size and formation of dislocation lines/networks were observed. In order to understand responsible mechanisms further, in-situ TEM thin-foil annealing experiments in combination with temperature ramps was presented in section 4.2, which showed vacancy-mediated dislocation loop shrinkage phenomenon and a distinct cavity shrinkage behaviour.

To further clarify and deepen the understanding, isothermal in-situ TEM thin-foil annealing was continued, and results are reported in this section. The effects of local vacancy supersaturation are further considered to elucidate loop's annealing kinetics. Several possible scenarios based on loops neighbouring microstructure evolution are presented and discussed. In addition, the

influence of loop type, alloying elements segregation and free surface are also discussed. Part of the work presented in this section has been published in Ref. [108].

4.3.1 Materials and experimental

For investigations on as-irradiated material (15 dpa, 330 °C) and TEM lamellae preparation refers to section 4.1.1. Similar to section 4.2.1, a high-resolution FEI Tecnai G^2 F20 X-TWIN microscope operating at 200 kV equipped with a Gatan double-tilt heating holder (Model 652) were employed for in-situ annealing experiments. The isothermal in-situ annealing experiments were conducted on separately prepared fresh lamellae at 550 °C and 600 °C for 3 hours, respectively. All the lamellae were heated up to the corresponding elevated temperature with a temperature ramp of 18 K/min. The available Gatan digital micrograph software assisted in observing real-time microstructure evolution, capturing images, and recording videos for detailed analysis. As in such experiments, specimen's drift is an inevitable issue, for analysing microstructure evolution, the same area of interest was tracked carefully during the whole span of experiment. Furthermore, the selected diffraction condition was continuously checked and maintained during the whole duration of in-situ experiments. The thickness of the areas of interest was measured by electron energy loss spectroscopy (EELS) with an uncertainty of ~10%, which is included in our statistical analysis. However, this value is not significant compared with a ~25% statistical error [27].

Generally, g·b analysis (where g is the diffraction vector) with weak-beam dark-field (WBDF) technique is used to identify the dislocation loops Burgers vector b and calculate their density in irradiated material [16]. Alternatively, as both ½<111> and <100> type loops also manifest characteristic shapes under specific zone axis orientations [125], in this in-situ study loop types are identified using simulated dislocation-loop maps with crystallographic information (for more details see Ref. [125]). Furthermore, as it was relatively difficult to track microstructure evolution in WBDF condition, kinematic bright-field (KBF) condition was mainly employed during in-situ investigations. Loops with sizes less than 5 nm are not considered for KBF analysis due to ambiguity in recognizing smaller loops. However, as WBDF technique can image complex strain field of loops more precisely, WBDF investigations were also carried out after in-situ PIA at 600 °C to elucidate the small loop size distribution (mostly between 2 and 5 nm). Such result obtained from WBDF investigation is compared with as-irradiated condition. Moreover, -1.5 µm under-focus condition is employed during TEM-BF imaging of voids in the present investigations. To avoid any inappropriate estimation further, the black dot features

(that are usually less than 2 nm under weak beam condition and 5 nm under kinematical condition) are excluded in this study.

4.3.2 As-irradiated condition

TEM characterization of as-irradiated EUROFER97 steel (15 dpa, 330 °C) was performed on fresh prepared lamellae prior to in-situ annealing. An example of the representative microstructure taken via KBF and WBDF techniques under g = 002 diffraction condition near [100] zone axis is shown in Figure 4-15. As evident, the irradiated microstructure manifests homogenous distribution of the dark-contrast dislocation loops. According to the simulated dislocation-loop map [125], the edge-on loops marked with blue circles are found to be <100> type while the elliptical-shaped loops marked with red circles are identified to be ½<111> type. For loops quantitative WBDF analysis, several images were acquired, and statistic method was employed to calculate dislocation loop density to be (8.6 ± 2.2) x 10^{21} m^{-3} and mean size as 7.1 ± 0.3 nm. By applying the loops invisibility criteria (g·b = 0) and the statistical method for Burgers vector determination [131], the visible ½<111> and <100> type loop fractions are found to be 37% and 63%, respectively [108]. Additionally, the smaller loops are mostly found to be of ½<111> type and the larger ones are dominantly <100> type. Furthermore, apart from dislocation loops, appreciable density of line dislocations, voids, elemental clusters and segregation were also observed (for more see Ref. [66])**.** In order to investigate the effect of PIA on the evolution of dislocation loops, isothermal annealing investigations were carried out, which are presented in the following sections.

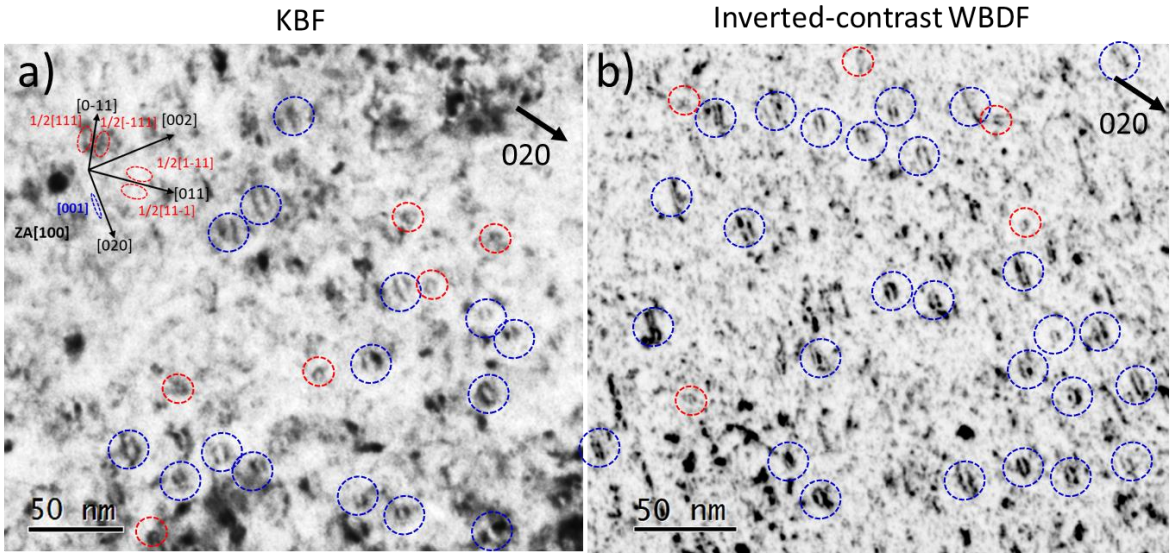

Figure 4-15: (a) TEM-KBF and (b) inverted-contrast TEM-WBDF micrographs taken under g = 020 diffraction condition near [100] zone axis presents representative as-irradiated (330 °C, 15 dpa) EUROFER97 microstructure. Corresponding simulated dislocation-loop map [125] overlaid over KBF

micrograph shows projected dislocation loops excited by g = 020 condition. The high density of nano-scale dark-contrast features visible in the micrographs are irradiation-induced dislocation loops. The edge-on loops marked with blue circles are found to be of <100> type while the elliptical-shaped loops marked with red circles are identified to be of ½<111> type [108].

4.3.3 Isothermal thin-foil annealing at 550 °C

Figure 4-16 presents in-situ TEM-KBF micrographs at four different annealing time points at 550 °C taken under g = 0-11 diffraction condition near [100] zone axis. A high density of edge-on dislocation loops with a double-arc contrast were observed parallel or perpendicular to the [002] or [020] directions in all KBF micrographs. According to the corresponding simulated dislocation-loop map for [100] zone axis [125], most visible loops are identified to be of <100> type. Comparing acquired micrographs and loop size distribution plot at four annealing time points at 550 °C (shown in Figure 4-17), no noticeable change in the visible loops' density was observed. The evolution of the visible loop density and mean size upon annealing is also listed in Table 4-4. These results are consistent with our previous study, see Ref. [148].

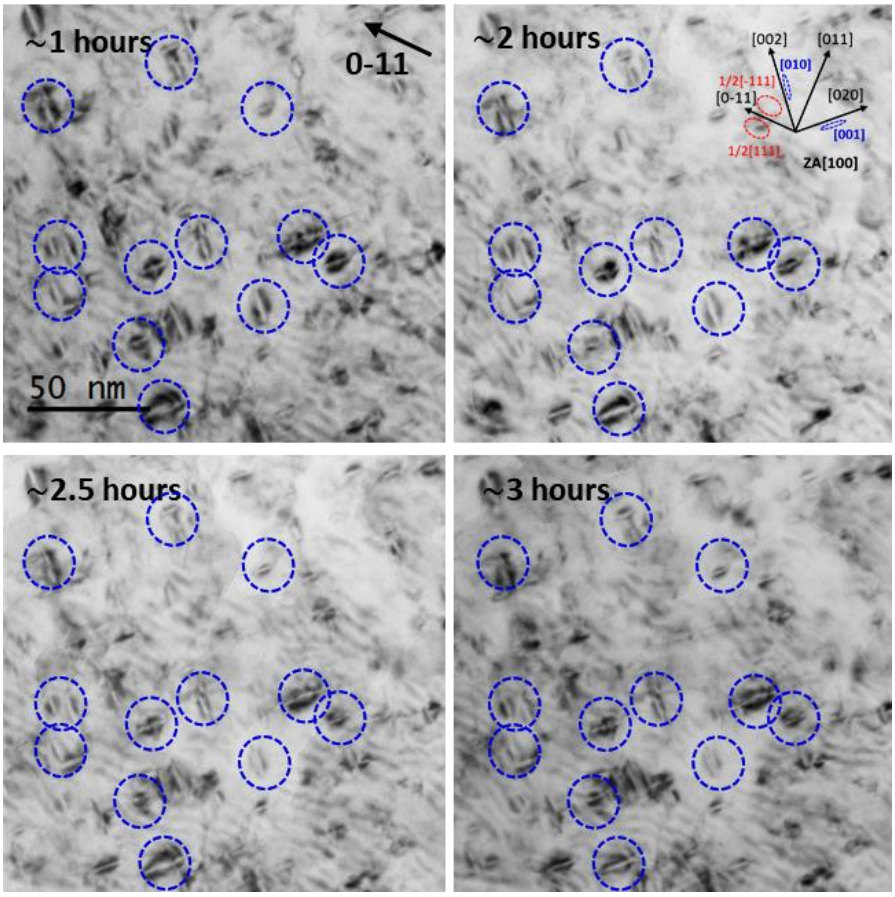

Figure 4-16: In-situ TEM-KBF micrographs at four different annealing time points at 550 °C taken under g = 0-11 condition near [100] zone axis. Corresponding simulated dislocation-loop map [125] overlaid over 2 hour KBF micrograph shows projected dislocation loops excited by g = 0-11. Several identified large <100> loops are marked with blue circle [108].

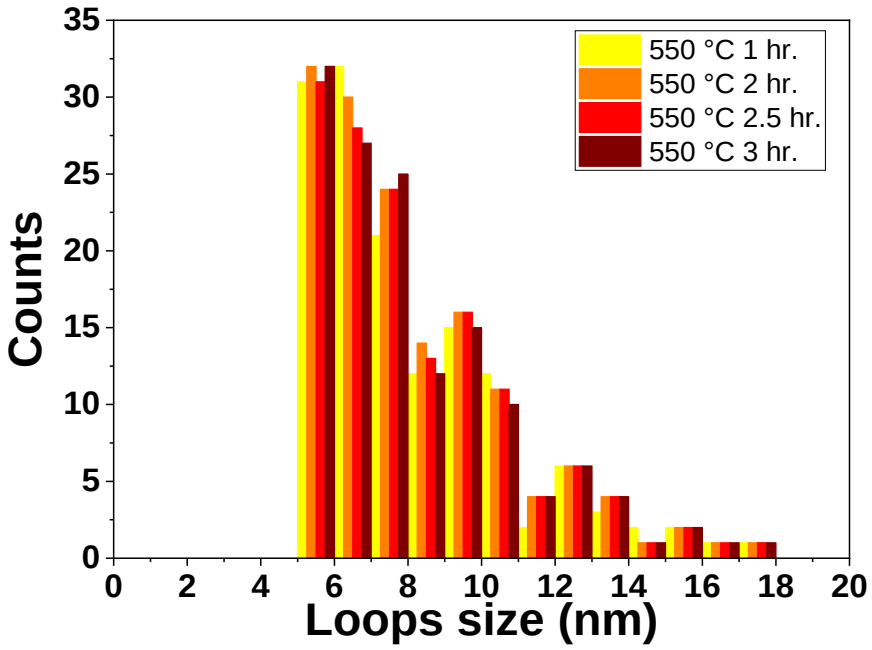

Figure 4-17: Dislocation loop size distribution evolution obtained via in-situ TEM-KBF investigations at 550 °C from total investigated area of ~ 0.2 µm^2. For the present investigated conditions, almost no change in the visible loop density and their mean size is observed. Loop size less than 5 nm are excluded in the quantitative analysis due to ambiguity in recognizing loops [108].

Table 4-4: Visible dislocation loop density and size evolution upon annealing at 550 °C at four different time points [108].

Isothermal annealing at 550 °C [Hour]	**Dislocation loop density [$\times 10^{21} m^{-3}$]**	**Dislocation loop mean size [nm]**
1	5.22 ± 0.52	8.0 ± 0.3
2	5.19 ± 0.52	8.1 ± 0.3
2.5	5.22 ± 0.52	8.2 ± 0.3
3	5.15 ± 0.52	8.1 ± 0.3

4.3.4 Isothermal thin-foil annealing at 600 °C

Figure 4-18 presents in-situ TEM-KBF micrographs at four different annealing time points at 600 °C taken under g = -110 diffraction condition near [110] zone axis. At this diffraction condition, the majority of dislocation loops manifest oval shape, and their longitudinal axis are aligned parallel to the [002] direction. According to the corresponding simulated dislocation-loop map for [110] zone axis [125], these visible loops are identified to be of <100> type. Comparing acquired micrographs and loop size distribution plot at four annealing time points

at 600 °C (shown in Figure 4-19), a steady drop of visible loops' density (with a decrease of ~21% after 2.5 h) is observed. Additionally, a careful analysis of the loop size distribution plot shows an increase in the visible loop mean size by about 36% after annealing at 600 °C for 2.5 hours. The evolution of the visible loop density and mean size upon annealing is also shown in Table 4-5.

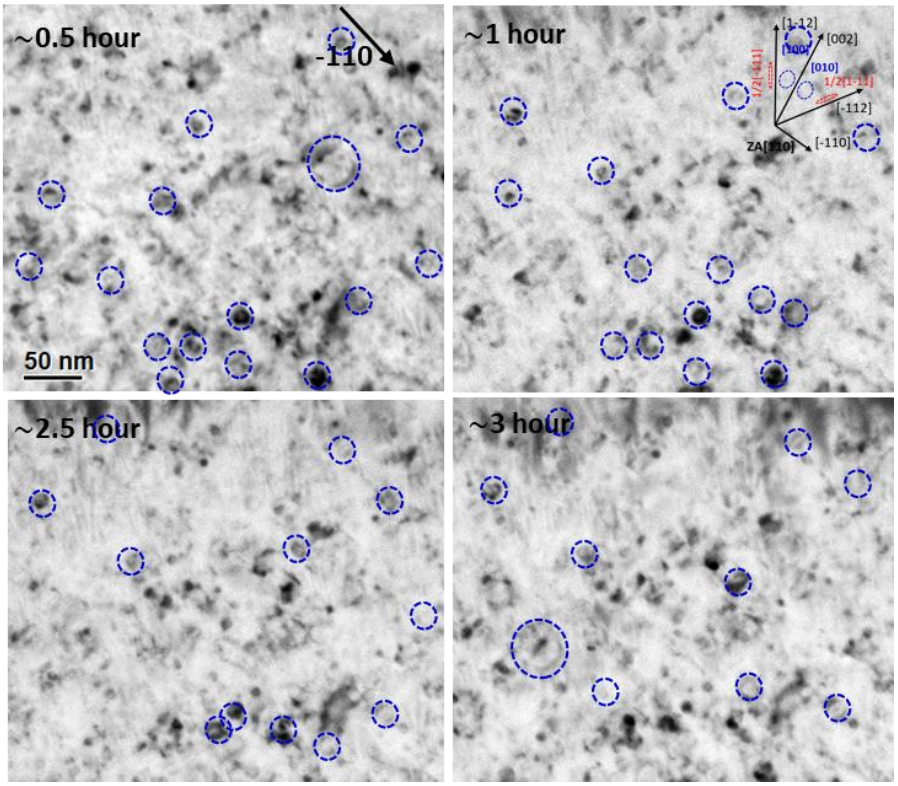

Figure 4-18: In-situ TEM-KBF micrographs at four different annealing time points at 600 °C taken under g = -110 condition near [110] zone axis. Corresponding simulated dislocation-loop map [125] overlaid over 2 hour KBF micrograph shows projected dislocation loops excited by g = -110. Several identified large <100> loops are marked with blue circle [108].

Table 4-5: Visible dislocation loop density and size evolution upon annealing at 600 °C at four different time points [108].

Isothermal annealing @600 °C [Hour]	**Dislocation loop density [$\times 10^{21} m^{-3}$]**	**Dislocation loop mean size [nm]**
0.5	3.18 ± 0.32	8.7 ± 0.3
1	3.14 ± 0.31	10.4 ± 0.3
2.5	2.59 ± 0.26	11.3 ± 0.3
3	2.52 ± 0.25	11.8 ± 0.3

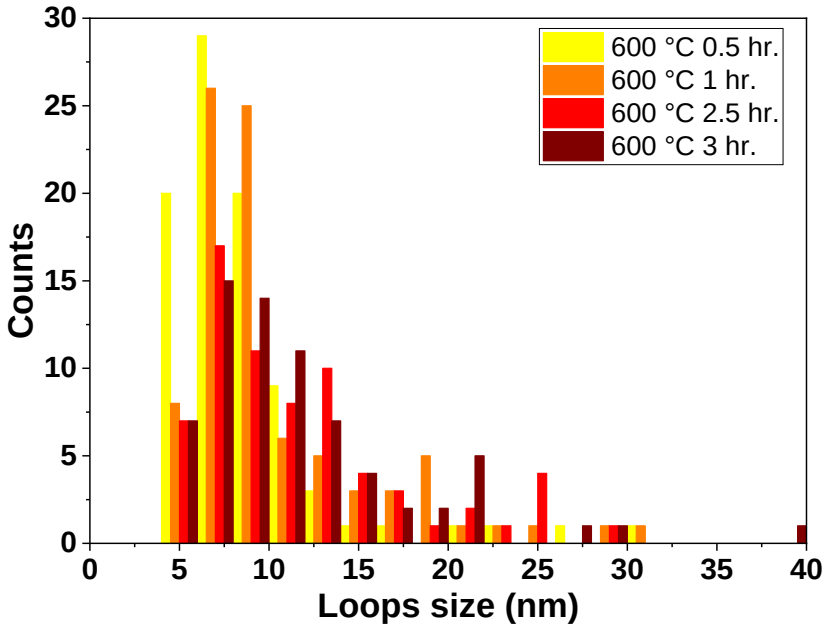

Figure 4-19: Dislocation loop size distribution evolution obtained via in-situ TEM-KBF investigations at 600 °C from total investigated area of ~ 0.4 μm^2. The loop density deceased (witnessed as the frequency reduction of the dark-contrast features) and their mean size increased gradually from 600 °C 0.5 h to 600 °C 3 h. Loop size less than 5 nm are excluded in the quantitative analysis due to *ambiguity in recognizing loops* [108].

For additional quantitative analysis, WBDF technique is employed after in-situ PIA to characterize evolution of smaller loops of less than 5 nm. Figure 4-20a and Figure 4-20b present inverted-contrast WBDF micrographs taken after PIA under conditions $g(4.1g)$ with g = {002} diffraction vector and $g(6.1g)$ with g = {-110} diffraction vector, respectively. According to the corresponding simulated loop map, the edge-on dislocation loops in Figure 4-20a and oval dislocation loops in Figure 4-20b are identified to be of <100> type. It is interesting to note that some large <100> loops shows quasi-rectilinear shape with one segment along [-110] direction whilst the other along [002] direction under g = {-110} condition near zone axis [110]. Such presence of quasi-rectilinear <100> loops can be attributed to the elastically-anisotropic property of α-iron at high temperature (≥500 °C) [157]. Detailed discussion of <100> loop shape evolution is presented in section 4.4.

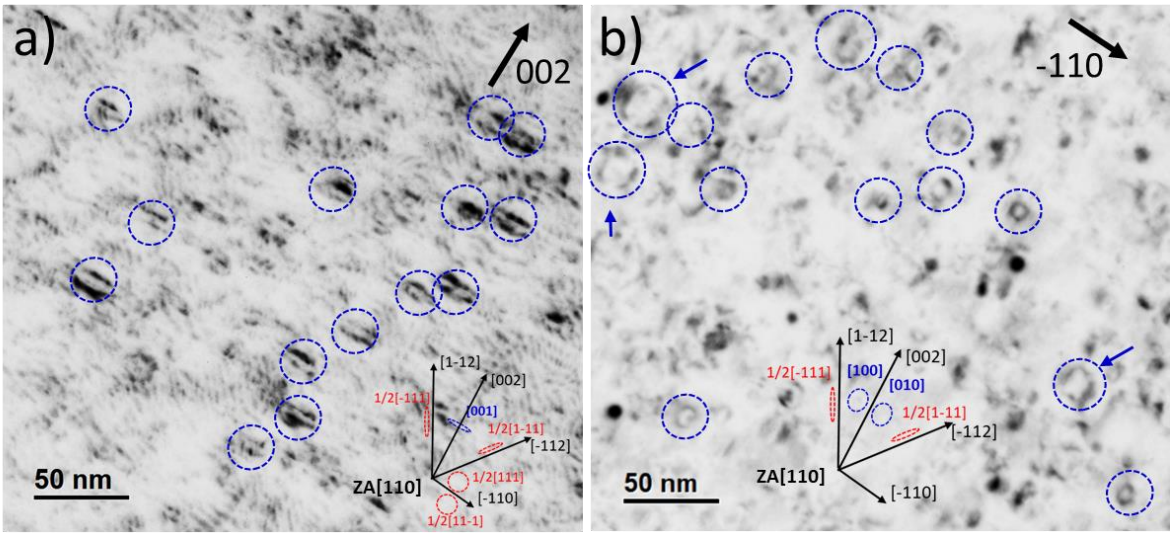

Figure 4-20: Inverted-contrast TEM-WBDF micrographs taken under (a) g(4.1g) diffraction condition with g = {002} and (b) g(6.1g) with diffraction condition g = {-110} near [110] zone axis after in-situ isothermal annealing at 600 °C for 3 hours. According to the corresponding simulated dislocation-loop map [125], the <100> loops marked with blue circles show edge-on contrast under g = {002} condition whilst elliptical contrast under g = {-110}condition [108]. In addition, some quasi-rectilinear loops are marked with blue arrows.

Using statistical method for loops analysis, the total loop density and mean size were determined to be (5.28 ± 1.3) x 10^{21} m^{-3} and 10.7 ± 0.3 nm, respectively from WBDF investigations. Additionally, the comparison of the loop size distributions, obtained via WBDF investigations, for as-irradiated and PIA conditions is shown in Figure 4-21.

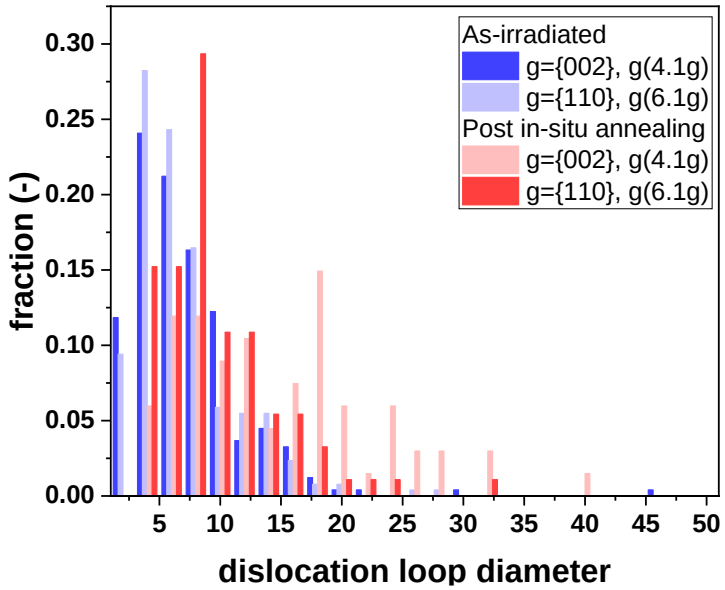

Figure 4-21: The comparison of the loop size distributions, obtained via WBDF investigations, for as-irradiated condition and after PIA at 600 °C for 3 hours from total investigated area of ~ 0.5 µm^2. To exclude FIB damage, the plot does not show case data of black dots which are below 2 nm [108].

Evidently, after PIA, the loop size distribution counts are significantly lower, and it shifts towards higher size. This evolution suggests existence of dislocation loop shrinkage as well as coarsening phenomena. Quantitatively via WBDF analysis, in comparison to the as-irradiated state, there is a reduction of dislocation loop density by ~38% and an increase in their mean size by ~ 51%. Furthermore, the fraction of ½<111> type loops decreased from 37% in the as-irradiated state to 18% after PIA at 600 °C for 3 hours.

4.3.5 Isothermal thin-foil annealing at 625 °C

Above 600 °C, pronounced dislocations activities along with dislocation loops annihilation were observed. Figure 4-22 presents exemplary sequential KBF-TEM micrographs of such activity taken under 110 diffraction condition at 625 °C. Though sample drift and fast microstructural evolution made video acquisition difficult, a real-time observation revealed that thermally activated line dislocation swept out a dislocation loop (black dot feature marked with light blue arrow). As frequently observed during experiments, the gliding line dislocation escaped out of the thin-foil's free surface.

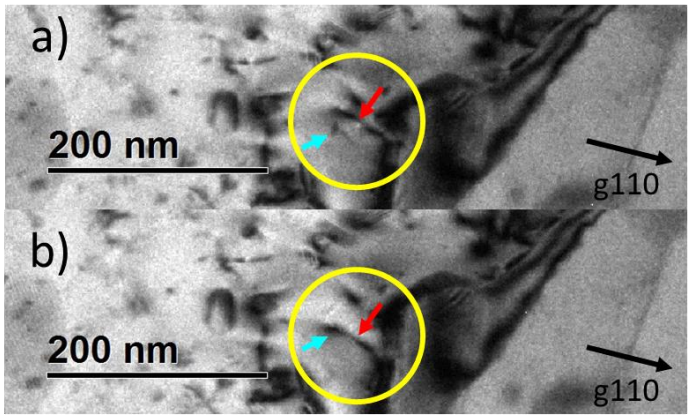

Figure 4-22: In-situ KBF-TEM micrographs (a-b) show a gliding dislocation (marked with red arrow) interact with a dislocation loop (black dot feature marked with light blue arrow) at 625 °C. The images were taken under g = 110 diffraction condition. The time interval between (a) and (b) is around about 1 second [108].

4.3.6 Discussion

In comparison to annealing at 550 °C for 3 hours, noticeable dislocation loop evolution in terms of their density reduction and mean size increment is observed at 600 °C. The reduction of dislocation loop density can be attributed to: 1) loop shrinkage/annihilation and/or 2) loop coarsening. Direct observation of the shrinkage phenomenon for both ½<111> and <100> type loops was previously reported in our preliminary in-situ PIA investigations [148].

During PIA, the thermally mobilized vacancies will migrate through the matrix and under absence of concurrent sinks will be attracted to the loops periphery [13, 26]. From Equation 4-2, at a given temperature T, C_{loop} will be lower than C_{eq}, due to the loop's curvature force ($\approx E/r$). Therefore, a vacancy flux will occur down the concentration gradient to the loop. If the vacancy concentration at some distance away from the loop can be maintained, based on spherical diffusion approximation [94], the continuous vacancy flux to the loop's periphery will lead to its shrinkage due to annihilation of self-interstitial atoms (SIAs) ; and thereby, reducing loop's size. In addition, from Equation 4-3, loop will shrink faster as its size deceases (for more see Ref. [148]).

It is of importance to note that the vacancies concentration in the close proximity of loops (and hence, the incoming flux) can be altered by the nature and distribution of the neighbouring external sources and sinks (e.g., voids, loops, free surface etc.). These scenarios along with influence of loop type and alloying elements segregation on loop annealing kinetics are discussed in the following subsections.

4.3.6.1 Influence of neighbouring microstructure

(a) Scenario 1: Presence of cavities and dislocations in the loops' neighbourhood

In as-irradiated EUROFER97, three-dimensional vacancy aggregates (cavities) and/or line dislocations are often present in the loops' neighbourhood. And since during PIA both voids as well as line dislocations can act as the strong sources and sinks for the point defects, their simultaneous evolution could accelerate the loop shrinkage phenomenon.

Such an evolution of three cavities observed during PIA of neutron-irradiated EUROFER97 is shown in Figure 4-23. As evident, upon increasing temperature from 550 °C and holding at 600 °C for ~ 5 minutes, two cavities (marked with red arrows) were annealed out, while the other marked cavity (with blue arrow) shrank to a smaller size (Figure 4-23b). Noticeably, the direct observation of such small cavity-loop interaction via in-situ TEM annealing is hard, since small cavities show contrast only at specific defocus condition whilst loops are usually visible at in-focus condition. However, cavity evolution observed here still suggests that they shrink/annihilate by emitting vacancies or absorbing SIAs, which would increase the local vacancy concentration in loops' neighbourhood [158]. Furthermore, at elevated temperatures, vacancies emitted during thermally activated climb of nearby edge dislocations could also increase local vacancy concentration. Therefore, under these momentarily events of vacancy supersaturation by external vacancy sources, a loop in the population could behave as an

isolated loop and will shrink fast. Indeed, fast loop shrinkage along with simultaneous neighbouring line dislocations movements were observed often upon annealing neutron-irradiated EUROFER97 at 600 °C, see Ref [148]. It is of interest that Rovelli et al. [159] considered such a loop and cavity configuration theoretically and showed that the presence of voids in the loops' neighbourhood accelerate their annihilation.

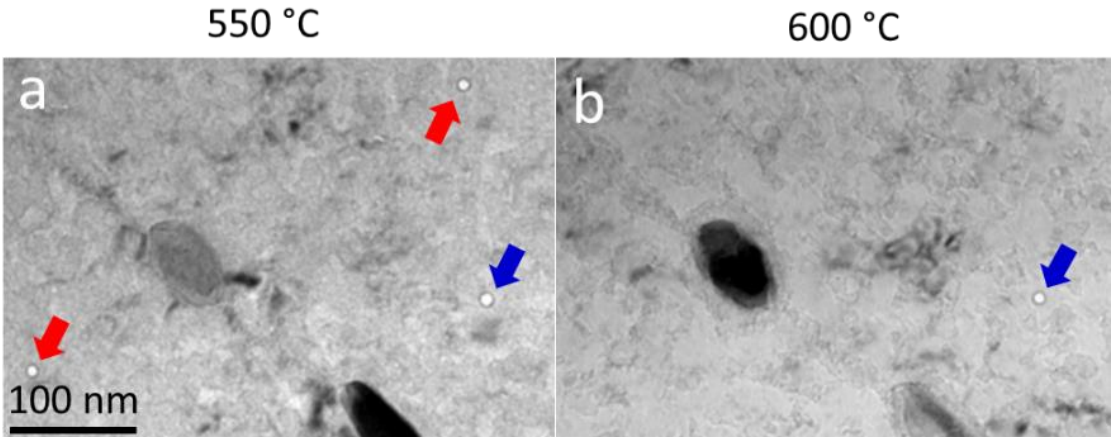

Figure 4-23: TEM-BF micrographs (taken at -1.5 μm under-focus condition) show three cavities evolution upon annealing neutron-irradiated EUROFER97 from 550 (a) to 600 °C (b). Evidently, upon increasing temperature from 550 °C (with 10 K/min) and holding at 600 °C, two cavities (marked with red arrows) were annealed out, while the other marked cavity (with blue arrow) shrank to a smaller size [108].

(b) Scenario 2: Presence of other competing loops

Due to very high density of dislocation loops in neutron-irradiated EUROFER97, several loops if present in the close proximity could also simultaneously compete for vacancies during PIA. And if sufficient vacancies are not present in the loops' neighbourhood, a loop in the population cannot behave as an isolated loop, i.e. loop's associated local vacancy concentration will be altered by other existing neighboring loops, as they will compete for vacancies. This competition for vacancies will be dictated by the size of the loops, discussed below.

Figure 4-24a presents one such example where several relatively small loops are present in the close proximity of the marked large <100> loop (taken from Ref. [148]). As evident upon continuing annealing from 550 °C to 600 °C for 2 hours (compare Figure 4-24a and b), the marked large loop shrank at much slower rate than its neighbouring smaller counterparts. This is because smaller loops, due to their higher associated curvature force, will preferentially attract thermal vacancies more than the nearby larger counterpart. And assuming that there are not enough vacancies to maintain uniform shrinkage for all loops, the smaller loops shrink first

and fast. Therefore, the resultant depletion of vacancies will lead to the slower shrinkage of the larger loop.

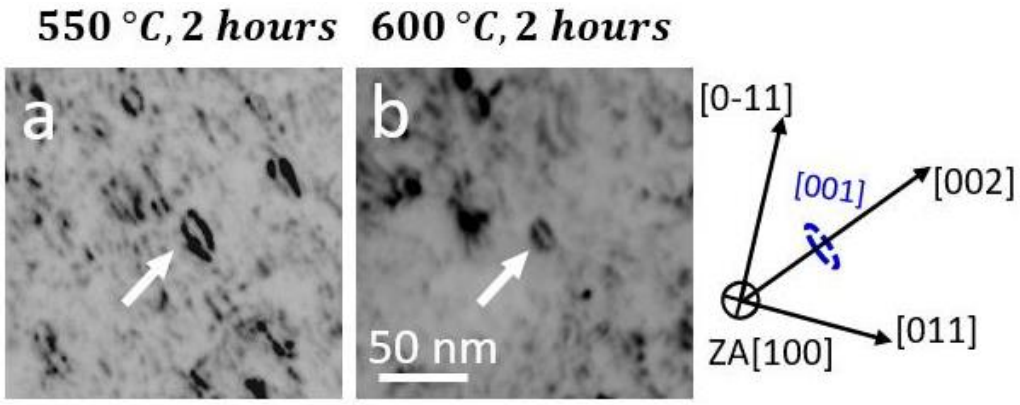

Figure 4-24: In-situ inverted-contrast TEM-WBDF micrographs taken at a) 550 °C, 2 hours and (b) 600 °C, 2 hours annealing time-points in neutron-irradiated EUROFER97 [148]. The images were taken under g = 002, g(4.1g) near [100] zone axis. According to the corresponding simulated loop map in right, all resolvable loops are identified to be of <100> type. Evidently, the marked large <100> type loop shrank at a much slower rate than its neighbouring smaller counterparts [108].

4.3.6.2 Influence of loop type

Quantitative analysis after annealing at 600 °C for 3 hours shows that the estimated fraction of ½<111> type loops decreased from 37% to 18%. This can be attributed to the fast shrinkage of ½<111> type loops as reported previously [148]. In this section as well, the size distribution obtained after PIA from WBDF investigations reveals a pronounced reduction of small loops (less than 5 nm, see Figure 4-21), which in as-irradiated state are mostly found to be of ½<111> type [126]. In contrast to this, <100> type loops are found relatively stable, as they shrank at a much slower rate than their ½<111> counterparts (for example see Figure 4-24 and its caption).

Nevertheless, apart from the fast shrinkage, ½<111> type loops could also be absorbed by the neighbouring large sessile <100> loops. Figure 4-25 presents such a case where a small ½<111> type loop appears to be absorbed by a larger neighbouring edge-on <100> type loop. In such an absorption phenomenon, loop-loop elastic interaction appears to play an important role, due to their close proximity [22, 160]. Arakawa et al. [22] also reported such phenomenon upon in-situ annealing electron-irradiated pure α-Fe. In addition, they observed individual transformation of a small interstitial loop with Burgers vector of ½<111> to <100> even without any contact with external dislocations. However, the latter case is not observed in our present investigations. Therefore, preferential loop type dependent evolution of the irradiated microstructure also dictates overall loop size distribution.

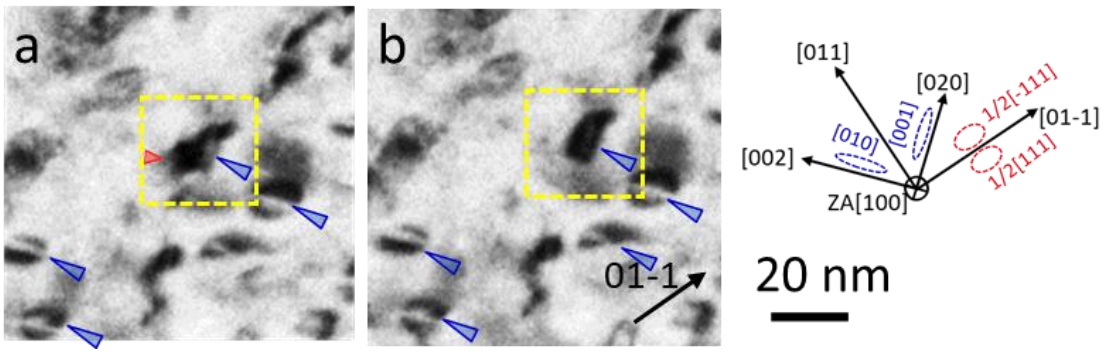

Figure 4-25: In-situ TEM-KBF micrographs taken under g = 01-1 diffraction condition near [100] zone axis at 600 °C. The time interval between (a) and (b) is less than 1 second. According to the corresponding simulated loop map in right [125], the edge-on loops are identified to be <100> type (marked with blue arrows) while the elliptical loop is identified to be ½<111> type (marked with red arrow). Evidently, ½<111> type loop appears to be absorbed by the neighbouring large sessile <100> loop [108].

4.3.6.3 Influence of alloying elements segregation

In contrast to pure α-iron, different alloying elements (Cr, Ni, Si, Mn, and P) are known to decorate the periphery of dislocation loops in irradiated EUROFER97 steel in order to relax associated dilatational-strain field [65, 132]. This segregation is known to suppress dislocation loops self-climb and their evolution during annealing. For example, Arakawa et al. [65] found that at elevated temperatures the ½<111> loop shrinkage and motion are significantly suppressed by Cr segregation at the loops periphery owing to the migration of couples of Cr and a vacancy towards loops and trapping of Cr at the periphery of loops. Additionally, Yoshida et al. [141] suggested that Cr at dislocation loops could reduce the absorbing reaction between dislocation loops and interstitials, which could suppress their coarsening behaviour. Besides, the segregation could also influence the annealing behavior of dislocation loops based on their size and the intrinsic nature of their type, for more details see section 4.2.4.

4.3.6.4 Influence of free surface

Since PIA experiments in the present study are carried out using thin foils (thickness: ~100 nm), consideration of surface effect is essential, as surface is an effective sink for point defects [138, 156]. From vacancies viewpoint, this is expected to suppress their supersaturation (as vacancies will rush to the free surface), especially close to the thin-foil surface. And therefore, as there are insufficient thermal vacancies for the loop evolution, the loops will not shrink even if the curvature force tries to contract them.

As shown in section 4.3.3, no obvious shrinkage and/or growth of the loops were observed under isothermal annealing at 550 °C for 3 hours. However, previous bulk PIA investigations

at similar conditions revealed a significant reduction of the loop density (by ~ 69 %) [126]. This implies that during PIA sufficient thermal vacancies generated in the bulk material are mainly exploited for relatively faster loop evolution in comparison to that in the present thin-foil annealing experiments. However, as temperature was raised to 600 °C in the present investigations, the reduction of loop density (by ~ 38%) was apparent. Nevertheless, though the annealing trends are similar, the reduction of loop density in the present investigations is still far from that observed after bulk PIA experiments. Therefore, to exclude surface effects and to better visualize other simultaneous operating mechanisms (e.g. loop coarsening and dislocation tangles formation [126]), isothermal thicker-foil annealing experiments were planned. The results of these investigations are reported in detail in the section 4.4.

4.3.7 Summary

In summary, in-situ TEM thin-foil annealing experiments were carried out on neutron-irradiated EUROFER97 at 550 °C and 600 °C to study irradiation-induced dislocation loop annealing kinetics. In comparison to annealing at 550 °C for 3 hours, noticeable dislocation loop evolution in terms of their density reduction and mean size increment was observed at 600 °C. For the present thin-foil annealing experiments, this is mainly linked to the vacancy-mediated loop shrinkage phenomenon. In general, the vacancy flux occurring down the concentration gradient defines the annealing behaviour of dislocation loops. Nonetheless, the spontaneous evolution of the loops neighbouring microstructure substantially alters their annealing kinetics.

Owning to EUROFER97's complex microstructure, various scenarios originate in terms of the presence or absence of local external sources and sinks. If sufficient vacancy sources exist nearby, a loop in the population behaves as an isolated loop. In such a case, besides curvature force, incoming vacancy flux from the loop's neighboring shrinking cavities and/or line dislocations climb contribute to its faster shrinkage. Nevertheless, if vacancy sources are insufficient, a loop in the population cannot behave as an isolated loop, as other existing loops compete for vacancies. This competition of vacancies is dictated by the availability of vacancies and the sizes of the loops, which finally alters their corresponding shrinkage rate. In addition, intrinsic nature of the loop type as well as their size govern their corresponding evolution which finally defines loop type fraction in the annealed state. Furthermore, for the loops that are in the close proximity of each other, loop-loop interactions along with loops absorption are also important phenomena. Besides, the influence of the segregation on the annealing behavior of dislocation loops varies with the loop size and the intrinsic nature of the loop type.

Finally, in contrast to the observed loop shrinkage phenomenon, no significant coarsening was observed in the present thin-foil annealing experiments. Additionally, apart from the similar annealing trends, the reduction of loop density is still far from that observed after bulk PIA experiments [126]. This appears to be a consequence of the surface effects. Therefore, to exclude surface effects and to better visualize other concurrent mechanisms (e.g. loop coarsening and dislocation tangles formation [126]), isothermal thicker-foil annealing experiments were designed. The results are reported in detail in the next section.

4.4 Post-irradiation isothermal thick-foil annealing

As mentioned in above sections, in contrast to the bulk annealing results, neither loop coarsening, nor the formation of dislocation lines/networks were observed in our thin-foil annealing experiments (conducted at 550 °C). Besides, though appreciable loop coarsening were observed at 600 °C, an extensive formation of dislocation lines/networks was not generally examined in the thin-foil annealing experiments. This discrepancy is expected to be a result of surface effects, which are known to play substantial role in the thin-foil annealing experiments. Typically, the evolution of prismatic-dislocation loops is dictated by (1) diffusivity of the point defects, (2) line-tension of the dislocation loop and (3) the supersaturation of point defects in the vicinity of the loop. In thin-foil annealing experiments, the degree of point defects supersaturation is limited, since surfaces are known to be the effective sinks for point defects. Therefore, to emulate bulk annealing results, thoughtful thick-foil annealing experiments are required wherein points defects supersaturation is expected to be substantial because of the suppressed surface effects [156].

Consequently, to confirm and to delineate various associated mechanisms and to clarify inconsistency between thin-foil and bulk annealing experiments, dedicated isothermal thick-foil PIA investigations were carried out on EUROFER97. The important observations from these experiments are reported and discussed in this section. Part of the work presented in this section has been published in Ref. [161].

4.4.1 Materials and experimental

For investigations on as-irradiated material (15 dpa, 330 °C) refers to 4.1.1. Several 3 µm thick lamellae were lifted-out from the undeformed regions of the previously electrochemically polished irradiated sample and were attached onto the molybdenum TEM half-grid by Platinum deposition (see Figure 4-26a). For as-irradiated microstructure characterization, some of these lamellae were thinned down to electron transparency (to a thickness of round 100 nm) with

multiple passes of a low-energy Ga^+ ion-beam. Whereas, others thick lamellae were subsequently annealed in vacuum in a high-resolution FEI Tecnai G2 F20 X-TWIN microscope operating at 200 kV and equipped with a Gatan double-tilt heating holder (Model 652). Figure 4-26b presents time-temperature profiles for annealing experiments conducted at 550 °C for 1, 2 and 3 hours. For both heating (for attaining 550 °C) and cooling, the 17.5 K/min temperature ramp was employed. Post-annealing, the thick lamellae were subsequently transferred to FIB-SEM for the final thinning to electron transparency (to a thickness of around 100 nm) with multiple passes of a low-energy ion-beam (see Figure 4-26c).

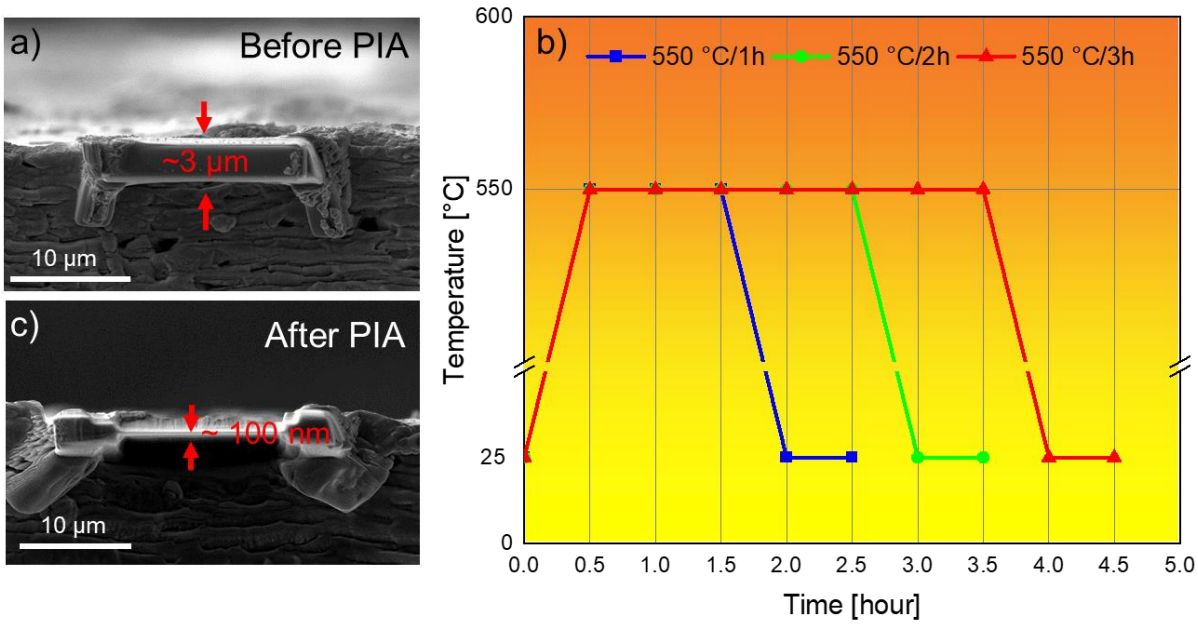

Figure 4-26: (a) SEM micrograph showing a 3 µm thick lamella (welded on to a molybdenum TEM grid) before isothermal TEM annealing experiment. (b) Time-temperature schemes for isothermal TEM annealing experiments conducted at 550 °C for 1, 2 and 3 hours. (c) SEM micrograph showing an annealed lamella that was thinned down to electron transparency (to a thickness of around 100 nm) for TEM investigations [161].

Generally, g·b analysis (g is the diffraction vector) with weak beam dark-field (WBDF) technique was employed to identify the dislocation loops Burgers vector b and estimate their density [16]. Alternatively, as both ½<111> and <100> type loops also manifest characteristic projected contrast under specific zone axis orientations [125], in this study loop type are also identified using simulated dislocation-loop map with crystallographic information in kinematic bright-field (KBF) condition. The underestimation of the loop density due to partial invisibility is resolved by using the statistical method for Burgers vector analysis [131]. Thickness of the regions of interest was determined in TEM by employing electron energy loss spectroscopy

(EELS) log-ratio method, which has an uncertainty of 10% [129]. In general, most FIB induced damage contrast is similar to that of the irradiation-induced black dots. Therefore, to avoid any inappropriate estimation, the black dot features are excluded in this study.

4.4.2 Isothermal thick-foil annealing at 550 ° C for 1 hour

Figure 4-27a presents the representative microstructure of an as-irradiated (15 dpa, 330 °C) EUROFER97 acquired under g = {110} KBF condition. Apparently, the as-irradiated microstructure manifests a high density of homogenously distributed dislocation loops and black dots. Based on the projection angle between the loop habit plane and TEM viewing screen [125], loops exhibit circular or elliptical contrast (Figure 4-27a). For loops statistical analysis, weak-beam technique was employed. Using several acquired micrographs (not shown here), the total visible loop density and mean size are found to be $(8.6 \pm 2.6) \times 10^{21}$ m^{-3} and 7.1 ± 0.6 nm, respectively (for more details see Refs. [48, 126]). Furthermore, by applying loop invisibility criteria (g·b=0) and the statistical method for Burgers vector determination [131], the ½<111> and <100> type loops are found to be about 37% and 63%, respectively. Additionally, the smaller loops are mostly found to be of ½<111> type and the larger ones are dominantly <100> type. Furthermore, apart from dislocation loops, appreciable density of line dislocations, cavities, elemental clusters and segregation were also observed (for more see Ref. [66]).

Figure 4-27b presents representative microstructure of a post-irradiation annealed EUROFER97 (at 550 °C for 1 hour) acquired under g = {110} KBF condition. In contrast to the as-irradiated state, PIA microstructure manifests a high density of dislocation lines/tangles as well as loops that appear to have coarsened with near circular, rectilinear and irregular shapes. An example of an inverted-contrast WBDF micrograph taken under g = 110 diffraction condition near [110] zone axis is shown in Figure 4-28a. Under this selected diffraction condition, loops with rectilinear shape are evident. Additionally, these rectilinear loops have their side-edges parallel to the <100> directions, respectively. According to the simulated dislocation-loop map (shown in Figure 4-28b), nearly all of these visible loops are identified to be of <100> type [125]. On further careful observation, several coarsened rectilinear loops appear to be interacting along <100> directions (see for example enlarged Figure 4-28c), while few others appear to have merged; and thus, forming irregular/complex geometries (see enlarged Figure 4-28d and Figure 4-28e). Noticeably, WBDF condition could image complex strain field around loops corner more accurately than KBF condition (compare Figure 4-28a

and Figure 4-27b). This is because WBDF technique allows narrower image peaks due to the small value of the effective extinction length [16].

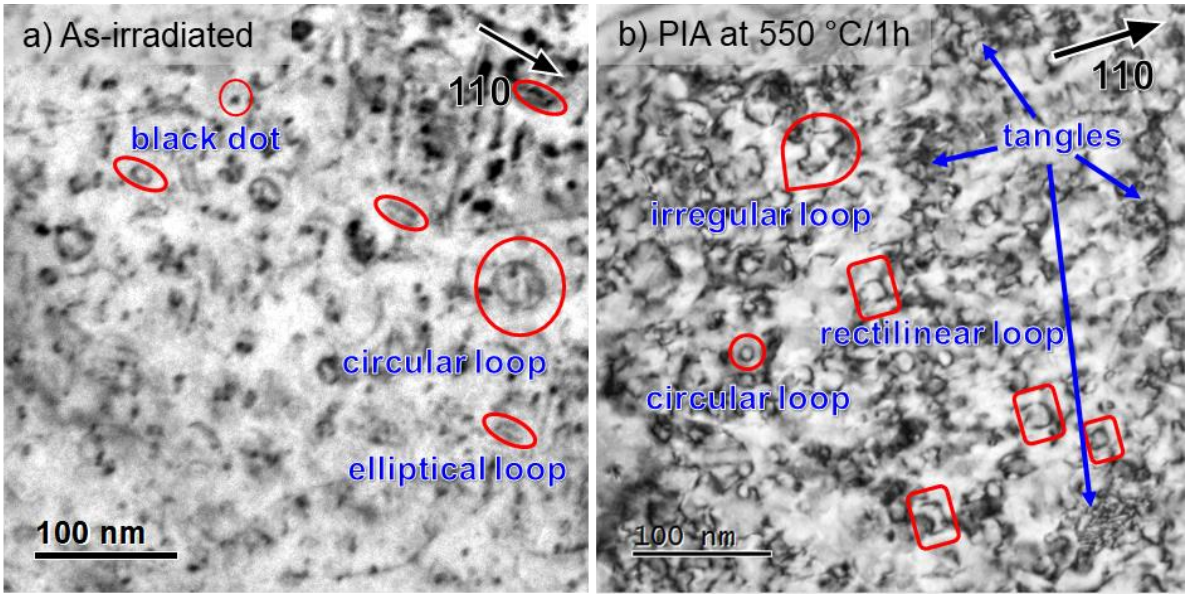

Figure 4-27: KBF-TEM micrographs acquired under g = {110} diffraction condition show (a) as-irradiated (15 dpa, 330 °C) and (b) post-irradiation annealed (550 °C/1h) microstructures of EUROFER97. The as-irradiated microstructure manifests a high density of black dots and loops of near circular shape. In contrast, post-irradiation annealed microstructure mainly manifests a high density of dislocation lines/tangles as well as loops that appear coarsened with near circular, rectilinear and irregular shapes [161].

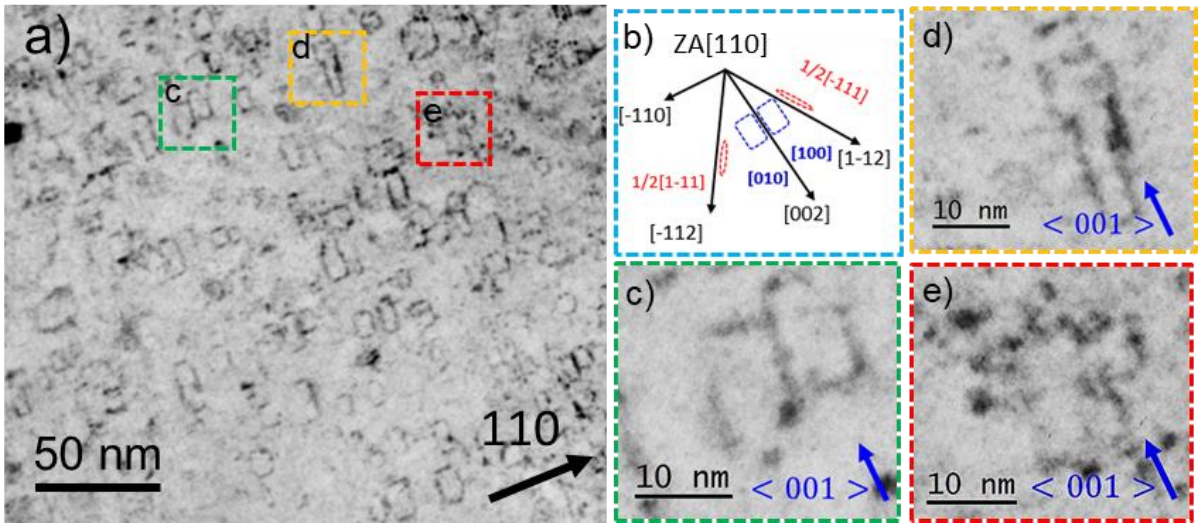

Figure 4-28: (a) Inverted-contrast WBDF-TEM micrograph taken under g(6.1g) with g = {110} diffraction condition near [110] zone axis after PIA of EUROFER97 at 550 °C for 1 hour. A high-density of rectilinear loops with their edges parallel to the <100> directions are apparent. According to the corresponding simulated loop map in (b) all of these visible loops are identified to be of <100> type, which seems coarsened and often interacting along <001> direction (c). At few instances loops also appear to have merged; and thus, forming irregular/complex geometries (d-e) [161].

By additionally applying loops invisibility criteria (g·b = 0) and the statistical method for Burgers vector determination [131], the <100> loop fraction is found to increase from ~63% in as-irradiated condition to ~98% after PIA at 550 °C for 1 hour. Using several acquired micrographs, the total visible loop density and mean size after PIA are found to be (6.8 ± 2.0) x 10^{21} m^{-3} and 10.4 ± 0.6 nm, respectively. Quantitatively, after PIA at 550 °C for 1 hour, there is an average reduction of the visible dislocation loop density by ~ 22% and an increment in their average mean size by ~ 46%. Moreover, upon comparing visible loop size distribution plots for both conditions (see Figure 4-29), it is evident that the distribution shifts towards higher size after PIA. Furthermore, the large loop fraction (with size > 10 nm) increased from 21% to 52%, while the small loop fraction (size < 5 nm) decreased from 36% to 4%. Together from above results and our previous in-situ investigations [108, 148], the PIA of EUROFER97 at 550 °C for 1 hour leads to dislocation loop shrinkage/annihilation, coarsening/merging and dislocation lines/tangles formation.

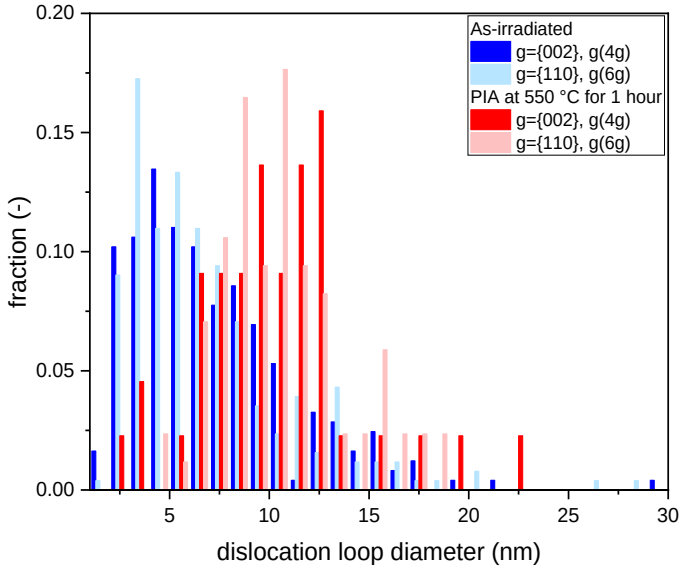

Figure 4-29: Visible dislocation loop size distribution plots for the as-irradiated (15 dpa, 330 °C) and post-irradiation annealed (550 °C for 1 hour) EUROFER97 estimated via WBDF technique. Evidently, after PIA, the loop size distribution shifts towards higher size [161].

4.4.3 Isothermal thick-foil annealing at 550 ° C for 2 and 3 hours

To further investigate the effect of annealing time, additional PIA experiments were carried out. Figure 4-30a and b present representative microstructures of a post-irradiation annealed EUROFER97 at 550 °C for 2 hours and 3 hours, respectively. The shown KBF micrographs are taken under g = {011} diffraction condition near [100] zone axis. According to the overlaid

simulated dislocation-loop map [125] in Figure 4-30a, after 2 hours PIA, several edge-on loops marked with blue frames were identified to be of <100> type. Additionally, a high density of dislocation segments (marked with blue arrows) is apparent after 2 hours annealing. Upon increasing annealing duration further (up to 3 hours), a more pronounced transition from dislocation loops dominated to dislocation segments/tangles dominated microstructure transpires (see, Figure 4-30b). Compared with Figure 4-30a, more extended dislocation lines/segments are visible.

At both annealing conditions, the individual dislocation segments are found to be aligned along [020] and [002] directions. These segments appear to be the remnant portions of coarsened <100> loops, which probably have been cut by the surface during lamella fabrication. In addition, dislocation tangles are likely formed by the coarsened <100> loops interactions (discussed later). Therefore, with such complexity, obtaining accurate loop dimensions at these annealing conditions was difficult. Quantitative analysis of dislocation loops is presented in section 4.5.1.

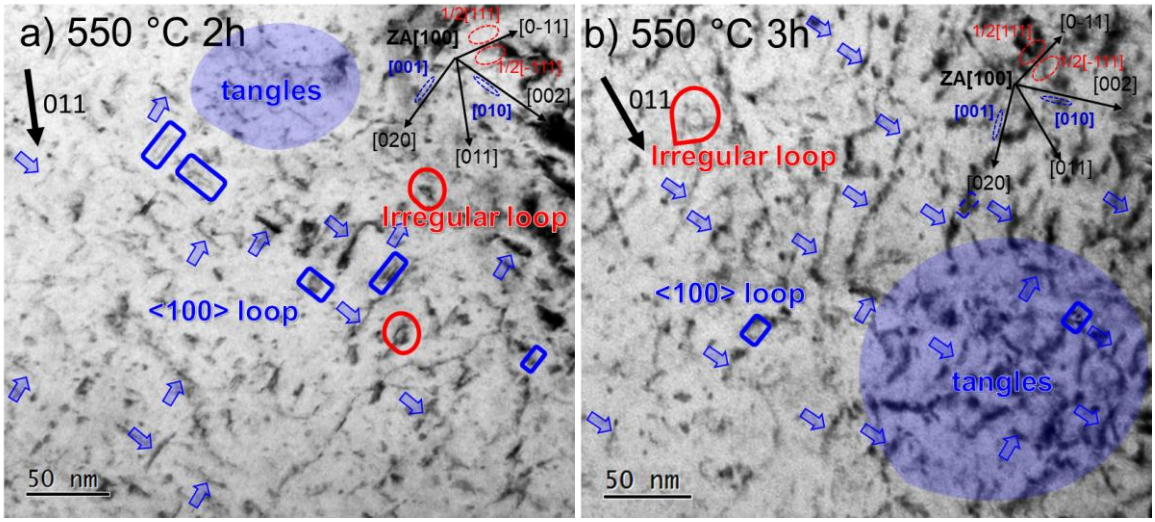

Figure 4-30: KBF-TEM micrographs acquired under g = {011} diffraction condition near zone axis [100] after PIA of EUROFER97 at 550 °C for (a) 2 hours and (b) 3 hours. Corresponding overlaid simulated dislocation-loop map [125] shows projected dislocation loops excited by g = {011}. Several identified <100> loops (mainly after 2 hours) are marked with blue frame whilst some represented irregular loops are marked with red frame in both micrographs. In addition, a high density of <100> loop segments are marked with blue arrows in both micrographs. Furthermore, larger areas of containing dislocation tangles are also observed after PIA at 550 °C for 3 hours [161].

4.4.4 Discussion

Above results reveal that thick-foil annealing of a neutron-irradiated EUROFER97 at 550 °C resulted in a reduction of dislocation loop density and increment of their mean size. This can be attributed to the dislocation loop shrinkage/annihilation as well as their coarsening/merging

phenomena. By performing in-situ TEM thin-foil annealing experiments, vacancy-mediated loop shrinkage phenomenon was indeed observed, discussed separately in Refs. [148]. Whereas, sessile <100> loops coarsening, along with their merging, is apparent from the present investigations. Furthermore, from statistical analysis, nearly all visible loops after PIA are found to be of <100> type. This consequently indicates that during annealing either small ½<111> loops shrank and/or consumed by the growing larger <100> loops. Indeed, ½<111> loops shrinkage as well as their merging into relatively larger <100> loops were observed during our in-situ PIA investigations [108, 148].

Besides, in comparison to the quasi-circular loops in as-irradiated condition, the majority of <100> loops appear rectilinear in the annealed state (550 °C, 1 hour). This can be attributed to the combination of the particular crystallographic symmetry of the {100} planes, change in iron's elastic anisotropy with temperature and the detailed growth mechanism of the loops, which is discussed below.

In an isotropic medium, every edge orientation of a pure-edge prismatic loop is equivalent; and therefore, the loop is expected to be circular. As illustrated in Figure 4-31a, the periphery of a circular loop could be considered comprising of a large number of jogs. However, α-iron lattice is elastically-anisotropic at room temperature and its elastic anisotropy increases further with temperature [157]. Therefore, the anisotropic elastic free energy of dislocations in α-iron is strongly influenced by the temperature [157, 162]. Fitzgerald and Yao [162] using anisotropic linear-elastic theory demonstrated that the lowest-energy directions for prismatic [100](100) loops above 500 °C are [001] and [010]. Therefore, it is reasonable to assume that during annealing neighbouring incoming atoms align themselves along loops' peripheral lowest-energy directions (i.e. <100>), leading to their coarsening (see Figure 4-31b). As the systematic growth of loops along their periphery continues, this apparently reduces their original jogs concentration (defined as the number of jogs per unit length) (see Figure 4-31c and Figure 4-31d). This coarsening phenomenon could be perceived as a non-conservative climb process in terms of the movement of jogs towards one end of the loop side. Thus, upon annealing, a quasi-circular loop in as-irradiated condition will reduce its curvature (dislocation line length) as well as peripheral jogs concentration to coarsen into a near rectilinear loop.

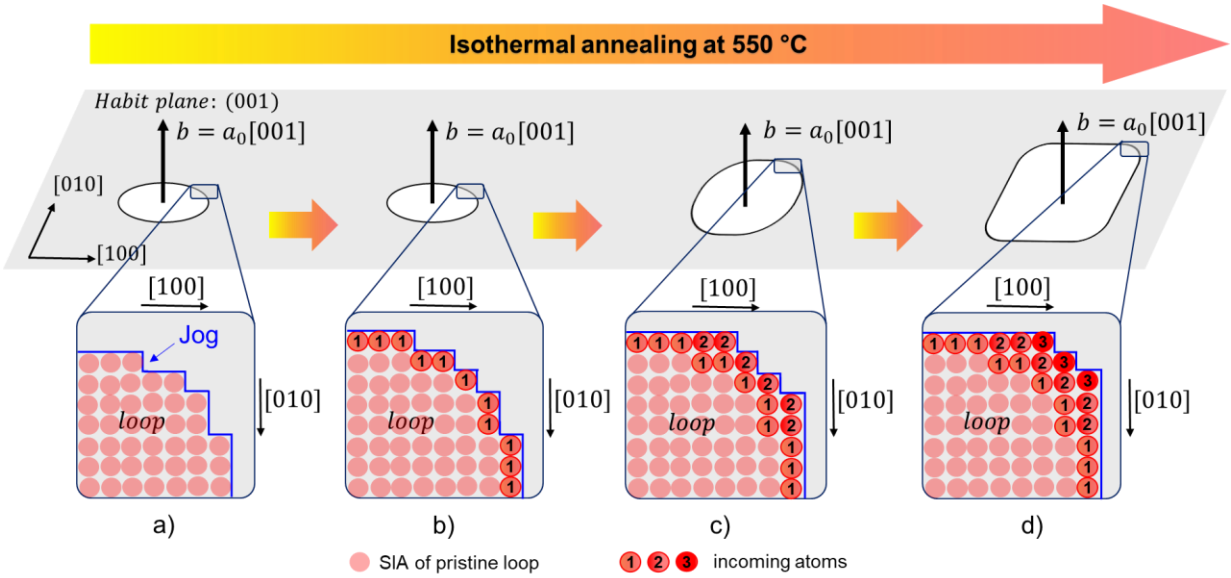

Figure 4-31: Schematic illustrations present proposed <100> type loop coarsening and simultaneous shape evolution phenomenon that occurs upon PIA EUROFER97 at 550 °C. (a) A quasi-circular loop is visualized with a high concentration of jogs at its periphery. (b-d) The <100> loop grow by the alignment of neighbouring incoming atoms along its lowest-energy directions, [001] and [010] respectively. This eventually causes loop coarsening by simultaneous reduction of the original peripheral jogs concentration. This can also be perceived as a non-conservative climb process in terms of the movement of jogs towards one end of the loop side, causing a quasi-circular loop to transform into a near rectilinear one [161].

As loops coarsen, they could interact along their lowest-energy directions, see WBDF micrograph in Figure 4-28c and schematic in Figure 4-32a. These interacting loops could thereafter merge to form larger loops of various geometries. These geometries depend on the merging-loops Burgers vectors, sizes and numbers. For example, two coplanar loops with same Burgers vector and size will form a large rectilinear in-plane loop (see Figure 4-32a and Figure 4-32b). Whereas, two or more coplanar loops with same Burgers vector but with different sizes could merge to form a large irregular in-plane loop (see WBDF micrographs in Figure 4-28d-e and schematic in Figure 4-32c). Additionally, merging of two or more non-coplanar loops (with different Burgers vectors, for example [100] and [001] or ½<111> and <100>) will always lead to the formation of three-dimensional (3D) structures (Figure 4-32d-f), which will appear irregular in TEM based on their 2D projections. Besides, other irradiation-induced microstructural features, such as Cr-enriched clusters [163] as well as elemental segregation around loop's periphery [132], could suppress the annealing behaviour of dislocation loops [141], leading to their irregular shape.

With continued annealing, the merged-loops structures further evolve into complicated geometries, as they interact with other coarsened loops, merged structures and grain boundaries.

This complex situation of merging and/or annihilation will lead to the development of dislocation tangles. However, it is noteworthy that during sample preparation large merged-loops will also be cut by the surface and the remaining structure in thin-foil will appear as dislocations tangles in TEM.

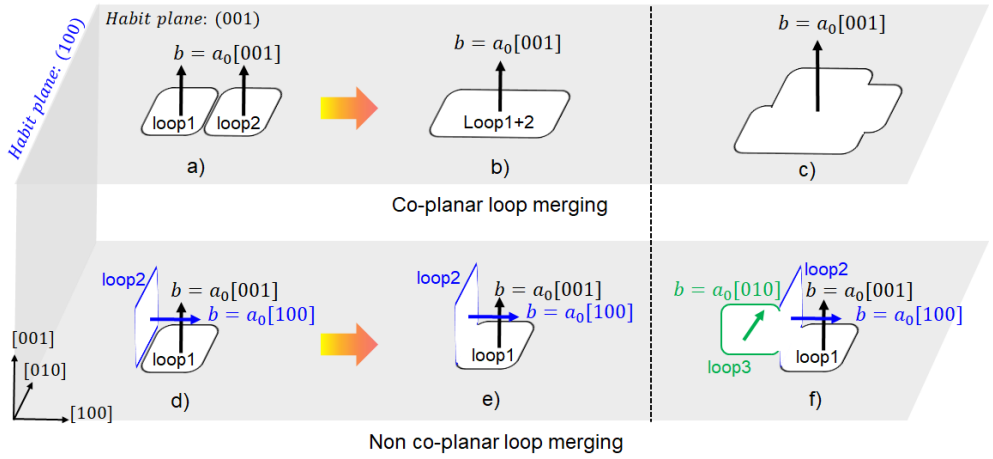

Figure 4-32: Schematic illustrations for (a) two coplanar <100> loops interacting along <010> direction, (b) a large <100> loop formed due to the merging of two similar coplanar <100> loops and (c) an irregular large loop formed due to the merging of several coplanar <100> loops. Schematic illustrations (d-f) present non-coplanar loops interaction and merging scenarios, leading to the formation of three-dimensional (3D) structures [161].

Finally, in accordance with our previously reported bulk PIA results [126], present thick-foil annealing experiments confirm appreciable recovery of the irradiation-induced dislocation loops and their transition into dislocation lines/tangles. However, to explain near complete recovery of mechanical properties of irradiated EUROFER97, understanding the evolution of other irradiation-induced defects such as Cr-enriched clusters upon PIA is mandatory. This requires post-irradiated annealed samples to be characterized via techniques such atom-probe tomography (APT), which should be planned for future.

4.4.5 Summary

In summary, thick-foil annealing investigations on neutron-irradiated EUROFER97 were carried out at 550 °C to delineate various loop annealing kinetics phenomena. In general, PIA results in dislocation loop shrinkage/annihilation as well as their coarsening/merging phenomena. This altogether leads to the reduction of the initial dislocation loop density with a simultaneous increase in their mean size. Clear coarsening of the irradiation-induced quasi-circular <100> loops into their rectilinear versions occurs by a non-conservative climb process. This includes emission of vacancies and alignment of incoming neighbouring atoms along loops lowest energy directions (i.e. <100>). In such a manner, quasi-circular loop reduces its

curvature (dislocation line tension) and peripheral jogs concentration, which can be perceived in terms of the movement of jogs towards one end of the loop side. As loops coarsen, they interact as well as merge to form larger loops of various geometries. The post-merging geometries depend on the merging-loops Burgers vectors, sizes and numbers. With continued annealing, the merged-loops structures will further evolve into complicated geometries and the complex situation of merging and/or annihilation will lead to the development of dislocation tangles.

Finally, in contrast to the previously reported thin-foil annealing results [148], where due to the strong surface effects only dislocation loop shrinkage phenomenon was observed, present thick-foil annealing investigations complement and provide complete description of the dislocation loop annealing behaviour in neutron-irradiated EUROFER97. The observed microstructural recovery explains the partial recovery of mechanical properties upon PIA in terms of dislocation loop evolution and will help in designing annealing procedures for similar neutron-irradiated materials/components.

4.5 Correlation of microstructural and mechanical properties of neutron-irradiated EUROFER97 steel

This section summarizes the results of TEM quantitative analysis of radiation-induced defects in the as-irradiated condition and post-irradiation annealed conditions. Moreover, the dispersed barrier hardening (DBH) model was used to correlate the microstructural and mechanical properties of neutron-irradiated EUROFER97 steel. Emphasis was put on studying the effect of thermal evolution of irradiation-induced defects on the recovered mechanical properties.

4.5.1 Summary of quantitative analysis of radiation-induced defects

4.5.1.1 Dislocation loops

As revealed by WBDF analysis in section 4.4.4, PIA thick-foil at 550 °C for 1 hour resulted in dislocation loop shrinkage/annihilation, coarsening/merging and dislocation lines/tangles formation. For the quantitative analysis of dislocation loop evolution at 550 °C for 2 and 3 hours, WBDF technique (reflection {002} and {110}) was further applied to access loop density and mean size. Figure 4-33(a-d) shows the representative microstructure imaged under g = {002} diffraction condition before and after PIA at three isothermal annealing time points (1, 2 and 3 hours). Since the majority of loops under selected diffraction conditions show edge-on contrast, the major axis of these edge-on loops was taken as a measure of their size. Additionally, the

corresponding loop size distribution obtained via WBDF investigations (as presented Figure 4-34) indicates that the increase of loop mean size (shift of size distribution) is accompanied with the reduction of smaller loops as well as the increase of the larger loops. This confirms the continuous coarsening of dislocation loops for longer annealing time at 550 °C.

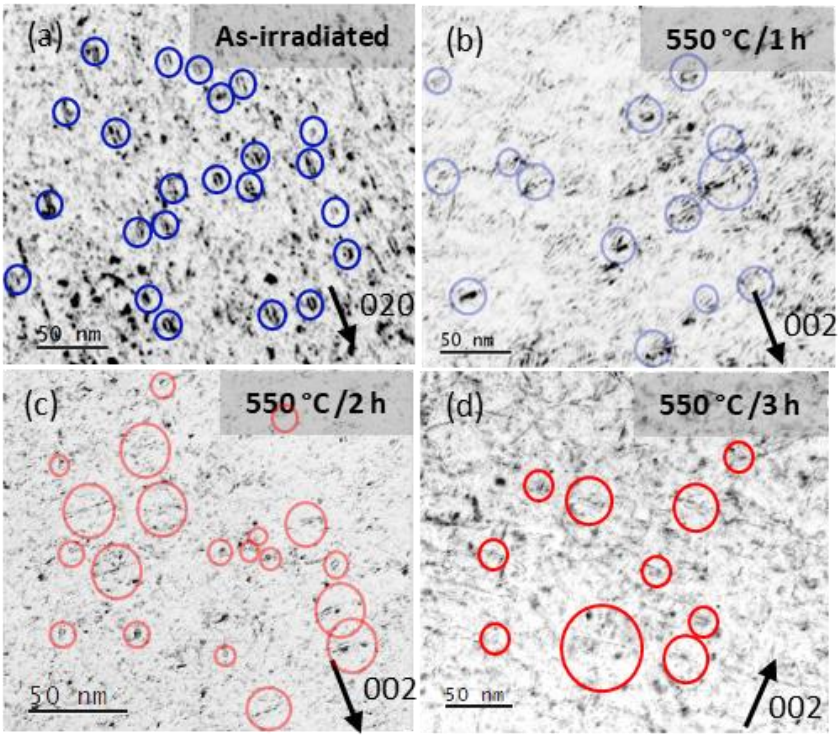

Figure 4-33: Inverted contrast TEM-WBDF micrographs at four different conditions in thick-foils: (a) as-irradiated condition (15 dpa, 330 °C), (b) PIA thick-foils at 550 °C for 1 hour, (c) PIA thick-foils at 550 °C for 2 hours and (d) PIA thick-foils at 550 °C for 3 hours. All the represented micrographs are taken under g={002} condition.

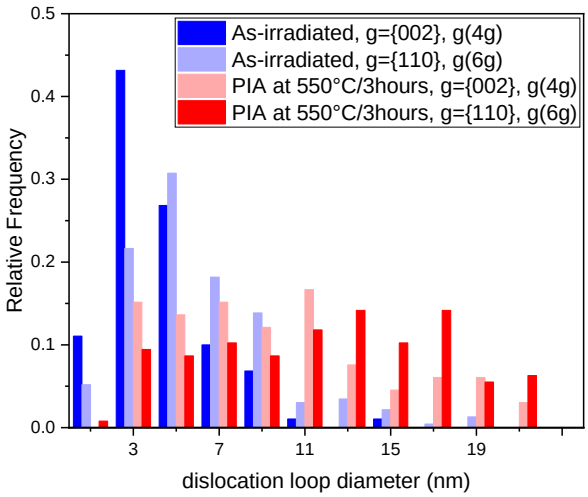

Figure 4-34: Dislocation loop size distributions for the WTZ irradiated and post-irradiation annealed (550 °C/ 3h) EUROFER97 steel (from section 4.4). A clear reduction in dislocation loop density and distribution shift towards higher size is apparent after annealing at 550 °C/ 3h.

Figure 4-35 summarizes the statistics of two types of dislocation loops based on the WBDF analysis. In general, a gradual reduction of the total loop density and increase of loop mean size is apparent upon PIA at 550 °C and such evolution continued with increasing annealing time. Moreover, by applying the loop invisibility criteria and the statistical method for Burgers vector determination [31], the density and mean size for both type loops are presented in Figure 4-35a and Figure 4-35b respectively.

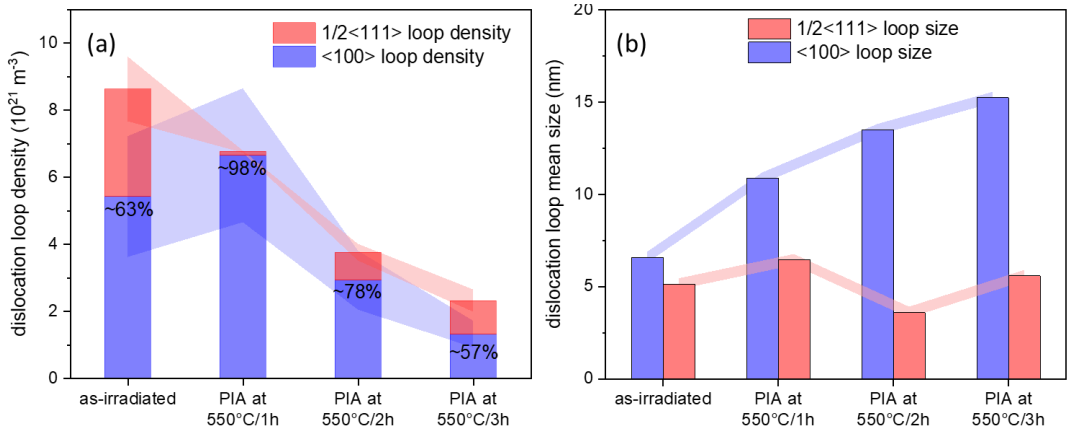

Figure 4-35: Summary of (a) dislocation loop density (with <100> loop fraction) and (b) loop size evolution in as-irradiated (15 dpa, 330 °C) and three different PIA conditions at 550 °C. Statistics of ½<111> loops are presented in red shaded area of the stacked columns whilst that of <100> loops are presented in the blue shaded area of the stacked columns.

It is noteworthy that the density of <100> loops initially increased after PIA at 550 °C for 1 hour. This slight increase of <100> loop density might be attributed to the shear reaction of two ½<111> loops which consequently leads to the formation of <100> loops [49]. On the other hand, both ½<111> loops shear reactions and their fast shrinkage [108] result in the reduction of ½<111> loop density. In addition, simulations also predict that <100> loops can be formed direct from C15 clusters at comparably high temperature [164]. However, such abovementioned phenomena mainly prevailed at the initial stage of annealing, i.e. at 550 °C for ~1 hour. With continued annealing (up to 3 hours), <100> loops start to merge and form complicated dislocation microstructure such as dislocation networks and line dislocations which as a result leads to a gradual reduction of their density [161].

Another interesting aspect to notice is that the <100> loop fraction after 2- and 3-hours isothermal annealing is ~78% and ~57% respectively. As some of the large <100> loops continue to grow and merge with increasing annealing time at 550 °C, only some segments of these loops were identified in the TEM micrographs due to the FIB cutting procedures. These segments are in general shown as line dislocation features and are typically excluded in the

loops quantitative analysis and hence, leads to a certain underestimation of <100> loop fraction and also density.

Table 4-6 summaries the dislocation loop density and mean size before and after PIA at 550 °C for 3 hours obtained via WBDF technique, including the statistics of both thick-foil post-irradiation annealed and bulk post-irradiation annealed EUROFER97 steel. Although an appreciable reduction of loop density after PIA is evident, quantitatively, there is almost no difference in the loop density between 3 hours' thick-foil and bulk PIA at 550 °C. Nevertheless, the increase of dislocation loop mean size in the thick-foil EUROFER97 steel after PIA at 550 °C for 3 hours is more obvious than that in the bulk one. Such discrepancy is associated with the different <100> loop fraction in both cases. For the bulk post-irradiation annealed EUROFER97, the <100> loop fraction is ~48% [126] which is lower than that in the thick-foil under the same annealing condition (~57%). Furthermore, as presented in Figure 4-35b, <100> loop mean size undergo a gradual increase upon PIA, whereas the change of the size of their ½<111> counterparts almost remain unchanged.

Table 4-6: Summary of quantitative data of the dislocation loops in the WTZ irradiated (15 dpa, 330 °C) and post-irradiation annealed (550 °C/1,2 and 3h) EUROFER97 samples.

Conditions	**Total loop density (x 10^{21} m^{-3})**	**Loop mean size (nm)**	**<100> loop fraction (%)**	**Ref.**
WTZ irradiated (15 dpa, 330 °C)	~8.6	~7.1	~63	[108]
WTZ PIA (thick-foil) 550 °C/1h	~6.8	~10.4	~98	[161]
WTZ PIA (thick-foil) 550 °C/2h	~3.8	~9.21	~78	This section
WTZ PIA (thick-foil) 550 °C/3h	~2.3	~12.4	~57	This section
WTZ PIA (bulk) 550 °C/3h	~2	~8	~48	[126]

4.5.1.2 Cavities

As demonstrated in section 4.1, post-irradiation annealing EUROFER97 steel (bulk material) at 550 °C for 3 hours leads to an appreciable cavities coarsening with their density reduction and mean size increment. Here, similar investigations were also carried out on the annealed thick-foils after 1, 2 and 3 hours isothermal annealing at 550 °C (see section 4.4). Cavities in these samples also exhibit nonuniform distribution, as both cavity-rich areas and cavity-free areas were observed in as-irradiated samples (see section 4.1.3). Therefore, quantitative analysis

of cavities evolution was only carried out on cavity-rich areas as presented in Figure 4-36. As evident, local cavities size distribution shifts towards higher size with an increment of mean size up to 2 hours' annealing at 550 °C. In addition, there is no obvious difference of cavities size distribution between 2 and 3 hours' annealing except for a small increment in their mean size. Noticeably, several merged cavities with irregular shape (marked in Figure 4-36d and g) were identified in both samples after 2 and 3 hours PIA. Nevertheless, such merged cavities were not commonly observed in the as-irradiated samples (see Figure 4-5ab).

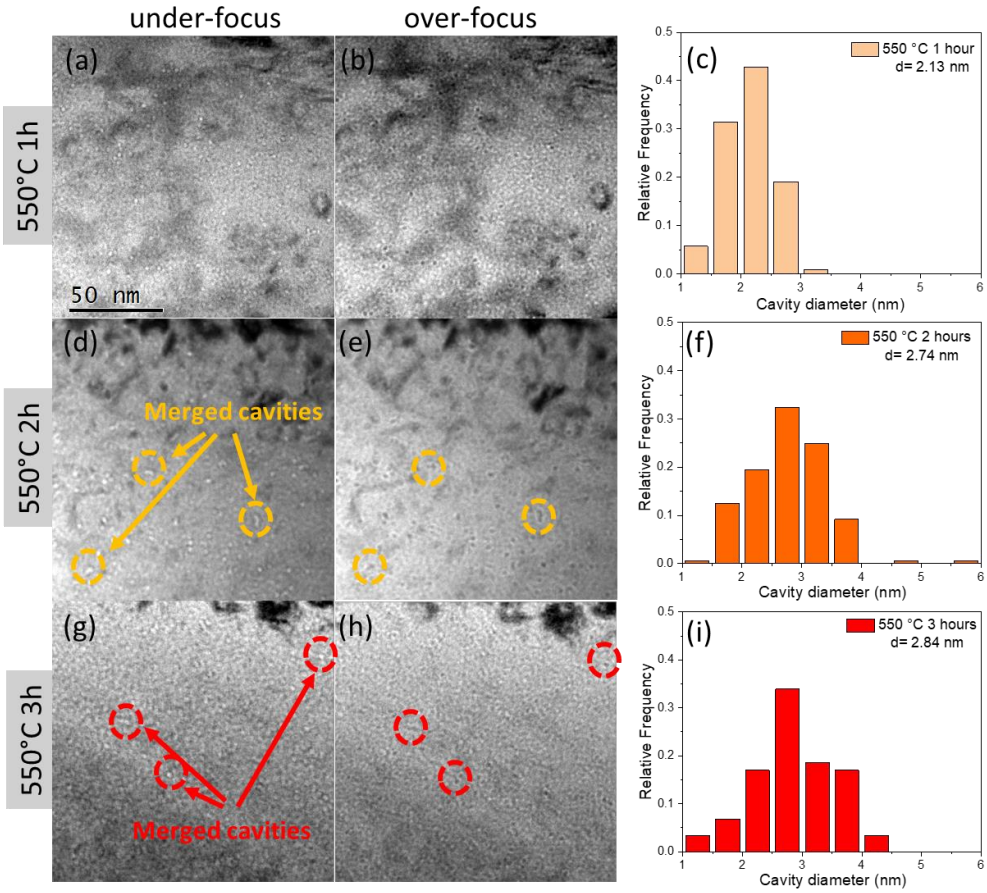

Figure 4-36: Typical BF-micrographs present cavity distribution in a (a, b) PIA 550 °C/ 1h, (d, e) PIA 550 °C/1h and (g, h) PIA (550 °C/3h) EUROFER97 samples. (a/d/g) taken at under-focus -1.5 µm condition and (b,e,h) at over-focus +1.5 µm condition). Cavities size distribution along with their average size d for the three PIA conditions is shown in (c,f,i). Some merged cavities with irregular shape are identified after 2 and 3 hours PIA at 550 °C.

As evident, the mean size of cavities (d=2.8 nm) under 3 hours' annealing in thick-foils agrees well to that (d=2.9 nm) under 3 hours' annealing in the bulk materials (see section 4.1.3). From the mean size viewpoint, this reconfirms the cavity coarsening after PIA. However, such coarsening phenomenon is in general not observed in the in-situ TEM thin-foil annealing experiments (see section 4.3). The discrepancy between the cavity shrinkage/annihilation

during thin-foil annealing and growth/coarsening in the thick-foils as well as in the bulk materials annealing is analogous to the dislocation loop scenario. The emitted vacancies from the shrunk cavities as observed in section 4.2.3, for instance, can reach free surfaces before being absorbed by any other sinks during thin-foil annealing experiments. However, in the case of bulk materials where the surface effect can be neglected, these emitted vacancies can either be absorbed by their neighboring cavities (in cavity-rich areas) and/or contribute to the shrinkage of interstitial type dislocation loops. In addition, it is noteworthy that the presence of other sinks such as line dislocations, grain boundaries around cavity-rich areas can also consume the emitted vacancies during PIA.

4.5.2 Effect of radiation-induced dislocation loops on hardening

Previous study from Weiss et al. [67] estimated the hardening contributed by dislocation loops (calculated by Equation 2-5) to 252 MPa for neutron-irradiated EUROFER97 steel (15 dpa/ 330 °C). It should be noticed that their calculation is primarily based on following assumptions:

- The obstacle strength factor for both loop types at the corresponding temperature is 0.6. In other words, <100> and ½<111> loops have the same obstacle strength for mobile dislocation.
- Black dots are also considered in the quantitative analysis of dislocation loops; and hence, defects density (dislocation loops + black dots) is higher than the current study whereas their mean size is lower as the size of black dots features are usually less than 2 nm.

As the fraction of <100> loops in the as-irradiated condition is more than 50 % [108], it is essential to distinguish the hardening contributions from both type of loops. According to a parametric study by Lambrecht et al. [165], a quadratic superposition law like

$$\Delta\sigma_{tot(loop)} = \sqrt{\Delta\sigma_{\frac{1}{2}<111>loop}{}^2 + \Delta\sigma_{<100>loop}{}^2} \qquad \text{Equation 4-4}$$

was used to taken into account the contributions of ½<111> loops ($\Delta\sigma_{\frac{1}{2}<111>loop}$) and <100> loops ($\Delta\sigma_{<100>loop}$). Combining Equation 2-5 and Equation 4-4, the hardening model using the root-sum-square superposition can be written as

$$\Delta\sigma_{tot(loop)} = M\mu b\sqrt{\alpha^2_{\frac{1}{2}<111>} N_{\frac{1}{2}<111>} d_{\frac{1}{2}<111>} + \alpha^2_{<100>} N_{<100>} d_{<100>}} \qquad \text{Equation 4-5}$$

where the Taylor factor *M* for BCC materials is 3.06 [166]; the magnitude of the Burgers vector of the moving dislocation b is 0.249 (assuming all dislocations have a Burgers vector of the

type ½<111> [167]); lattice parameter of BCC iron, $a_0 = 0.288\,nm$ [67]; the shear modulus was taken from the Fe-10Cr model alloys at a temperature of 300 °C (μ=75.3 GPa) [168]; obstacle strength of the defects α for ½<111> loops is 0.17 whilst for <100> loops is 0.33 [169] without considering the alloying elements decoration. Additionally, the values of loop density and mean size for both type of loops are separately calculated by statistic method.

Table 4-7: Calculation of radiation-induced dislocation loop strengthening based on obstacle strengthening model.

Condition	Loop type	Density (10^{21}/m^3)	mean size (nm)	Strengthening (MPa)	Total strengthening (MPa)
as-irradiated	1/2<111> loop	3.21	5.1	40.3	120.1
	<100> loop	5.42	6.6	113.2	
PIA at 550°C/1h	1/2<111> loop	0.11	6.5	8.3	161.5
thick-foil	<100> loop	6.65	10.9	161.2	
PIA at 550°C/2h	1/2<111> loop	0.83	3.6	16.9	120.4
thick-foil	<100> loop	2.93	13.5	119.3	
PIA at 550°C/3h	1/2<111> loop	1.00	5.6	23.1	88.1
thick-foil	<100> loop	1.32	15.2	85.0	
PIA at 550°C/3h	1/2<111> loop	1.04	2.5	13.6	71.0
Bulk material	<100> loop	0.96	13.9	59.3	

Table 4-7 summarizes the strengthening contributed by ½<111> and <100> type dislocation loops under different conditions in the neutron-irradiated EUROFER97 steel. The calculated total strengthening contributed by loops in the as-irradiated condition is 120.1 MPa, which is about half of the value calculated by previous study (252 MPa [67]) in which the black dots are also counted as dislocation loops. In this work, only loop contrast microstructure is considered for all investigated conditions. Furthermore, the used strength factors for both types of loops are lower than that used in the previous study. It is noteworthy that the value of total strengthening after 1 hour's PIA at 550 °C is even higher than that in the as-irradiated condition. From dislocation loop microstructure viewpoint, though the total loop density decreases, the density of <100> loops as well as their mean size increased, which overall leads to the higher strengthening. In addition, as <100> loops are typically considered stronger barrier to dislocation motion than their ½<111> counterparts in accordance with the superposition rule

(obstacle strength of the defects α for ½<111> loops is 0.17 whilst for <100> loops is 0.33) [169].

Indeed, <100> loops play significant role during the whole span of PIA. As mentioned in section 4.4.2, at the initial stage of PIA at 550 °C (about 1 hour), <100> loops primarily undergo a coarsening process via emitting vacancies or accepting SIAs before they merge with neighbouring loops. With continued annealing time, many <100> loops start to merge in a coplanar and non-coplanar fashion which in the end form extended line dislocations or segments of dislocation networks. In comparison to loops, these extended dislocation segments will be a relatively weak obstacle for mobile dislocations. Moreover, these segments could also annihilate upon interacting with mobile dislocations, which will also lead to the material's softening. Eventually, merely considering the contribution from dislocation loops, 3 hours' PIA at 550 °C of bulk materials gives rise to ~41% reduction of the total strengthening.

4.5.3 Effect of black dots on hardening

Black dot, as its name describes, shows black dots features under TEM and is known to be important factor that contributes to the hardening. These nano-sized features are homogenously distributed in the matrix in the as-irradiated condition (for example see Figure 4-2a) and are typically less than 2 nm, which makes their size determination difficult via TEM investigation. Figure 4-37 shows representative magnified micrographs imaged via HAADF-STEM technique which contains black dots features before and after PIA (550 °C/3h). As evident, corresponding PIA leads to a noticeable reduction of black dots density (black dots features are marked with red circles and blue triangles). Moreover, most black dots are no longer isolated and appear to be integrated/decorated on the line dislocations during the formation of dislocation networks at elevated temperature. Though a discernible determination of their size evolution is statistically inaccessible via STEM, there is about 80% reduction of their density after PIA based on the quantitative analysis. Assuming that the size and obstacle strength factor of black dots remains the same after PIA and black dots are all of ½<111> type dislocation loops, such amount of density reduction leads to ~55% reduction of the black dots induced strengthening estimated by hardening model.

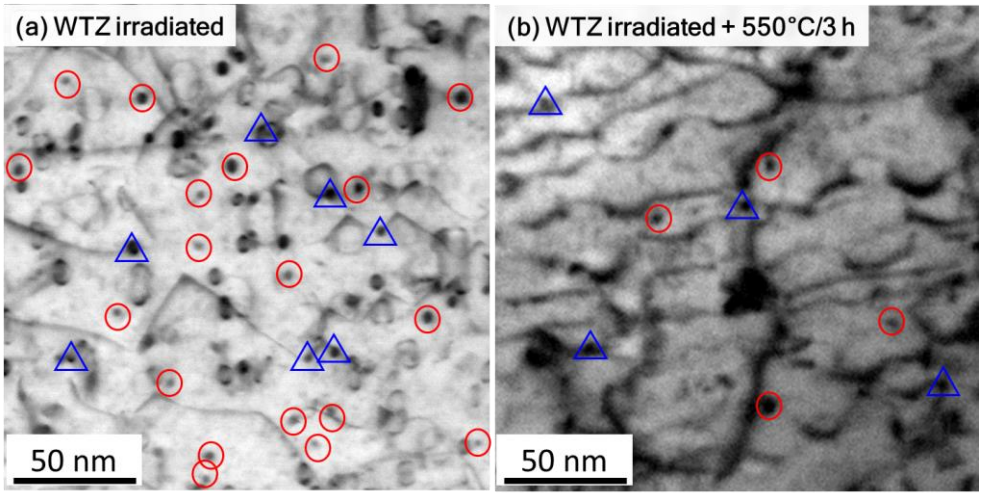

Figure 4-37: Inverted-contrast HAADF-STEM micrographs taken close to the <110> zone-axis orientations present a representative microstructure of a (a) WTZ irradiated (15 dpa, 330 °C) and (b) subsequently annealed (550 °C/3h) bulk EUROFER97 samples. Several isolated defects show black dot features and are marked with red circles whereas defects marked with blue triangles appears to be incorporated on the dislocation loops and/or dislocation lines/ networks. ((b) is adapted from [126])

It should be mentioned that due to the limitations of characterizing techniques, the influence of alloy elements decorations on the black dots as well as dislocation loops is excluded in the hardening estimation. However, as revealed by the atom probe tomography (APT) investigations [132], Cr, Mn and other alloying elements indeed segregated at different parts of the loops (black dots). Therefore, the effects of alloying elements segregations on the obstacle strength factors (α) of dislocation loops, black dots and α' precipitates should be clarified by the correlative APT investigations as well as dedicated atomistic modelling.

4.5.4 Summary

In summary, estimations based on DBH model shows that the contribution from pure dislocation loop evolution on the recovery of the mechanical property due to PIA (550 °C/ 3h) on EUROFER97 steel is ~41% where the alloying elements segregation on the loops is not considered herein. Similarly, the significant reduction of the black dots density is also responsible for the substantial recovery of hardening in neutron-irradiated EUROFER97 steel. However, current TEM cannot determine the chemical composition of the nanometre-sized dislocation loops and black dots, which requires further APT investigations. Moreover, the measured cavity density in this work is about one order of magnitude lower than that of dislocation loops and black dots. In addition, their densities could be overestimated due to their inhomogeneous distribution. Therefore, the contribution of cavities evolution on the recovery of hardening is not carried out. Nevertheless, the observed shrinkage of cavities during PIA alters the local vacancy concentration and thus promotes the overall microstructure evolution.

Chapter 5 Conclusions and perspectives

The main objective of this work is to understand how neutron irradiation-induced defects in the European reduced-activation ferritic martensitic steel EUROFER97 evolves upon post-irradiation annealing so as to explain how nearly complete recovery of the mechanical properties transpired. Emphasis was put on the analysis of temperature effects on radiation-induced dislocation loops and cavities evolution and corresponding annealing kinetics via in-situ TEM investigations. Considering the unicity and difficulty in characterizing complicated radioactive materials, particularly at elevated temperatures, in-situ TEM annealing experiments were carried out in the hot cell of Fusion Materials Laboratory at Karlsruhe Institute of Technology. In-situ TEM experiments herein were designed to directly observe the evolution of radiation-induced defects and elucidate their responsible annealing kinetics whereas the TEM experiments on bulk-annealed samples were conceptualized for providing unbiased statistics of defects analysis.

In the first step, systematic TEM investigations reconfirmed the status of dislocation loops in the as-irradiated EUROFER97 (15 dpa, 330 °C) samples prepared via focused-ion beam polishing, including loops of an interstitial nature, Burgers vector (a_0/2<111>and a_0<100>), quasi-circular shape, density and size distribution. Both WBDF and STEM-HAADF techniques confirmed high density of uniformly distributed dislocation loops and black dots in the as-irradiated condition, which provided a solid statistical base for further in-situ TEM investigations. In addition, the statistics of cavities were also substantially improved compared with early works. Nevertheless, in contrast to dislocation loops and black dots, the density of cavities was found to be lower and their distribution was inhomogeneous.

The defects annealing kinetics were revealed by in-situ TEM experiments, including thermal ramping and isothermal annealing tests. The shrinkage of dislocation loops and cavities were directly observed at elevated temperature via (K)BF/WBDF imaging techniques, which was mainly linked to the vacancy-mediated diffusion process. For the dislocation loop, the vacancy flux occurring down the concentration gradient essentially determines the annealing behaviour of dislocation loops. Due to the curvature force, loops shrink faster at smaller size. Nonetheless, loops alloying elements decorations and the spontaneous neighbouring defects evolution further dictates the annealing kinetics of dislocation loops. For isolated loops, in addition to their

curvature force, the incoming vacancy flux generated by the local vacancy supersaturation contributes to loops faster shrinkage. On the other hand, the shrinkage of some loops in the population are strongly retarded owing to the competition of required vacancies by other loops and/or defects. Furthermore, <100> type loops are found sessile and shrank significantly slower than ½<111> loops. Also, in the near proximity of <100> type loops, some small ½<111> loops appeared to be absorbed due to their elastic interaction. This partially explains the reduction of ½<111> loop fraction after PIA. For cavities, their shrinkage is predominantly governed by the vacancy emission. Simulation based on rate theory indicates the emission rate of vacancy is strongly influenced by the He/Vac ratio. Additionally, the emitted vacancies from the cavities promotes the local vacancy supersaturation.

Significant loop coarsening was also revealed and further confirmed by TEM investigations on both bulk and thick-foils annealing experiments. Loop coarsening process is accompanied with loop shrinkage/annihilation process, both of which leads to loop density reduction and mean size increase. At the initial stage upon isothermal annealing at 550 °C, apparent growth of the quasi-circular <100> loops into their rectilinear versions occurs by a non-conservative climb process. Afterwards, loops start to merge and form larger loops with a variety of geometries, which depends on the merging-loops Burgers vector, size and numbers. With continued annealing till 3 hours, dislocation networks/tangles were eventually formed by the further evolution of large merged-loops with more or less complicated geometries.

The quantitative TEM investigations complete the PIA study and provide good statistics for the correlation of microstructural and mechanical properties. The observed dislocation microstructure evolution partially explains the recovery of hardening upon post-irradiation annealing. In addition, black dots are believed to substantially contribute to the recovery owing to significant reduction of their density. Nevertheless, their contribution to the overall microstructure evolution during PIA remains unclear. In addition, some small defects that are beyond TEM's resolution such as CrMn-rich clusters, might also contribute to the recovery of hardening. Therefore, some suggestions are proposed for future works as follows.

As the density of black dots in the current investigated material is even higher than that of dislocation loops, it is necessary to understand their nature and composition in the future work. It is reasonable to assume some of the black dots are small ½<111> type dislocation loops as ½<111> type loops are typically smaller than <100> type loops [126]. Nevertheless, this conjecture should be verified and confirmed via high-resolution (HR) TEM. Moreover, a bigger challenge is to obtain quantitative information of such high density of black dots by time-

consuming HR-TEM. Another assumption of the composition of the black dots is that some of them can be alloying elements clusters, which present 2D disc-shape contrast under TEM. Indeed, APT has already revealed that high density population of CrMn-rich spherical clusters are present in neutron-irradiated EUROFER97 [132]. Furthermore, in addition to the dislocation loops and CrMn-rich clusters, some fraction of these black dots features can also be FIB damages, which are produced during final polishing processes. To further exclude such effect, Helios 5 PFIB (Plasma-FIB) DualBeam from Thermo Fisher Scientific, for instance, can be applied to produce high quality TEM lamellae. Since PFIB is equipped with a new column, which enables low energy Xe+ final polishing, the damages can be eliminated to a larger extent.

Once the black dots are identified, the second question would be their role in the thermal annealing process. The difficulty is to know where the alloying elements segregate on the black dots and/or dislocation loops. It is occasionally observed in the current study that some large loops stopped their shrinkage at smaller size and eventually presented black dots feature under TEM. This could be attributed to the alloying elements segregation on the core of black dots which eventually prevents their further shrinkage. However, to achieve direct experimental evidence, dedicated in-situ high-resolution STEM technique is required. Nonetheless, correlative APT investigations would be a possible solution to understand CrMn-rich cluster evolution after PIA. More analytical investigations are required to determine what these nano-sized features are and understand how they influence the microstructure evolution. Furthermore, for cavities, EELS investigations are required to study the state of He in the cavities. In addition, in-situ EELS investigations are required to provide experimental evidence of the statement that higher He/Vac ratio retards the vacancy emission rate of the shrunk cavity. As the information of dislocation loops during the whole span of PIA is available, simulation based on rate theory can be applied to reproduce the microstructure evolution during PIA and confirm the proposed mechanisms.

Publications list

Following publications are from this dissertation:

Ref. [108] Q. Yuan, A. Chauhan, E. Gaganidze, J. Aktaa, In-situ TEM investigations of dislocation loop annealing kinetics in neutron-irradiated 9% Cr RAFM steel, Journal of Nuclear Materials, 558 (2022) 153365.

Ref. [126] A. Chauhan, Q. Yuan, C. Dethloff, E. Gaganidze, J. Aktaa, Post-irradiation annealing of neutron-irradiated EUROFER97, Journal of Nuclear Materials 548 (2021) 152863.

Ref. [148] Q. Yuan, A. Chauhan, E. Gaganidze, J. Aktaa, Direct observation of dislocation loop shrinkage upon annealing neutron-irradiated Fe-9Cr alloy, Journal of Nuclear Materials 542 (2020) 152401.

Ref. [149] J. Gao, Q. Yuan, E. Gaganidze, J. Aktaa, On the shrinkage of neutron irradiation-induced cavities in Eurofer97 steel upon heating, Philosophical Magazine (2022) 1-26.

Ref. [161] Q. Yuan, A. Chauhan, E. Gaganidze, J. Aktaa, Dislocation loop coarsening and shape evolution upon annealing neutron-irradiated RAFM steel, Journal of Nuclear Materials 558 (2022) 153366.

References

[1] IEA- International Energy Agency, online, https://www.iea.org/fuels-and-technologies/nuclear.

[2] ITER Organization, online, https://www.iter.org/proj/inafewlines.

[3] G. Federici, L. Boccaccini, F. Cismondi, M. Gasparotto, Y. Poitevin, I. Ricapito, An overview of the EU breeding blanket design strategy as an integral part of the DEMO design effort, Fusion Engineering and Design, 141 (2019) 30-42.

[4] G. Federici, W. Biel, M. Gilbert, R. Kemp, N. Taylor, R. Wenninger, European DEMO design strategy and consequences for materials, Nuclear Fusion, 57 (2017) 092002.

[5] S.J. Zinkle, J.T. Busby, Structural materials for fission & fusion energy, Materials today, 12 (2009) 12-19.

[6] E. Gaganidze, J. Aktaa, Assessment of neutron irradiation effects on RAFM steels, Fusion Engineering and Design, 88 (2013) 118-128.

[7] E. Gaganidze, H.-C. Schneider, B. Dafferner, J. Aktaa, High-dose neutron irradiation embrittlement of RAFM steels, Journal of Nuclear Materials, 355 (2006) 83-88.

[8] E. Gaganidze, H.-C. Schneider, C. Petersen, J. Aktaa, A. Povstyanko, V. Prokhorov, R. Lindau, E. Materna-Morris, A. Möslang, E. Diegele, R. Lässer, B. Van der Schaaf, E. Lucon, Mechanical properties of reduced activation ferritic/martensitic steels after high dose neutron irradiation, Proceedings of 22nd IAEA Fusion Energy Conference, Geneva, Switzerland, October 13–18, 2008, FT/P 2-1.

[9] M.R. Gilbert, K. Arakawa, Z. Bergstrom, M.J. Caturla, S.L. Dudarev, F. Gao, A. Goryaeva, S. Hu, X. Hu, R.J. Kurtz, Perspectives on multiscale modelling and experiments to accelerate materials development for fusion, Journal of Nuclear Materials, 554 (2021) 153113.

[10] L. Malerba, G. Ackland, C. Becquart, G. Bonny, C. Domain, S.L. Dudarev, C.-C. Fu, D. Hepburn, M.-C. Marinica, P. Olsson, Ab initio calculations and interatomic potentials for iron and iron alloys: Achievements within the Perfect Project, Journal of Nuclear Materials, 406 (2010) 7-18.

[11] K. Nordlund, Historical review of computer simulation of radiation effects in materials, Journal of Nuclear Materials, 520 (2019) 273-295.

[12] N. Soneda, T. Diaz de La Rubia, Migration kinetics of the self-interstitial atom and its clusters in bcc Fe, Philosophical Magazine A, 81 (2001) 331-343.

[13] C. Domain, C. Becquart, L. Malerba, Simulation of radiation damage in Fe alloys: an object kinetic Monte Carlo approach, Journal of Nuclear Materials, 335 (2004) 121-145.

[14] C. Dethloff, E. Gaganidze, V.V. Svetukhin, J. Aktaa, Modeling of helium bubble nucleation and growth in neutron irradiated boron doped RAFM steels, Journal of nuclear materials, 426 (2012) 287-297.

[15] A. Gokhman, F. Bergner, Cluster dynamics simulation of point defect clusters in neutron irradiated pure iron, Radiation Effects and Defects in Solids, 165 (2010) 216-226.

[16] M. Jenkins, Characterisation of radiation-damage microstructures by TEM, Journal of Nuclear Materials, 216 (1994) 124-156.

[17] M. Klimenkov, A. Möslang, E. Materna-Morris, H.-C. Schneider, Helium bubble morphology of boron alloyed EUROFER97 after neutron irradiation, Journal of Nuclear Materials, 442 (2013) S52-S57.

[18] M. Klimenkov, P. Vladimirov, U. Jäntsch, V. Kuksenko, R. Rolli, A. Möslang, N. Zimber, New insights into microstructure of irradiated beryllium based on experiments and computer simulations, Scientific Reports, 10 (2020) 1-17.

[19] W. Jesser, J. Horton, L. Scribner, Adaptation of an ion accelerator to a high voltage electron microscope, Radiation Effects, 29 (1976) 79-82.

[20] A. Taylor, J.R. Wallace, E.A. Ryan, A. Philippides, J.R. Wrobel, In situ implantation system in Argonne national laboratory Hvem-tandem facility, Nuclear Instruments and Methods in Physics Research, 189 (1981) 211-217.

[21] S. Furuno, K. Hojou, H. Otsu, T.A. Sasaki, K. Izui, T. Tsukamoto, T. Hata, System for in situ observation and chemical analysis of materials during dual-ion beam irradiation in an electron microscope, Microscopy, 41 (1992) 273-276.

[22] K. Arakawa, M. Hatanaka, E. Kuramoto, K. Ono, H. Mori, Changes in the burgers vector of perfect dislocation loops without contact with the external dislocations, Physical Review Letters, 96 (2006) 125506.

[23] Y. Li, G. Ran, Y. Guo, Z. Sun, X. Liu, Y. Li, X. Qiu, Y. Xin, The evolution of dislocation loop and its interaction with pre-existing dislocation in He+-irradiated molybdenum: in-situ TEM observation and molecular dynamics simulation, Acta Materialia, 201 (2020) 462-476.

[24] B. Burton, Theoretical analysis of annealing behaviour of mixed distributions of dislocation loops, voids, and gas bubbles: comparison with annealing behaviour of irradiated reactor component, Materials Science and Technology, 8 (1992) 602-610.

[25] P. Derlet, S. Dudarev, Microscopic structure of a heavily irradiated material, Physical Review Materials, 4 (2020) 023605.

[26] Z. Yao, M.L. Jenkins, M. Hernandez-Mayoral, M.A. Kirk, The temperature dependence of heavy-ion damage in iron: A microstructural transition at elevated temperatures, Philosophical Magazine, 90 (2010) 4623-4634.

[27] M. Klimenkov, U. Jäntsch, M. Rieth, A. Möslang, Correlation of microstructural and mechanical properties of neutron irradiated EUROFER97 steel, Journal of Nuclear Materials, 538 (2020) 152231.

[28] T.S. Byun, J.-H. Baek, O. Anderoglu, S.A. Maloy, M.B. Toloczko, Thermal annealing recovery of fracture toughness in HT9 steel after irradiation to high doses, Journal of Nuclear Materials, 449 (2014) 263-272.

[29] H. Watanabe, S. Masaki, S. Masubuchi, N. Yoshida, Y. Kamada, Radiation induced hardening of ion irradiated RPV steels, Journal of Nuclear Materials, 417 (2011) 932-935.

[30] A. Tavassoli, Assessment of austenitic stainless steels, Fusion Engineering and Design, 29 (1995) 371-390.

[31] T. Muroga, Vanadium alloys for fusion blanket applications, Materials Transactions, 46 (2005) 405-411.

[32] A. Iveković, S. Novak, G. Dražić, D. Blagoeva, S.G. de Vicente, Current status and prospects of SiCf/SiC for fusion structural applications, Journal of the European Ceramic Society, 33 (2013) 1577-1589.

[33] A. Möslang, E. Diegele, M. Klimiankou, R. Lässer, R. Lindau, E. Lucon, E. Materna-Morris, C. Petersen, R. Pippan, J. Rensman, Towards reduced activation structural materials data for fusion DEMO reactors, Nuclear Fusion, 45 (2005) 649.

[34] N. Baluc, R. Schäublin, P. Spätig, M. Victoria, On the potentiality of using ferritic/martensitic steels as structural materials for fusion reactors, Nuclear Fusion, 44 (2003) 56.

[35] U. Stamm, H. Schroeder, The influence of helium on the high temperature mechanical properties of DIN 1.4914 martensitic steel, Journal of Nuclear Materials, 155 (1988) 1059-1063.

[36] H. Tanigawa, E. Gaganidze, T. Hirose, M. Ando, S. Zinkle, R. Lindau, E. Diegele, Development of benchmark reduced activation ferritic/martensitic steels for fusion energy applications, Nuclear Fusion, 57 (2017) 092004.

[37] R. Lindau, A. Moslang, M. Rieth, M. Klimiankou, E. Materna-Morris, A. Alamo, A.A.F. Tavassoli, C. Cayron, A.M. Lancha, P. Fernandez, N. Baluc, R. Schaublin, E. Diegele, G. Filacchioni, J.W. Rensman, B. van der Schaaf, E. Lucon, W. Dietz, Present development status of EUROFER and ODS-EUROFER for application in blanket concepts, Fusion Engineering and Design, 75-79 (2005) 989-996.

[38] M. Gilbert, S. Dudarev, S. Zheng, L. Packer, J.-C. Sublet, An integrated model for materials in a fusion power plant: transmutation, gas production, and helium embrittlement under neutron irradiation, Nuclear Fusion, 52 (2012) 083019.

[39] G.S. Was, Fundamentals of Radiation Materials Science: Metals and Alloys, Springer New York, New York, NY, 2017, pp. 167-205.

[40] J. Harder, D. Bacon, The structure of small interstitial clusters in bcc metals modelled with N-body potentials, Philosophical Magazine A, 58 (1988) 165-178.

[41] J. Marian, B.D. Wirth, J.M. Perlado, Mechanism of formation and growth of < 100 > interstitial loops in ferritic materials, Physical Review Letters, 88 (2002) 255507.

[42] C.-C. Fu, F. Willaime, P. Ordejón, Stability and mobility of mono-and di-interstitials in α-Fe, Physical Review Letters, 92 (2004) 175503.

[43] F. Willaime, C. Fu, M. Marinica, J. Dalla Torre, Stability and mobility of self-interstitials and small interstitial clusters in α-iron: ab initio and empirical potential calculations, Nuclear Instruments and Methods in Physics Research Section B: Beam Interactions with Materials and Atoms, 228 (2005) 92-99.

[44] M. Kiritani, H. Takata, K. Moriyama, F.E. Fujita, Mobility of lattice vacancies in iron, Philosophical Magazine A, 40 (1979) 779-802.

[45] C.C. Fu, F. Willaime, First principles calculations in iron: structure and mobility of defect clusters and defect complexes for kinetic modelling, Comptes Rendus Physique, 9 (2008) 335-342.

[46] J. Beeler Jr, R. Johnson, Vacancy clusters in α-iron, Physical Review, 156 (1967) 677.

[47] B.D. Wirth, How does radiation damage materials?, Science, 318 (2007) 923-924.

[48] C. Dethloff, E. Gaganidze, J. Aktaa, Review and critical assessment of dislocation loop analyses on EUROFER 97, Nuclear Materials and Energy, 15 (2018) 23-26.

[49] B. Eyre, R. Bullough, On the formation of interstitial loops in bcc metals, Philosophical Magazine, 12 (1965) 31-39.

[50] B.D. Wirth, G.R. Odette, D. Maroudas, G.E. Lucas, Dislocation loop structure, energy and mobility of self-interstitial atom clusters in bcc iron, Journal of Nuclear Materials, 276 (2000) 33-40.

[51] D. Terentyev, L. Malerba, M. Hou, Dimensionality of interstitial cluster motion in bcc-Fe, Physical Review B, 75 (2007) 104108.

[52] K. Arakawa, K. Ono, M. Isshiki, K. Mimura, M. Uchikoshi, H. Mori, Observation of the one-dimensional diffusion of nanometer-sized dislocation loops, Science, 318 (2007) 956-959.

[53] H.X. Xu, R.E. Stoller, Y.N. Osetsky, D. Terentyev, Solving the Puzzle of < 100 > Interstitial Loop Formation in bcc Iron, Physical Review Letters, 110 (2013) 265503.

[54] Y. Zhang, X.-M. Bai, M.R. Tonks, S.B. Biner, Formation of prismatic loops from C15 Laves phase interstitial clusters in body-centered cubic iron, Scripta Materialia, 98 (2015) 5-8.

[55] R. Alexander, M.-C. Marinica, L. Proville, F. Willaime, K. Arakawa, M. Gilbert, S. Dudarev, Ab initio scaling laws for the formation energy of nanosized interstitial defect clusters in iron, tungsten, and vanadium, Physical Review B, 94 (2016) 024103.

[56] Q. Peng, F.J. Meng, Y.Z. Yang, C.Y. Lu, H.Q. Deng, L.M. Wang, S. De, F. Gao, Shockwave generates < 100 > dislocation loops in bcc iron, Nature Communications, 9 (2018) 4880.

[57] J. Chen, N. Gao, P. Jung, T. Sauvage, A new mechanism of loop formation and transformation in bcc iron without dislocation reaction, Journal of Nuclear Materials, 441 (2013) 216-221.

[58] F. Granberg, J. Byggmästar, A.E. Sand, K. Nordlund, Cascade debris overlap mechanism of< 100> dislocation loop formation in Fe and FeCr, EPL (Europhysics Letters), 119 (2017) 56003.

[59] H.X. Xu, R.E. Stoller, Y.N. Osetsky, D. Terentyev, Solving the Puzzle of < 100 > Interstitial Loop Formation in bcc Iron, Physical Review Letters, 110 (2013).

[60] N. Gao, Z.W. Yao, G.H. Lu, H.Q. Deng, F. Gao, Mechanisms for <100> interstitial dislocation loops to diffuse in BCC iron, Nature Communications, 12 (2021) 225.

[61] K. Yabuuchi, R. Kasada, A. Kimura, Effect of alloying elements on irradiation hardening behavior and microstructure evolution in BCC Fe, Journal of Nuclear Materials, 442 (2013) S790-S795.

[62] S. Xu, Z. Yao, M. Jenkins, TEM characterisation of heavy-ion irradiation damage in FeCr alloys, Journal of Nuclear Materials, 386 (2009) 161-164.

[63] D. Hone, Self-Diffusion in Liquid He, Physical Review, 121 (1961) 669-673.

[64] S. Porollo, A. Dvoriashin, A. Vorobyev, Y.V. Konobeev, The microstructure and tensile properties of Fe–Cr alloys after neutron irradiation at 400 C to 5.5–7.1 dpa, Journal of Nuclear Materials, 256 (1998) 247-253.

[65] K. Arakawa, M. Hatanaka, H. Mori, K. Ono, Effects of chromium on the one-dimensional motion of interstitial-type dislocation loops in iron, Journal of Nuclear Materials, 329 (2004) 1194-1198.

[66] C. Dethloff, E. Gaganidze, J. Aktaa, Microstructural defects in EUROFER 97 after different neutron irradiation conditions, Nuclear Materials and Energy, 9 (2016) 471-475.

[67] O.J. Weiss, E. Gaganidze, J. Aktaa, Quantitative characterization of microstructural defects in up to 32 dpa neutron irradiated EUROFER97, Journal of Nuclear Materials, 426 (2012) 52-58.

[68] Z. Jiao, S. Taller, K. Field, G. Yeli, M.P. Moody, G.S. Was, Microstructure evolution of T91 irradiated in the BOR60 fast reactor, Journal of Nuclear Materials, 504 (2018) 122-134.

[69] R. Schaeublin, D. Gelles, M. Victoria, Microstructure of irradiated ferritic/martensitic steels in relation to mechanical properties, Journal of Nuclear Materials, 307 (2002) 197-202.

[70] G.S. Was, Fundamentals of Radiation Materials Science: Metals and Alloys, Springer New York, New York, NY, 2017, pp. 669-733.

[71] B. Singh, A. Foreman, H. Trinkaus, Radiation hardening revisited: role of intracascade clustering, Journal of Nuclear Materials, 249 (1997) 103-115.

[72] R. Stoller, S. Zinkle, On the relationship between uniaxial yield strength and resolved shear stress in polycrystalline materials, Journal of Nuclear Materials, 283 (2000) 349-352.

[73] A. Seeger, Kristallphysik II / Crystal Physics II, Springer Berlin Heidelberg, Berlin, Heidelberg, 1958, pp. 1-210.

[74] A. Foreman, M. Makin, Dislocation movement through random arrays of obstacles, Canadian Journal of Physics, 45 (1967) 511-517.

[75] G. Odette, G. Lucas, Recent progress in understanding reactor pressure vessel steel embrittlement, Radiation Effects and Defects in Solids, 144 (1998) 189-231.

[76] E. Gaganidze, C. Petersen, E. Materna-Morris, C. Dethloff, O.J. Weiss, J. Aktaa, A. Povstyanko, A. Fedoseev, O. Makarov, V. Prokhorov, Mechanical properties and TEM examination of RAFM steels irradiated up to 70 dpa in BOR-60, Journal of Nuclear Materials, 417 (2011) 93-98.

[77] A. Whapham, M. Makin, The hardening of lithium fluoride by electron irradiation, Philosophical Magazine, 5 (1960) 237-250.

[78] G.S. Was, Fundamentals of Radiation Materials Science: Metals and Alloys, Springer New York, New York, NY, 2017, pp. 793-856.

[79] T. Yamamoto, G.R. Odette, H. Kishimoto, J.-W. Rensman, P. Miao, On the effects of irradiation and helium on the yield stress changes and hardening and non-hardening embrittlement of~ 8Cr tempered martensitic steels: Compilation and analysis of existing data, Journal of Nuclear Materials, 356 (2006) 27-49.

[80] M. Rieth, M. Schirra, A. Falkenstein, P. Graf, S. Heger, H. Kempe, R. Lindau, H. Zimmermann, EUROFER 97. Tensile, charpy, creep and structural tests, Forschungszentrum Karlsruhe in der Helmholtz-Gemeinschaft, Wissenschaftliche Berichte FZKA 6911, October 2003.

[81] J.W. Rensman, NRG Irradiation Testing: Report on 300°C and 60°C Irradiated RAFM Steels, Final Report for subtask TW2-TTMS-001a D06 and TW2-TTMS-001b D12, Petten, August 2005, 20023/05.68497/P.

[82] J.J. Holmes, R.E. Robbins, J.L. Brimhall, B. Mastel, Elevated Temperature Irradiation Hardening in Austenitic Stainless Steel, Acta Metallurgica, 16 (1968) 955-967.

[83] Y. Ishiyama, M. Kodama, N. Yokota, K. Asano, T. Kato, K. Fukuya, Post-irradiation annealing effects on microstructure and helium bubbles in neutron irradiated type 304 stainless steel, Journal of Nuclear Materials, 239 (1996) 90-94.

[84] J. Busby, G. Was, E. Kenik, Post-irradiation annealing of dislocation microstructure and radiation-induced segregation in proton-irradiated stainless steels, MRS Online Proceedings Library Archive, 540 (1998).

[85] E. Gaganidze, C. Petersen, Post irradiation examination of RAF/M steels after fast reactor irradiation up to 71 dpa and < 340°C (ARBOR 2) : RAFM steels: metallurgical and mechanical characterisation. (KIT Scientific Reports ; 7596), 2011.

[86] H.-C. Schneider, C. Petersen, A.V. Povstyanko, A.E. Fedoseev, O. Makarov, Repeatability of irradiation damage and of recovery by post-irradiation annealing of EUROFER base steels, Fusion Engineering and Design, 124 (2017) 1019-1023.

[87] E. Gaganidze, B. Dafferner, H. Ries, R. Rolli, H.-C. Schneider, J. Aktaa, Irradiation programme HFR phase IIb - SPICE. Impact testing on up to 16.3 dpa irradiated RAFM steels; Forschungszentrum Karlsruhe in der Helmholtz-Gemeinschaft, Wissenschaftliche Berichte FZKA 7371, April 2008.

[88] J.T. Busby, G.S. Was, E.A. Kenik, Post-Irradiation Annealing of Dislocation Microstructure and Radiation-Induced Segregation in Proton-Irradiated Stainless Steels, MRS Online Proceeding, Library 540 (1998) 495–500.

[89] N. Hashimoto, S. Goto, S. Inoue, E. Suzuki, Annealing effect on microstructural recovery in 316L and A533B, Journal of Nuclear Materials, 495 (2017) 1-5.

[90] Z. Jiao, J. Hesterberg, G.S. Was, Effect of post-irradiation annealing on the irradiated microstructure of neutron-irradiated 304L stainless steel, Journal of Nuclear Materials, 500 (2018) 220-234.

[91] Z. Yao, M. Hernández-Mayoral, M. Jenkins, M. Kirk, Heavy-ion irradiations of Fe and Fe–Cr model alloys Part 1: Damage evolution in thin-foils at lower doses, Philosophical Magazine, 88 (2008) 2851-2880.

[92] K. Arakawa, T. Amino, H. Mori, Direct observation of the coalescence process between nanoscale dislocation loops with different Burgers vectors, Acta Materialia, 59 (2011) 141-145.

[93] P.M. Anderson, J.P. Hirth, J. Lothe, Theory of Dislocations (3rd edition), Cambridge University Press, New York, 2017, p. 20.

[94] B. Burton, M.V. Speight, The Coarsening and Annihilation Kinetics of Dislocation Loops, Philosophical Magazine a-Physics of Condensed Matter Structure Defects and Mechanical Properties, 53 (1986) 385-402.

[95] G.S. Was, Fundamentals of Radiation Materials Science: Metals and Alloys, Springer New York, New York, NY, 2017, pp. 207-252.

[96] L. Schäfer, M. Schirra, K. Ehrlich, Mechanical properties of low activating martensitic 8–10% CrWVTa steels of type OPTIFER, Journal of nuclear materials, 233 (1996) 264-269.

[97] R. Lindau, M. Schirra, First results on the characterisation of the reduced-activation-ferritic-martensitic steel EUROFER, Fusion engineering and design, 58 (2001) 781-785.

[98] R. Lindau, A. Möslang, M. Schirra, Thermal and mechanical behaviour of the reduced-activation-ferritic-martensitic steel EUROFER, Fusion engineering and design, 61 (2002) 659-664.

[99] M. Mahler, G. Po, Y. Cui, N. Ghoniem, J. Aktaa, Microstructure-specific hardening of ferritic-martensitic steels pre and post 15 dpa neutron irradiation at 330° C: A dislocation dynamics study, Nuclear Materials and Energy, 26 (2021) 100814.

[100] H. Tanigawa, R.L. Klueh, N. Hashimoto, M.A. Sokolov, Hardening mechanisms of reduced activation ferritic/martensitic steels irradiated at 300 C, Journal of Nuclear Materials, 386 (2009) 231-235.

[101] P. Fernandez, A.M. Lancha, J. Lapena, M. Hernandez-Mayoral, Metallurgical characterization of the reduced activation ferritic/martensitic steel Eurofer'97 on as-received condition, Fusion Engineering and Design, 58-59 (2001) 787-792.

[102] K.D. Zilnyk, V.B. Oliveira, H.R.Z. Sandim, A. Moslang, D. Raabe, Martensitic transformation in Eurofer-97 and ODS-Eurofer steels: A comparative study, Journal of Nuclear Materials, 462 (2015) 360-367.

[103] C. Dethloff, E. Gaganidze, J. Aktaa, Quantitative TEM analysis of precipitation and grain boundary segregation in neutron irradiated EUROFER97, Journal of Nuclear Materials, 454 (2014) 323-331.

[104] C. Petersen, J. Aktaa, E. Diegele, E. Gaganidze, R. Lässer, E. Lucon, E. Materna-Morris, A. Möslang, A. Povstyanko, V. Prokhorov, Mechanical properties of reduced activation ferritic/martensitic steels after European reactor irradiations, Proceedings of 21st IAEA Fusion Energy Conference, Chengdu, China, October 16–21, 2006, FT/1-4Ra.

[105] O. Weiss, Präparation radioaktiver TEM-Proben im Fusionsmateriallabor, (2011).

[106] C.A. Volkert, A.M. Minor, Focused ion beam microscopy and micromachining, Mrs Bulletin, 32 (2007) 389-399.

[107] S. Reyntjens, R. Puers, A review of focused ion beam applications in microsystem technology, Journal of Micromechanics and Microengineering, 11 (2001) 287.

[108] Q. Yuan, A. Chauhan, E. Gaganidze, J. Aktaa, In-situ TEM investigations of dislocation loop annealing kinetics in neutron-irradiated 9% Cr RAFM steel, Journal of Nuclear Materials, 558 (2022) 153365.

[109] Y.N. Huang, H.T. Zhang, M.A. Auger, Z.L. Hong, H.P. Ning, M.J. Gorley, P.S. Grant, M.J. Reece, H.X. Yan, S.G. Roberts, Microstructural comparison of effects of hafnium and titanium additions in spark-plasma-sintered Fe-based oxide-dispersion strengthened alloys, Journal of Nuclear Materials, 487 (2017) 433-442.

[110] A. Aitkaliyeva, J.W. Madden, B.D. Miller, J.I. Cole, J. Gan, Comparison of preparation techniques for nuclear materials for transmission electron microscopy (TEM), Journal of Nuclear Materials, 459 (2015) 241-246.

[111] B. Horvath, R. Schaublin, Y. Dai, Flash electropolishing of TEM lamellas of irradiated tungsten, Nuclear Instruments & Methods in Physics Research Section B-Beam Interactions with Materials and Atoms, 449 (2019) 29-34.

[112] D.B. Williams, C.B. Carter, Transmission Electron Microscopy: A Textbook for Materials Science, Springer US, Boston, MA, 2009, pp. 141-171.

[113] D.B. Williams, C.B. Carter, Transmission Electron Microscopy: A Textbook for Materials Science, Springer US, Boston, MA, 2009, pp. 371-388.

[114] A. Howie, M.J. Whelan, Diffraction Contrast of Electron Microscope Images of Crystal Lattice Defects .2. Development of a Dynamical Theory, Proceedings of the Royal Society of London Series a-Mathematical and Physical Sciences, 263 (1961) 217-237.

[115] A. Howie, M.J. Whelan, Diffraction Contrast of Electron Microscope Images of Crystal Lattice Defects .3. Results and Experimental Confirmation of Dynamical Theory of Dislocation Image Contrast, Proceedings of the Royal Society of London Series a-Mathematical and Physical Sciences, 267 (1962) 206-230.

[116] S. Nishikawa, S. Kikuchi, Diffraction of cathode rays by calcite, Nature, 122 (1928) 726-726.

[117] D.B. Williams, C.B. Carter, Transmission Electron Microscopy: A Textbook for Materials Science, Springer US, Boston, MA, 2009, pp. 311-322.

[118] P. Ewald, Zur Theorie der Interferenzen der Röntgenstrahlen in Kristallen, Physikalische Zeitschrift, 14 (1913) 465.

[119] D.B. Williams, C.B. Carter, Transmission Electron Microscopy: A Textbook for Materials Science, Springer US, Boston, MA, 2009, pp. 463-481.

[120] M. Wilkens, M. Ruhle, F. Haussermann, Transmission Electron-Microscopy of Small Point-Defect Clusters in Crystals - Potentialities and Limitations of Diffraction Contrast Analysis, Journal De Microscopie, 16 (1973) 199.

[121] D. Cockayne, The principles and practice of the weak - beam method of electron microscopy, Journal of microscopy, 98 (1973) 116-134.

[122] J. Haley, F. Liu, E. Tarleton, A. Cocks, G. Odette, S. Lozano-Perez, S. Roberts, Helical dislocations: Observation of vacancy defect bias of screw dislocations in neutron irradiated Fe–9Cr, Acta Materialia, 181 (2019) 173-184.

[123] D.B. Williams, C.B. Carter, Transmission Electron Microscopy: A Textbook for Materials Science, Springer US, Boston, MA, 2009, pp. 441-461.

[124] M. Klimenkov, E. Materna-Morris, A. Moslang, Characterization of radiation induced defects in EUROFER 97 after neutron irradiation, Journal of Nuclear Materials, 417 (2011) 124-126.

[125] B. Yao, D.J. Edwards, R.J. Kurtz, TEM characterization of dislocation loops in irradiated bcc Fe-based steels, Journal of nuclear materials, 434 (2013) 402-410.

[126] A. Chauhan, Q. Yuan, C. Dethloff, E. Gaganidze, J. Aktaa, Post-irradiation annealing of neutron-irradiated EUROFER97, Journal of Nuclear Materials, 548 (2021) 152863.

[127] A. Foreman, H. Von Harrach, D. Saldin, The TEM contrast of faceted voids, Philosophical Magazine A, 45 (1982) 625-645.

[128] M. Rühle, M. Wilkens, Defocusing contrast of cavities, Crystal Lattice Defects, 6 (1975) 129-140.

[129] T. Malis, S. Cheng, R. Egerton, EELS log-ratio technique for specimen-thickness measurement in the TEM, Journal of electron microscopy technique, 8 (1988) 193-200.

[130] D. Joy, R. Egerton, D. Maher, Progress in the quantitation of electron energy-loss spectra. In Scanning Electron Microscopy, AMF O'Hare, Chicago, 1979, pp. 817-826.

[131] A. Prokhodtseva, B. Decamps, A. Ramar, R. Schaublin, Impact of He and Cr on defect accumulation in ion-irradiated ultrahigh-purity Fe(Cr) alloys, Acta Materialia, 61 (2013) 6958-6971.

[132] B. Gómez-Ferrer, C. Dethloff, E. Gaganidze, L. Malerba, C. Hatzoglou, C. Pareige, Nano-hardening features in high-dose neutron irradiated Eurofer97 revealed by atom-probe tomography, Journal of Nuclear Materials, (2020) 152228.

[133] E. Materna-Morris, M. Klimenkov, A. Möslang, The Influence of Boron on Structural Properties of Martensitic 8-10% Cr-Steels, Materials Science Forum, Trans Tech Publ, 2013, 877-882.

[134] W. Van Renterghem, A. Al Mazouzi, S. Van Dyck, Influence of post irradiation annealing on the mechanical properties and defect structure of AISI 304 steel, Journal of Nuclear Materials, 413 (2011) 95-102.

[135] J. Busby, G. Was, E. Kenik, Isolating the effect of radiation-induced segregation in irradiation-assisted stress corrosion cracking of austenitic stainless steels, Journal of Nuclear Materials, 302 (2002) 20-40.

[136] C. Xu, W.Y. Chen, X. Zhang, Y.Q. Wu, M.M. Li, Y. Yang, Effects of neutron irradiation and post-irradiation annealing on the microstructure of HT-UPS stainless steel, Journal of Nuclear Materials, 507 (2018) 188-197.

[137] K. Arakawa, M.-C. Marinica, S. Fitzgerald, L. Proville, D. Nguyen-Manh, S.L. Dudarev, P.-W. Ma, T.D. Swinburne, A.M. Goryaeva, T. Yamada, Quantum de-trapping and transport of heavy defects in tungsten, Nature Materials, (2020) 1-4.

[138] S. Moll, T. Jourdan, H. Lefaix-Jeuland, Direct Observation of Interstitial Dislocation Loop Coarsening in alpha-Iron, Physical Review Letters, 111 (2013) 015503.

[139] J.C. Haley, S.A. Briggs, P.D. Edmondson, K. Sridharan, S.G. Roberts, S. Lozano-Perez, K.G. Field, Dislocation loop evolution during in-situ ion FeCrAl alloys, Acta Materialia, 136 (2017) 390-401.

[140] B.C. Masters, Dislocation Loops in Irradiated Iron, Philosophical Magazine, 11 (1965) 881-893.

[141] N. Yoshida, A. Yamaguchi, T. Muroga, Y. Miyamoto, K. Kitajima, Characteristics of point defects and their clustering in pure ferritic steels, Journal of Nuclear Materials, 155 (1988) 1232-1236.

[142] C. Pokor, Y. Brechet, P. Dubuisson, J.-P. Massoud, A. Barbu, Irradiation damage in 304 and 316 stainless steels: experimental investigation and modeling. Part I: Evolution of the microstructure, Journal of Nuclear Materials, 326 (2004) 19-29.

[143] B.C. Masters, Dislocation Loops in Irradiated Iron, Philosophical Magazine, 11 (1965) 881-&.

[144] K. Fukuya, M. Nakano, K. Fujii, T. Torimaru, Y. Kitsunai, Separation of microstructural and microchemical effects in irradiation assisted stress corrosion cracking using post-irradiation annealing, Journal of Nuclear Science and Technology, 41 (2004) 1218-1227.

[145] W. Liu, Y. Ji, P. Tan, C. Zhang, C. He, Z. Yang, Microstructure evolution during helium irradiation and post-irradiation annealing in a nanostructured reduced activation steel, Journal of Nuclear Materials, 479 (2016) 323-330.

[146] H. Trinkaus, B. Singh, Helium accumulation in metals during irradiation–where do we stand?, Journal of Nuclear Materials, 323 (2003) 229-242.

[147] B.H. Duan, F. Bergner, C. Heintze, K. Vogel, S. Akhmadaliev, T.S. Wang, Post-irradiation annealing behaviour of oxide dispersion strengthened Fe-Cr alloys studied by nanoindentation, Philosophical Magazine Letters, 98 (2018) 536-546.

[148] Q. Yuan, A. Chauhan, E. Gaganidze, J. Aktaa, Direct observation of dislocation loops shrinkage upon annealing neutron-irradiated Fe-9Cr alloy, Journal of Nuclear Materials, 542 (2020) 152401.

[149] J. Gao, Q. Yuan, E. Gaganidze, J. Aktaa, On the shrinkage of neutron irradiation-induced cavities in Eurofer97 steel upon heating, Philosophical Magazine, (2022) 1-26.

[150] S. Zinkle, W. Wolfer, G. Kulcinski, L. Seitzman, II. Effect of oxygen and helium on void formation in metals, Philosophical Magazine A, 55 (1987) 127-140.

[151] F.S. Buffington, K. Hirano, M. Cohen, Self Diffusion in Iron, Acta Metallurgica, 9 (1961) 434-439.

[152] J. Kucera, B. Million, J. Ruzickova, V. Foldyna, A. Jakobova, Self-Diffusion of Iron in Alpha-Phase of Iron and Fe-Cr Alloys, Acta Metallurgica, 22 (1974) 135-140.

[153] D. Terentyev, F. Bergner, Y. Osetsky, Cr segregation on dislocation loops enhances hardening in ferritic Fe–Cr alloys, Acta Materialia, 61 (2013) 1444-1453.

[154] O.V. Borodin, V.N. Voyevodin, V.F. Zelenskij, I.M. Neklyudov, P.V. Platonov, Radiation damage studies of the 10 to 13% chromium-containing steels and alloys irradiated with heavy ions, Effects of Radiation on Materials: 15th International Symposium, ASTM International, Philadelphia, January 1992, 1157–1166

[155] M. Puigvi, Y.N. Osetsky, A. Serra, Point-defect clusters and dislocation loops in bcc metals: continuum and atomistic study, Philosophical Magazine, 83 (2003) 857-871.

[156] J. Silcox, M. Whelan, Direct observations of the annealing of prismatic dislocation loops and of climb of dislocations in quenched aluminium, Philosophical Magazine, 5 (1960) 1-23.

[157] S.L. Dudarev, R. Bullough, P.M. Derlet, Effect of the alpha-gamma phase transition on the stability of dislocation loops in bcc iron, Physical Review Letters, 100 (2008) 135503.

[158] B. Burton, The interaction between a dislocation loop and a gas bubble, Philosophical Magazine A, 52 (1985) 669-688.

[159] I. Rovelli, S. Dudarev, A. Sutton, Non-local model for diffusion-mediated dislocation climb and cavity growth, Journal of the Mechanics and Physics of Solids, 103 (2017) 121-141.

[160] J. Turnbull, The coalescence of dislocation loops by self climb, Philosophical Magazine, 21 (1970) 83-94.

[161] Q. Yuan, A. Chauhan, E. Gaganidze, J. Aktaa, Dislocation loop coarsening and shape evolution upon annealing neutron-irradiated RAFM steel, Journal of Nuclear Materials, 558 (2022) 153366.

[162] S.P. Fitzgerald, Z. Yao, Shape of prismatic dislocation loops in anisotropic α-Fe, Philosophical Magazine Letters, 89 (2009) 581-588.

[163] K. Wang, C.M. Parish, K.G. Field, L. Tan, Y. Katoh, Segregation behavior and phase instability of Eurofer97 after neutron irradiation to 72 dpa, Journal of Nuclear Materials, 547 (2021) 152834.

[164] J. Byggmästar, F. Granberg, Dynamical stability of radiation-induced C15 clusters in iron, Journal of Nuclear Materials, 528 (2020) 151893.

[165] M. Lambrecht, E. Meslin, L. Malerba, M. Hernandez-Mayoral, F. Bergner, P. Pareige, B. Radiguet, A. Almazouzi, On the correlation between irradiation-induced microstructural features and the hardening of reactor pressure vessel steels, Journal of Nuclear Materials, 406 (2010) 84-89.

[166] N. Hashimoto, T. Byun, K. Farrell, S. Zinkle, Deformation microstructure of neutron-irradiated pure polycrystalline metals, Journal of Nuclear Materials, 329 (2004) 947-952.

[167] A. Chauhan, F. Bergner, A. Etienne, J. Aktaa, Y. de Carlan, C. Heintze, D. Litvinov, M. Hernandez-Mayoral, E. Onorbe, B. Radiguet, A. Ulbricht, Microstructure characterization and strengthening mechanisms of oxide dispersion strengthened (ODS) Fe-9% Cr and Fe-14% Cr extruded bars, Journal of Nuclear Materials, 495 (2017) 6-19.

[168] G. Speich, A. Schwoeble, W.C. Leslie, Elastic constants of binary iron-base alloys, Metallurgical Transactions, 3 (1972) 2031-2037.

[169] K.G. Field, X. Hu, K.C. Littrell, Y. Yamamoto, L.L. Snead, Radiation tolerance of neutron-irradiated model Fe–Cr–Al alloys, Journal of Nuclear Materials, 465 (2015) 746-755.

List of figures

List of tables

Permission for reuse of published content

Listed below are the licenses allowing the use of previously published work in the current thesis Ref. [6, 27, 39, 65, 67, 76, 92, 103, 107, 112, 113, 119, 123, 125]. No licenses was required for content use from Refs. [2, 11, 52, 60, 108, 126, 148, 161].

Ref. [6] E. Gaganidze, J. Aktaa, Assessment of neutron irradiation effects on RAFM steels, Fusion Engineering and Design, 88 (2013) 118-128.

ELSEVIER LICENSE TERMS AND CONDITIONS	
Jan 11, 2023	
This Agreement between Qian Yuan ("You") and Elsevier ("Elsevier") consists of your license details and the terms and conditions provided by Elsevier and Copyright Clearance Center.	
License Number	5465901000277
License date	Jan 11, 2023
Licensed Content Publisher	Elsevier
Licensed Content Publication	Fusion Engineering and Design
Licensed Content Title	Assessment of neutron irradiation effects on RAFM steels
Licensed Content Author	Ermile Gaganidze, Jarir Aktaa
Licensed Content Date	Mar 1, 2013
Licensed Content Volume	88
Licensed Content Issue	3
Licensed Content Pages	11
Start Page	118
End Page	128
Type of Use	reuse in a thesis/dissertation
Portion	figures/tables/illustrations
Number of figures/tables/illustrations	1
Format	both print and electronic
Are you the author of this Elsevier article?	No
Will you be translating?	No
Title	Evolution of irradiation defects in fusion structural steels at high temperatures
Institution name	Karlsruhe Institute of Technology
Expected presentation date	Jan 2023
Portions	Fig. 2 on page 121
Requestor Location	Qian Yuan Hermann-von-Helmholtz-Platz 1 Eggenstein-Leopoldshafen, 76344 Germany Attn: Karlsruhe Insitute of Technology, Germany
Publisher Tax ID	GB 494 6272 12
Total	0.00 EUR

Ref. [27] M. Klimenkov, U. Jäntsch, M. Rieth, A. Möslang, Correlation of microstructural and mechanical properties of neutron irradiated EUROFER97 steel, Journal of Nuclear Materials, 538 (2020) 152231.

ELSEVIER LICENSE **TERMS AND CONDITIONS**	
Jan 11, 2023	
This Agreement between Qian Yuan ("You") and Elsevier ("Elsevier") consists of your license details and the terms and conditions provided by Elsevier and Copyright Clearance Center.	
License Number	5465901189502
License date	Jan 11, 2023
Licensed Content Publisher	Elsevier
Licensed Content Publication	Journal of Nuclear Materials
Licensed Content Title	Correlation of microstructural and mechanical properties of neutron-irradiated EUROFER97 steel
Licensed Content Author	M. Klimenkov, U. Jäntsch ,M. Rieth, A. Möslang
Licensed Content Date	Sep 1, 2020
Licensed Content Volume	538
Licensed Content Issue	n/a
Licensed Content Pages	1
Start Page	152231
End Page	0
Type of Use	reuse in a thesis/dissertation
Portion	figures/tables/illustrations
Number of figures/tables/illustrations	3
Format	both print and electronic
Are you the author of this Elsevier article?	No
Will you be translating?	No
Title	Evolution of irradiation defects in fusion structural steels at high temperatures
Institution name	Karlsruhe Institute of Technology
Expected presentation date	Jan 2023
Portions	Graphic abstract, Fig. 6b, Fig. 11
Requestor Location	Qian Yuan Hermann-von-Helmholtz-Platz 1 Eggenstein-Leopoldshafen, 76344 Germany Attn: Karlsruhe Insitute of Technology, Germany
Publisher Tax ID	GB 494 6272 12
Total	0.00 EUR

Ref. [39] G.S. Was, Fundamentals of Radiation Materials Science: Metals and Alloys, Springer New York, New York, NY, 2017, pp. 167-205.

SPRINGER NATURE LICENSE TERMS AND CONDITIONS	
Jan 11, 2023	
This Agreement between Qian Yuan ("You") and Springer Nature ("Springer Nature") consists of your license details and the terms and conditions provided by Springer Nature and Copyright Clearance Center.	
License Number	5465901445124
License date	Jan 11, 2023
Licensed Content Publisher	Springer Nature
Licensed Content Publication	Springer eBook
Licensed Content Title	Point Defect Formation and Diffusion
Licensed Content Author	Gary S. Was
Licensed Content Date	Jan 1, 2017
Type of Use	Thesis/Dissertation
Requestor type	academic/university or research institute
Format	print and electronic
Portion	figures/tables/illustrations
Number of figures/tables/illustrations	4
Will you be translating?	no
Circulation/distribution	1 - 29
Author of this Springer Nature content	no
Title	Evolution of irradiation defects in fusion structural steels at high temperatures
Institution name	Karlsruhe Institute of Technology
Expected presentation date	Jan 2023
Portions	Fig. 4.4 on page 169, Fig. 4.8 on page 171, Fig. 4.9 (b) on page 173, Fig. 4.11 (b) on page 175
Requestor Location	Qian Yuan Hermann-von-Helmholtz-Platz 1 Eggenstein-Leopoldshafen, 76344 Germany Attn: Karlsruhe Insitute of Technology, Germany
Total	0.00 EUR

Ref. [65] K. Arakawa, M. Hatanaka, H. Mori, K. Ono, Effects of chromium on the one-dimensional motion of interstitial-type dislocation loops in iron, Journal of Nuclear Materials, 329 (2004) 1194-1198.

ELSEVIER LICENSE
TERMS AND CONDITIONS

Jan 11, 2023

This Agreement between Qian Yuan ("You") and Elsevier ("Elsevier") consists of your license details and the terms and conditions provided by Elsevier and Copyright Clearance Center.

License Number	5465910253509
License date	Jan 11, 2023
Licensed Content Publisher	Elsevier
Licensed Content Publication	Journal of Nuclear Materials
Licensed Content Title	Effects of chromium on the one-dimensional motion of interstitial-type dislocation loops in iron
Licensed Content Author	K Arakawa, M Hatanaka, H Mori, K Ono
Licensed Content Date	Aug 1, 2004
Licensed Content Volume	329
Licensed Content Issue	n/a
Licensed Content Pages	5
Start Page	1194
End Page	1198
Type of Use	reuse in a thesis/dissertation
Portion	figures/tables/illustrations
Number of figures/tables/illustrations	1
Format	both print and electronic
Are you the author of this Elsevier article?	No
Will you be translating?	No
Title	Evolution of irradiation defects in fusion structural steels at high temperatures
Institution name	Karlsruhe Institute of Technology
Expected presentation date	Jan 2023
Portions	Fig. 2 on page 1196
Requestor Location	Qian Yuan Hermann-von-Helmholtz-Platz 1 Eggenstein-Leopoldshafen, 76344 Germany Attn: Karlsruhe Insitute of Technology, Germany
Publisher Tax ID	GB 494 6272 12
Total	0.00 EUR

Ref. [67] O.J. Weiss, E. Gaganidze, J. Aktaa, Quantitative characterization of microstructural defects in up to 32 dpa neutron irradiated EUROFER97, Journal of Nuclear Materials, 426 (2012) 52-58.

ELSEVIER LICENSE
TERMS AND CONDITIONS

Jan 11, 2023

This Agreement between Qian Yuan ("You") and Elsevier ("Elsevier") consists of your license details and the terms and conditions provided by Elsevier and Copyright Clearance Center.

License Number	5465910371807
License date	Jan 11, 2023
Licensed Content Publisher	Elsevier
Licensed Content Publication	Journal of Nuclear Materials
Licensed Content Title	Quantitative characterization of microstructural defects in up to 32dpa neutron-irradiated EUROFER97
Licensed Content Author	Oliver J. Weiß, Ermile Gaganidze, Jarir Aktaa
Licensed Content Date	Jul 1, 2012
Licensed Content Volume	426
Licensed Content Issue	1-3
Licensed Content Pages	7
Start Page	52
End Page	58
Type of Use	reuse in a thesis/dissertation
Portion	figures/tables/illustrations
Number of figures/tables/illustrations	2
Format	both print and electronic
Are you the author of this Elsevier article?	No
Will you be translating?	No
Title	Evolution of irradiation defects in fusion structural steels at high temperatures
Institution name	Karlsruhe Institute of Technology
Expected presentation date	Jan 2023
Portions	Fig. 1a on page 53, Fig. 3 on page 54
Requestor Location	Qian Yuan Hermann-von-Helmholtz-Platz 1 Eggenstein-Leopoldshafen, 76344 Germany Attn: Karlsruhe Insitute of Technology, Germany
Publisher Tax ID	GB 494 6272 12
Total	0.00 EUR

Ref. [76] E. Gaganidze, C. Petersen, E. Materna-Morris, C. Dethloff, O.J. Weiss, J. Aktaa, A. Povstyanko, A. Fedoseev, O. Makarov, V. Prokhorov, Mechanical properties and TEM examination of RAFM steels irradiated up to 70 dpa in BOR-60, Journal of Nuclear Materials, 417 (2011) 93-98.

ELSEVIER LICENSE
TERMS AND CONDITIONS

Jan 11, 2023

This Agreement between Qian Yuan ("You") and Elsevier ("Elsevier") consists of your license details and the terms and conditions provided by Elsevier and Copyright Clearance Center.

License Number	5465940497854
License date	Jan 11, 2023
Licensed Content Publisher	Elsevier
Licensed Content Publication	Journal of Nuclear Materials
Licensed Content Title	Mechanical properties and TEM examination of RAFM steels irradiated up to 70dpa in BOR-60
Licensed Content Author	E. Gaganidze, C. Petersen, E. Materna-Morris, C. Dethloff, O.J. Weiß, J. Aktaa, A. Povstyanko, A. Fedoseev, O. Makarov, V. Prokhorov
Licensed Content Date	Oct 1, 2011
Licensed Content Volume	417
Licensed Content Issue	1-3
Licensed Content Pages	6
Start Page	93
End Page	98
Type of Use	reuse in a thesis/dissertation
Portion	figures/tables/illustrations
Number of figures/tables/illustrations	1
Format	both print and electronic
Are you the author of this Elsevier article?	No
Will you be translating?	No
Title	Evolution of irradiation defects in fusion structural steels at high temperatures
Institution name	Karlsruhe Institute of Technology
Expected presentation date	Jan 2023
Portions	Fig. 4 on page 96
Requestor Location	Qian Yuan Hermann-von-Helmholtz-Platz 1 Eggenstein-Leopoldshafen, 76344 Germany Attn: Karlsruhe Insitute of Technology, Germany
Publisher Tax ID	GB 494 6272 12
Total	0.00 EUR

Ref. [92] K. Arakawa, T. Amino, H. Mori, Direct observation of the coalescence process between nanoscale dislocation loops with different Burgers vectors, Acta Materialia, 59 (2011) 141-145.

ELSEVIER LICENSE TERMS AND CONDITIONS	
Jan 11, 2023	
This Agreement between Qian Yuan ("You") and Elsevier ("Elsevier") consists of your license details and the terms and conditions provided by Elsevier and Copyright Clearance Center.	
License Number	5465940669049
License date	Jan 11, 2023
Licensed Content Publisher	Elsevier
Licensed Content Publication	Acta Materialia
Licensed Content Title	Direct observation of the coalescence process between nanoscale dislocation loops with different Burgers vectors
Licensed Content Author	K. Arakawa, T. Amino, H. Mori
Licensed Content Date	Jan 1, 2011
Licensed Content Volume	59
Licensed Content Issue	1
Licensed Content Pages	5
Start Page	141
End Page	145
Type of Use	reuse in a thesis/dissertation
Portion	figures/tables/illustrations
Number of figures/tables/illustrations	1
Format	both print and electronic
Are you the author of this Elsevier article?	No
Will you be translating?	No
Title	Evolution of irradiation defects in fusion structural steels at high temperatures
Institution name	Karlsruhe Institute of Technology
Expected presentation date	Jan 2023
Portions	Fig. 2 on page 143
Requestor Location	Qian Yuan Hermann-von-Helmholtz-Platz 1 Eggenstein-Leopoldshafen, 76344 Germany Attn: Karlsruhe Insitute of Technology, Germany
Publisher Tax ID	GB 494 6272 12
Total	0.00 EUR

Ref. [103] C. Dethloff, E. Gaganidze, J. Aktaa, Quantitative TEM analysis of precipitation and grain boundary segregation in neutron irradiated EUROFER97, Journal of nuclear materials, 454 (2014) 323-331.

ELSEVIER LICENSE
TERMS AND CONDITIONS

Jan 11, 2023

This Agreement between Qian Yuan ("You") and Elsevier ("Elsevier") consists of your license details and the terms and conditions provided by Elsevier and Copyright Clearance Center.

License Number	5465940782220
License date	Jan 11, 2023
Licensed Content Publisher	Elsevier
Licensed Content Publication	Journal of Nuclear Materials
Licensed Content Title	Quantitative TEM analysis of precipitation and grain boundary segregation in neutron-irradiated EUROFER97
Licensed Content Author	Christian Dethloff, Ermile Gaganidze, Jarir Aktaa
Licensed Content Date	Nov 1, 2014
Licensed Content Volume	454
Licensed Content Issue	1-3
Licensed Content Pages	9
Start Page	323
End Page	331
Type of Use	reuse in a thesis/dissertation
Portion	figures/tables/illustrations
Number of figures/tables/illustrations	2
Format	both print and electronic
Are you the author of this Elsevier article?	No
Will you be translating?	No
Title	Evolution of irradiation defects in fusion structural steels at high temperatures
Institution name	Karlsruhe Institute of Technology
Expected presentation date	Jan 2023
Portions	Fig. 1 on page 324, Fig. 2 on page 325
Requestor Location	Qian Yuan Hermann-von-Helmholtz-Platz 1 Eggenstein-Leopoldshafen, 76344 Germany Attn: Karlsruhe Insitute of Technology, Germany
Publisher Tax ID	GB 494 6272 12
Total	0.00 EUR

Ref. [107] S. Reyntjens, R. Puers, A review of focused ion beam applications in microsystem technology, Journal of Micromechanics and Microengineering, 11 (2001) 287

CCC Marketplace

This is a License Agreement between Qian Yuan/Karlsruhe Insitute of Technology ("User") and Copyright Clearance Center, Inc. ("CCC") on behalf of the Rightsholder identified in the order details below. The license consists of the order details, the Marketplace Order General Terms and Conditions below, and any Rightsholder Terms and Conditions which are included below.

All payments must be made in full to CCC in accordance with the Marketplace Order General Terms and Conditions below.

Order Date	11-Jan-2023	Type of Use	Republish in a thesis/dissertation
Order License ID	1310094-1	Publisher	INSTITUTE OF PHYSICS PUBLISHING
ISSN	0960-1317	Portion	Image/photo/illustration

LICENSED CONTENT

Publication Title	Journal of micromechanics and microengineering : structures, devices, and systems	Country	United Kingdom of Great Britain and Northern Ireland
		Rightsholder	IOP Publishing, Ltd
Author/Editor	Institute of Physics (Great Britain)	Publication Type	Journal
Date	01/01/1991		
Language	English		

REQUEST DETAILS

Portion Type	Image/photo/illustration	Distribution	Worldwide
Number of Images / Photos / Illustrations	1	Translation	Original language of publication
Format (select all that apply)	Print, Electronic	Copies for the Disabled?	No
Who Will Republish the Content?	Academic institution	Minor Editing Privileges?	No
Duration of Use	Life of current and all future editions	Incidental Promotional Use?	No
Lifetime Unit Quantity	Up to 499	Currency	EUR
Rights Requested	Main product		

NEW WORK DETAILS

Title	Evolution of irradiation defects in fusion structural steels at high temperatures	Institution Name	Karlsruhe Institute of Technology
		Expected Presentation Date	2023-01-31
Instructor Name	Jarir Aktaa		

ADDITIONAL DETAILS

Order Reference Number	N/A	The Requesting Person/Organization to Appear on the License	Qian Yuan/Karlsruhe Insitute of Technology

REUSE CONTENT DETAILS

Title, Description or Numeric Reference of the Portion(s)	N/A	Title of the Article/Chapter the Portion Is From	Focused-ion beam (FIB)
Editor of Portion(s)	N/A	Author of Portion(s)	Institute of Physics (Great Britain)
Volume of Serial or Monograph	N/A	Issue, if Republishing an Article From a Serial	N/A
Page or Page Range of Portion	Fig. 4-4	Publication Date of Portion	1991-01-01

Ref. [112] D.B. Williams, C.B. Carter, Transmission Electron Microscopy: A Textbook for Materials Science, Springer US, Boston, MA, 2009, pp. 141-171.

SPRINGER NATURE LICENSE
TERMS AND CONDITIONS

Jan 11, 2023

This Agreement between Qian Yuan ("You") and Springer Nature ("Springer Nature") consists of your license details and the terms and conditions provided by Springer Nature and Copyright Clearance Center.

License Number	5465950680197
License date	Jan 11, 2023
Licensed Content Publisher	Springer Nature
Licensed Content Publication	Springer eBook
Licensed Content Title	The Instrument
Licensed Content Author	David B. Williams, C. Barry Carter
Licensed Content Date	Jan 1, 2009
Type of Use	Thesis/Dissertation
Requestor type	academic/university or research institute
Format	print and electronic
Portion	figures/tables/illustrations
Number of figures/tables/illustrations	3
Will you be translating?	no
Circulation/distribution	1 - 29
Author of this Springer Nature content	no
Title	Evolution of irradiation defects in fusion structural steels at high temperatures
Institution name	Karlsruhe Institute of Technology
Expected presentation date	Jan 2023
Portions	Fig. 9.1(B) on page 142, Fig. 9.12 on page 153, Fig. 9.18 on page 159
Requestor Location	Qian Yuan Hermann-von-Helmholtz-Platz 1 Eggenstein-Leopoldshafen, 76344 Germany Attn: Karlsruhe Insitute of Technology, Germany
Total	0.00 EUR

Ref. [113] D.B. Williams, C.B. Carter, Transmission Electron Microscopy: A Textbook for Materials Science, Springer US, Boston, MA, 2009, pp. 371-388.

SPRINGER NATURE LICENSE
TERMS AND CONDITIONS

Jan 11, 2023

This Agreement between Qian Yuan ("You") and Springer Nature ("Springer Nature") consists of your license details and the terms and conditions provided by Springer Nature and Copyright Clearance Center.

License Number	5465950847155
License date	Jan 11, 2023
Licensed Content Publisher	Springer Nature
Licensed Content Publication	Springer eBook
Licensed Content Title	Amplitude Contrast
Licensed Content Author	David B. Williams, C. Barry Carter
Licensed Content Date	Jan 1, 2009
Type of Use	Thesis/Dissertation
Requestor type	academic/university or research institute
Format	print and electronic
Portion	figures/tables/illustrations
Number of figures/tables/illustrations	1
Will you be translating?	no
Circulation/distribution	1 - 29
Author of this Springer Nature content	no
Title	Evolution of irradiation defects in fusion structural steels at high temperatures
Institution name	Karlsruhe Institute of Technology
Expected presentation date	Jan 2023
Portions	Fig. 22.13 on page 380
Requestor Location	Qian Yuan Hermann-von-Helmholtz-Platz 1 Eggenstein-Leopoldshafen, 76344 Germany Attn: Karlsruhe Insitute of Technology, Germany
Total	0.00 EUR

Ref. [119] D.B. Williams, C.B. Carter, Transmission Electron Microscopy: A Textbook for Materials Science, Springer US, Boston, MA, 2009, pp. 463-481.

SPRINGER NATURE LICENSE
TERMS AND CONDITIONS

Jan 11, 2023

This Agreement between Qian Yuan ("You") and Springer Nature ("Springer Nature") consists of your license details and the terms and conditions provided by Springer Nature and Copyright Clearance Center.

License Number	5465951014811
License date	Jan 11, 2023
Licensed Content Publisher	Springer Nature
Licensed Content Publication	Springer eBook
Licensed Content Title	Weak-Beam Dark-Field Microscopy
Licensed Content Author	David B. Williams, C. Barry Carter
Licensed Content Date	Jan 1, 2009
Type of Use	Thesis/Dissertation
Requestor type	academic/university or research institute
Format	print and electronic
Portion	figures/tables/illustrations
Number of figures/tables/illustrations	2
Will you be translating?	no
Circulation/distribution	1 - 29
Author of this Springer Nature content	no
Title	Evolution of irradiation defects in fusion structural steels at high temperatures
Institution name	Karlsruhe Institute of Technology
Expected presentation date	Jan 2023
Portions	Fig. 27.5 on page 467, Fig. 27.9 on page 469
Requestor Location	Qian Yuan Hermann-von-Helmholtz-Platz 1 Eggenstein-Leopoldshafen, 76344 Germany Attn: Karlsruhe Insitute of Technology, Germany

Ref. [123] D.B. Williams, C.B. Carter, Transmission Electron Microscopy: A Textbook for Materials Science, Springer US, Boston, MA, 2009, pp. 441-461.

SPRINGER NATURE LICENSE TERMS AND CONDITIONS	
Jan 11, 2023	
This Agreement between Qian Yuan ("You") and Springer Nature ("Springer Nature") consists of your license details and the terms and conditions provided by Springer Nature and Copyright Clearance Center.	
License Number	5465951145614
License date	Jan 11, 2023
Licensed Content Publisher	Springer Nature
Licensed Content Publication	Springer eBook
Licensed Content Title	Imaging Strain Fields
Licensed Content Author	David B. Williams, C. Barry Carter
Licensed Content Date	Jan 1, 2009
Type of Use	Thesis/Dissertation
Requestor type	academic/university or research institute
Format	print and electronic
Portion	figures/tables/illustrations
Number of figures/tables/illustrations	1
Will you be translating?	no
Circulation/distribution	1 - 29
Author of this Springer Nature content	no
Title	Evolution of irradiation defects in fusion structural steels at high temperatures
Institution name	Karlsruhe Institute of Technology
Expected presentation date	Jan 2023
Portions	Fig. 26.9 on page 449
Requestor Location	Qian Yuan Hermann-von-Helmholtz-Platz 1 Eggenstein-Leopoldshafen, 76344 Germany Attn: Karlsruhe Insitute of Technology, Germany
Total	0.00 EUR

Ref. [125] B. Yao, D.J. Edwards, R.J. Kurtz, TEM characterization of dislocation loops in irradiated bcc Fe-based steels, Journal of nuclear materials, 434 (2013) 402-410.

ELSEVIER LICENSE TERMS AND CONDITIONS	
Jan 11, 2023	
This Agreement between Qian Yuan ("You") and Elsevier ("Elsevier") consists of your license details and the terms and conditions provided by Elsevier and Copyright Clearance Center.	
License Number	5465951302768
License date	Jan 11, 2023
Licensed Content Publisher	Elsevier
Licensed Content Publication	Journal of Nuclear Materials
Licensed Content Title	TEM characterization of dislocation loops in irradiated bcc Fe-based steels
Licensed Content Author	B. Yao, D.J. Edwards, R.J. Kurtz
Licensed Content Date	Mar 1, 2013
Licensed Content Volume	434
Licensed Content Issue	1-3
Licensed Content Pages	9
Start Page	402
End Page	410
Type of Use	reuse in a thesis/dissertation
Portion	figures/tables/illustrations
Number of figures/tables/illustrations	1
Format	both print and electronic
Are you the author of this Elsevier article?	No
Will you be translating?	No
Title	Evolution of irradiation defects in fusion structural steels at high temperatures
Institution name	Karlsruhe Institute of Technology
Expected presentation date	Jan 2023
Portions	Fig. 2 on page 404
Requestor Location	Qian Yuan Hermann-von-Helmholtz-Platz 1 Eggenstein-Leopoldshafen, 76344 Germany Attn: Karlsruhe Insitute of Technology, Germany
Publisher Tax ID	GB 494 6272 12
Total	0.00 EUR

Appendix 1 Chemical composition of EUROFER 97 in wt% [7]

Heat	EUROFER 97	Reference RAFM steels			10–11% Cr–NiMoVNb
		GA3X	F82H-mod	OPTIFER-Ia	MANET-I
	83697		9741	664	53645
Cr	8.91	9.17	7.7	9.33	10.8
W	1.08	2.12	2.04	0.965	n.s.
Mn	0.48	0.042	0.16	0.50	0.76
V	0.2	0.314	0.16	0.26	0.2
Ta	0.14	0.011	0.009	0.066	n.s.
C	0.12	0.159	0.09	0.10	0.14
Si	0.04	n.s.	0.11	0.06	0.37
P	0.005	n.s.	0.002	0.0046	0.005
S	0.004	n.s.	0.002	0.005	0.004
Ni	0.02	0.021	0.021	0.005	0.92
Mo	<0.001	0.0077	0.003	0.005	0.77
Nb	0.0017	0.011	0.0101	0.009	0.16
Al	0.009	0.015	0.0016	0.008	0.054
B	0.001	n.s.	0.0004	0.0062	0.0085
N	0.02	0.0018	0.008	0.0153	0.02
O	0.0008	n.s.	n.s.	n.s.	n.s.
Co	0.006	0.003	0.0037	n.s.	0.01
Cu	0.0015	0.0017	0.0063	0.035	0.015
Zr	<0.005	n.s.	0.01	n.s.	0.059
Ce	n.s.	n.s.	n.s.	<0.001	n.s.
Ti	0.006	0.001	0.004	0.007	n.s.
As	<0.005	n.s.	n.s.	0.0093	n.s.
Sb	<0.005	n.s.	n.s.	<0.0002	n.s.
Sn	<0.005	n.s.	n.s.	0.0005	n.s.
Fe	Balance	Balance	Balance	Balance	Balance

Appendix 2: Detailed procedures for preparing TEM lamella via FIB technique for nuclear material

In section 3.2.2, FIB technique was introduced and a general procedure for preparing TEM lamella was briefly presented. Here, a detailed procedure with suggested parameters is listed. It is necessary to mention that this procedure is merely a reference for preparing steel samples via FEI Scios Dual beam. For preparing TEM lamella from other materials, parameters for each procedure should be modified.

Protective layer deposition (see Figure 3-6b)

- Electron beam (e-beam) deposition (stage tilt: 0°)
    - Pattern/application: Rectangular/Pt e-dep surface (insert GIS)
    - Recommended Pt pattern size: 15×5×0.2 µm
    - Recommended e-beam setting: 2 kV and 1.6 nA
- Ion beam (i-beam) deposition (stage tilt: 52°)
    - Pattern/application: Rectangle/Pt dep (insert GIS)
    - Recommended Pt pattern size: 15×5×2.3 µm
    - Recommended i-beam setting: 30 kV and 0.3 nA

Hints: The deposited Pt layer should be thick enough to withstand the final milling process.

(a) Trenching for both side (see Figure 3-6c)

1) Rough cross-section (stage tilt: 52°)
    - Milling pattern/Application: Regular cross-section (RSS)/Si
    - Recommended pattern size is: 20×12×6 µm
    - Recommended i-beam setting: 30 kV and 15 nA
2) Wedge shape cut (stage tilt: 52°±1.3°)
    - Milling pattern/Application: Clean cross-section (CCS)/Si
    - Recommended pattern size: 20×2×6 µm
    - Recommended i-beam setting: 30 kV and 5 nA

Hints: The final width of the Pt deposition after this step should be about 1 µm.

(b) Undercut and in-situ lift out (see following micrograph)

1) J-cut (stage tilt: 7°)
    - Milling pattern/Application: Rectangle/Si

- Recommended pattern size: see yellow patterns (set parallel milling)

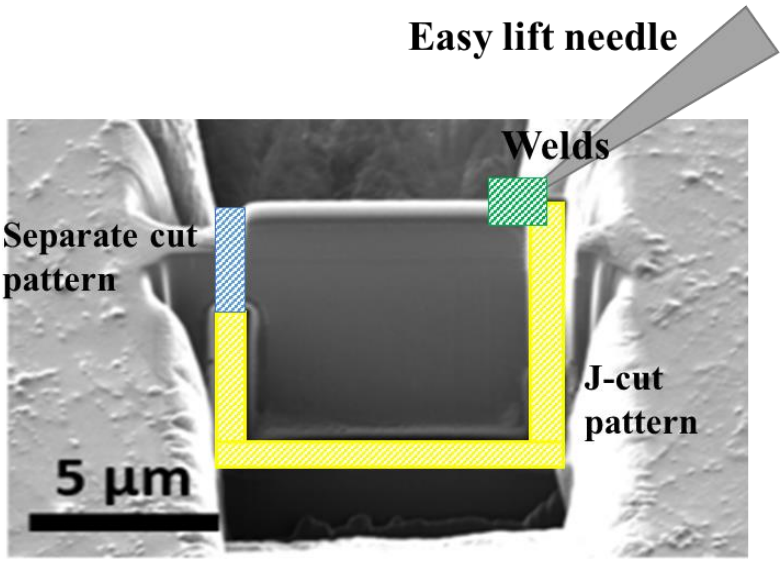

- Recommended i-beam setting: 30 kV and 1 nA

2) Insert Easy lift needle (stage tilt: 0°)
3) Welding (stage tilt: 0°)
    - Pattern/Application: Rectangle/Pt dep (insert GIS)
    - Recommended pattern size is: see green pattern (depends on the needle geometry)
    - Recommended i-beam setting: 30 kV and 0.5 nA
4) Separation cut (stage tilt: 0°)
    - Milling pattern/Application: Rectangle/Si
    - Recommended pattern size: see blue pattern
    - Recommended i-beam setting: 30 kV and 1 nA
5) Lift out (stage tilt: 0°)

Hints: Before inserting the Easy lift needle, tilt the stage to 30° to examine in e-beam panel whether all the patterned areas are fully cut.

(c) Attaching sample to TEM lift-out grid (see Figure 3-6d)

1) Insert Easy lift needle and attach the sample to the lift-out grids (see following micrograph) (stage tilt: 0°)
    - Pattern/Application: Rectangle/Pt dep (insert GIS)
    - Recommended pattern size is: see green patterns (depends on the needle geometry)

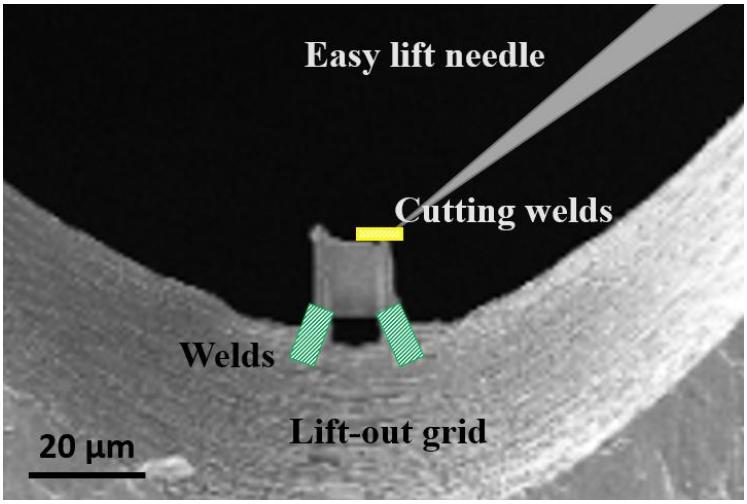

- Recommended i-beam setting: 30 kV and 1 nA

2) Separate the Easy lift needle (stage tilt: 0°)
    - Pattern/Application: Rectangle/Si
    - Recommended pattern size is: see yellow pattern
    - Recommended i-beam setting: 30 kV and 1 nA
3) Retract the Easy lift needle and weld the back side of lamella (stage tilt: 0°)

Hints: The lift-out grid should be fixed upright to the e-beam.

(d) Final milling (detailed milling parameters please refer to Table 3-1)

Appendix 3: Excitation error for Fe.

Constant	Value	Unit
h	6.63E-34	Nms
m_e	9.11E-31	kg
e	1.60E-19	C
c	3.00E+08	m/s

Parameter	Value	Unit
HT	200	kV
L	0.74	m
Lambda	2.74E-12	m
LambdaR	2.51E-12	m

m and n can be found in [119]

m	n	g	g=(110)	g=(002)	g=(112)	g=(220)	g=(103)	g=(222)	g=(213)
		d_{hkl} (m^{-1})	4.93E+09	6.98E+09	8.55E+09	9.87E+09	1.10E+10	1.21E+10	1.31E+10
		s_g (nm^{-1})							
3	3		0.061	0.122	0.183	**0.244**	**0.305**	**0.366**	**0.427**
3.05	3.1		0.064	0.128	0.192	0.256	0.320	0.385	0.449
3.1	3.2		0.067	0.134	**0.201**	0.269	0.336	0.403	0.470
3.15	3.3		0.070	0.140	0.211	0.281	0.351	0.421	0.491
3.2	3.4		0.073	0.147	0.220	0.293	0.366	0.440	0.513
3.25	3.5		0.076	0.153	0.229	0.305	0.382	0.458	0.534
3.3	3.6		0.079	0.159	0.238	0.317	0.397	0.476	0.556
3.35	3.7		0.082	0.165	0.247	0.330	0.412	0.494	0.577
3.4	3.8		0.085	0.171	0.256	0.342	0.427	0.513	0.598
3.45	3.9		0.089	0.177	0.266	0.354	0.443	0.531	0.620
4	4		0.092	0.183	0.275	0.366	0.458	0.549	0.641
4.05	4.1		0.095	0.189	0.284	0.378	0.473	0.568	0.662
4.1	4.2		0.098	0.195	0.293	0.391	0.488	0.586	0.684
4.15	4.3		0.101	**0.201**	0.302	0.403	0.504	0.604	0.705
4.2	4.4		0.104	0.208	0.311	0.415	0.519	0.623	0.726
4.25	4.5		0.107	0.214	0.320	0.427	0.534	0.641	0.748
4.3	4.6		0.110	0.220	0.330	0.440	0.549	0.659	0.769
4.35	4.7		0.113	0.226	0.339	0.452	0.565	0.678	0.791
4.4	4.8		0.116	0.232	0.348	0.464	0.580	0.696	0.812
4.45	4.9		0.119	0.238	0.357	0.476	0.595	0.714	0.833
5	5		0.122	0.244	0.366	0.488	0.610	0.733	0.855
5.05	5.1		0.125	0.250	0.375	0.501	0.626	0.751	0.876
5.1	5.2		0.128	0.256	0.385	0.513	0.641	0.769	0.897
5.15	5.3		0.131	0.262	0.394	0.525	0.656	0.787	0.919
5.2	5.4		0.134	0.269	0.403	0.537	0.671	0.806	0.940
5.25	5.5		0.137	0.275	0.412	0.549	0.687	0.824	0.961
5.3	5.6		0.140	0.281	0.421	0.562	0.702	0.842	0.983
5.35	5.7		0.143	0.287	0.430	0.574	0.717	0.861	1.004
5.4	5.8		0.147	0.293	0.440	0.586	0.733	0.879	1.026
5.45	5.9		0.150	0.299	0.449	0.598	0.748	0.897	1.047
6	6		0.153	0.305	0.458	0.610	0.763	0.916	1.068
6.05	6.1		0.156	0.311	0.467	0.623	0.778	0.934	1.090
6.1	6.2		0.159	0.317	0.476	0.635	0.794	0.952	1.111
6.15	6.3		0.162	0.324	0.485	0.647	0.809	0.971	1.132
6.2	6.4		0.165	0.330	0.494	0.659	0.824	0.989	1.154
6.25	6.5		0.168	0.336	0.504	0.671	0.839	1.007	1.175
6.3	6.6		0.171	0.342	0.513	0.684	0.855	1.026	1.196
6.35	6.7		0.174	0.348	0.522	0.696	0.870	1.044	1.218
6.4	6.8		0.177	0.354	0.531	0.708	0.885	1.062	1.239
6.45	6.9		0.180	0.360	0.540	0.720	0.900	1.080	1.261

7	7		0.183	0.366	0.549	0.733	0.916	1.099	1.282
7.05	7.1		0.186	0.372	0.559	0.745	0.931	1.117	1.303
7.1	7.2		0.189	0.378	0.568	0.757	0.946	1.135	1.325
7.15	7.3		0.192	0.385	0.577	0.769	0.961	1.154	1.346
7.2	7.4		0.195	0.391	0.586	0.781	0.977	1.172	1.367
7.25	7.5		0.198	0.397	0.595	0.794	0.992	1.190	1.389
7.3	7.6		**0.201**	0.403	0.604	0.806	1.007	1.209	1.410
7.35	7.7		0.204	0.409	0.613	0.818	1.022	1.227	1.431
7.4	7.8		0.208	0.415	0.623	0.830	1.038	1.245	1.453
7.45	7.9		0.211	0.421	0.632	0.842	1.053	1.264	1.474
8	8		0.214	0.427	0.641	0.855	1.068	1.282	1.496
8.05	8.1		0.217	0.433	0.650	0.867	1.084	1.300	1.517
8.1	8.2		0.220	0.440	0.659	0.879	1.099	1.319	1.538
8.15	8.3		0.223	0.446	0.668	0.891	1.114	1.337	1.560
8.2	8.4		0.226	0.452	0.678	0.903	1.129	1.355	1.581
8.25	8.5		0.229	0.458	0.687	0.916	1.145	1.373	1.602
8.3	8.6		0.232	0.464	0.696	0.928	1.160	1.392	1.624
8.35	8.7		0.235	0.470	0.705	0.940	1.175	1.410	1.645
8.4	8.8		0.238	0.476	0.714	0.952	1.190	1.428	1.667
8.45	8.9		0.241	0.482	0.723	0.964	1.206	1.447	1.688
9.15	9.3		0.253	0.507	0.760	1.013	1.267	1.520	1.773

Appendix 4 Truth table

$g \cdot b$ invisibility criterion for $g_{\{110\}}$ and $g_{\{200\}}$

g \ b	**100**	**-100**	**010**	**0-10**	**001**	**00-1**	**111**	**-1-1-1**	**-111**	**1-1-1**	**1-11**	**-11-1**	**11-1**	**-1-11**
110	1	-1	1	-1	0	0	1	-1	0	0	0	0	1	-1
-110	-1	1	1	-1	0	0	0	0	1	-1	-1	1	0	0
1-10	1	-1	-1	1	0	0	0	0	-1	1	1	-1	0	0
-1-10	-1	1	-1	1	0	0	-1	1	0	0	0	0	0	0
101	1	-1	0	0	1	-1	1	-1	0	0	1	-1	0	0
-10-1	-1	1	0	0	-1	1	-1	1	0	0	-1	1	0	0
10-1	1	-1	0	0	-1	1	0	0	-1	1	0	0	1	-1
-101	-1	1	0	0	1	-1	0	0	1	-1	0	0	-1	1
011	0	0	1	-1	1	-1	1	-1	1	-1	0	0	0	0
0-1-1	0	0	-1	1	-1	1	-1	1	-1	1	0	0	0	0
01-1	0	0	1	-1	-1	1	0	0	0	0	-1	1	1	-1
0-11	0	0	-1	1	1	-1	0	0	0	0	1	-1	-1	1
200	2	-2	0	0	0	0	1	-1	-1	1	1	-1	1	-1
-200	-2	2	0	0	0	0	-1	1	1	-1	-1	1	-1	1
020	0	0	2	-2	0	0	1	-1	1	-1	-1	1	1	-1
0-20	0	0	-2	2	0	0	-1	1	-1	1	1	-1	-1	1
002	0	0	0	0	2	-2	1	-1	1	-1	-1	1	-1	1
00-2	0	0	0	0	-2	2	-1	1	-1	1	1	-1	1	-1